THE DESIGN AND DURABILITY OF ADHESIVELY-BONDED JOINTS

Daniel Kong Toon Ng

Imperial College

A thesis submitted for the degree of MPhil/PhD

ABSTRACT

The design and durability of adhesively-bonded scarf joints were investigated in the present project. The geometrical design parameters of the scarf joint design were optimised for maximum load carrying capability. This was undertaken by employing analytical, finite element as well as experimental approaches. The results indicated that relatively low scarf angles and thin scarf tip thickness were essential to the increase of the strength of scarf joints.

The durability of adhesively-bonded joints was also investigated by performing fatigue tests in 'hot/wet' conditions. The results indicated that the silane pretreatment (GPS) is capable of providing a significant increase in durability of the joints when compared to the grit-blast and degrease (GBD) treatment. In addition, it was also observed that the GPS treated joints never failed at the adhesive/adherend interface; whilst the GBD treated joints tested in 'hot/wet' fatigue conditions always failed at the adhesive/adherend interface. This was also observed for medium scale repair panels tested in both 'dry' and 'hot/wet' fatigue conditions.

Predictions of the fatigue threshold using the finite element approach were in good agreement with the experimental results. In addition, predictions of the failure loci for the various joint designs and test conditions were also in good agreement with the experimental results.

ACKNOWLEDGEMENTS

I would first like to thank my parents and my companion for their constant support, attention and reassurance.

I would like to thank, Prof. A.J. Kinloch, for his enthusiasm and encouragements, in addition to his guidance and technical assistance throughout the present project. Also, I would like to thank Prof. S.J. Shaw (Qinetiq) and Dr. R.D. Allington (Dstl) for financially supporting this project as well as for the numerous discussion meetings held throughout the course of the present project..

I would also like to thank the guys in room 393, especially Sasha and Keith, for helping me prepare this thesis. Also, thank you for all those extra-curricular activities that kept us healthy and happy.

Also, I would like to thank the technical support team in the department (Nick, Daniel, Tom Nolan and Hugh) for assisting me in running the experiments as well as keeping things interesting down there.

CONTENTS

Abstract 2

Acknowledgements 3

Contents 4

Nomenclature 10

List of figures 13

List of tables 24

1. **Chapter 1: Introduction**.....28
    - 1.1 Motivation 28
    - 1.2 Aims and objectives 29
    - 1.3 Outline of thesis 30
2. **Chapter 2: Background theory** 32
    - 2.1 Introduction 32
    - 2.2 Interfacial contact 33
        - 2.2.1 Introduction 33
        - 2.2.2 Wetting 34
        - 2.2.3 Surface energies 34
    - 2.3 Mechanism of adhesion 35
        - 2.3.1 Introduction 35
        - 2.3.2 Adsorption theory.....35
        - 2.3.3 Diffusion theory 36
        - 2.3.4 Mechanical interlocking 37
    - 2.4 Surface treatments 37
        - 2.4.1 Introduction 37
        - 2.4.2 Mechanical treatments.....38
        - 2.4.3 Chemical treatments 38
        - 2.4.4 Silane primers 39
        - 2.4.5 Effect of application condition of the silane surface treatment... 42
    - 2.5 The design of adhesively-bonded joints 45
        - 2.5.1 Introduction 45
        - 2.5.2 Design criteria 46

2.5.3 Overlap joints 47
2.5.4 Scarf joints ... .52
2.6 The fracture of adhesively-bonded joints 54
2.6.1 Introduction 54
2.6.2 Stress intensity factor approach 55
2.6.3 Energy balance approach 58
2.7 The fatigue life of adhesively-bonded joints 63
2.7.1 Introduction 63
2.7.2 Environmental attack 65
2.7.3 Water uptake of bulk adhesive 66
2.7.4 Fatigue life prediction 68
2.8 Adhesively-bonded repairs 71
2.8.1 Introduction 71
2.8.2 Considerations and practices 73
2.8.3 Analytical analysis of crack patch repair 76
2.9 Chapter summary 79
3. Chapter 3: Material properties and experimental methods 82
3.1 Introduction.....82
3.2 Material properties 82
3.2.1 Adhesives 82
3.2.2 High strength aluminium alloys 83
3.2.3 Carbon fibre reinforced plastic 85
3.3 Surface treatments 86
3.3.1 Grit blast and degrease (GBD) 87
3.3.2 GBD and silane (GPS) 87
3.3.3 GBD and chromic acid etching (CAE) 88
3.4 Joint preparation 88
3.5 Experimental procedures 90
3.5.1 Introduction 90
3.5.2 Monotonically-loaded test 91
3.5.3 Fatigue and durability test 91
3.6 Adhesively-bonded repair 94
3.6.1 Introduction 94

3.6.2 Repair procedure 94
3.6.3 Durability test of adhesively-bonded repair panels 96
3.7 Chapter summary 99
4. Chapter 4: Optimization of the scarf joint design 100
4.1 Introduction 100
4.2 Analytical analysis 102
4.3 Finite element analyses 104
4.3.1 Introduction 104
4.3.2 Linear-elastic finite element analyses 104
4.3.3 Elastic-plastic finite element analyses 104
4.3.4 Mesh dependencies of the finite element models 105
4.4 Definition of coordinate systems and failure criteria 106
4.4.1 Coordinate systems 106
4.4.2 Critical stress value for linear-elastic analyses 106
4.4.3 Failure criteria for elastic-plastic analyses 107
4.5 Effects of scarf tip thickness 107
4.5.1 Introduction 107
4.5.2 Analytical analysis 108
4.5.3 Elastic finite element analysis 111
4.5.4 Elastic-plastic finite element analysis 116
4.5.5 Experimental results 118
4.6 Effects of scarf angle 121
4.6.1 Introduction 121
4.6.2 Analytical analysis 122
4.6.3 Elastic finite element analysis 124
4.6.4 Elastic-plastic finite element analysis 128
4.6.5 Experimental results 131
4.7 Effects of fillet size 133
4.7.1 Introduction 133
4.7.2 The effect of adhesive fillet size 134
4.7.3 The effect of adhesive fillet entry angle, θ_f 135
4.8 Effect of temper grade of the aluminium alloy adherends 137
4.8.1 Introduction 137

4.8.2 Elastic plastic finite element analysis 138
4.8.3 Experimental results 141
4.9 Comparison between the scarf joint and overlap joint design 142
4.9.1 Introduction 142
4.9.2 Elastic finite element analysis 143
4.9.3 Elastic-plastic finite element analysis 145
4.9.4 Experimental results 148
4.10 Chapter summary 149
5. Chapter 5: Effect of surface treatments – coupon test results 154
5.1 Introduction 154
5.2 Monotonically-loaded test 155
5.2.1 Introduction 155
5.2.2 Scarf joint (t_{st} = 0.4mm; 'L157' T6) [Al-alloy/Al-alloy] 155
5.2.3 Scarf joint (t_{st} = 0.15mm; 'L157' T6) [Al-alloy/Al-alloy]....157
5.2.4 Scarf joint (t_{st} = 0.15mm; 'L156' T4) [Al-alloy/Al-alloy] ...158
5.2.5 Overlap joint ('L157' T6) [Al-alloy/Al-alloy] 159
5.2.6 Single hybrid scarf joint (t_{st} = 0.15mm, 'L156' T4) [Al-alloy/CFRP] 160
5.2.7 Double hybrid scarf joint (t_{st} = 0.15mm, 'L157' T6) [Al-alloy/CFRP] 162
5.2.8 Comparisons of joint designs 164
5.3 Constant amplitude 'dry' fatigue tests 165
5.3.1 Introduction 165
5.3.2 Scarf joint (t_{st} = 0.4mm) [Al-alloy/Al-alloy] 166
5.3.3 Scarf joint (t_{st} = 0.15mm) [Al-alloy/Al-alloy] 167
5.3.4 Comparison of joint designs 168
5.4 Constant amplitude 'hot/wet' fatigue tests 169
5.4.1 Introduction 169
5.4.2 Scarf joint (t_{st} = 0.4mm) [Al-alloy/Al-alloy] 169
5.4.3 Scarf joint (t_{st} = 0.15mm) [Al-alloy/Al-alloy] 171
5.4.4 Overlap joint [Al-alloy/Al-alloy] 173
5.4.5 Single hybrid scarf joint (t_{st} = 0.15mm) [Al-alloy/CFRP] 174
5.4.6 Double hybrid scarf joint (t_{st} = 0.15mm) [Al-alloy/CFRP] ...177

5.4.7 Comparison of joint designs 179
5.4.8 'Back face' strain gauging results 179
5.5 Chapter summary 181
6. Chapter 6: Prediction of the fatigue life-time of adhesively-bonded joints..185
6.1 Introduction 185
6.2 Prediction of adherend failure 186
6.3 Prediction of adhesive and interfacial failure 189
6.3.1 Introduction 189
6.3.2 Fracture mechanics approach to fatigue failure predictions .189
6.3.3 Curve fitting the fracture mechanics data 192
6.3.4 Relevance of the curve fitting parameters 195
6.3.5 Relationship between G_{max}, a and T_{max} for different joint design 199
6.4 Fatigue life-time prediction 206
6.4.1 Introduction 206
6.4.2 Fatigue life-time predictions 207
6.4.3 Discussion 212
6.5 Chapter summary 215
7. Chapter 7: Repaired aluminium alloy panels 217
7.1 Introduction 217
7.2 Experimental results 218
7.2.1 Introduction 218
7.2.2 Fatigue test results 219
7.2.3 Failure loci of crack patched repair panels 222
7.3 Analytical and finite element analysis of crack patching 227
7.3.1 Calculation of Stress intensity factors, K_u and K_r 227
7.3.2 Effect of bending on single sided repairs 228
7.3.3 Finite element calculation of $K_r(a)$ 230
7.4 Future considerations 234
7.5 Chapter summary 235
8. Chapter 8: Conclusions and recommendations for future work 237
8.1 Introduction 237
8.2 Conclusions 238

8.2.1 Optimization of the scarf joint design 238
8.2.2 Effects of surface treatments – coupon test results 240
8.2.3 Prediction of the fatigue life-time of adhesively-bonded joints...
.....243
8.2.4 Repaired aluminium alloy panels 243
8.3 Recommendations for future work 245
References 247

NOMENCLATURE

English alphabet

a	crack length
Δc	Finite element length
C	Compliance (displacement / load)
D	Diffusion coefficient
E_s	Young's modulus of the adherend (subscripts 1 and 2 denotes adherend 1 and 2 respectively)
E_p	Young's modulus of cracked panel
E_r	Young's modulus of repair patch
f	Frequency
ΔG	Applied strain energy release rate range
G_a	Shear modulus of the adhesive
G_c	Critical strain energy release rate
G_{max}	Maximum strain energy release rate
G_{min}	Minimum strain energy release rate
G_s	Shear modulus of the adherend
G_{th}	Threshold strain energy release rate
ΔH_v	Molar heat of vaporization
J	J-integral
K	Stress intensity factor (subscripts I, II and III denotes the mode of loading, mode I, mode II and mode III respectively)
K_0	Stress intensity factor for unrepaired panel
K_c	Critical stress intensity factor
K_∞	Stress intensity factor for a semi-infinite crack in a single-sided crack patch repair
K_r	Stress intensity factor for crack patched repair panel
l	Bond length
M_t	Mass of water adsorbed at time t
M_∞	Equilibrium water uptake
N_f	Number of fatigue cycles to failure
P	Applied load

R Stress ratio

S Stiffness ratio

S_c Stress concentration factor

t Thickness of the adherend (subscripts 1 and 2 denotes adherend 1 and adherend 2 respectively)

t_a Thickness of the adhesive

t_p Thickness of cracked panel

t_r Thickness of repair patch

ΔT Temperature range

T Temperature

u horizontal displacement

U Elastic stored energy

v vertical displacement

V Molar volume

w Width of specimen

W_a Thermodynamic work of adhesion

W_{al} Thermodynamic work of adhesion in liquid

W_d External work done

T_{max} Maximum applied load per unit width

Greek letters

α_1, α_2 Elastic material constants for a bimaterial interface

α_{therm} Thermal expansion coefficient

δ_s Solubility parameter

δ_t Critical crack-tip opening displacement

ε_m Mean strain level

ε_{min} Minimum applied strain

ε_{max} Maximum applied strain

ε_{therm} Thermal strain

γ_{lv} Surface free energy per unit area of liquid-vapour phase

γ_{sl} Surface free energy per unit area of solid-liquid phase

γ_{sv} Surface free energy per unit area of solid-vapour phase

κ Dimensionless bending moment factor

ν	Poisson's ratio (subscript s and a denotes adherend and adhesive respectively)
θ	Contact angle
θ	Scarf angle
$\Delta\sigma$	Applied stress range
σ_c	Critical stress state
σ_{ij}	Stress in the ij plane (ij is the Cartesian coordinate)
σ_m	Mean stress level
σ_{max}	Maximum applied stress
σ_{min}	Minimum applied stress
σ_y	Yield stress
τ_0	Global applied shear stress
τ_{max}	Maximum shear stress

Abbreviations

Al-alloy	Aluminium alloy
ARL	Aeronautical and Maritime Research Laboratory
BFRP	Boron fibre reinforced plastic
CAE	Chromic acid etching
CFRP	Carbon fibre reinforced plastic
CTHERM	Non-dimensionalized thermal mismatch term
DERA	Defence evaluation research agency, UK
ETR	adherend stiffness ratio
FE	Finite element method
GBD	grit-blast and degrease
GPS	γ-glycidoxypropyltrimethoxysilane primer
SIMS	Static secondary ion mass spectroscopy
ToSIMS	high mass resolution time-of-flight secondary ion mass spectrometry

LIST OF FIGURES

Chapter 2

Figure 2.1: Stationary liquid drop on solid surface

Figure 2.2: Diagram showing peel ply used prior to adhesive bonding of carbon fibre reinforced plastics (CFRP)

Figure 2.3: Proposed schematic diagram of the mechanism of adhesion for epoxy adhesive/GPS/ferric oxide surfaces [20]

Figure 2.4: High resolution ToFSIMS spectrum of grit-blasted aluminium coated with GPS, at nominal mass 71 [18]

Figure 2.5: Effect of concentration of γ-aminopropyltriethoxysilane in an aqueous solution used as a primer to pretreat sapphire on the 180° peel energy of an α-Al_2O_3/polyethylene laminate [25]

Figure 2.6: Common designs of adhesively-bonded joints

Figure 2.7: The three common stress states (a) direct (normal) stress (b) shear stress (c) cleavage (peel) stress

Figure 2.8: Schematic representation of Volkersen model of an overlap joint (a) unloaded (b) loaded in tension, elastic adherends and (c) distribution of elastic shear stress in the adhesive layer

Figure 2.9: Schematic representation of (a) loading eccentricity in an overlap joint and (b) reduction of loading eccentricity as joint is loaded

Figure 2.10: Three primary loads of loading (a) mode I or tensile mode (b) mode II or shearing mode (c) mode III or tearing mode

Figure 2.11: Elliptical crack of length, $2a$ in a uniformly stressed, infinite plate

Figure 2.12: General configuration at the free-edge of two bonded dissimilar material

Figure 2.13: Schematic diagram showing crack growth of length Δc of an existing crack of length, a

Figure 2.14: Schematic representation of the crack closure integral method using the finite element method of (a) 4 noded and (b) 8 noded isoparametric elements

Figure 2.15: Variation of strain energy release rate components with crack tip element size in single overlap joint [49]

Figure 2.16: Contours enclosing a crack tip

Figure 2.17: Crack growth rate, da/dN as a function of ΔG_I for epoxy/aluminium TDCB joints [59]
Figure 2.18: Effect of outdoor weathering on the strength of epoxy-polyamide/aluminium alloy structural joints (a) Hot/wet tropical site (b) hot/dry desert site [57]
Figure 2.19: Experimental determination of water uptake in bulk adhesive
Figure 2.20: Predictions of the fatigue life-time of adhesively-bonded overlap joints using (a) the *J*-integral method and (b) analytical solution [63]
Figure 2.21: The increasing use of composite materials on commercial airplanes [86]
Figure 2.22: Overlapping composite plies used to stiffened joint ends in a scarf joint design
Figure 2.23: Common failure modes of composite materials: (a) in-plane damage (b) microbuckling (c) delamination
Figure 2.24: Plots of crack growth versus number of fatigue cycles for crack patched repair panels subjected to various heat-treatment conditions [64]
Figure 2.25: Schematic diagram of a uncracked panel bonded with a patch on one surface. This is used to explain the equivalent crack opening stress, σ_0.
Figure 2.26: Schematic representation of an elliptical crack patch repair.
Figure 2.27: Variation of K_r with crack length, a with the two upper bounds K_0 and K_∞

Chapter 3

Figure 3.1: Shear stress-strain response of FM73 M
Figure 3.2: Experimental and FE predicted tensile stress-strain response of the T4 and T6 2014A aluminium alloys
Figure 3.3: Curing parameters of IM7/8552 carbon fibre reinforced plastic according to Hexcel Corp
Figure 3.4: Experimental and predicted tensile stress-strain response of a 2mm thick composite laminate with a stacking order of $[0, \pm 45, 90]_{2s}$
Figure 3.5: Main joint designs used in current project (a) aluminium alloy single scarf joint (b) aluminium alloy overlap joint (c) aluminium alloy/CFRP single scarf joint (d) aluminium alloy/CFRP double scarf joint (e) presence of scarf tip in a scarf joint
Figure 3.6: Manufacturing of adhesively-bonded joints using a hot press

Figure 3.7: Schematic diagram showing the experimental setup of the 'hot/wet' accelerated fatigue tests

Figure 3.8: (a) diagram showing positioning of strain gauge on adhesively-bonded joint (b) typical strain gauge reading curve observed for crack initiation and crack propagation periods in tension-tension fatigue tests

Figure 3.9: Schematic diagram showing the location of the centre hole and the two sawed notches from the horizontal sides of the centre hole in the aluminium alloy panel

Figure 3.10: Schematic diagram showing the configuration used to produce the adhesively-bonded repair panels

Figure 3.11: Schematic diagram of the experimental setup of the adhesively-bonded repair panel tests conducted in water

Chapter 4

Figure 4.1: Schematic diagram of a scarf joint and definition of symbols used in subsequent sections (a) 3D image of a scarf joint showing the presence of the adhesive fillet as a result of the scarf tip thickness (b) front view of a scarf joint (c) front, detailed, view of a scarf adherend

Figure 4.2: Free body diagram of scarf joint

Figure 4.3: Mesh refinement of the adhesive layer

Figure 4.4: Effect of mesh density in the adhesive layer on the stress components at the (a) centre of the adhesive layer, $y' = 0$ (b) near the interface, $y' = 0.4t_a$

Figure 4.5: Global and local coordinate system used to define stress orientation

Figure 4.6: Plot of maximum shear strain in the adhesive against the thickness ratio, t_{st}/t for scarf joints with adherend thickness 2mm, 4mm and 6mm

Figure 4.7: Shear stress distribution in the adhesive layer for different scarf tip thickness, t_{st} using the analytical solution

Figure 4.8: Normalised direct stress distribution at the centre of the adhesive layer (y' = 0) plotted against distance along the bond length for different scarf tip thickness, t_{st}

Figure 4.9: Normalised peel stress distribution at the centre of the adhesive layer (y' = 0) plotted against distance along the bond length for different scarf tip thickness, t_{st}

Figure 4.10: Normalised shear stress distribution at the centre of the adhesive layer (y' = 0) plotted against distance along the bond length for different scarf tip thickness, t_{st}

Figure 4.11: Normalised direct stress distribution near the adhesive/adherend interface ($y' = 0.4t_a$) plotted against distance along the bond length for different scarf tip thickness, t_{st}

Figure 4.12: Normalised peel stress distribution near the adhesive/adherend interface ($y' = 0.4t_a$) plotted against distance along the bond length for different scarf tip thickness, t_{st}

Figure 4.13: Normalised shear stress distribution near the adhesive/adherend interface ($y' = 0.4t_a$) plotted against distance along the bond length for different scarf tip thickness, t_{st}

Figure 4.14: Variation of the direct stress distribution across the thickness of the adherend opposite a scarf tip with scarf tip thickness, t_{st}

Figure 4.15: Predicted load-displacement curves of scarf joints with scarf tip thickness, t_{st} = 0.15mm and 0.4mm using elastic-plastic finite element analysis

Figure 4.16: Comparison of the maximum (a) shear strain, (b) shear stress, (c) adherend Mises equivalent stress and (d) adhesive Mises equivalent stress in the adhesive layer for scarf joints with scarf tip thickness, t_{st} = 0.4mm and 0.15mm

Figure 4.17: Results from the experimental monotonically-loaded tension tests of scarf joints with scarf tip thickness, t_{st} = 0.4mm and 0.15mm

Figure 4.18: Schematic diagram showing adherend failure in scarf joint specimens. Adherend yielding was observed before final fracture of the specimens

Figure 4.19: Shear stress distribution in the adhesive layer for different scarf angle, θ predicted using the analytical solution

Figure 4.20: Normalised direct stress distribution in the middle of the adhesive layer (y' = 0) plotted against the distance along the bond length for different scarf angles, θ

Figure 4.21: Normalised peel stress distribution in the middle of the adhesive layer (y' = 0) plotted against the distance along the bond length for different scarf angles, θ

Figure 4.22: Normalised shear stress distribution in the middle of the adhesive layer ($y' = 0t_a$) plotted against the distance along the bond length for different scarf angles, θ

Figure 4.23: Normalised direct stress distribution near the adhesive/adherend interface ($y' = 0.4t_a$) plotted against the distance along the bond length for different scarf angles, θ

Figure 4.24: Normalised peel stress distribution near the adhesive/adherend interface ($y' = 0.4t_a$) plotted against the distance along the bond length for different scarf angles, θ

Figure 4.25: Normalised shear stress distribution near the adhesive/adherend interface ($y' = 0.4t_a$) plotted against the distance along the bond length for different scarf angles, θ

Figure 4.26: Comparison of the maximum stress components in the adhesive and the adherend for different scarf angles, θ

Figure 4.27: Predicted load-displacement curves of scarf joints with scarf angles, $\theta =$ 1.5°, 1.8° and 5° using elastic-plastic finite element analysis

Figure 4.28: Comparison of the maximum (a) shear strain, (b) shear stress, (c) adherend Mises equivalent stress and (d) adhesive Mises equivalent stress in the adhesive layer for scarf joints with scarf angles, $\theta =$ 1.5°, 1.8° and 5°

Figure 4.29: Results from the experimental monotonically-loaded tension tests of scarf joints with scarf angle, $\theta =$ 1.5°, 1.8° and 5°

Figure 4.30: Schematic diagram showing adhesive failure in scarf joint specimens

Figure 4.31: Schematic diagram showing the adhesive fillet outside the effective bond length in a scarf joint. (a) no fillet (b) fillet with entry angle, θ_f and (c) full adhesive fillet

Figure 4.32: Percentage reduction of the maximum stress components in the adhesive and adherend for different fillet sizes

Figure 4.33: Peel stress contour plots of scarf joint designs with adhesive entry angle (a) $\theta_f = 30°$ and (b) $\theta_f = 60°$

Figure 4.34: Percentage reduction of the maximum stress components in the adhesive fillet and the adherend for different adhesive fillet entry angles, θ_f

Figure 4.35: Percentage reduction of the maximum stress components in the adhesive fillet and the adherend for different adhesive fillet entry angle, θ_f and equal adhesive fillet area of $1mm^2$

Figure 4.36: Mises equivalent stress contours from elastic-plastic finite element analysis showing gross adherend plastic yielding with increase of applied load

Figure 4.37: Predicted load-displacement curves of scarf joints with L157 (T6) and L156 (T4) aluminium alloy adherends using elastic-plastic finite element analysis

Figure 4.38: Comparison of the maximum (a) shear strain, (b) shear stress, (c) adherend Mises equivalent stress and (d) adhesive Mises equivalent stress in the adhesive layer for scarf joints with 'L157' (T6) and 'L156' (T4) aluminium alloy adherends

Figure 4.39: Results from the experimental monotonically-loaded tension tests of scarf joints with 'L157' (T6) and 'L156' (T4) aluminium alloy adherends

Figure 4.40: Schematic diagram of the global and local coordinate systems used for the overlap joint design

Figure 4.41: Joint bending observed in adhesively-bonded (a) scarf joint and (b) overlap joint with an applied load, P of 5kN

Figure 4.42: Normalized direct stress distribution at the centre of the adhesive layer (y' = 0) plotted against distance along the bond length for the scarf joint and overlap joint design

Figure 4.43: Normalized peel stress distribution at the centre of the adhesive layer (y' = 0) plotted against distance along the bond length for the scarf joint and overlap joint design

Figure 4.44: Normalized shear stress distribution at the centre of the adhesive layer (y' = 0) plotted against distance along the bond length for the scarf joint and overlap joint design

Figure 4.45: Predicted load-displacement curves of the scarf joints and overlap joint design using elastic-plastic finite element analysis

Figure 4.46: Comparison of the maximum (a) shear strain, (b) shear stress, (c) adherend Mises equivalent stress and (d) adhesive Mises equivalent stress in the adhesive layer for the scarf joint and overlap joint design

Figure 4.47: Results from the experimental monotonically-loaded tension tests of the scarf joints and overlap joint design

Figure 4.48: Comparison of the durability of adhesively-bonded scarf joints and overlap joints surface treated with (a) the GBD surface treatment and (b) the GPS surface treatment

Chapter 5

Figure 5.1: Comparison of the static failure loads of aluminium alloy scarf joints with a scarf tip thickness of t_{st} = 0.4mm and 'L157' (T6) for different surface treatments

Figure 5.2: Comparison of the static failure loads of aluminium alloy scarf joints with a scarf tip thickness of t_{st} = 0.15mm and 'L157' (T6) for different surface treatments

Figure 5.3: Comparison of the static failure loads of aluminium alloy scarf joints with a scarf tip thickness of t_{st} = 0.15mm and 'L156' (T4) aluminium alloy adherends for different surface treatments

Figure 5.4: Comparison of the static failure loads of 'L157' (T6) aluminium alloy overlap joints for different surface treatments

Figure 5.5: Finite element analysis of the aluminium alloy/CFRP hybrid scarf joint. The outline diagram is the undeformed shape while the deformed shape is represented by the adhesive (in colour)

Figure 5.6: Comparison of the static strength of GBD and GPS surface treated CFRP/'L156' (T4) aluminium alloy hybrid scarf joints

Figure 5.7: Comparison of the static failure loads of 'L157' (T6) aluminium alloy/CFRP double scarf joints for different surface treatments

Figure 5.8: Pictures showing the (a) double hybrid scarf joint with the aluminium alloy adherends positioned at the outer surface of the joint, (b) double hybrid scarf joint design with the CFRP adherends positioned at the outer surface of the joint, (c) bending of the 'released' adherend (aluminium alloy) and crack propagation in the adhesive layer and (d) non-bending of the 'released' adherend (CFRP composite) and failure in adhesive and composite

Figure 5.9: Comparison of the fatigue performance of aluminium alloy scarf joints with a scarf tip thickness of t_{st} = 0.4mm for different surface treatments
Figure 5.10: Schematic diagram of the adherend failure locus observed in fatigue tests
Figure 5.11: Comparison of the fatigue performance of aluminium alloy scarf joints with a scarf tip thickness of t_{st} = 0.15mm for different surface treatments
Figure 5.12: Comparison of the 'hot/wet' durability performance of aluminium alloy scarf joints with a scarf tip thickness of t_{st} = 0.4mm for GBD and GPS surface treatments
Figure 5.13: Comparison of the 'dry' and 'hot/wet' fatigue performance of aluminium alloy scarf joints with a scarf tip thickness of t_{st} = 0.4mm for the GBD and GPS surface treatments
Figure 5.14: Comparison of the 'hot/wet' durability performance of aluminium alloy scarf joints with a scarf tip thickness of t_{st} = 0.15mm for GBD and GPS surface treatments
Figure 5.15: Typical fracture surface of GBD surface treated aluminium alloy scarf joints tested in 'hot/wet' fatigue conditions
Figure 5.16: Comparison of the 'dry' and 'hot/wet' fatigue performance of aluminium alloy scarf joints with a scarf tip thickness of t_{st} = 0.15mm for the GBD and GPS surface treatments
Figure 5.17: Comparison of the fatigue strength of GBD and GPS surface treated aluminium alloy overlap joints
Figure 5.18: Typical fracture surface of (a) GBD surface treated aluminium alloy overlap joints and (b) GPS surface treated aluminium alloy overlap joints tested in 'hot/wet' fatigue conditions
Figure 5.19: Comparison of the 'hot/wet' fatigue performance of aluminium alloy/CFRP hybrid scarf joints with a scarf tip thickness of t_{st} = 0.15mm for the GBD and GPS surface treatments
Figure 5.20: Fracture surface of (a) GBD and (b) GPS surface treated aluminium alloy/CFRP hybrid scarf joints tested in 'hot/wet' fatigue conditions
Figure 5.21: Comparison of the 'hot/wet' fatigue performance of aluminium alloy scarf joints and aluminium alloy/CFRP scarf joints with a scarf tip thickness of t_{st} = 0.15mm for GBD and GPS surface treatments

Figure 5.22: Durability performance of GBD and GPS surface treated double aluminium alloy/CFRP hybrid scarf joints with a scarf tip thickness of t_{st} = 0.15mm

Figure 5.23: Typical strain gauge reading plot for an aluminium alloy scarf joint model with a scarf tip thickness, t_{st} = 0.15mm tested in 'hot/wet' fatigue conditions where failure was observed to be at the adhesive/adherend interface

Figure 5.24: Comparison of the crack initiation period with the total fatigue life of GBD surface treated aluminium alloy scarf joints with a scarf tip thickness of t_{st} = 0.15mm tested in 'hot/wet' fatigue conditions

Chapter 6

Figure 6.1: Predicted fatigue strength of the aluminium alloy adherend for the various joint designs used in this project

Figure 6.2: The tapered double cantilever beam (TDCB) joint geometry used to obtain fracture mechanics data of an adhesive system

Figure 6.3: Comparison of the fatigue data of GPS and CAE surface treated TDCB joints tested in 'dry' and 'hot/wet' conditions [4]

Figure 6.4: Comparison of the fatigue data of GBD surface treated TDCB joints tested in 'dry' and 'hot/wet' conditions [4]

Figure 6.5: Figure 6.5: Curve fitting of the TDCB fatigue data obtained from [4] using equation 2.3 for the (a) GBD 'dry' tests and (b) GBD 'hot/wet' tests

Figure 6.6: Curve fitting of the TDCB fatigue data obtained from [4] using equation 2.3 for the (a) GPS 'dry' tests and (b) GPS 'hot/wet' tests

Figure 6.7: Effect of the C_T fitting parameter of the modified Paris law on (a) the curve fitting of the fracture mechanics data and (b) the predicted shape of the σ_{max}-N_f curve

Figure 6.8: Effect of the n fitting parameter of the modified Paris law on (a) the curve fitting of the fracture mechanics data and (b) the predicted shape of the σ_{max}-N_f curve

Figure 6.9: Effect of the n_1 fitting parameter of the modified Paris law on (a) the curve fitting of the fracture mechanics data and (b) the predicted shape of the σ_{max}-N_f curve

Figure 6.10: Effect of the n_2 fitting parameter of the modified Paris law on (a) the curve fitting of the fracture mechanics data and (b) the predicted shape of the σ_{max}-N_f curve

Figure 6.11: Typical relationship between G_{max}, T_{max} and a for an adhesive system assuming linear elastic material properties

Figure 6.12: The predicted relationship between G_{max}, T_{max} and a for interfacial and adhesive (cohesive) crack growth in the scarf joint design with a scarf tip thickness of t_{st} = 0.4mm

Figure 6.13: The predicted relationship between G_{max}, T_{max} and a for interfacial and adhesive (cohesive) crack growth in the scarf joint design with a scarf tip thickness of t_{st} = 0.15mm

Figure 6.14: Stress contour plot in the adhesive subjected to a temperature drop of ΔT=100°C

Figure 6.15: The predicted relationship between G_{max}, T_{max} and a for interfacial and adhesive (cohesive) crack growth in the single CFRP/Al-alloy hybrid scarf joint design with a scarf tip thickness of t_{st} = 0.15mm

Figure 6.16: The predicted relationship between G_{max}, T_{max} and a for interfacial and adhesive (cohesive) crack growth in the double CFRP/Al-alloy hybrid scarf joint design with a scarf tip thickness of t_{st} = 0.15mm

Figure 6.17: Prediction of the fatigue strength of aluminium alloy scarf joints with a scarf tip thickness of t_{st} = 0.4mm in 'dry' fatigue conditions

Figure 6.18: Prediction of the fatigue life-time of aluminium alloy scarf joints with a scarf tip thickness of t_{st} = 0.4mm in 'hot/wet' fatigue conditions

Figure 6.19: Prediction of the fatigue performance of aluminium alloy scarf joints with a scarf tip thickness of t_{st} = 0.15mm tested in 'dry' fatigue conditions for different surface treatments

Figure 6.20: Prediction of the 'hot/wet' durability of aluminium alloy scarf joints with a scarf tip thickness of t_{st} = 0.15mm for GBD and GPS surface treatments

Figure 6.21: Prediction of the 'hot/wet' durability performance of CFRP/aluminium alloy single scarf joints with GBD and GPS surface treated aluminium alloy adherends

Figure 6.22: Prediction of the 'hot/wet' durability of CFRP/aluminium alloy double scarf joints with GBD and GPS surface treated aluminium alloy adherends

Chapter 7

Figure 7.1: Comparison of fatigue the crack growth of un-repaired and repaired panels for the GBD and GPS surface treatments

Figure 7.2: Comparison of the fatigue crack growth rate between the repaired and un-repaired crack patched panels

Figure 7.3: Fracture surface of the GBD 'dry' specimen (a) adhesive failure (b) adhesive/aluminium alloy adherend interfacial failure viewed from the aluminium alloy fracture surface(c) adhesive/aluminium alloy adherend interfacial failure viewed from the CFRP composite fracture surface

Figure 7.4: Fracture surface of the GBD 'hot/wet' specimen (a) adhesive failure (b) adhesive/aluminium alloy adherend interfacial failure viewed from the aluminium alloy fracture surface (c) adhesive/aluminium alloy adherend interfacial failure viewed from the CFRP composite fracture surface

Figure 7.5: Fracture surface of the GPS 'hot/wet' specimen (a) adhesive/aluminium alloy adherend interfacial failure viewed from the CFRP composite fracture surface (b) adhesive/aluminium alloy adherend interfacial failure viewed from the aluminium alloy fracture surface (c) CFRP fibre failure at the centre of the repair patch

Figure 7.6: Comparison between the stress intensity factor for the unrepaired panel, K_u and the repaired panels, K_r with and without bending effects

Figure 7.7: Quarter FE model of a repair panel and insert showing a blow-up view of the crack tip

Figure 7.8: Mises stress distribution at the crack tip for with an applied stress of 75MPa

Figure 7.9: Variation of G_{max}/T_{max}^2 for different crack lengths, a, at different locations across the thickness of the aluminium alloy panel

Figure 7.10: Comparison between finite element and theoretical prediction of the repair stress intensity factor, K_r

LIST OF TABLES

Chapter 2

Table 2.1: Fatigue life data of riveted and riveted + bonded overlap joints [2]

Table 2.2: Surface energy or chemically treated aluminium surfaces subsequent to primary amine silane deposition [10]

Table 2.3: Effect of pretreatment on aluminium alloy overlap joint using a two-part cold-cure epoxy [3]

Table 2.4: Apparent thickness of GPS film on grit-blasted aluminium [23]

Table 2.5: Effect of water on the thermodynamic work of adhesion of various interfaces [9]

Table 2.6: Comparison of diffusion coefficients from bulk adhesives and adhesive joint (epoxy/aluminium) of FM73 [52]

Table 2.7: Comparison of material properties of CFRP and metallic materials [66]

Table 2.8: Examples of the current applications of adhesively-bonded composite repair carried out by ARL [60]

Chapter 3

Table 3.1: Material properties of FM73 M

Table 3.2: Material properties of aluminium alloys L156 and L157

Table 3.3: Lamina material properties of IM7/8552 (manufacturer's data)

Chapter 4

Table 4.1: Critical stress values used to normalize stress components

Table 4.2: Failure criteria used in elastic-plastic finite element analysis

Table 4.3: Geometrical parameters of scarf joint models, with 2mm thick adherends, used to investigate the effects of scarf tip thickness, t_{st}

Table 4.4: Example of the iteration procedure used to calculate the maximum shear strain in the adhesive layer at the overlap terminus

Table 4.5: Summary of the predicted failure load of scarf joints with scarf tip thickness, t_{st} = 0.4mm and 0.15mm using elastic-plastic finite element analysis

Table 4.6: Comparison between the experimental and predicted failure load and failure locus of scarf joints with scarf tip thickness, t_{st} = 0.15mm and 0.4mm

Table 4.7: Geometrical parameters of scarf joint models, with 2mm thick adherends, used to investigate the effects of scarf angle, θ

Table 4.8: Results from the iteration procedure used to calculate the maximum shear strain in the adhesive layer at the overlap terminus for different scarf angles, θ

Table 4.9: Summary of the predicted failure load of scarf joints with scarf angles, θ= 1.5°, 1.8° and 5° using elastic-plastic finite element analysis

Table 4.10: Comparison between the experimental and predicted failure load and failure locus of scarf joints with scarf angle, θ= 1.5°, 1.8° and 5°

Table 4.11: Summary of the predicted failure load of scarf joints with 'L157' (T6) and 'L156' (T4) aluminium alloy adherends using elastic-plastic finite element analysis

Table 4.12: Comparison between the experimental and predicted failure load and failure locus of scarf joints with 'L157' (T6) and 'L156' (T4) aluminium alloy adherends

Table 4.13: Summary of the predicted failure load of the scarf and the overlap joint designs using elastic-plastic finite element analysis

Table 4.14: Comparison between the experimental and predicted failure load and failure locus of the scarf joint and overlap joint design

Chapter 5

Table 5.1: Geometrical parameters of the various joint designs used in the investigation of the effects of surface treatments using the monotonically-loaded test method

Table 5.2: Summary of the comparison of the failure loads and failure loci of aluminium alloy scarf joints with a scarf tip thickness of t_{st} = 0.4mm and 'L157' (T6) for different surface treatments

Table 5.3: Summary of the comparison of the failure loads and failure loci of aluminium alloy scarf joints with a scarf tip thickness of t_{st} = 0.15mm and 'L157' (T6) for different surface treatments

Table 5.4: Summary of the comparison of the failure loads and failure loci of aluminium alloy scarf joints with a scarf tip thickness of t_{st} = 0.15mm and 'L156' (T4) aluminium alloy adherends for different surface treatments

Table 5.5: Summary of the comparison of the failure loads and failure loci of 'L157' (T6) aluminium alloy overlap joints for different surface treatments

Table 5.6: Summary of the comparison of the failure loads and failure loci of single hybrid CFRP/'L156' (T4) aluminium alloy scarf joints for different surface treatments

Table 5.7: Summary of the comparison of the failure loads and failure loci of 'L157' (T6) aluminium alloy/CFRP double hybrid scarf joints for different surface treatments

Table 5.8: Summary of the failure loads, failure loci and joint efficiencies of the various joint designs employed in the present project tested under monotonically-loaded test conditions for different surface treatments

Table 5.9: Summary of the fatigue thresholds and failure loci of the scarf joint designs with a scarf tip thickness of t_{st} = 0.4mm and 0.15mm tested in 'dry' fatigue conditions for different surface treatments

Table 5.10: Summary of the fatigue thresholds and failure loci of the joint designs tested in 'hot/wet' fatigue conditions for different surface treatments (taken at a number of fatigue cycles, N_f = 1 million cycles)

Chapter 6

Table 6.1: Predicted stress concentration in the aluminium alloy adherend for the various joint designs used in this project

Table 6.2: The fracture toughness and threshold strain energy release rates of the various adhesive systems [4]

Table 6.3: Curve fitting data used to curve fit the experimental fracture mechanics data of the GBD system obtained from [4]

Table 6.4: Curve fitting data used to curve fit the experimental fracture mechanics data of the GPS system obtained from [4]

Table 6.5: Prediction of the 'hot/wet' fatigue threshold of the GBD surface treated aluminium alloy scarf joints using equation 6.10

Table 6.6: Comparison of the predicted fatigue threshold and failure locus with the experimental results

Chapter 7

Table 7.1: Surface treatment and testing environment of the crack patched repair panels used in this investigation

CHAPTER 1

INTRODUCTION

1.1 Motivation

The joining of structural components has always been a subject of interest to design engineers. This interest is rightly justified, as a joint often proves to be the weak point in a structure. The basic philosophy of joining two components that are carrying loads is to transmit the load-carrying capability from one component to the other as smoothly as possible. In the aerospace industry, mechanical fasteners have been the traditional means of joining components. There are many advantages of this joining technique, mainly that the load is spread out by the numerous fasteners and hence this reduces the concentration of stress on a singular point. However, as advanced as this means of joining is, there is still a major concern that the concentration of stresses around an individual fastener hole will cause fatigue or creep problems. Indeed, there have been past cases where fatigue cracks have grown between fastener rows and caused catastrophic failure of a structural component. The reason for the lack of fatigue durability of a mechanical fastener can be explained by the fact that the stresses around an individual mechanical fastener are still relatively high and may therefore lead to the initiation and propagation of fatigue cracks.

The development of adhesives technology has presented an alternative means of joining structural components. In the aerospace industry, the use of adhesives has been

able to improve significantly the fatigue life of a structure. This is because, an adhesive joint allows the stresses to be distributed evenly across the width of the joint, significantly reducing the local stress concentrations commonly encountered in mechanically fastened joints. The use of adhesives technology, however, causes some additional problems to the design engineers. Adhesives used in the aerospace industry are mainly based upon rubber-toughened epoxies and, in particular, it has been reported that the interfacial adhesion to aluminium alloy joints is highly susceptible to moisture attack. The durability of aluminium alloy joints can, however, be improved by employing a surface pretreatment for the adherends. Indeed, surface pretreatments are often used to increase the interfacial adhesion and protect the adhesive/adherend interface from environmental attack. Surface treatments such as grit blasting and phosphoric acid anodising (PAA) form the basis of standard protocols in most aircraft repair handbooks. However, the most effective surface treatments currently being used for aluminium alloy joints are strong acids and are a hazard to the environment.

1.2 Aims and objectives

A main theme of the present project is to investigate the effects of surface treatments on the durability of adhesive joints, especially with bonded repair joints in mind. Of particular interest is the fatigue durability of aluminium alloy joints which have been surface treated using a γ-glycidoxypropyltrimethoxysilane (GPS) organosilane surface treatment. This surface treatment is considered to be environmental friendly and easier to use than the current acid etching and anodizing techniques. The performance of this surface treatment will be compared with two other commonly used surface treatments for aluminium alloy joints: a grit blasting and degreasing (GBD) surface treatment and a chromic acid etching (CAE) surface treatment.

Below is a list of the main objectives.

1) To optimize the scarf joint design, as this joint design will be used as the main joint design in the project. The reason for using the scarf joint design is because the scarf joint design is considered more efficient than the commonly used overlap joint design

and is frequently used in adhesively-bonded repair designs. The optimization of the scarf joint geometry will be carried out by using analytical, finite element (FE) and experimental methods. The scarf joint geometry will be optimized for maximum load-carrying ability.

2) To predict the fatigue life-time of adhesively-bonded scarf joints using an energy balance approach that employs the fracture mechanics data measured for the same adhesive system.

3) To investigate the fatigue performance of adhesively bonded hybrid joints using aluminium alloy and carbon fibre composite adherends. Coupon tests of the previously determined optimized scarf joint geometry, as well as a double scarf joint geometry, will be used.

4) To study the effects of residual thermal stresses on the fatigue performance of composite/aluminium alloy scarf joints.

5) To investigate the performance of centre-cracked aluminium alloy panels which have been repaired using a single-sided external crack patch technique. These tests represent relatively large-scale components on which to validate the ideas developed during the present research.

6) To predict therefore the effect of different surface treatments on the fatigue durability of the various types of joints.

1.3 Outline of thesis

The outline of the thesis is given in the list below:

Chapter 2: This chapter presents the background theories and a literature review relevant to the project.

Chapter 3: This chapter discusses the material properties of the various materials used, the manufacturing process employed for the adhesively-bonded joints and the various experimental tests methods used in this project.

Chapter 4: This chapter presents the design and optimization of the scarf joint geometry using analytical, finite element and experimental methods. In addition, a comparison between the overlap joint geometry and the scarf joint geometry will also be presented in this chapter.

Chapter 5: Experimental results from the investigations of the effects of surface treatments on the static, fatigue and durability performance of adhesively-bonded scarf joints are presented in this chapter. In addition, experimental results of the composite/aluminium alloy hybrid joints will be discussed.

Chapter 6: This chapter discusses the prediction of the fatigue life-time of adhesively-bonded joints using the energy balance approach. In addition, the significance of the fitting parameters for the modified Paris law, which is an important aspect of the predictive model, will also be reviewed.

Chapter 7: Experimental results of the crack patched repair panels tested in 'dry' and 'hot/wet' fatigue conditions are presented in this chapter. This is followed by a discussion of the theoretical and finite element predictions of the reduction in the stress intensity factor for the repaired panels.

Chapter 8: This chapter will present the main conclusions from this project. In addition, recommendations for future work are also given.

CHAPTER 2

LITERATURE SURVEY

2.1 Introduction

Adhesive bonding has been used in many applications since early times. Natural adhesives such as beeswax and gum were used before the development of adhesion and adhesives science to create weapons and armour, as well as cooking utensils. In the present age, the use of adhesive bonding is widespread and encompasses many aspects of human life, from pressure sensitive adhesives, such as 'Post-it' notes, to the joining of structural components in the aerospace industry.

In the present research, we will concentrate on the use of structural adhesives in the aerospace industry. The development of structural adhesives for the aerospace industry has proved to be invaluable as adhesive bonding is able to offer new possibilities for the joining of components. One of the main advantages of adhesive bonding over conventional methods of joining, such as mechanical fasteners, is that adhesive bonding allows a load to be transferred far more evenly from one component to the other. This in turn reduces stress concentrations around fastener holes and, as a result, prolongs the life of structural components. The use of adhesively-bonded joints in aerospace structures has been proven to increase the fatigue life of structural components by as much as thirty times compared to riveted joints, see Table 2.1. Another major advantage of adhesive

bonding is the suitability of this technique to join dissimilar materials and thin sheet materials.

Table 2.1: Fatigue life data of riveted and riveted + bonded lap joints [2]

Adherend thickness (mm)	Stress (MPa)	Life (kcycles)	
		Riveted	Riveted + bonded
0.8	78-196	6	297
0.8	69-177	30	440

The use of adhesives for load bearing structures has to be carefully designed and researched. The right design of adhesive joints is important to ensure that the joint realises its full potential. It is well known that adhesives are best used when they are loaded in shear or compression. On the other hand, adhesives are often relatively weak when loaded in tension.

In the following sections, the fundamentals of adhesive bonding, such as the fundamentals of achieving adhesion and the various mechanisms of adhesion, are first discussed. Then the role of surface treatments for improving adhesion is discussed. This is followed by a review of the design of adhesive joints, where the overlap joint and the scarf joint designs will be discussed in detail. Brief reviews of the principles of fracture mechanics and the fatigue behaviour of adhesive joints are then presented. Lastly, a summary of the use of adhesives for repairing damaged aerospace structures is given.

2.2 Interfacial contact

2.2.1 Introduction

In order for adhesion to take place, it is necessary that interfacial contact is established between the adhesive and the adherend. In other words, the adhesive needs to be able to spread over the bonding surface and displace air and other contaminants that may be present on the surface. The ability of an adhesive to achieve interfacial contact with a solid surface defines the suitability of any adhesive/adherend combination. This can be investigated via the wetting equilibria of the adhesive/adherend system and from the free energy of the adhesive/adherend interface.

2.2.2 Wetting

The wettability of a surface is defined as the extent to which a liquid is capable of spreading on top of a solid surface. This can be shown quantitatively as a liquid drop sitting in equilibrium on a solid surface. The liquid drop will form a parabolic shape and makes an angle to the adjacent surface, termed the contact angle, see Figure 2.1. The contact angle can be used as a measure of wettability of an adhesive/adherend combination. A contact angle of $\theta = 0$ signifies that liquid will spontaneously spread across the solid surface. As $\theta > 0$, the liquid becomes stationary. However, the liquid can still spread when $\theta > 0$ if an external pressure is applied to the liquid. The Young equation [1] relates the surface free energy per unit area of solid vapour, γ_{sv}, liquid-vapour, γ_{lv} and solid-liquid, γ_{sl} to the equilibrium contact angle, θ.

$$\gamma_{sv} = \gamma_{sl} + \gamma_{lv} \cos\theta \quad \text{.....(2.1)}$$

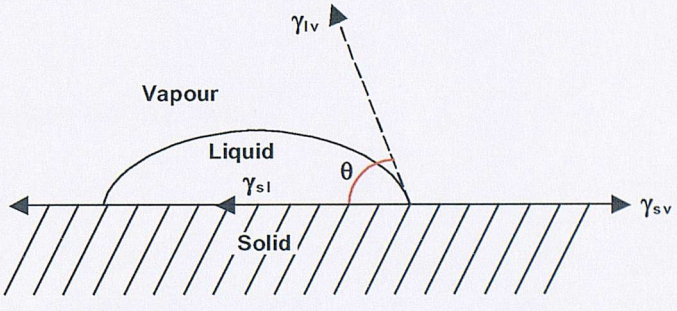


Figure 2.1: Stationary liquid drop on solid surface

2.2.3 Surface energies

Surface energy is generated at the surface of a liquid or solid. As the atoms at the surface are pulled toward the bulk material, the atomic bond length at the surface decreases. This results in an increase of energy at the surface, called the surface energy. The surface energy of a solid can be enhanced by surface pretreatments. Table 2.2 summarises the improvement in the surface energy of aluminium surfaces that can be achieved using chemical surface treatments [10].

Table 2.2: Surface energy of chemically treated aluminium surfaces subsequent to primary amine silane deposition[10]

Surface treatments	Surface energy (mJ/m^2)
degreased	49 ± 4
Chromic acid etching	44 ± 4
Phosphoric acid anodising	76 ± 2
Chromic acid anodising	68 ± 4

Different materials exhibit different surface energies and can be categorized into low surface energy and high surface energy materials. Organic compounds such as polymers are grouped into the first category, where surface free energies are typically less than about 100 mJ/m^2. On the other hand, metals, metal oxides and ceramics belong to the second group where surface energies are typically greater than 500 mJ/m^2, for clean surfaces.

2.3 Mechanism of adhesion

2.3.1 Introduction

Now that the mechanism for interfacial contact of adhesives has been established, we turn our attention to the intrinsic adhesive forces which may act across the interface, and the nature and magnitude of these forces. They are a number of theories to describe the intrinsic adhesion, namely: the (a) adsorption theory, (b) diffusion theory, (c) mechanical interlocking and (d) electronic theory. One or more of these mechanisms may occur in a particular adhesive system. For structural applications, mechanical interlocking, diffusion theory and the adsorption theory are the most relevant theories.

2.3.2 Adsorption theory

The adsorption theory is perhaps the most widely applicable theory for the intrinsic mechanism of adhesive bonding. The theory proposes that interatomic and intermolecular forces are present at the interface of the adhesive and the adherend. These forces are categorized into two categories: primary and secondary forces. The van der Waals forces, as well as hydrogen bonds, are categorized as secondary forces and are relatively low in

magnitude compared to the primary forces. Nevertheless, there has been evidence that secondary forces alone are sufficient to provide a strong bond at the adhesive/adherend interface [9]. Assuming only secondary bonds are acting at an adhesive/adherend interface, the thermodynamic work of adhesion, W_a, can be determined using the Dupré equation, equation 2.2. The thermodynamic work of adhesion, W_a, is defined as the work required to separate a unit area of a solid and a liquid phase that forms an interface across which only secondary forces are present [9].

$$W_a = \gamma_s + \gamma_{lv} - \gamma_{sl} \quad \text{.....(2.2)}$$

(Note that in the Dupré equation, γ_s is used instead of γ_{sv}. This, as pointed out by Wake [5], is because γ_{sv} would have implied that the calculated work of adhesion, W_a is referring to the adhesion failure between the bulk liquid and a layer of molecules of the liquid one molecule thick.)

Primary forces are ionic, covalent and metallic interfacial bonds. They are chemical bonds that sometimes form across the interface. The use of primers in particular has been reported to show evidence of the existence of primary covalent bonds at the interface, as will be discussed later. The most common type of such organometallic primers is the silane-based primer. The use of silane-based primers is further discussed in section 2.4.4. Primers are often used to enhance adhesion and used to provide improved resistance of the interface to attack by moisture. The mechanism by which silane-based primers work to achieve these aims were unknown until more recent reports showed evidence of the formation of strong primary bonds between the primer and the adhesive and adherend [4,18,29].

2.3.3 Diffusion theory

The diffusion theory [21] states that the intrinsic adhesion of polymers to themselves and to each other is due to mutual diffusion of polymer molecules across the interface. This in turn requires the chain segments of the polymers to possess sufficient mobility and are mutually soluble. The solubility parameter, δ_s is defined by equation 2.3 where ΔH_v is the molar heat of vaporization, R is the gas constant, T is the temperature (K) and V is the molar volume.

$$\delta_s = \left(\frac{\Delta H_v - RT}{V} \right)^{1/2} \quad \text{.....(2.3)}$$

The theory of diffusion appears to hold true only for cases where the above mentioned two conditions are satisfied (e.g. autohesion of elastomers and in the solvent welding of compatible, amorphous plastics). In a polymer/metal interface, it was noted that the increase of interfacial strength is due to improvement in the adsorption of the polymeric material rather than by the above classical diffusion mechanism [19].

2.3.4 Mechanical interlocking

Mechanical interlocking is self explanatory, whereby the intrinsic forces are of a mechanical form and are generated by irregular surface topology which may be caused by mechanical or chemical surface treatments. However, the fact that good adhesion is attainable on macroscopically smooth surfaces suggests that this theory might not be of wide applicability [9].

2.4 Surface treatments

2.4.1 Introduction

The role a surface treatment plays in a bonding process is crucial in many ways. The type of surface treatments employed is dependent on the adhesive/adherend system and on the bonding conditions. Surface treatments are often crucial for the bonding of high surface energy materials such as aluminium alloys. This is because high surface energy materials attract atmospheric contamination more readily. In addition, most metallic materials come with some form of protective coating (such as protective oils, grease, etc.) that in most cases needs to be removed before the application of adhesive bonding. Furthermore, in order to attain high durability for the adhesive bond, relatively complex and expensive (often chemical) surface treatments need to be used to ensure that the intrinsic forces at the adhesive/adherend interface do not fail in the presence of water; and thereby allow layers of water molecules to form a weak boundary layer. This will be further discussed in section 2.7.2 where we consider environmental attack and the durability of adhesively-bonded joints. Here, we will concentrate on the use of surface treatments on two

materials, high strength aluminium alloy and carbon fibre reinforced plastic (CFRP), as these materials were used in the present project.

2.4.2 Mechanical treatments

Mechanical surface treatments come in the form of grit-blasting or hand abrasion. Grit-blasting can use alumina grit or fine sand. For CFRP, low-pressure grit-blasting is often used to provide a relatively rough bonding surface. Another way of surface treating CFRP is to use the peel-ply method, see Figure 2.2. A ply of fabric, commonly made of woven or knitted nylon, is installed on the bonding surface and is only removed just before bonding [84]. However, it was found that it is extremely difficult to ensure that the peel-ply does not leave behind some form of contamination, usually in the form of release agents. Nevertheless, in practice, some residual release agent from the peel-ply is tolerable or the use of an abrasion method such as grit-blasting can be used following the removal of the peel-ply.

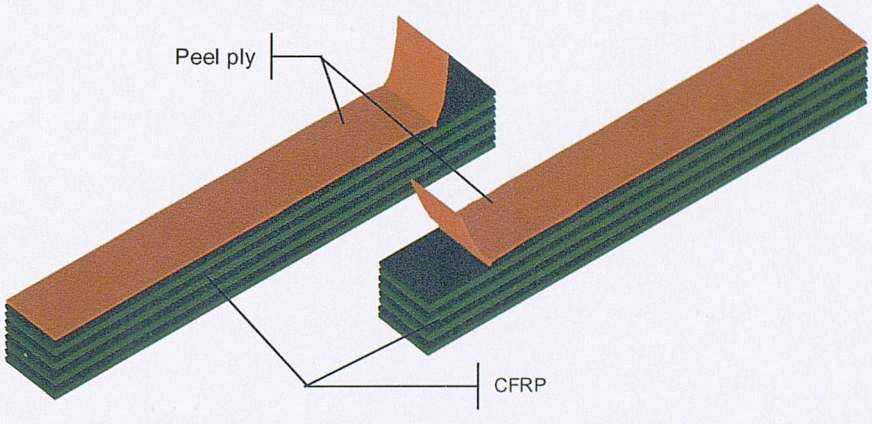


Figure 2.2: Diagram showing peel ply used prior to adhesive bonding of carbon fibre reinforced plastics (CFRP)

2.4.3 Chemical treatments

Aluminium alloys are often surface treated prior to bonding with some form of chemical treatment to enhance the durability of the bonded joint. This is because the high surface energy of the aluminium oxide layer makes the interface and oxide prone to water attack [9]. In the aerospace industry, aluminium alloys are often used in the building of an

aircraft because of their low density and high strength. The durability of bonded joints of aluminium alloys hence becomes an important issue. Common surface treatments employed by the aerospace industry are acid etching and anodizing processes and Table 2.3 shows the effect of the type of surface treatment used on the joint strength of aluminium alloy bonded lap joints [3]. It can be clearly seen that the grit blast and degrease surface treatment is inferior compared to the other chemical surface treatments.

Table 2.3: Effect of pretreatment on aluminium alloy overlap joints using a two-part cold-cured epoxy [3]

Surface treatments	Strength (MPa)	Coefficient of variation (%)
Solvent wipe	11.7	44.7
Grit blasting	12.0	14.1
Chromic acid etching	24.8	13.0
Chromic acid anodising	24.1	9.7

2.4.4 Silane primers

Chemical surface treatments can be expensive and the acids commonly used in these surface treatments are a hazard to the environment. Thus, the use of primers for surface treating high surface energy materials is becoming increasingly popular. The silane primers in particular are popular and were first used to pretreat fibre composites in the 1940s to increase the environmental durability of glassfibre reinforced plastic composites (GRP). Silanes are generally in the form of $Y(CH_2)_nSiX_3$, where $0 < n < 3$, Y is an organofunctional group that can react with the matrix in a composite or the adhesive. X is a hydrolysable group on silicon that, in the presence of water, hydrolyses and initiates a complex cascade of reactions that involves the formation of silanols (SiOH) that are responsible for bond formation with the adherend. Silanes are usually prepared as a dilute solution in water or in a water/ethanol solution. The reason for mixing the silane solution with alcohol is to avoid the formation of large oligomers [11] while the silane hydrolyses to create silanols before the application of adhesive bonding.

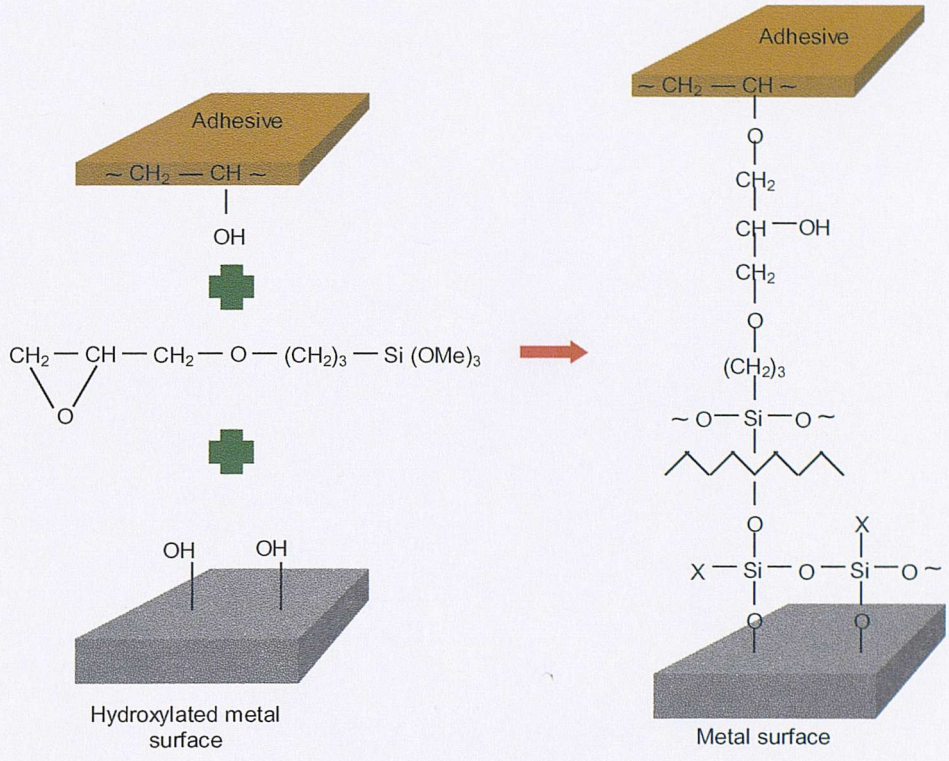


Figure 2.3: Proposed schematic diagram of the mechanism of adhesion for epoxy adhesive/GPS primer/ferric oxide interfaces [20]

There has been evidence that silane primers are capable of reinforcing the intrinsic mechanism of an adhesive/adherend interface by the formation of primary bonds [4, 20]. Gettings and Kinloch [20] have investigated the interfacial bonding between γ-glycidoxypropyltrimethoxysilane (GPS) and mild steel adherends using X-ray photoelectron and static secondary ion mass (SIMS) spectroscopy. They postulated that evidence of SiO_2H^-, $SiOH^+$ and SiO_2^- in the spectrum suggests that a polysiloxane structure on the metal substrate could have formed from the polymerization of the silane primer. The polysiloxane structure forms many adsorption sites per molecule and as a result, the primer does not behave as a weak boundary layer. In addition, evidence of the $FeSiO^+$ ion was also detected. This suggested the formation of Fe-O-Si bonds between the metal oxide and the siloxane primer (see Figure 2.3)

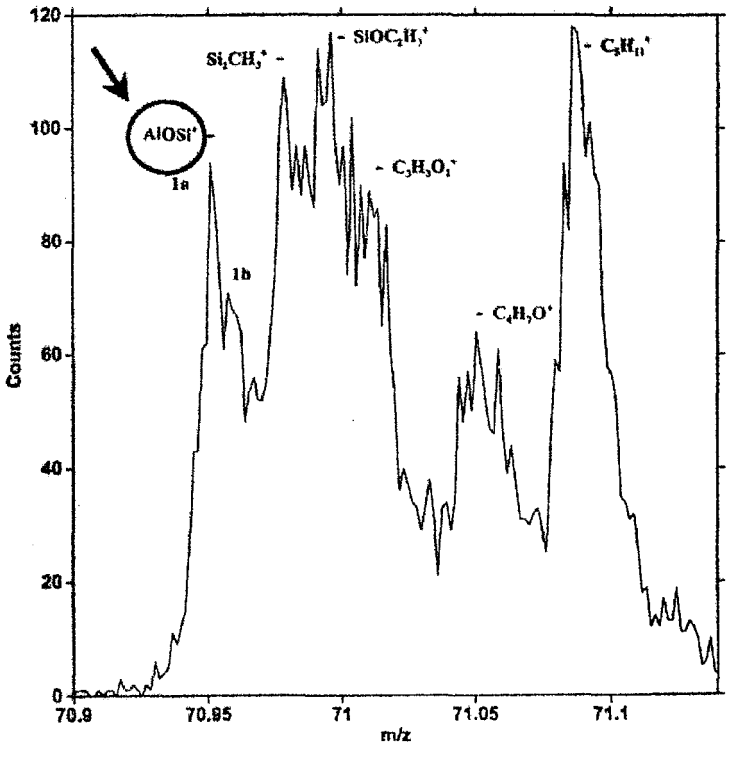


Figure 2.4: High resolution ToFSIMS spectrum of grit-blasted aluminium coated with GPS, at nominal mass 71 [18]

Interestingly, it was found that organosilane primers such as GPS enhance the durability of an epoxy adhesive/steel adhesive system more effectively than for an epoxy adhesive/aluminium alloy adhesive system [24]. Sennett *et al.* have shown that this behaviour could be attributed to the fact that both ends of the GPS molecule have a tendency to attach themselves to the alumina surface. As a result, the functional epoxy end of the molecule would not be available to react with the subsequently deposited adhesive. In the case of steel, the silicon-bearing end reacts quickly with the steel surface, but the epoxy functionality is much slower to reach the surface. On the other hand, the high polarity of the alumina surface (relative to iron oxide) binds all primer functional groups to the surface and inhibits the formation of a continuously, covalently bonded path from the oxide surface to the bulk adhesive. However, evidence of siloxane bonds at the interface of an organosilane and aluminium oxide surface was found recently by using high mass resolution time-of-flight secondary ion mass spectrometry (ToFSIMS) [4,18]. These workers found that, by using a caesium ion source, ToFSIMS was able to show

convincingly the existence of the $AlOSi^+$ species on GPS treated aluminium alloy surfaces (Figure 2.4).

2.4.5 Effect of application conditions of the silane surface treatment

A brief discussion of the effects of application conditions of the GPS surface treatment is given here. There are several ways whereby the effectiveness of the GPS surface treatment can be optimized. The main variables that can be considered are:

- Solution concentration
- Solution pH
- Drying time
- Drying temperature

2.4.5.1 Solution concentration

The concentration of a silane solution affects the thickness of the silane film [22]. Sung *et. al* [25] showed that the optimum solution concentration for an α-Al_2O_3/polyethelene laminate is between 1-3 % v/v, see Figure 2.5. The same effect was also observed for an epoxy adhesive/aluminium alloy interface where Mazza [26] reported that cohesive failure was observed for 'Boeing wedge' test specimens with the silane solution concentration between 1-3 % v/v. This is because at higher solution concentrations, the formation of a relatively thick and weakly polymerized polysiloxane constituted a weak boundary layer between the adherend and the silane film. This weak layer was found to be the site for joint failure.

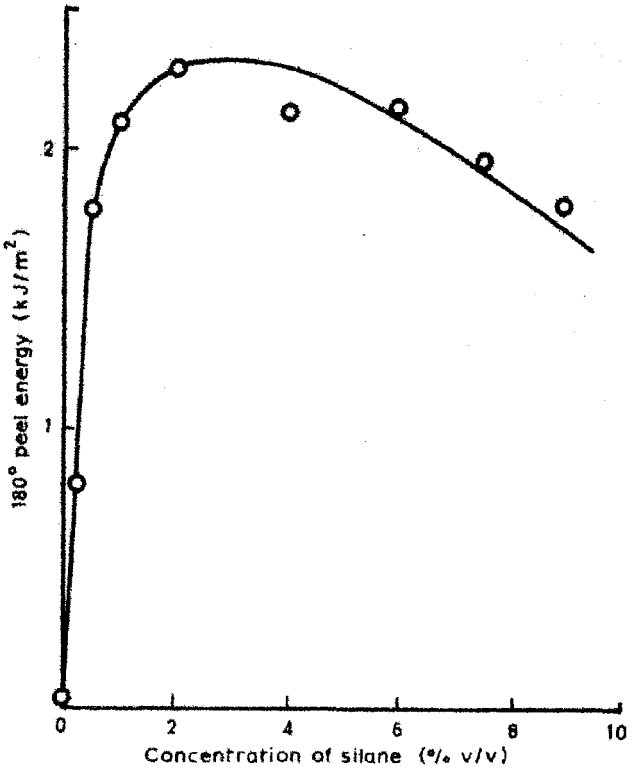


Figure 2.5: Effect of concentration of γ-aminopropyltriethoxysilane in an aqueous solution used as a primer to pretreat sapphire on the 180° peel energy of an α-Al_2O_3/polyethylene laminate [25]

2.4.5.2 Solution pH

The solution pH can also affect the rate at which the silane solution hydrolyses, and this in turn affects the silane film thickness. It has been suggested that the silane solution should be adjusted to have a pH of around 4. This is because, at pH 4, the hydrolysis rate is very fast and hence the formation of oligomers (i.e. small clusters of molecules) is minimized [4]. As a result, the silane in solution will be mainly monomeric (i.e. single molecules) in nature which can react completely and forms a dense silane film without defects. However, it was reported by Mazza [26] that no significant difference in failure locus was observed for 'Boeing wedge' test specimens with the silane solution in the range of pH 4 to 7.2.

2.4.5.3 Drying time

Mazza [26] also showed that by using a 1% GPS pretreatment for 'Boeing wedge' specimens, hydrolysis times (i.e. the time the solution was allowed to stand prior to its

use) of 45 minutes and 1 hour led to 100% cohesive failure within the adhesive; shorter or longer hydrolysis times led to inferior results with interfacial failure being recorded. Sung et al. [25] also showed that for longer drying times than about 1 hour, a decrease in joint durability was observed.

2.4.5.4 Drying temperature

Mazza [26] also found that by increasing the drying temperature of silane films from room temperature to 93°C, the joint durability of wedge specimens increased and all the joints failed cohesively in the adhesive. However, at higher temperatures still, Mazza observed an increase in crack growth rate in the 'Boeing wedge' specimens. Hence, he concluded that a drying temperature of 93°C was the optimum drying temperature. The same conclusion was reached by Abel et al. [23] where, by using XPS and ToFSIMS analyses, they found that increasing the drying temperature of silane solutions increased the cross link density of a GPS film on grit-blasted surface. Furthermore, they showed that overheating could lead to degradation of the deposited film (see Table 2.4). This is because at higher temperatures the condensation of silanol groups produces a dense silane network that limits the respective mobilities of silane and adhesive [4]. As a result, the formation of an interpenetrating network with the polymeric adhesives becomes difficult. This explains the reason for the drop in the durability of the GPS surface treated 'Boeing wedge' test specimens carried out by Mazza when higher drying temperatures (i.e. > 93°C) for the silane solution were used.

Table 2.4: Apparent thickness of GPS film on grit-blasted aluminium [23]

Drying temperature (°C)	Film thickness (nm)
23	2.9
50	1.8
93	2.0
120	0.8

2.5 The design of adhesively-bonded joints

2.5.1 Introduction

The design of an adhesively-bonded joint is crucial to the structural integrity of the joint. It is recognized that the maximum performance of adhesively-bonded joints can be achieved when the adhesive is loaded in shear or compression. Figure 2.6 shows some of the more common joint designs that follow this philosophy [84]. In addition, it can be observed that in all the joint designs shown, the adhesive layer is either parallel or orientated at a small angle to the longitudinal plane. This is to allow the adhesive to be loaded in a state of shear. However, when sufficiently high loads are applied to the joints, the joints will bend and cleavage or peel stresses can be generated at the overlap terminus. This is caused by the eccentricity of loading.

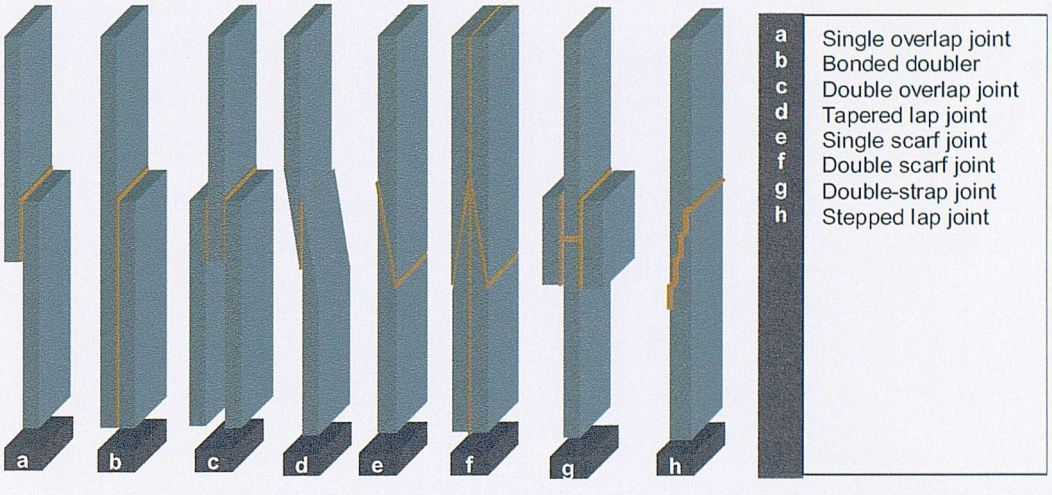


Figure 2.6: Common designs of adhesively-bonded joints

Depending on the design of an adhesively-bonded joint, the adhesive layer can be subjected to three kinds of stresses. They are the direct (normal) stresses, the shear stresses and the peel (cleavage) stresses (see Figure 2.7). The direct or normal stresses are the stresses acting normal to the plane on which they act and may be tensile or compressive. Shear stresses are stresses acting parallel to the plane on which they act and the peel or cleavage stresses are generated (1) when there is loading eccentricity or a bending moment in the joint or (2) if one or both of the adherends are flexible. Hence, even if an adhesively-bonded joint is designed to be purely in a state of shear, peel and

cleavage stresses may still appear when the joint is loaded and these stresses are often the cause of joint failure. However, the peel and cleavage stresses can be reduced by using geometrical optimizing procedures. For example, the double and tapered lap joints are geometrically optimized designs of the basic overlap joint design, see Figure 2.6.

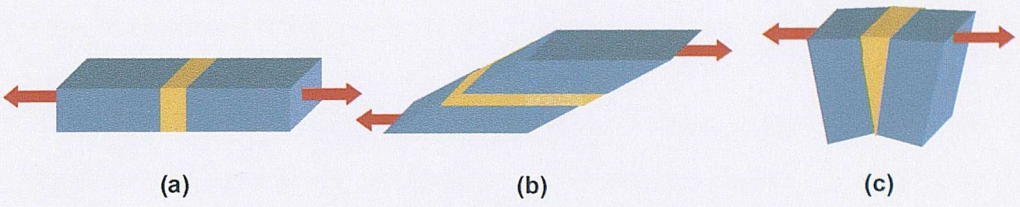


Figure 2.7: The three common stress states (a) direct (normal) stress (b) shear stress (c) cleavage (peel) stress

As mentioned in the introduction to this chapter, one of the main advantages of adhesively-bonded joints is that the applied loads can be transferred more evenly across the joint. Hence, adhesively-bonded joints are usually analysed in the plane strain condition, where the transverse stresses across the plane of the joint are usually ignored. Plane strain assumes that there is a stress component but no deformation in the transverse direction across the plane of the joint. However, plane strain assumptions do not occur in real structural components. Indeed, it is understood that plane strain condition gives a more conservative prediction compared to the plane stress condition while the stress state in real structures will occur somewhere between these two limits. In terms of using finite element modelling and analytical methods to examine the stress distribution in adhesively-bonded joints, two-dimensional modelling has the advantage of reducing computational time and three dimensional complexities.

The next section will review the methods used to design adhesively-bonded joints as well as the design criteria that are commonly used. This is followed by a review section of the design and optimization of the overlap and the scarf joint geometry.

2.5.2 Design criteria

Two methods commonly used to examine and optimize the geometrical parameters of adhesively-bonded joints are analytical methods and finite element methods. Also, the design of an adhesively-bonded joint can be undertaken via a linear elastic analysis or an

elastic-plastic analysis. Linear elastic analyses are useful to optimize geometrical parameters of a particular design when it is expected that the adhesively-bonded joint will be mainly loaded within the elastic region. This is usually the case in aerospace applications as adhesively-bonded joints are subjected to fatigue loads according to the flight cycles of an aircraft and are rarely loaded to give gross plastic deformation. In addition, linear elastic analyses are computationally economical.

Linear elastic analyses often make use of stress concentration factors to rank joint designs. As mentioned in the previous section, adhesively-bonded joints performed best when the adhesive is loaded in shear or compression. Hence, linear elastic analyses can be used to minimize peel (cleavage) and tensile stresses in a joint design. This type of analysis will be further discussed in the following sections, as well as in Chapter Four where linear elastic analyses are used to optimize the scarf joint design.

Elastic-plastic analyses are used when the full behaviour of an adhesively-bonded joint is needed. This type of analysis is commonly used to predict the static failure loads of adhesively-bonded joints. Unlike the fatigue loading cases, adhesively-bonded joints under static loads are usually designed to sustain some form of plasticity especially in the adherends before final failure of the joint. Hence, a linear elastic analysis will not accurately predict the failure strength of the joint. In any type of analysis, in order to predict failure, a failure criterion has to be established. The commonly used failure criteria are the critical shear stress/strain criterion and the von Mises equivalent stress criteria for two dimensional analyses. In addition, failure in the adherend needs to be predicted and the von Mises equivalent stress is normally used in the two dimensional case.

2.5.3 Overlap joints

2.5.3.1 Volkersen model

Analytical solutions of the stress distributions in adhesively-bonded joints were first investigated by Volkersen [6]. He used a simple two dimensional, linear elastic model to investigate the stress distribution in an overlap joint design. He proposed the use of the differential shear strain theorem. The adherends are assumed to be elastic and hence the tensile strain in the adherends decreases from the applied tensile strain at the beginning of

the overlap region to zero at the end of the overlap region. The two adherends are orientated on opposite sides of the adhesive layer and will attempt to pull the joint apart under the action of an applied tensile load. The magnitudes of the tensile strains depend on the stiffness of the adherends (see Figure 2.8b). As a result, the shear stress distribution in the adhesive layer is parabolic in form with the maximum stresses near the ends of the overlap region (see Figure 2.8c). This phenomenon is termed the differential shear strain. Volkersen showed that a stress concentration factor, S_c could be calculated based on the maximum shear stresses (near the end of the overlap region), τ_{max} and the global applied shear stress, τ_0. By assuming that the adhesive and the adherends are elastic solids, the stress concentration factor (see equation 2.4) can be shown to be related to the elastic material constants of the adherends, E_{s1} and E_{s2} (where subscripts 1 and 2 are the adherends 1 and 2), the shear modulus of the adhesive, G_a, the bond length, l_a, the thickness of the adherends, t_i, where subscript i denotes adherend 1 or 2, and the thickness of the adhesive, t_a (see Figure 2.8a). The stress concentration factor, S_c is defined as:

$$S_c = \frac{\tau_{\max}}{\tau_0} = \left(\frac{\Delta}{W}\right)^{1/2}\left[\frac{W-1+\cosh(\Delta W)}{\sinh(\Delta W)^{1/2}}\right] \quad \text{.....(2.4)}$$

where Δ is a dimensionless coefficient:

$$\Delta = \frac{G_a l_a^2}{E_{s2} t_2 t_a} \quad \text{.....(2.5)}$$

and W is defined by:

$$W = \frac{(E_{s1} t_1 + E_{s2} t_2)}{E_{s1} t_1} \quad \text{.....(2.6)}$$

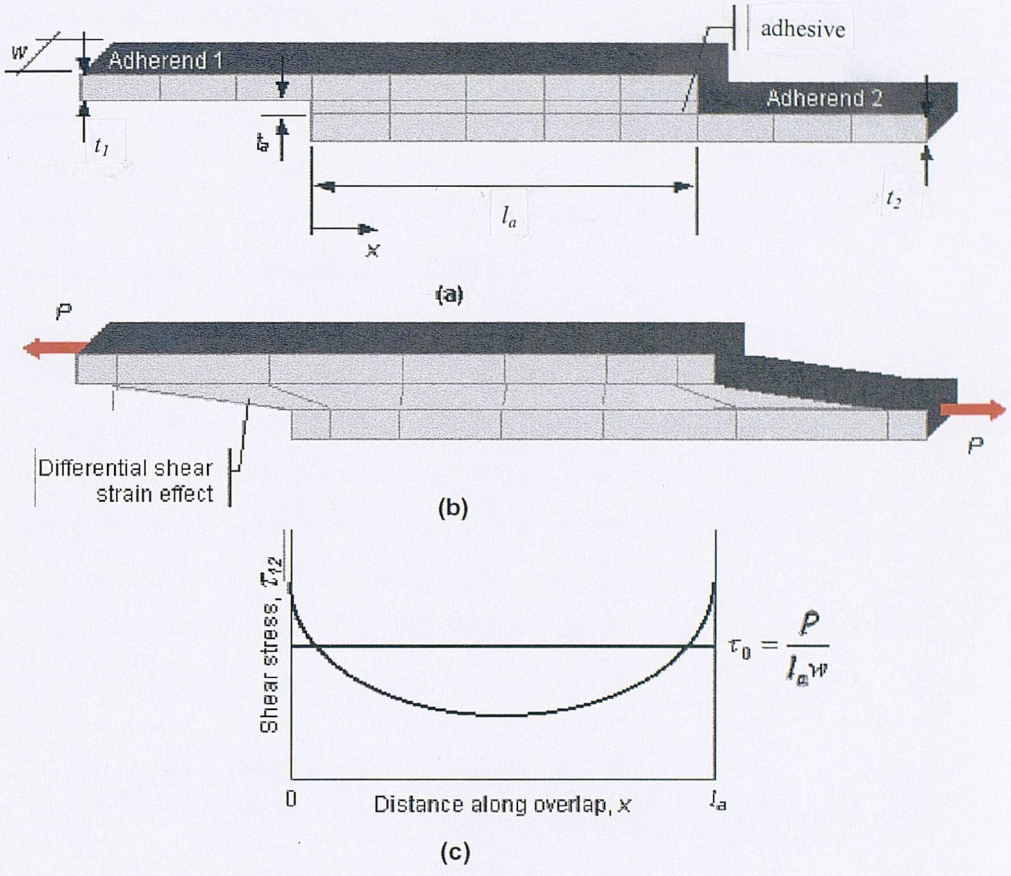


Figure 2.8: Schematic representation of the Volkersen model of an overlap joint (a) unloaded (b) loaded in tension, elastic adherends and (c) distribution of the elastic shear stress in the adhesive layer

2.5.3.2 Goland and Reissner model

Volkersen's theory is, however, incomplete as he neglected the effect of loading eccentricity and the resulting bending moment effects on the overlap joint geometry. As discussed above, an overlap joint will experience bending moments at the ends of the overlap region due to loading eccentricity (see Figure 2.9a). Goland et al. [7] took into account bending moment effects from the eccentricity of loading in an overlap joint by introducing the dimensionless bending moment factor, κ:

$$\frac{1}{\kappa} = 1 + 2\sqrt{2}\tanh\left\{\left(\frac{3}{2}\left(1-\nu_s^2\right)\right)^{1/2}\frac{l_a}{2t_a}\left(\frac{P}{E_s w t}\right)^{1/2}\right\} \quad \text{.....(2.7)}$$

where ν_s is the Poisson's ratio of the adherend. Interestingly, this result shows that as the applied load increases, κ decreases. This indicates that as a load is applied to the joint, the

joint is rotated at the overlap ends to correct the loading eccentricity (see Figure 2.9b). In other words, if a joint can be designed to have pre-deformed adherends, the effect of loading eccentricity can be reduced. This is the basis for the design of scarf joints and other designs such as tapered lap joints and double lap joints. Goland and Reissner showed that the stress concentration factor in the adhesive of a single overlap joint including bending moment effects is given by:

$$S_c = \frac{\tau_{max}}{\tau_0} = \frac{1+3\kappa}{4}(2\Delta)^{1/2}\coth(2\Delta)^{1/2} + \frac{3}{4}(1-\kappa) \quad \text{.....(2.8)}$$

The significance of loading eccentricity can be shown by comparing the Volkersen model with the Goland and Reissner model. Assuming a long overlap length, $l_a \rightarrow \infty$, κ becomes unity and, by combining equations 2.4 and 2.8, it can be shown that the analysis by Goland and Reissner predicts that the shear stress concentration factor is half of that of the Volkersen model.

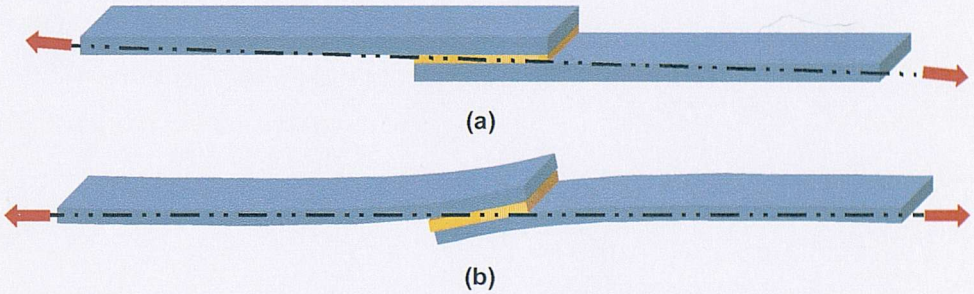


Figure 2.9: Schematic representation of (a) loading eccentricity in an overlap joint and (b) reduction of loading eccentricity as joint is loaded

2.5.3.3 Later developments

Hart-Smith has more recently showed that the Goland and Reissner analysis overestimates the bending moment by applying the simplified assumption that no relative deformation across the bond line is present in the joint [15]. Hart-Smith showed that the peak peel stress at the overlap terminus is related to the bending moment caused by the loading eccentricity:

$$\sigma_{yy_{max}} = M_e\sqrt{\frac{E_a}{2t_a D}} \quad \text{.....(2.9)}$$

where E_a is the modulus of the adhesive and D is the bending stiffness of the adherends. M_e is the bending moment in the adherends at the ends of the overlap and is given by:

$$M_e = \frac{P(t+t_a)}{2\left(1+\xi\frac{l_a}{2}+\frac{1}{6}\xi^2\left(\frac{l_a}{2}\right)^2\right)} \quad \text{.....(2.10)}$$

$$\xi = \sqrt{\frac{P}{D}} \quad \text{.....(2.11)}$$

In his analysis, Hart-Smith pointed out that the key to reducing the stress concentration factor lies in the length of the bonded region. He showed that for an overlap-to-thickness ratio (l_a/t) of 8 (typical of laboratory test coupons), the structural efficiency (i.e. the failure strength/ultimate tensile strength of the adherend) is approximately 36%. On the other hand, for l_a/t = 80 (typical of structural joints in aerospace applications), the structural efficiency is more than 90%. This is because the stress intensity factor is inversely proportional to the bending moment factor. He then showed that for long overlap regions, adhesively-bonded overlap joints typically failed in the adherend due to the bending moment effects. He also showed that adhesive failure either by shear or peel stresses often only occurs if the adherends are relatively thick or the overlap-to-thickness ratio is low [32].

The classical Volkersen and Goland and Reissner analyses have also been improved by various other workers. For example, Hart-Smith [15-17] formulated an elastic-plastic analytical solution for an overlap joint. He used an idealized elastic-plastic adhesive shear stress/strain curve and postulated that failure would occur when the adhesive reached its critical shear strain value. Tsai *et al.* [33] included adherend shear deformation into the classical Goland and Reissner analysis. They showed that this improved solution provides a better prediction for the shear stress distribution in the adhesive particularly when composite adherends are used. On the other hand, Abdel Wahab [28] proposed a fracture mechanics approach for designing adhesively-bonded overlap joints. In his work, he assumed linear elastic fracture mechanics and used the crack closure integral method via finite element analysis to derive two design overlap lengths that correspond to the prediction of adherend and adhesive/adherend interfacial failure. Although this method represents an alternative way to the design of adhesively-

bonded joints, it is however recognised that the optimum joint design can be more readily obtained by considering the stress concentration factors in the joint.

2.5.3.4 End effects

Many researchers have also looked at the effect of the spew fillet on the stress distribution in the overlap region [8,12,29-31]. They found that the presence of spew fillets at the overlap ends could significantly reduce the peak peel stresses in an overlap joint. In addition, peel stresses can be reduced by tapering the adherend at the overlap terminus. The effect of spew fillet and the optimization of the overlap end of double lap joints were also investigated by Adams *et al.* [12]. They showed that by tapering the adherend and including an adhesive spew fillet at the overlap terminus, a three-fold increase in joint strength was predicted numerically (via finite element analysis) and was also observed experimentally. Nevertheless, the size and shape of the adhesive fillet is very difficult to control in practice. However, the suggestion to taper the adherends near the overlap terminus has proven to be a popular method for optimising the design of overlap joints.

2.5.4.5 Conclusions

The classical analyses of the overlap joint geometry by Volkersen and Goland and Reissner proved to be the spark for later developments on the stress analysis of adhesively-bonded joints. Recent developments in the use of finite element analysis has greatly simplified the process of optimising adhesively-bonded joints, especially when non-linear geometries are used (e.g. adhesive spew fillets and tapered adherends are employed). Indeed, both these theoretical and experimental approaches has shown that, apart from extending the length of the bond region, geometrical optimization at the overlap terminus can also improve the efficiency of adhesively-bonded joints.

2.5.4 Scarf joints

Scarf joints are modified overlap joints that have tapered adherends. These tapered adherends are designed to reduce loading eccentricity in the joint (see Figure 2.6e). The tapered adherends reduce the differential strain at the overlap ends and thus reduce the stress concentration in the joint. However, the scarf joint design introduces a new geometrical parameter, the scarf angle, θ. As $\theta = 90°$, the scarf joint will represent a butt joint and as $\theta = 0°$, the scarf joint will become an overlap joint. Hence, it can be readily

seen that with small scarf angles, the adhesively-bonded joint will be loaded with a high mode II / mode I ratio (i.e. the shear mode to tensile mode ratio). Webber [34] showed that the failure load of scarf joints increases as the scarf angle decreases. He tested pre- and co-cured scarf repairs using CFRP materials. Soutis et al. [38] investigated CFRP scarf joints and showed that the optimum angle to achieve optimum joint strength for scarf joints to be 5°. However, these analyses assumed that the scarf tip is sharp to a singular point. In practice, this is impossible to manufacture. The effect of the thickness of the scarf tip is investigated in the current project and will be discussed in section 4.2.

Lubkin [35] was the first to formulate an analytical solution for the scarf joint design and he utilized a linear-elastic model and assumed no bending moment at the overlap ends. Hart-Smith [13,36] computed the shear stress distribution in a scarf joint by using a multi-layer superposition method that assumed that the tapered overlap region is made up of multiple thin overlap joints. Hence, with a sufficiently large number of steps, the scarf joint solution could, in theory, be obtained. Much like his work on the overlap joint design, Hart-Smith presented a thorough investigation into the design of scarf joints. He also investigated the effects of stiffness difference due to the use of dissimilar adherend stiffness and different coefficients of thermal expansion, on the stress concentration factor in a scarf joint [13]. Assuming similar adherends, the average shear stress in the adhesive is:

$$\tau_0 = \frac{P\sin(2\theta)}{2t} \quad \text{.....(2.12)}$$

Hart-Smith's elastic solution for the scarf joint design is in the form of differential equations but it does not use standard closed-form integrals. However, he also investigated the use of an elastic-ideal plastic analysis that leads to an explicit lower-bound solution that is accurate for most practical material and geometrical combinations [13].

Analytical solutions of the stress distributions in the adhesive of a scarf joint have also been reported by Nguyen and Kedward [14] and Gleich *et al.* [37]. Gleich *et al.* included the effect of blunt adherend tips in their investigation. They used a linear elastic analysis via the finite difference method to solve the governing differential equations for

the shear and peel stress distributions in the adhesive. Their analysis also includes bending moment effects at the overlap terminus. Nguyen and Kedward investigated a simplified analytical solution for tubular scarf joints. In their analysis, the bending moment effect was neglected due to the restraint on out-of-plane deflections of tubular scarf joints. They also proposed the use of an empirical formula to describe any non-linear behaviour of the adhesive material. They showed that, for identical adherends, the first derivative of the shear strain in the adhesive is the same at both ends of the overlap. This then formed the boundary condition for the second order differential equation of the shear strain in the adhesive. Using a Runge-Kutta method, or a finite difference method, the governing differential equations can then be solved numerically. This method is also used in the current project as a first approximation to optimize the scarf joint design. A brief derivation of the governing equations is given later in section 4.2.

Although analytical solutions of the scarf joint design can be used to optimise joint designs, they are however inadequate to model subtle changes in the geometrical parameters (e.g. adhesive spew fillet) and often require complex equations when adherend plasticity or bending moment effects are included in the analysis. Recent developments have shown that optimization of the geometrical parameters of adhesively-bonded joints are best carried out using finite element analyses which are readily capable of modelling non-uniform geometries. In addition, effects of material plasticity and adherend bending can be easily incorporated into these analyses. In the present project, the finite element method will be the main design method used to optimise the scarf joint design.

2.6 The fracture of adhesively-bonded joints

2.6.1 Introduction

The previous section described the various methods used in the design of adhesively-bonded joints. However, they do not show the behaviour of the joints after a sufficiently large flaw has initiated and propagated to final fracture of the joint. Understanding the behaviour of adhesively-bonded joints after crack initiation is particularly useful when investigating the toughness of the bonded joints, identifying failure mechanisms and understanding the fatigue characteristics of adhesively-bonded joints. The theory of

fracture mechanics of adhesively-bonded joints is not much different from the classical fracture mechanics of homogenous materials, where the underlying basis is that fracture occurs from pre-existing flaws in the material. There are two main methods to characterize crack growth, the strain energy method and the stress intensity method. These will be discussed briefly in the next two sections.

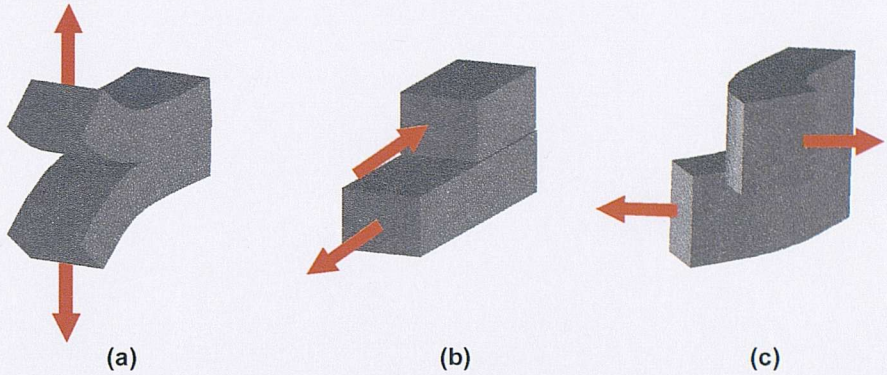


Figure 2.10: Three primary modes of loading (a) mode I or tensile mode (b) mode II or shearing mode (c) mode III or tearing mode

In the current project, the principles of fracture mechanics are used in the prediction of the service life of adhesively-bonded joints. For this application, linear elastic fracture mechanics (LEFM) is assumed. Hence, in the following discussions, only LEFM will be discussed. There are three primary modes of loading, mode I or the tensile mode, mode II or the in-plane shearing mode and mode III or the tearing mode, see Figure 2.10. These three modes of loading yield different governing equations and require different fracture mechanics testing.

2.6.4 Stress intensity factor approach

Irwin [27] showed that the classical Westegaard stress functions for a near field stress concentration around a crack tip can be related to the parameter, K known as the stress intensity factor (equation 2.13).

$$\sigma_{ij} = \frac{K}{(2\pi r)^{1/2}} f_{ij}(\theta) \quad \text{.....(2.13)}$$

Subscripts i and j correspond to the Cartesian coordinate system 1-2 shown in Figure 2.11. Using the stress intensity factor, K as a fracture criterion, the stress intensity factor,

K_c can be expressed in the form shown in equation 2.14 where Q is a function that is dependent on the geometry of the body and σ_c is the critical applied stress. The subscript k is the corresponding mode of loading (i.e. I, II or III as shown in Figure 2.10).

$$K_{kc} = Q\sigma_c a^{1/2} \quad \text{.....(2.14)}$$

Hence for fracture to occur,

$$K_k \geq K_{kc} \quad \text{.....(2.15)}$$

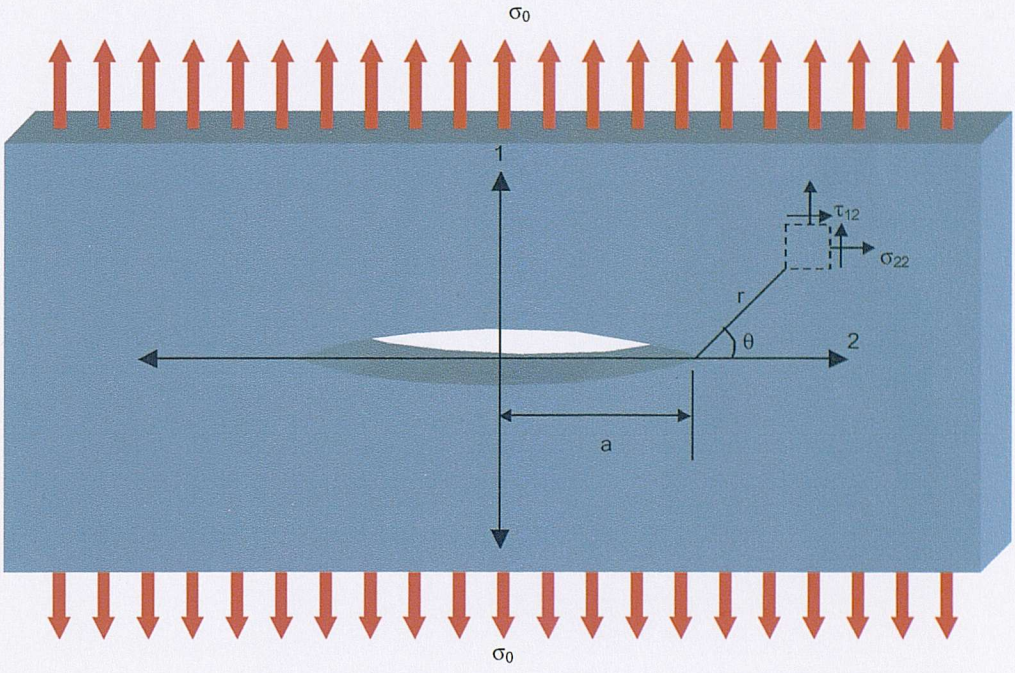


Figure 2.11: Elliptical crack of length, 2a in a uniformly stressed, infinite plate

The use of the stress intensity factor to describe cohesive failure in the adhesive for adhesively-bonded joints is sound. However, when evaluating the stress field at a bimaterial interface, it was found that the solution has a complex term and is oscillatory in nature, and hence the stress intensity factor changes sign as $r \rightarrow 0$ [9].

It is recognized that there exists a corner singularity at a bimaterial interface [39-42]. The stress singularity at the free edge corner of a bimaterial interface is generally in the form shown in equation 2.16 see Figure 2.12).

$$\sigma_{ij} = \sum_{l=1}^{N} K_l H_{ij}^{l}(\theta) r^{-\alpha_l} + \text{non-singular terms} \quad \text{.....(2.16)}$$

where r is the distance from the interface corner, $(i, j) \equiv (r, \theta)$, the parameter α_l is the order of singularity, K is the stress intensity factor and H^l_{ij} are functions that depend on the material mismatch parameters, α_1, α_2 and θ and are independent of the applied loading. The two elastic material constants for a bimaterial interface is given by [43]:

$$\alpha_1 = \frac{(\kappa_a + 1) - (\kappa_s + 1)G_a / G_s}{(\kappa_a + 1) + (\kappa_s + 1)G_a / G_s} \quad \alpha_2 = \frac{(\kappa_a - 1) - (\kappa_s - 1)G_a / G_s}{(\kappa_a + 1) + (\kappa_s + 1)G_a / G_s} \quad \text{..... (2.17)}$$

where for plane strain conditions, $\kappa = 3 - 4\nu$, the subscripts a and s denote the adhesive and the adherend respectively and G and ν are the shear modulus and Poisson's ratio respectively. The free-edge stress intensity factor, K is dependent on the loading conditions and the geometry of the joint, and hence details of calibration curves for various joint geometry and loading conditions are needed in order to calculate the free-edge stress intensity factor, K. There are two methods to determine K, (1) an extrapolation method which involves the matching of the asymptotic free-edge displacement or stress to the corresponding finite element results and (2) a path-independent contour integral which is based on the calculation of stresses and displacement fields far away from the interface corner. The second method is considered superior to the extrapolation method as it is mesh independent [40].

Nevertheless, the determination of the geometrical factor, Q is not straightforward especially when the subject of interest is of irregular shape. This is probably one of the main reasons for the more popular use of the energy balance approach to describe the fracture mechanics behaviour of adhesively-bonded joints. The energy balance approach will be reviewed in the next section.

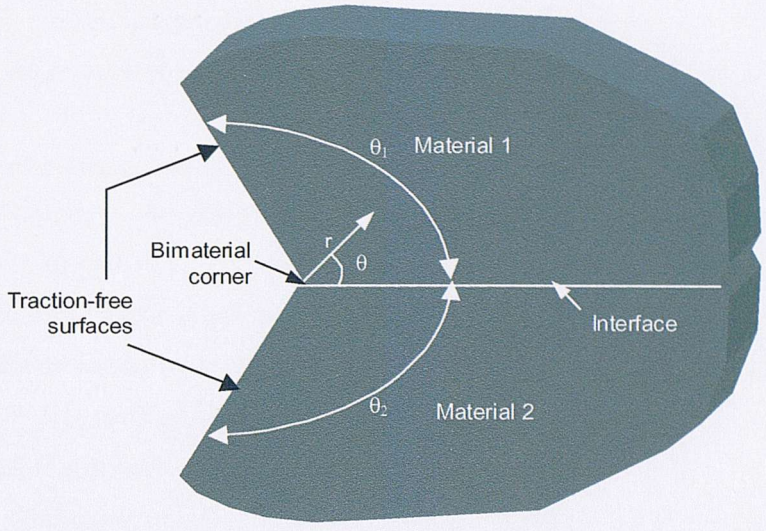


Figure 2.12: General configuration at the free-edge of two bonded dissimilar materials

2.6.5 Energy balance approach

Griffith [44] and later Orowan [45] proposed that fracture would occur when sufficient energy is released from creating new fracture surfaces as a crack grows in length. This critical energy is also referred to as the fracture energy or the critical strain energy release rate and is denoted as G_c. Assuming that the energy dissipated around a crack tip is independent of both the test geometry and the way in which the forces are applied, then in order for crack to grow, G_c is related to the external work done, W_d and the elastic stored energy U by:

$$\frac{\partial(W_d - U)}{\partial a} \geq G_c \quad \text{.....(2.18)}$$

where a is the half crack length in the Griffith's elliptical central crack model. The critical strain energy release rate can be expressed in the form of equation 2.19 by introducing the compliance of the structure, C (= displacement/load). Hence, G_c can be calculated via C by:

$$G_c = \frac{P_c^2}{2b}\frac{\partial C}{\partial a} \quad \text{.....(2.19)}$$

where P_c is the critical applied load and b is the width of the specimen. The energy balance approach is an attractive approach to predict the fracture of adhesively-bonded joints as the critical strain energy release rate, G_c, is a material property of a particular adhesive/adherend system (i.e. it is basically independent of joint geometry). There are two ways to obtain the strain energy release rate, G from the finite element method. They

are the crack closure integral method and the *J*-integral method. These methods will be discussed in more detail in the following subsections.

2.6.5.1 Crack closure integral method

Rybicki and Kanninen [46] showed that the strain energy release rate components, G_I and G_{II} could be obtained from the finite element method via a two-dimensional model (see Figure 2.13). Their analysis is based on Irwin's model [50] where the energy absorbed due to a small increment in crack growth is equal to the work required to close the crack to its original length. They obtained the strain energy release rate by considering the nodal forces and displacements at the immediate vicinity of a crack tip. This is shown in Figure 2.13. The equations of the strain energy release rates, G_I and G_{II}, corresponding to mode I and mode II loadings are given in equations 2.20.

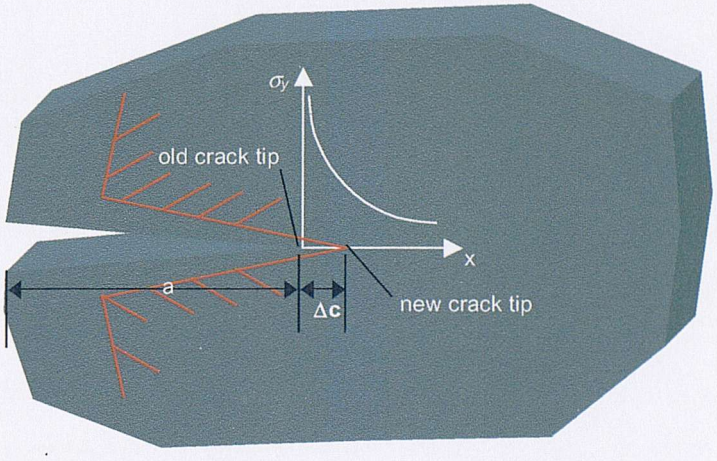


Figure 2.13: Schematic diagram showing crack growth of length Δc from an existing crack of length, a.

$$G_I = \lim_{\Delta c \to 0} \frac{1}{2\Delta c} F_{ym}(v_c - v_d) \quad \text{.....(2.20}a\text{)}$$

$$G_{II} = \lim_{\Delta c \to 0} \frac{1}{2\Delta c} F_{xm}(u_c - u_d) \quad \text{.....(2.20}b\text{)}$$

where Δc is the element length just before the crack tip, v and u are the vertical and horizontal displacements respectively and F_{ym} and F_{xm} are the vertical and horizontal forces that are required to 'close' the nodes **c** and **d** in Figure 2.14a. The subscripts, c and d correspond to the nodes, **c** and **d**. This was further improved to include eight noded

elements as well as singular elements by Raju [47] (see Figure 2.14b). The strain energy release rate equations using eight noded elements are shown in equations 2.21.

$$G_I = \lim_{\Delta c \to 0} \frac{1}{2\Delta c}\left[F_{ym}(v_c - v_d) + F_{ym}(v_p - v_l)\right] \quad \text{.....(2.21}a\text{)}$$

$$G_{II} = \lim_{\Delta c \to 0} \frac{1}{2\Delta c}\left[F_{xm}(u_c - u_d) + F_{xn}(u_p - u_l)\right] \quad \text{.....(2.21}b\text{)}$$

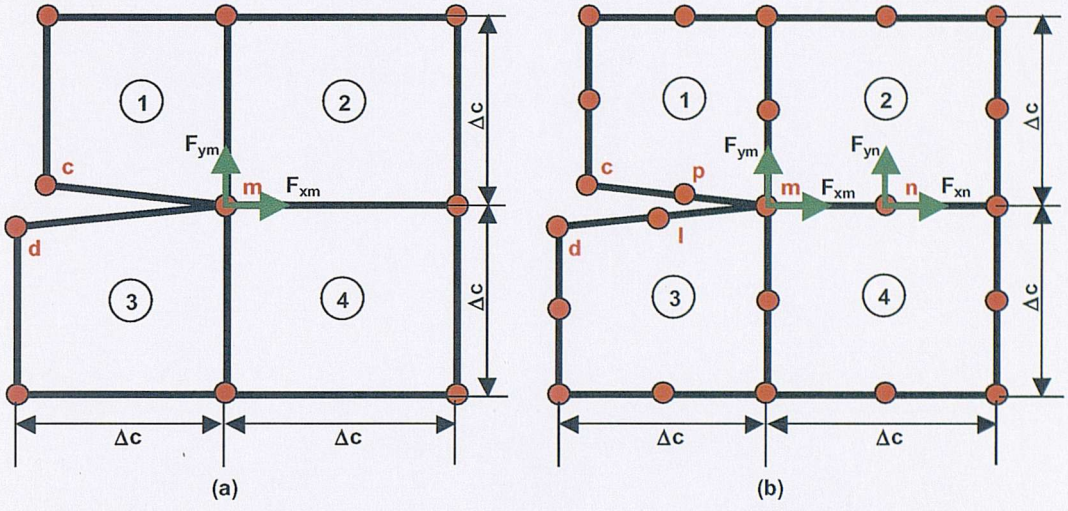


Figure 2.14: Schematic representation of the crack closure integral method using the finite element method of (a) 4 noded and (b) 8 noded isoparametric elements

One of the major criticisms of this method is that when the crack occurs at a bimaterial interface, it was found that as $\Delta c \to 0$, the strain energy release rate components exhibit an oscillatory nature. In other words, as the mesh around the crack tip becomes smaller, the strain energy release rate components exhibit non-uniform and oscillatory values. This is because of the mismatch of material properties at the bimaterial interface. This effect was shown by Hadavinia *et al.* [49] where they considered an interface crack in an overlap joint, Figure 2.15.

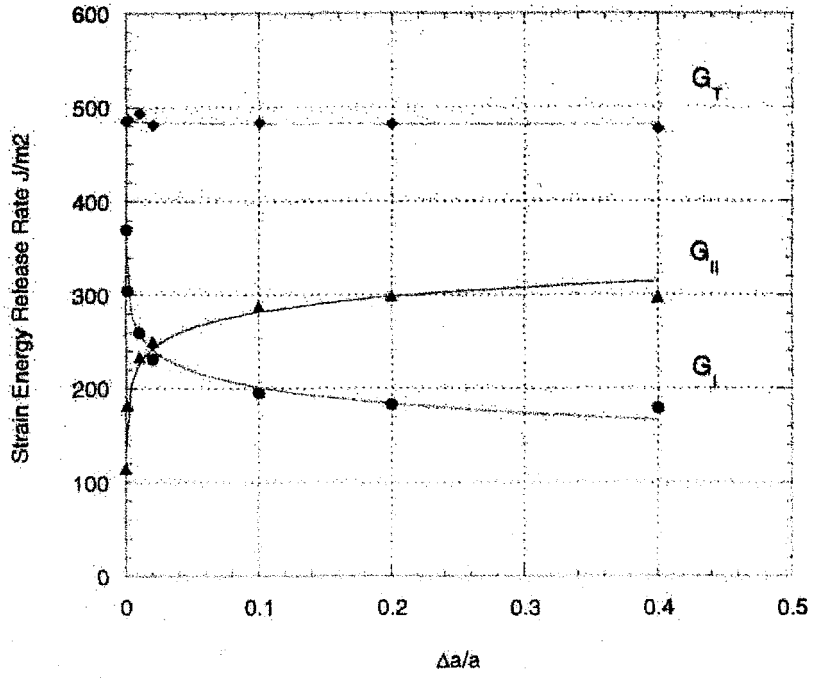


Figure 2.15: Variation of strain energy release rates components with crack tip element size in single overlap joint [49]

2.6.5.2 The *J*-integral method

The *J*-integral method was proposed by Rice [48] where he defined the energy field around a crack tip by considering an arbitrary contour, Γ, that envelops the crack tip. Consulting Figure 2.16, the contour, Γ, starting from the lower crack face and extending counter-clockwise around the crack tip to the upper face forms a closed loop. The *J*-integral is defined as:

$$J = \int_{\Gamma} W dx_2 - T_i \frac{\partial u_i}{\partial x_1} ds \quad \text{.....(2.22)}$$

where W is the strain energy density, T_i is the traction vector, u_i is the displacement vector and ds is the increment of the arc length along the contour Γ. The *J*-integral is path-independent and hence calculation of the *J*-integral via the finite element method, where mesh sensitivity is an issue, appears to be encouraging [55]. For linear elastic materials, it can be shown that the *J*-integral is synonymous with the strain energy release rate, G (see equation 2.23).

$$J = G \quad \text{.....(2.23)}$$

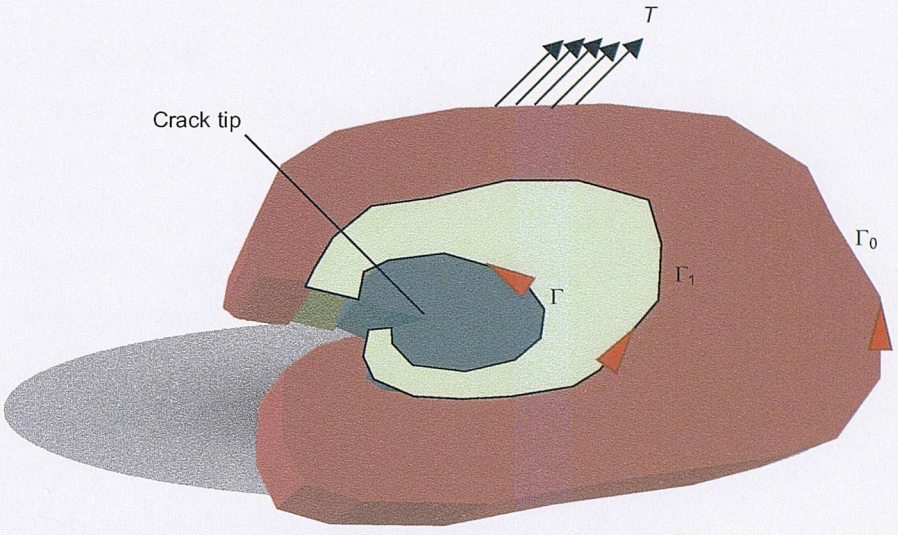


Figure 2.16: Contours enclosing a crack tip

It is interesting to note that the strain energy release rate is also related to the stress intensity factor where:

$$G = \frac{K^2}{E} \quad \text{.....(2.24)}$$

Hence, considering both equations 2.23 and 2.24,

$$J = G = \frac{K^2}{E} = \sigma_y \delta_t \quad \text{.....(2.25)}$$

where σ_y and δ_t are the yield stress and crack-tip opening displacement respectively. It can be clearly seen that the four fracture criteria (*J*-integral, strain energy release rate, stress intensity factor and the crack-tip opening displacement) are all related. Equation 2.25 is only true when the assumption of small scale yielding is applicable. Hence, when one of these fracture criteria is met, the other fracture criteria must reach their critical value. In this respect, the *J*-integral has an advantage in that it can be implemented easily into finite element codes and eliminates the need for extrapolated estimations (such as those found in the calculation of the stress intensity factors).

2.7 The fatigue life of adhesively-bonded joints

2.7.1 Introduction

In aerospace applications, one of the properties that an adhesively-bonded joint has to possess is good fatigue strength. As mentioned in the beginning of this chapter, adhesively-bonded joints, in theory, are far superior to joints where conventional mechanical fasteners are employed. As stated previously, the reason is that the applied load can be transmitted over a larger area (i.e. across the bond) rather than concentrating at a stress raiser (i.e. as with fastener holes). However, the fatigue performance of adhesively-bonded joints depends on many factors, ranging from loading conditions to environmental effects. The various factors affecting the fatigue performance of adhesively-bonded joints are given below:

• **Applied load amplitude** $\sigma_a = \frac{1}{2}(\sigma_{max}-\sigma_{min})$	• **Applied load range** $\Delta\sigma = \sigma_{max}-\sigma_{min}$	• **Mean stress level** $\sigma_m = \frac{1}{2}(\sigma_{max}+\sigma_{min})$
• **Stress ratio** $R = \sigma_{min}/\sigma_{max}$	• **Applied wave form** (sinusoidal, square, etc.)	• **Mean strain level** $\varepsilon_m=\frac{1}{2}(\varepsilon_{min}+\varepsilon_{max})$
• **Strain ratio** $\varepsilon_{min}/\varepsilon_{max}$	• **Specimen geometry**	• **Environmental effect** (water, salt, etc.)
• **Temperature** T	• **Surface treatment**	• **Frequency** *f*

There are two ways to present fatigue data. The first is by representing the crack growth data where the rate of crack growth, *da/dN* is plotted against the strain energy release rate range (or stress intensity factor range, ΔK) ΔG; or the maximum strain energy release rate, G_{max}, in a fatigue cycle. This method usually utilizes fracture mechanics data obtained from employing test geometries such as the tapered double cantilever beam (TDCB) and is used to obtain fatigue properties of a particular adhesive system (i.e. material employed, surface treatment, loading conditions, etc.). In addition, this method eliminates the uncertainty presented by the extent of the crack initiation period to the total fatigue life of adhesively-bonded joints; as the crack initiation period is essentially a micro-mechanics problem. The strain energy release rate range, ΔG, is defined as the difference between the maximum and the minimum strain energy release rate (see equation 2.26).

$$\Delta G = G_{max} - G_{min} \quad \text{.....(2.26)}$$

Hence, the fatigue crack growth rates can be represented by the Paris law [53]:

$$\frac{da}{dN} = C_T(\Delta G)^n \quad \text{.....(2.27)}$$

where C_T and n are fitting constants and depend on the loading conditions (stress amplitude, mean stress, stress ratio, frequency), material variables, environment and temperature. Equation 2.27 is used to fit the middle region (i.e. Region 2) of the fatigue crack growth data, see Figure 2.17. It can be clearly seen that equation 2.27 does not represent the top and bottom extremities of the fatigue curve (i.e. Region 1 and Region 3 on Figure 2.17). The significant increase in fatigue crack growth rate at the top right end of the graph represents the fracture toughness, G_c. While the divergence at the lower left end of the graph represents the threshold strain energy release rate, G_{th}. The sigmoidal form of Figure 2.17 can, however, be represented by a modified Paris law (equation 2.28) [54, 58]. The constants, n_1 and n_2 are fitting parameters of the divergence at the top and bottom end of the curve respectively.

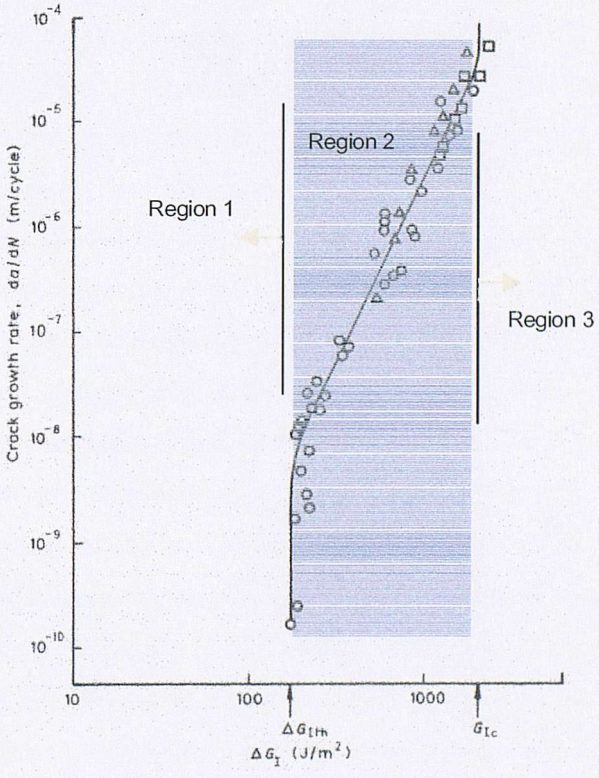


Figure 2.17: Crack growth rate, da/dN as a function of ΔG_I for epoxy/aluminium TDCB joints [59]

$$\frac{da}{dN} = C_T (G_{\max})^n \left\{ \frac{1 - \left(\frac{G_{th}}{G_{\max}} \right)^{n_1}}{1 - \left(\frac{G_{\max}}{G_c} \right)^{n_2}} \right\} \quad \text{.....(2.28)}$$

The second method commonly uses σ_a -N_f curves; where the amplitude of the cyclic applied stress (or load), σ_a, is plotted against the number of cycles to failure, N_f. This method of representing fatigue performance includes the crack initiation and crack propagation periods. The σ_{max}-N_f curves are commonly used to represent fatigue performance of adhesively-bonded coupon specimens such as the single lap joint geometry.

2.7.2 Environmental attack

Adhesively-bonded joints in aerospace structures may be particularly susceptible to environmental attack. This presents a major challenge to designers for maintaining good durability of the adhesive joints especially, when high surface energy adherends such as metals, glass and ceramics are used (see section 2.2.3). It was found that water (or moisture) exhibits the most deleterious effect on the durability of adhesively-bonded joints. Ironically, water is also the most commonly encountered substance. The presence of moisture coupled with a relatively high temperature and an applied load, can considerably reduce the fatigue strength of an adhesively-bonded structure. This is shown in Figure 2.18 where a dramatic reduction in the strength of epoxy-polyamide/aluminium alloy structural joints was observed when exposed to hot/wet tropical weather. If the assumption is that the mechanism of adhesion is via the interfacial secondary bonds, then it can be shown that the thermodynamic work of adhesion in the presence of water, W_{AI}, is negative. This indicates that the interface is unstable and will dissociate [9]. Values of the thermodynamic work of adhesion in an inert medium, W_A, and in water, W_{AL}, are shown in Table 2.5, where it can be seen that the epoxy/aluminium interface is indeed predicted to be unstable in the presence of water. In contrast, for a low surface energy material, such as a CFRP composite, the interface remains stable in the presence of water.

Table 2.5: Effect of water on the thermodynamic work of adhesion for various interfaces [9]

Interface	Inert medium: W_A	Water medium: W_{Al}
Epoxy adhesive/aluminium oxide	232	-137
Epoxy adhesive/ferric oxide (mild steel)	291	-255
Epoxy adhesive/CFRP	88 → 99	22 → 44

Gettings and Kinloch [20] have shown that by using organometallic silane-based primers the durability of adhesively-bonded joints could be improved. They proposed the formation of a polysiloxane layer and interfacial primary bonds between the silane layer (γ-glycidoxypropyltrimethoxysilane) and mild steel adherends that prevents moisture attack at the epoxy/adherend interface (see section 2.4.4 and Figure 2.3). Results from Abel *et al.* [18] and Adams [4] also suggest that this is the case for silane primed aluminium alloy adherends. The current project will investigate this further by undertaking experimental tests of GPS surface treated joints.

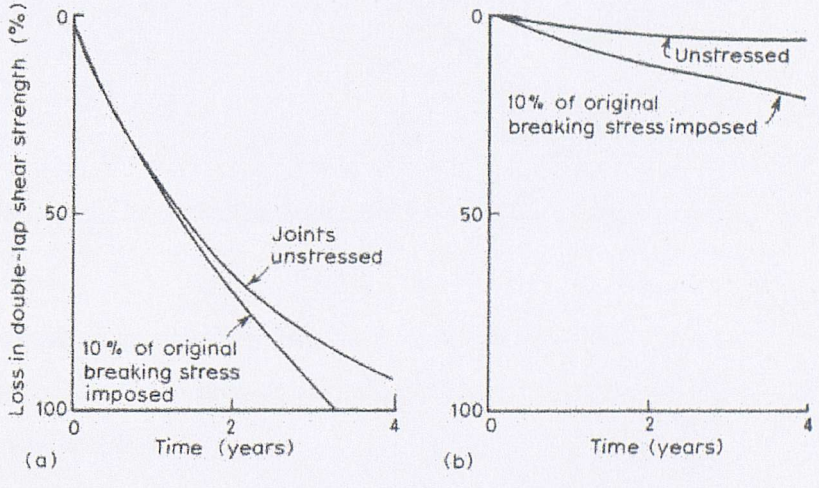


Figure 2.18: Effect of outdoor weathering on the strength of epoxy-polyamide/aluminium alloy structural joints (a) Hot/wet tropical site (b) hot/dry desert site [57]

2.7.3 Water uptake of bulk adhesive

In order to ascertain the saturation levels of water in the adhesive layer of an adhesively-bonded joint, water uptake tests of the bulk adhesive can be undertaken. However, it

should be noted that, the adhesive layer in an adhesively-bonded joint may experience higher diffusion rates than the bulk adhesive because of the effects of applied stresses and interfacial diffusion. The diffusion of moisture into the bulk adhesive can be characterized by the diffusion coefficient, D and its solubility, M_∞. The diffusion coefficient, D may be determined from the half-life of the sorption process, via equation 2.29 [61].

$$D = \frac{0.04919}{(t/l^2)_{0.5}} \quad \text{.....(2.29)}$$

where t is the time, $2l$ is the thickness of the sheet (see Figure 2.19) and $(t/l^2)_{0.5}$ is the time at which $M_t/M_\infty = 0.5$.

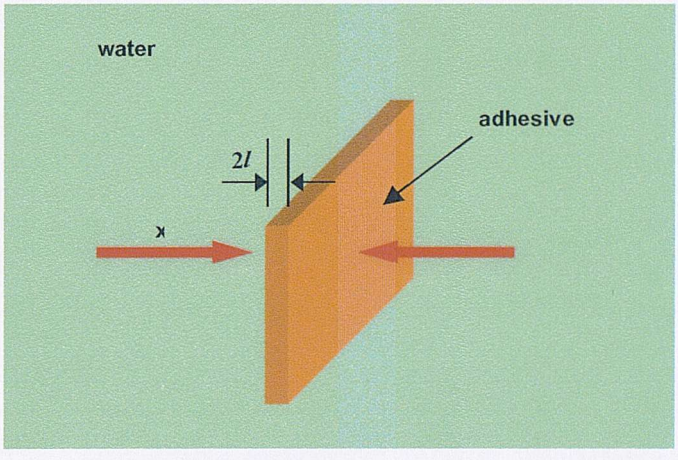


Figure 2.19: Experimental determination of water uptake in bulk adhesive

If the diffusion process obeys Fick's laws of diffusion [51] and the diffusion is in one dimension, then for a short period of water uptake time, the fractional uptake M_t/M_∞ can be shown to be given by:

$$\frac{M_t}{M_\infty} = \frac{4}{l}\left(\frac{Dt}{\pi}\right)^{1/2} \quad \text{.....(2.30)}$$

where M_t is the moisture absorbed at an exposure time t, and l is the thickness of the bulk adhesive (see Figure 2.19). This can also be expanded to a two-dimensional case, by considering the thickness in the x direction as $2l_1$ and the thickness in the y direction as

$2l_2$, the moisture absorbed at time t is related to the water concentrations, C_1 and C_2 by equation 2.31 [51].

$$M_t = \int_{-l_1}^{l_1} C_1 dx \int_{-l_2}^{l_2} C_2 dy \quad \text{.....(2.31)}$$

Another factor is that, the rate of water diffusion in an adhesively-bonded joint is greater than that in the bulk adhesive, Table 2.6 [52]. The increase in water uptake of the adhesive layer in an adhesively-bonded joint is attributed to the diffusion of water along the metal/polymer interface, termed wicking. In addition, increasing the operating temperature also increases the diffusion coefficient (see Table 2.6). It can be shown that in order to achieve 90% saturation in the middle of a TDCB joint, which is typically 10mm wide, the joint will need to be exposed to water for 96 months [56]. Hence, accelerated testing, via elevated testing temperature, is often used to determine the durability of a particular adhesive system. However, one should be careful not to impose unrealistically high testing temperature as this could result in anomalous failure modes [65].

Table 2.6: Comparison of the diffusion coefficients from bulk adhesive and adhesive joint (epoxy/aluminium) of FM73 [52]

Temperature (°C)	Relative humidity (%)	Bulk adhesive $D(x10^{-13}m^2s^{-1})$	Adhesive joint $D(x10^{-13}m^2s^{-1})$
20	70	2.8	3.6
20	95	1.7	3.9
40	70	8.0	10.3
40	95	4.2	4.1

2.7.4 Fatigue life predictions

Fracture mechanics data such as those shown in Figure 2.17 can be used to predict the fatigue life of other adhesively-bonded joint geometries (such as overlap joint) that uses the same adhesive system (i.e. adhesive/adherend material, surface treatment, environmental condition). As mentioned above, the fracture mechanics data can be fitted using equation 2.28. Hence, the number of cycles to failure, N_f can be predicted by integrating equation 2.28 with respect to the crack length, a. However, in order to achieve this, a relationship between the maximum strain energy release rate, G_{max}, the maximum applied load per unit width, T_{max} and the crack length, a has to be first established.

Kinloch and co workers investigated the use of the *J*-integral option in the finite element code, "ABAQUS" to obtain this relationship [54,63]. This method will also be used in the current project to predict the fatigue life-time of adhesively-bonded scarf joints. The detail description of this method is given in Chapter Six. It is sufficient to mention here that this method involves finite element modelling of the adhesively-bonded joint geometry. By theoretically growing a crack in the adhesive or at the interface (depending on which failure locus was observed experimentally), the relationship between the maximum strain energy release rate, G_{max}, the maximum applied load per unit width, T_{max}, and the crack length, a, can be obtained via the *J*-integral parameter.

Curley et al. [63] also formulated an analytical solution, for an overlap joint configuration, which related the maximum strain energy release rate, G_{max}, the maximum applied load per unit width, T_{max} and the crack length, a by:

$$G_{\max} = \frac{12}{E_s h^3}\left(\frac{T_{\max}(h+t_a)}{2}\right)^2\left(\frac{1}{(1+e[l-a]^2)}\right) \quad \text{.....(2.32)}$$

where E_s is the elastic modulus of the adherend, l is the half bond length, t_a is the thickness of the adhesive layer, h is the thickness of the adherend and e is given by equation 2.33.

$$e = \left(\frac{T_{\max}}{D_b}\right)^{1/2} \quad \text{.....(2.33)}$$

where D_b is the bending stiffness per unit width. They employed this relationship in equation 2.28 to predict the relationship between T_{max} and the number of cycles to failure, N_f, for single lap joints and some results from this approach are shown in Figure 2.20.

The main criticism of the two methods mentioned above is that mode I fracture mechanics data is used to predict an essentially mixed-mode (i.e. mode I/II) joint configuration, since the fracture mechanics data were obtained from a TDCB (i.e. mode I) test geometry. Some researchers had developed analytical solutions for the strain energy release rate components, i.e. G_I and G_{II} [59, 60]. However, it has been shown for

numerous different adhesive systems that the use of the total strain energy release rate, G, as used in equation 2.32 to predict the fatigue life-time of adhesively-bonded overlap joints is sufficiently accurate [54,56,63], Figure 2.20. Furthermore, it has been reported that G_{II} is approximately equal to G_I and hence equals to the total strain energy release rate, G, for most toughened epoxy adhesive [67]. However, as the applied load increases, the deviation of the fatigue life-time prediction from the experimental data did increase. This has been suggested to be caused by (1) the increase in the ratio of the crack initiation period to the total fatigue life-time of adhesively-bonded joints as the applied load is increased and (2) the sensitivity of the fitting parameters in the modified Paris law (i.e. equation 2.28). These two factors are discussed in more detail below.

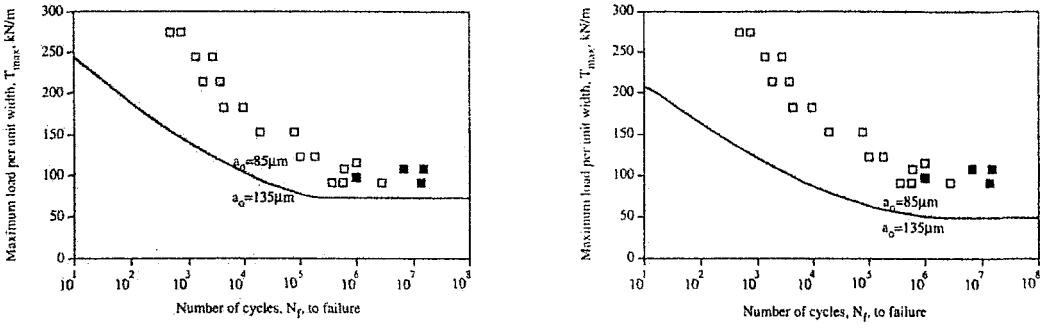


Figure 2.20: Prediction of the fatigue life-time of adhesively-bonded overlap joints using (a) the *J*-integral method and (b) analytical solution [63]

It should be noted that the prediction of the T_{max}-N_f curves of adhesively-bonded structural joints is based on fatigue crack growth. In other words, the methods mentioned above do not take into account the fraction of the crack initiation that is included in the total fatigue life. Taylor [80] had shown, by using the 'back-face strain gauging' technique, that the crack initiation period increases as the applied load increases, although typically it is not a significant fraction of the total fatigue lifetime of the joints.

It has been shown that the fitting parameters of the modified Paris law (see equation 2.28) affect the shape of the predicted fatigue life-time [56,63,80]. In particular, it has been suggested that the fitting parameters, C_T and n, for Region 2 of the fracture mechanics data (see Figure 2.17) are the dominant factors affecting the slope of the

predicted T_{max}-N_f curve. Furthermore, the inherent scatter of the fracture mechanics data in this region makes the determination of these fitting parameters difficult. In accelerated testing in 'hot'/wet conditions, the curve fitting parameters, C_T and n, in Region 2 are even more difficult to determine. This is because as the curve moves along Region 2 towards the fracture toughness, G_c, the effect of environmental attack reduces. Hence, the Region 2 of the fracture mechanics data is shortened.

2.8 Adhesively-bonded repairs

2.8.1 Introduction

One of the main advantages of adhesive bonding is the possibility of repairing metallic structures with composite materials. Carbon fibre reinforced composites (CFRP) are becoming more popular as they are light and strong and are use in their own right as structural materials for aerospace applications. They are also being widely used to repair aluminium alloy structures which have been damaged and contain cracks. Thus, these days, composite materials are used extensively in aerospace structures, Figure 2.21. However, a major problem in adhesively bonding CFRP to metallic structures may be the development of residual thermal stresses in the joint. This is because CFRP has a significantly lower thermal expansion coefficient compared to metallic materials, see Table 2.7.

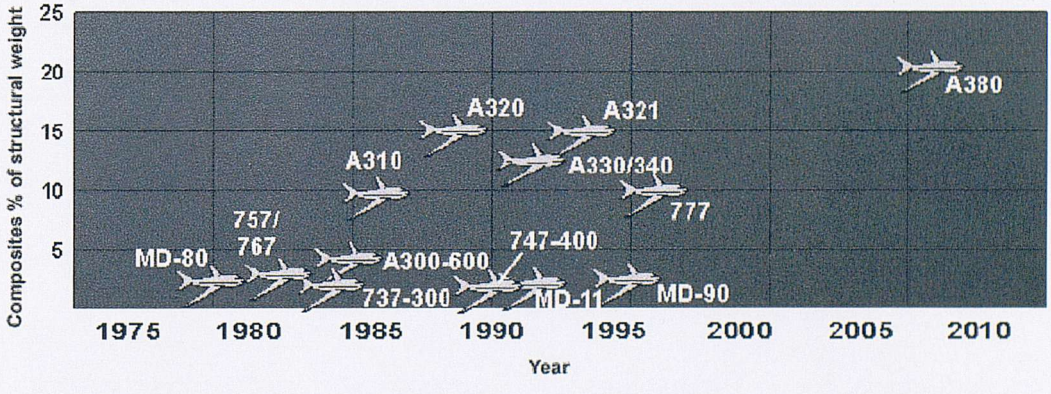


Figure 2.21: The increasing use of composite materials on commercial airplanes [86]

Table 2.7: Comparison of material properties of CFRP and metallic materials [66]

Materials	Elastic modulus GPa	Shear modulus GPa	Thermal expansion coefficient $(°C)^{-1} \times 10^{-6}$
Boron/epoxy (unidirectional)	208 max 20 min	7	4.5 min 23 max
carbon/epoxy (unidirectional)	130 max 12 min	5	0.4 min 28 max
Aluminium alloy (2024 T3)	72	27	23

Note: Maximum elastic modulus and minimum thermal expansion coefficient of the composites are in the (0°) fibre direction. The 90° direction is transverse to the fibre direction.

Due to the high cost of building new aircrafts and aircraft components, adhesively-bonded repairs, using composites, of ageing/damaged metallic aircrafts are receiving much attention. In particular, the Aeronautical and Maritime Research Laboratory (ARL) in Australia have pioneered the use of composites for in-situ repairs to damaged aircraft components [60]. Some of their achievements are shown in Table 2.8. They have shown that by using the relatively simple process of crack patching, using adhesively-bonded composite patches the structural integrity of damaged aircraft components could be restored to normal working levels.

Table 2.8: Examples of the current applications of adhesively-bonded composite repair carried out by ARL [60]

Defects	Parent material	Component	Aircraft	Comments
Stress-corrosion	7075 - T6	Wing plank	Hercules	Over 300 repairs since 1975
Fatigue	Mg alloy MSR	Landing wheel	Macchi	Life doubled, at least
Fatigue	AU4SG	Fin skin	Mirage	In service since 1978
Fatigue	AU4SG	Lower wing skin	Mirage	Over 150 repairs since 1979
Fatigue	2024 – T3	Upper wing skin	Nomad (fatigue test)	Over 105 900 simulated flying hours
Fatigue	2024 – T3	Door frame	Nomad (fatigue test)	Over 106 619 simulated flying hours
Stress-corrosion	7075 – T6	Console truss	F111	Service since 1980
Lightning burn	2024 – T3	Fuselage skin	Orion	Service since 1980

2.8.2 Considerations and practices

Many aspects of the design of adhesively-bonded repair are similar to that of the design of adhesively-bonded joints (see section 2.5). As discussed in section 2.5, the main philosophy in the design of adhesively-bonded joint is to reduce the transverse or the peel stresses that often appear at the overlap terminus. In addition, adhesively-bonded repairs also aim to reduce the stress intensity factor of the damaged component. Such repairs are undertaken by adhesively bonding a composite patch onto the damage area, either as an external patch or a flushed plug. There are numerous reports on the design principles and practices that are used in adhesively-bonded composite repair of metallic structures [60,66,70-75]. They typically cover the common practices in the manufacture of the composite materials, surface preparation for adhesive bonding and the design of the repair patch configurations. Much of the design principles are similar to those of adhesively-bonded metallic joints. Some of the improvements in repair design result from the advantage of using CFRP as the repair material. For example, thin overlapping composite plies (usually one ply thick, i.e. ~ 0.13mm) are often used in repair procedures for the scarf joint configuration, see Figure 2.22. The overlapping plies are used to prevent the joint from bending, and hence then reduce the peel stresses at the terminus of the overlap region.

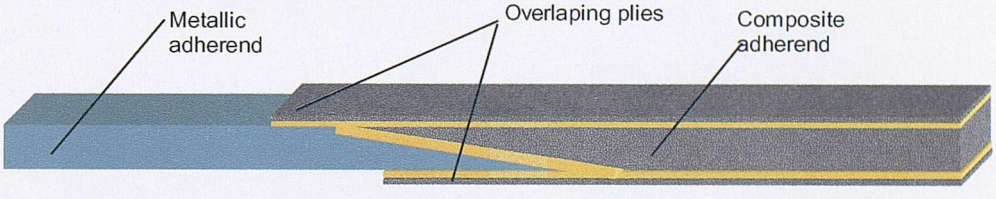


Figure 2.22: Overlaping composite plies used to stiffnened joint ends in a scarf joint design

However, the use of composite materials to repair metallic structures causes two major of problems. The first is that the introduction of composite material to a structural repair will require the full knowledge of the mechanical properties of the material. Secondly, most structural adhesives require elevated curing temperatures. This will cause residual thermal stresses to develop in the joint, since composite materials in general have significantly lower thermal expansion coefficients than metallic materials. These two points will be further discussed in the following sub sections.

2.8.2.1 CFRP characteristics

CFRP composites are typically composed of a carbon fibre mat, reinforced with an epoxy matrix. They usually come in thin lamina, or plies, of a thickness of approximately 0.13 mm, with uni-directionally oriented carbon fibre supported in an epoxy matrix. The laminae can be stacked to give any required thickness. In addition, the anisotropic behaviour of uni-directional laminae means that the stacking order (i.e. the orientation of the plies) of the laminate can be adjusted to give the required stiffness.

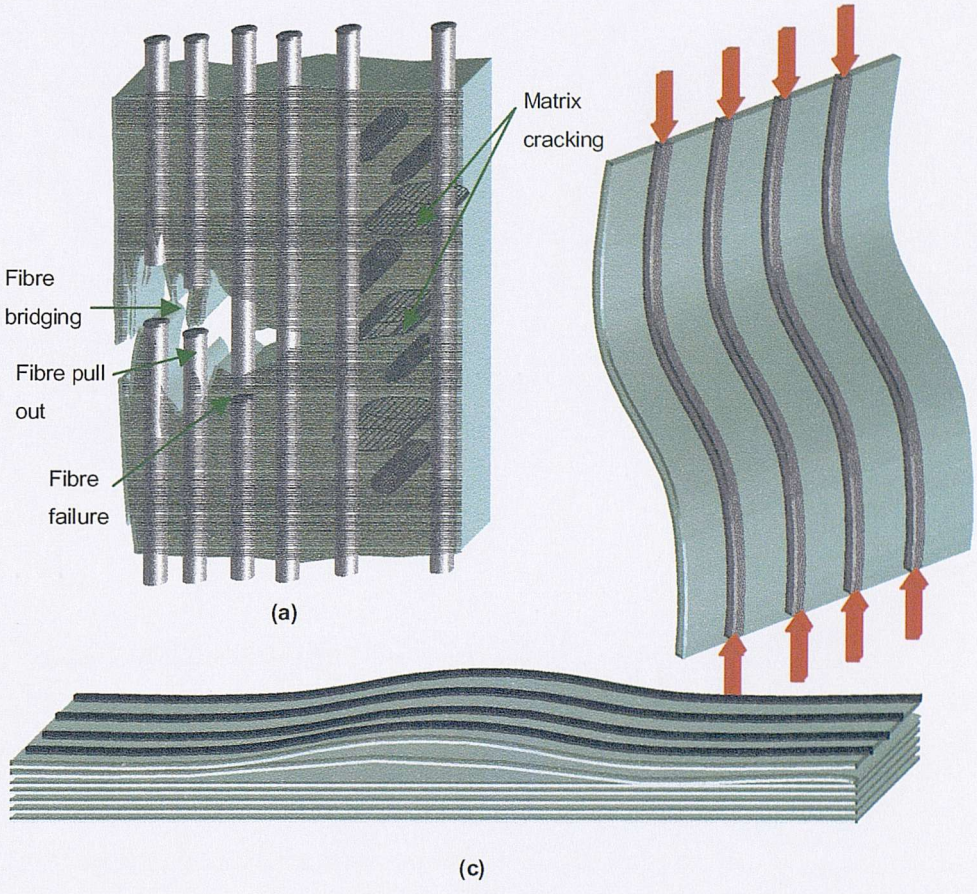


Figure 2.23: Common failure modes of composite materials: (a) in-plane damage (b) microbuckling (c) delamination

The design of a composite laminate is determined by the required loading conditions. For example, when a composite is loaded in the direction parallel to the carbon fibres, it can exhibit an extremely high strength. On the other hand, the strength of the composite laminate will be relatively lower when the composite laminate is loaded in a direction other than the direction parallel to the orientation of the carbon fibres. This is because of the contribution of the longitudinal strength of the carbon fibres to the strength

of the laminate is substantial (see Table 2.7). There are three common types of composite failure, (a) in-plane damage, (b) microbuckling and (c) ply delamination, see Figure 2.23. With tensile loading, the in-plane and delamination failure types are the common failure modes.

2.8.2.2 Effects of thermal residual stresses

As mentioned above, adhesive bonding of composite materials to metallic materials for structural applications often requires a high temperature curing adhesive to be used. A curing temperature of 120°C is common for aerospace structural adhesives. However, Table 2.7 showed that the thermal expansion coefficients of composites are significantly lower than those of metallic materials. The mismatch in thermal expansion coefficient of these two materials can cause the development of residual thermal stresses. An example of the effects of the residual thermal stresses is that in an unsymmetrical joint configuration (e.g. a single overlap joint and scarf joint), adhesive bonding of a composite adherend to a metallic adherend may cause the joint to become bowed. The thermal strain, of an isotropic material, caused by a change in temperature can be calculated by equation 2.34.

$$\varepsilon_{therm} = \alpha_{therm}\Delta T \quad \text{.....(2.34)}$$

where ε_{therm} is the thermal strain, α_{therm} is the thermal expansion coefficient and ΔT is the change in temperature. Hence, due to the higher thermal expansion coefficient of metallic materials, they will always expand (and contract) more than composite materials. As a result, an unsymmetrical joint will typically be bowed towards the metal side of the joint. The presence of residual thermal stresses in a cracked metallic panel repair using a bonded CFRP patch will increase the stress intensity factor, and hence increase the fatigue crack growth rate in the repaired panel, Figure 2.24.

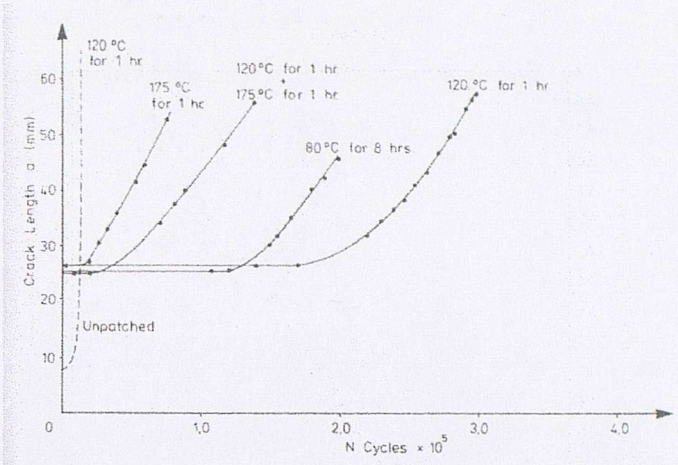


Figure 2.24: Plots of crack growth versus number of fatigue cycles for crack patched repair panels subjected to various heat-treatment conditions [64]

To reduce residual thermal stress effects, Baker [64] has suggested the use of boron fibre reinforced plastic (BFRP) instead of the more commonly used carbon fibre reinforced plastic (CFRP). This is because BFRP is 1.5 times stiffer than CFRP, has a higher fatigue strength and a higher thermal expansion coefficient (see Table 2.7). He also suggested that in laboratory testing, two unsymmetrical repair panels could be tested simultaneously by bonding two similar panels on either side of a honeycomb structure, since this would prevent bowing of the unsymmetrical repair panels due to the development of the residual thermal strains in the panels. Molent *et al.* [68] suggested that heating as small an area around the patch as possible could reduce residual thermal stresses. This is because the cooler structure surrounding the repair patch does not expand and hence will result in a lower effective thermal expansion coefficient than an unconstrained structure. In addition, Molent also suggested that by pre-stressing the bond region before bonding, the expected thermal contraction stresses could be negated. Indeed, this method is commonly used when repairing wing skins [68].

2.8.2 Analytical analysis of crack patch repair

Rose [69,77] has proposed a theoretical analysis for predicting the reduction in the stress intensity factor of adhesively-bonded, external, crack patch repairs. He suggested the use of a two-stage analysis where the first stage is to predict the equivalent crack opening stress, σ_0, in an uncracked plate with a bonded patch, assuming that there is no relative

displacement between the patch and the panel, Figure 2.25. However, Rose [76] stated that the analytical solution for the equivalent crack opening stress, σ_0, could only be solved analytically for certain simple shapes that possessed a uniform stress state in the patch.

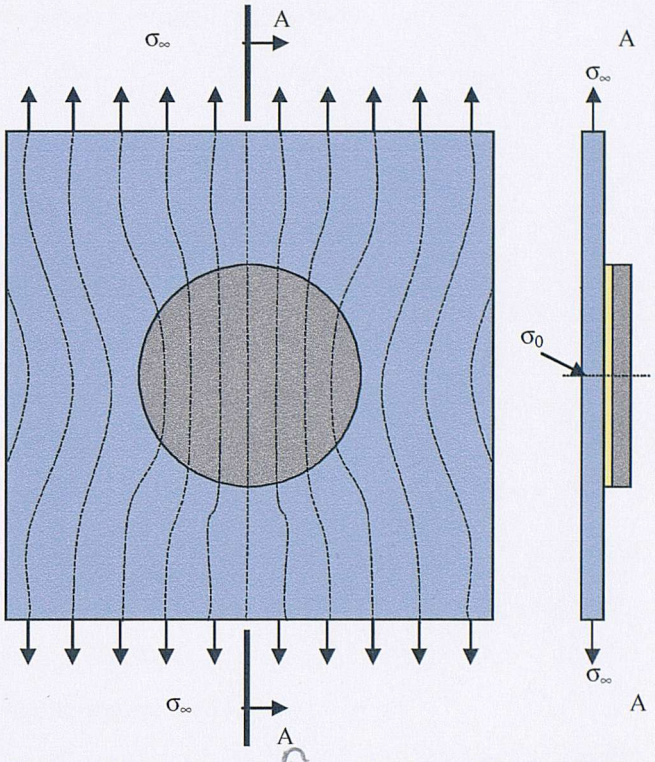


Figure 2.25: Schematic diagram of a uncracked panel bonded with a patch on one surface. This is used to explain the equivalent crack opening stress, σ_0.

The second stage is to utilize the predicted crack opening stress to predict the stress intensity factor of the repair panel. The stress intensity factor for a crack patch repair, K_r has two bound values, see Figure 2.26. The first of which is the stress intensity factor for an unrepaired panel, K_0, where K_0 is related to the square root of the crack length, a (see equation 2.35). The second bound is the stress intensity factor for a semi-infinite crack in a single-sided crack patch repair, K_∞ (see equation 2.36).

$$K_0 = \sigma_\infty \sqrt{\pi a} \quad \text{.....(2.35)}$$

$$K_\infty = \sigma_0 \sqrt{\pi \mathrm{A}} \quad \text{.....(2.36)}$$

The characteristic length, A, is related to the physical properties of the panel and the patch and is given by equation 2.37.

$$\pi A = \left(1+\frac{1}{S}\right)\beta^{-1} \quad \text{.....(2.37)}$$

where S and β are given by equation 2.38 and 2.39.

$$S = \frac{E_r t_r}{E_p t_p} \quad \text{.....(2.38)}$$

$$\beta^2 = \frac{G_a}{t_a}\left\{\frac{1}{E_p t_p}+\frac{1}{E_r t_r}\right\} \quad \text{.....(2.39)}$$

Here, the subscripts, p and r denote the parent (metallic panel) material and the repair patch (composite) respectively. As can be seen from equations 2.37, 2.38 and 2.39, the characteristic length, A is independent of the crack length, a, or the applied stress, σ_∞, and can be derived from the physical properties of the joint. Rose noted that for $a/A < 1$, the reduction in stress intensity factor for a crack patch repair is mainly due to the reduction from σ_∞ to σ_0. On the other hand, as $a/A > 1$, the reduction in stress intensity factor for a crack patch repair is due to the restraint of the opening crack displacement for a given value of σ_0. This is the physical basis for the upper bound of K_∞ to K_r and hence the existence of the characteristic length, A.

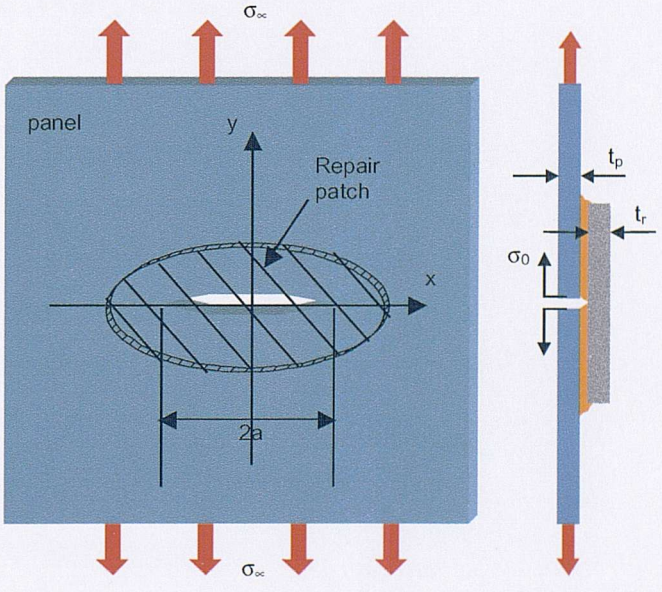


Figure 2.26: Schematic diagram of an elliptical crack patch repair

The stress intensity factor, K_r for a crack patch repair can be derived by interpolation from these two upper bounds (see Figure 2.27). This is given in equation 2.40.

$$K_r = \sigma_0 \sqrt{\frac{\pi a \mathrm{A}}{a + \mathrm{A}}} \quad \text{.....(2.40)}$$

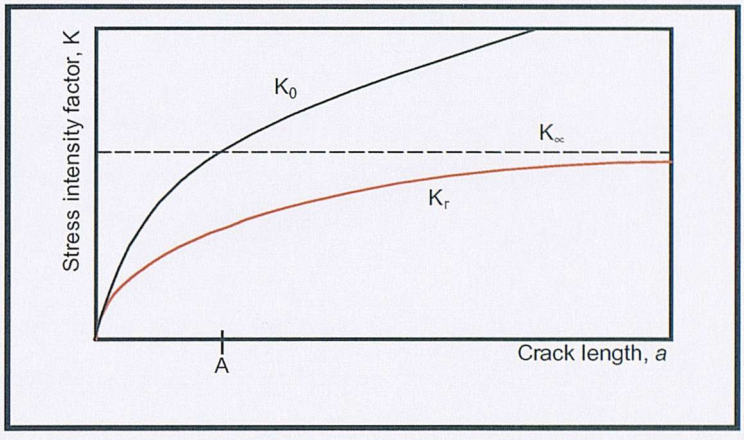


Figure 2.27: Variation of K_r with crack length, a, with the two upper bounds, K_0 and K_∞

As can be seen from the analysis provided by Rose, the analysis of the crack patch repair technique utilises fracture mechanics principles. The common procedures of obtaining, either, the stress intensity factor, K or the strain energy release rate, G have been reviewed in section 2.6. These same procedures can be used to optimise the crack patch repair system. For example, the thickness, ply orientation, shape and size of the composite patch. Geometrical optimisation of a crack patch repair system is generally carried out by comparing the stress intensity factor, K (or the strain energy release rate, G) for different geometrical parameters. The service life of a crack patch repair system can also be predicted by incorporating the Paris law equation (equation 2.27) with the relationship obtained for K (or G) and crack length, a.

2.9 Chapter summary

The following conclusions are drawn from this chapter:

1. The selection of the type of surface treatments depends on the adherend surface energy. Materials with low surface energy such as composite materials often only require mechanical abrasion techniques to provide a foundation for good adhesion to occur. On the other hand, materials with high surface energy such as metallic materials often needs further surface pretreatments such as chemical surface treatments or organosilane primers. This is especially important when good durability of the joint is required.

2. The use of organosilane primers has been shown to provide strong primary bonding at the adhesive/adherend interface. This improves the durability of the adhesively-bonded joint and is stable in the presence of moisture attack.

3. Another major factor affecting the performance of adhesively-bonded joints is the geometrical design of the joint. Adhesively-bonded joints are designed to be loaded mainly in shear or compression. Optimization of the design of adhesively-bonded joints can be carried out using classical analytical solutions or finite element analyses. The main aim of joint design optimization is to reduce peel stresses at the overlap terminus that often appears to be the cause of joint failure.

4. Classical fracture mechanics theories can be applied to adhesively-bonded joints. Prediction of crack growth in adhesively-bonded joints can be carried out using the stress intensity factor approach or the energy balance approach. The energy balance approach in particular is popular as it neglects the stress singularity at a crack tip that is often a problem when modelling cracks in finite element analyses.

5. Water (either in liquid or vapour form) is particularly damaging to adhesively-bonded joints. Water ingress into the adhesive/adherend interface can cause severe loss of structural integrity of the bonded joint. Accelerated testing of adhesively-bonded joints in the presence of water, high temperature and applied load can be used to investigate the durability of adhesively-bonded joints. However, care should be taken so that unrealistically high temperatures are used as this could cause abnormal failure modes.

6. Prediction of the fatigue threshold load of adhesively-bonded joints using the modified Paris law has been shown to give good comparison with experimental results. However, predictions of the fatigue life at low fatigue cycles are poor compared to experimental results. Two of the given explanations are that (1) the inherent scatter in the fracture mechanics data, especially in region 2 of the fracture curve, results in difficulties for determining the curve fitting parameters for the modified Paris law and (2) the increasing dominance of fatigue initiation period over the crack propagation period means that the prediction of fatigue crack growth will be conservative at high applied loads.

7. Composite materials are increasingly used in the repair of metallic components. However, one of the main problems of adhesively bonding composite materials with metallic materials is the resulting residual thermal stress from high temperature curing of the adhesive. The most effective way of reducing residual thermal stresses is to use a symmetrical joint design.

8. The use of composite patches to repair cracked aluminium alloy panels has been shown to be successful. The stress intensity factor of the cracked metallic panel is used as the design criterion for the composite patch. It was shown that the relatively simple process of external crack patching could increase significantly the fatigue life of a cracked metallic panel.

CHAPTER 3

MATERIAL PROPERTIES AND EXPERIMENTAL METHODS

3.1 Introduction

In the present chapter, the properties of the various materials used to manufacture the adhesively-bonded joints tested in the present project are described in detail. This is followed by a description of the various experimental procedures employed in this project. As mentioned in Chapter One, the two main aims of the present project are to optimise the scarf joint design and to determine the effect of the surface treatment on the durability of adhesively-bonded joints. Hence, monotonically-loaded tests, as well as fatigue tests, in both 'dry' and 'hot/wet' environment will be the main test procedures employed.

3.2 Material properties

3.2.1 Adhesive

The adhesive used is a rubber-toughened epoxy film adhesive, 'FM73 M', produced by Cytec Corp, USA. The adhesive is supported by a polyester mat to ease handling and repositioning of the adhesive. The adhesive is cured at 120°C for one hour and it is

recommended to have a pressure of 0.2-0.3 MPa applied to the joint during the curing process.

In order to undertake the numerical stress analyses in later chapters, it is necessary measure the shear stress-strain response of the adhesive and then to model this behaviour using a finite element analysis (FEA) approach. Chiu *et al.* [79] have measured the stress-strain behaviour of the FM 73M adhesive and their results are shown in Figure 3.1 and Table 3.1 and are appropriate for a rate of displacement of 1mm/min. The FEA model used was a single-element model and the results of the modelling studies are compared with the experimental results of Chiu *et al.* [79] in Figure 3.1.

Table 3.1: Material properties of FM73 M

Shear modulus, G (GPa)	Yield stress, τ_y (MPa)	Fracture stress, τ_f (MPa)	Fracture strain, γ_{af} (%)	Poisson's ratio, ν
0.58	31	44	61	0.35

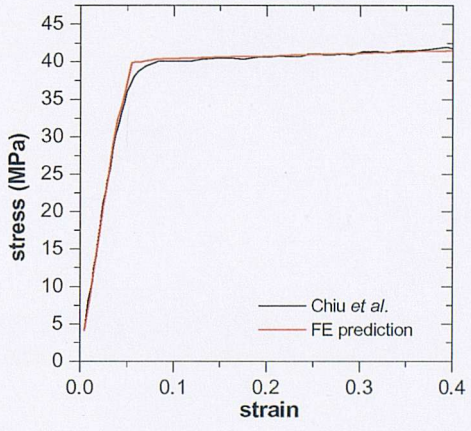


Figure 3.1: Shear stress-strain response of FM73 M

3.2.2 High strength aluminium alloys

All the materials used as adherends in this project have a nominal thickness of 2mm. Two aircraft grade aluminium alloys, 2014A, of different temper grades were used. Details of the various material properties of these aluminium alloys are listed in Table 3.2. Uniaxial tensile tests were carried out using 'dog-bone' specimens according to the ASTM standard, D557M-76. Extensometers were used to measure the accurate strain values. The two types of 2014A alloys listed in Table 3.2 are code-named 'L156' and 'L157'. The main

difference between these two types of aluminium alloy is the different temper grade of the alloy with 'L156' being a T4 material while 'L157' is a T6 material. Because of the difference in temper grades, the L156 alloy shows a reduction in tensile strength but an increase in ductility when compared with the L157 alloy. Both of these alloys will be used and the effects of the different temper grades will be discussed in section 4.5.

Table 3.2: Material properties of aluminium alloys L156 and L157

Aluminium alloy	Elastic modulus, E (GPa)	Yield stress, τ_y (MPa)	Fracture stress, τ_f (MPa)	Elongation (%)	Poisson's ratio, ν
'L156' (T4)	69	250	440	18	0.3
'L157' (T6)	69	450	480	9	0.3

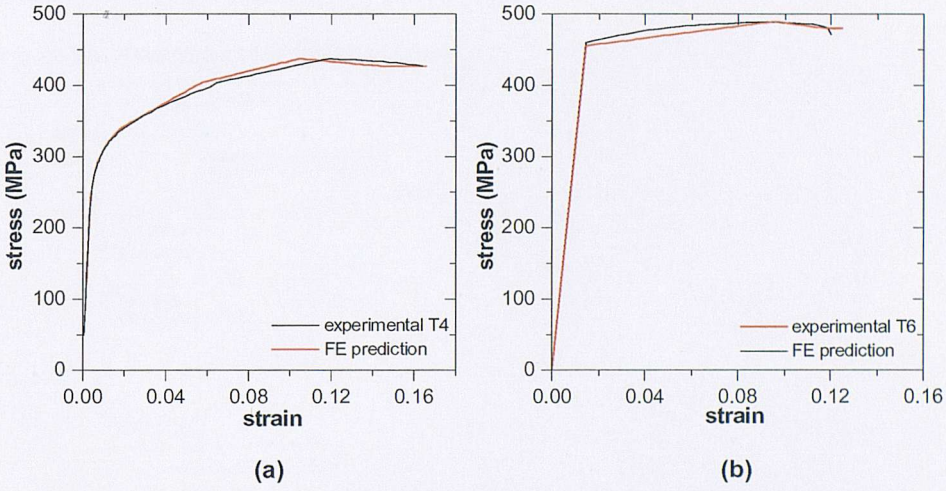
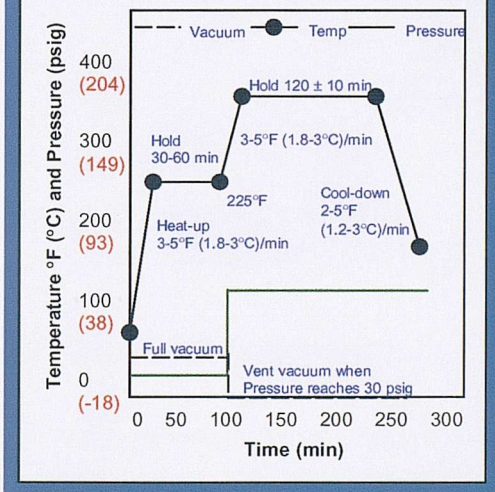


Figure 3.2: Experimental and FE predicted tensile stress-strain response of the T4 and T6 2014A aluminium alloys

Figure 3.2 shows the engineering stress-strain curves of the two aluminium alloys used in the present work. In addition, the figures also show the finite element models of the engineering stress-strain relationships of these two alloys. The finite element models were obtained by using a single continuum element and assumed non-linear geometrical deformation and two-dimensional plane strain conditions. Elastic-plastic material behaviour was assumed and a number of stress-strain points from the experimental stress-strain curves were employed to produce the hardening behaviour of the alloys.

3.2.3 Carbon fibre reinforced plastic

At a later stage in this project, carbon fibre reinforced plastic (CFRP) was used as the adherends: namely, CFRP was adhesively-bonded to aluminium alloy to simulate an aircraft repair. The CFRP used in this project is 'IM7/8552', where 'IM7' and '8552' are the fibre and the epoxy resin designations respectively. The CFRP was prepared from prepreg unidirectional rolls provided by Hexcel Corp, UK. The prepreg came with support backing films on either sides of the composite to prevent creasing and damage. Sixteen plies of CFRP laminae were used in a lay-up sequence of $[0,\pm45,90]_{2s}$, to produce a 2mm thick, quasi-isotropic laminate. The CFRP panels (600mm x 300mm) were then cured using an autoclave according to the manufacturers recommended curing parameters. The curing parameters are given below in Figure 3.3. The cured panels were then machined to the desired scarf angle and size.



IM7/8552 cure procedure:

Apply full vacuum and 15 psig pressure

Heat at 3-5°F (1.8-3°C)/minute to 225°F (107°C).

Hold at 225°F (107°C) for 30-60 minutes.

Raise pressure to 85-100 psig; vent vacuum when pressure reaches 30 psig.

Raise temperature to 350°F (177°C) at 3-5°F (1.8-3°C)/minute.

Hold at 350°F (177°C) for 120 ± 10 minutes.

Cool at 2-5°F (1.2-3°C) to 150°F (66°C) and vent pressure.

Figure 3.3: Curing parameters of IM7/8552 carbon fibre reinforced plastic according to Hexcel Corp

Tensile specimens of the 'IM7/8552' CFRP were manufactured to obtain its material properties. The laminate was 2mm thick with a stacking order of $[0,\pm45,90]_{2s}$. The width and gauge length of the tensile specimens were 24mm and 100mm respectively. The uniaxial test results are shown in Figure 3.4. Material properties of the lamina were obtained from the manufacturer's data sheet and are given in Table 3.3. Using these parameters, a finite element analysis of the CFRP was carried out to model the stiffness of the 16 ply laminate. The modelled stress-strain behaviour of the composite

laminate is shown in Figure 3.4.

Table 3.3: Lamina material properties of IM7/8552 (manufacturer's data)

Fibre orientation	Elastic modulus (GPa)	tensile strength (MPa)
0	164	2400
± 45	5.1	50
90	11.5	80

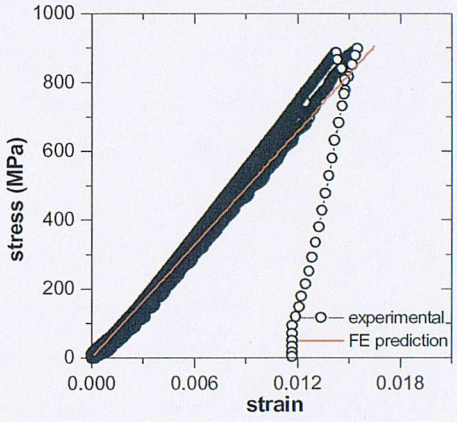


Figure 3.4: Experimental and predicted tensile stress-strain response of a 2mm thick composite laminate with a stacking order of $[0, \pm 45, 90]_{2s}$

3.3 Surface treatments

As was mentioned in the aims and objectives of this project (see section 1.2), one of the main aims of the current project is to investigate the effect of surface treatments on the performance of adhesively-bonded aluminium alloy joints. Of particular interest is the use of the organosilane primer, γ-glycidoxyproplytrimethoxysilane (GPS). The three surface treatments considered here are (a) grit blasting and degreasing (GBD), (b) a silane coupling agent (γ-glycidoxyproplytrimethoxysilane) (GPS) with an initial treatment using the GBD surface treatment, and (c) chromic acid etching (CAE), again with an initial treatment using the GBD surface treatment.

The use of GPS is in accordance with the international collaborative program led by The Structural Materials Centre at DERA, Farnborough. The treatment procedure of the GPS surface treatment was reported by Digby and Shaw [78]. The ideal conditions

used for the GPS surface treatment were also investigated and reported by Mazza [26]. (Effects of the application conditions of the GPS surface treatment were discussed in section 2.4.5.)

One of the most common and simple surface treatments for adhesive bonding is the grit blasting and degreasing (GBD) surface treatment. This method, as well as the CAE surface treatment, was included in this project to compare the results obtained with the GPS surface treatment. The GBD surface treatment is essentially a mechanical surface treatment that improves the roughness and cleanliness of the bonding surface by abrading the bonding surface using alumina grit. The CAE surface treatment is widely known as one of the best surface treatments for aluminium alloys because it promotes strong intrinsic adhesion at the adhesive/adherend interface (see section 2.4.3). In addition, the CAE surface treatment has been shown to provide good environmental durability in adhesively-bonded aluminium alloy joints. However, chromic acid is toxic and hence harmful to the environment. Furthermore, the CAE surface treatment requires the bonding surfaces to be immersed in a chromic acid bath. This proves to be time and cost consuming in real life applications where *in-situ* repair is often the preferred repair procedure. Hence, if the GPS surface treatment can provide good durability to adhesively-bonded aluminium alloy joints, the GPS surface treatment would be the preferred surface treatment, as it is simple and easy to use in field operations. The three surface treatment procedures used in this project are outlined below.

3.3.1 Grit blast and degrease (GBD)

- Acetone wipe to clean specimens.
- Grit blast specimens using 50μm aluminium oxide.
- Acetone wipe again to clean off alumina grit.
- Degrease specimen using a degreasing tank (1,1,1-Trichloroethylene).
- Allow to cool down to room temperature.

3.3.2 GBD and silane (GPS)

- Prepare silane solution.
  - 1% γ-GPS in de-ionized water.
  - Adjust pH of solution to 5.0 using acetic acid as necessary.
  - Stir continuously for 60 minutes using a Teflon bar and a polyethylene beaker.

- Note temperature and humidity.
- Apply silane solution immediately after stirring is completed.
- Apply silane solution with a brush for 10 minutes keeping the surface wet.
- Tip the sample vertical and tap on a paper towel to remove residual silane.
- Immediately insert samples into drying oven.
- Drying parameters are 93°C for 60 minutes.
- Let sample cool to below 30°C and bond immediately.

3.3.3 GBD and chromic acid etching (CAE)

- Heat chromic acid bath to 69°C. The chromic acid bath is composed of sulphuric acid, sodium dichromate, powdered aluminium and copper sulphate [80].
- Immerse specimens fully into chromic acid bath for 20 minutes.
- Rinse specimens with water and immerse in water tank for 10 minutes.
- Keep water running in water tank.
- Spray rinse specimens with distilled water.
- Dry specimens in oven.
- Ready to bond.

3.4 Joint preparation

The bonding procedure used throughout the present project involves curing the adhesive using a hot press machine. The surface pretreated panels were inserted into an aluminium alloy frame with a layer of adhesive between the two bonding surfaces. This was then clamped in between the hot plates in a hot press machine, see Figure 3.6. A pressure of 0.2-0.3MPa was then exerted onto the panel according to the procedure explained by Digby and Shaw [78]. The aluminium alloy frame acts as an alignment tool when placing the components of the adhesive joint together (the adherends and the adhesive). In addition, it also serves to prevent the adherends from moving, whilst the adhesive cures and so hardens. The adhesive, FM73 M, was cured at 120°C for 60 minutes and the adhesive joint was left to cool to room temperature using the water-cooling feature of the hot press machine. This took an additional 30 minutes.

Three types of joint designs were used in the present project. They are the single

overlap joint design, the single scarf joint design and the double scarf joint design, see Figure 3.5. One of the aims of this project is to optimize the scarf joint design. The optimization of the geometrical dimensions for the scarf joint design used in the project will be discussed in Chapter Four. In terms of adherend materials, the joints used in this project can be categorized into two categories: aluminium alloy joints and aluminium alloy/CFRP hybrid joints. The preparation procedure of the CFRP composite was given in section 3.2.3.

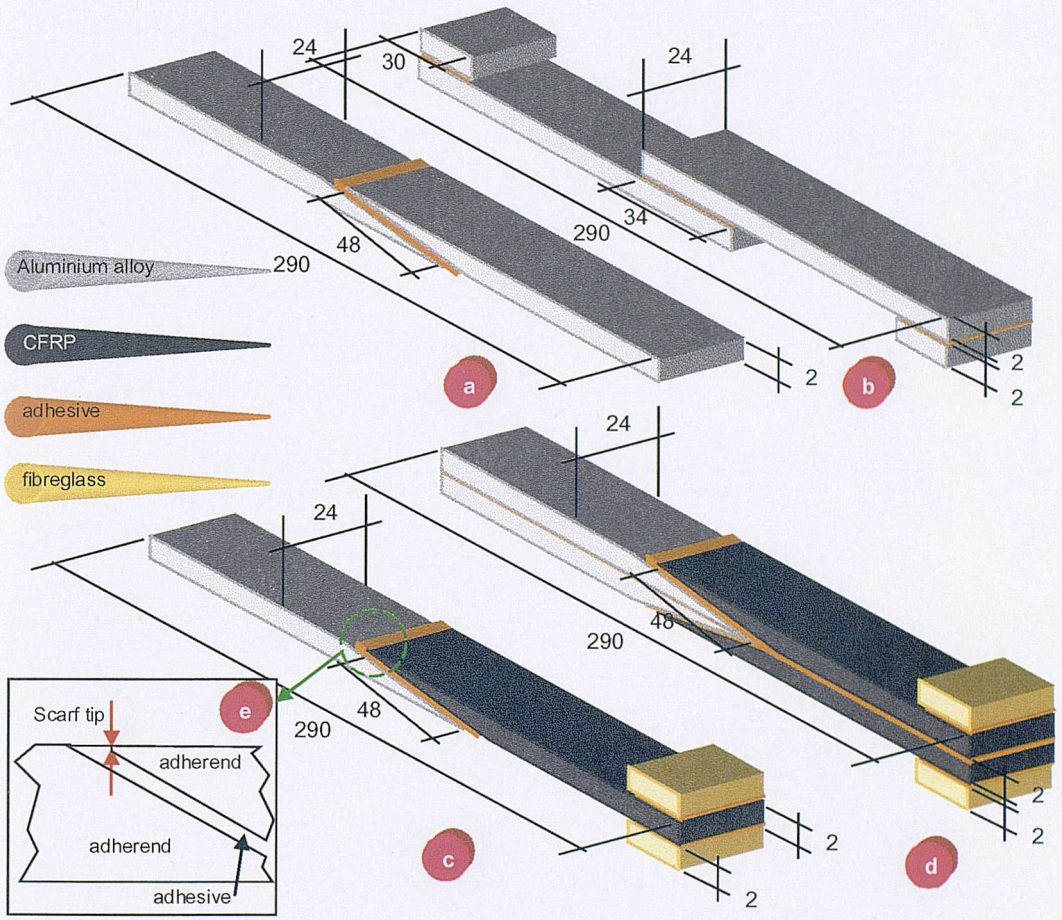


Figure 3.5: Main joint designs used in current project (a) aluminium alloy single scarf joint (b) aluminium alloy overlap joint (c) aluminium alloy/CFRP single scarf joint (d) aluminium alloy/CFRP double scarf joint (e) presence of scarf tip in a scarf joint

**Note: dimensions given in mm*

The scarf adherends were produced by using conventional milling machines. The thickness of the scarf tip, see Figure 3.5e, depends on the efficiency of holding down the adherend onto the machine bed to resist the reaction force from the milling action. It was found that by using a mechanical locking device, the thinnest scarf tip that could be produced without severe warping of the scarf adherend was 0.4mm. By using a vacuum

suction device to hold down the adherend, a scarf tip thickness of 0.15mm could be produced. The effect of scarf tip thickness on the performance of scarf joints will be discussed in section 4.5.

All the coupon joints were produced in the same way. The only difference being that fibreglass end tabs were used to protect the CFRP composite adherends from being damaged by the compressive stresses imposed by the wedge grips. The fibreglass end tabs were bonded using araldite room temperature curing adhesives and were bonded to the hybrid joints after the production of the joints. For the overlap joint design, aluminium alloy end tabs were used to eliminate the loading eccentricity in the joint geometry. The end tabs were adhesively-bonded to the adherends using the same adhesive as was used in the joint (i.e. FM73 M). The adhesive used for these end tabs was cured at the same time as the adhesive in the joint. Figure 3.6 shows the setup of the specimens for the curing of the adhesive. It can be seen that alignment plates, made of aluminium alloy, were used for the alignment of the overlap joint configuration.

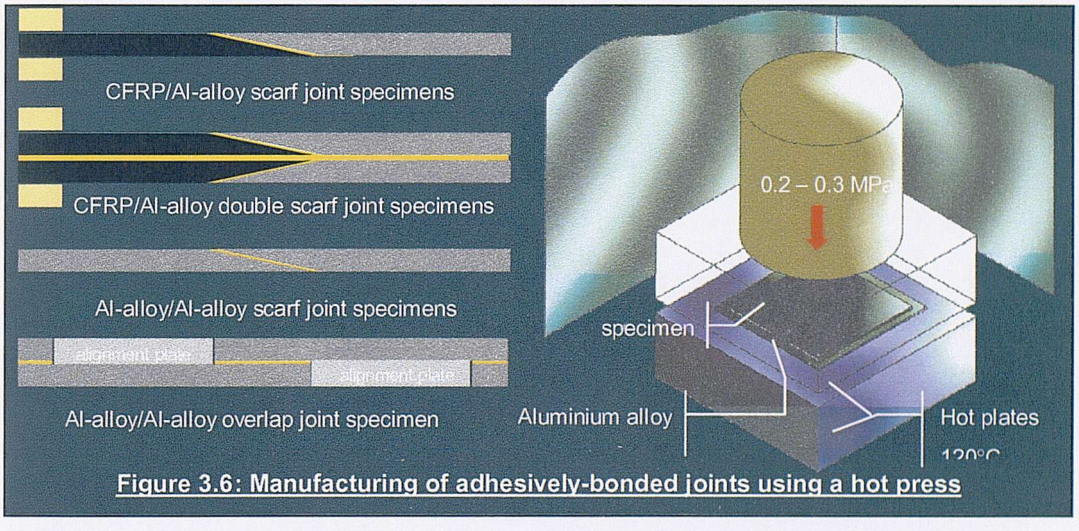


Figure 3.6: Manufacturing of adhesively-bonded joints using a hot press

3.5 Experimental procedures

3.5.1 Introduction

Monotonically-loaded and fatigue tests were used to compare the effects of geometrically-induced stress concentrations in the joint, as well as the effects of surface treatments. In addition, monotonically-loaded tests were used to compare the maximum

load carrying capability of the various joint designs used in this project. The effects of the test environment on the durability of adhesively-bonded joints were investigated using accelerated fatigue tests, where the joints were immersed in an aqueous bath. This will be discussed in Chapter Five. The following sub-sections provide more details of the various experiments that were employed throughout this project.

3.5.2 Monotonically-loaded tests

This test method involves the loading of the adhesive joint in tension using a constant displacement rate until the final fracture of the joint. The tests were carried out using an Instron tensile testing machine. . Specimens were gripped in the machine using Instron designated wedge grips. The load-deflection history was then recorded. All monotonically loaded tests were performed at the ambient temperature of 23 ± 1°C and room humidity (55% R.H.). A constant displacement rate of 1mm/min was used throughout the project.

3.5.3 Fatigue and durability tests

3.5.3.1 'Dry' fatigue tests

This test method involves loading the adhesive joint under cyclic fatigue loading with a prescribed loading frequency, load amplitude and mean value. As discussed in section 2.7, the fatigue performance of adhesively-bonded joints depends on many different operating parameters. Hence, in order to reduce the size of the experimental data, some of these parameters were fixed. A frequency, f of 5Hz and a stress ratio, R ($\sigma_{max}/\sigma_{min}$) of 0.1 were used. The varying loads were applied using a sinusoidal waveform. Fatigue tests were carried out in either a 'dry' or a 'hot/wet' test environment. The 'dry' tests were carried out at room temperature (23 ± 1°C) and with atmospheric humidity of 55% R.H. The specimens were fatigued to failure and the number of cycles to failure was recorded. The threshold load was taken to be the load where the service life reached 5-10 million cycles. Tests were stopped after this if no failure was observed. The stress-number of cycles to failure, σ_{max}-N_f, curves of the fatigue performance of the adhesively-bonded joints were thus obtained.

3.5.3.3 Durability tests ('hot/wet' tests)

It has been shown in section 2.7.2 that the environmental test conditions can significantly affect the durability of adhesively-bonded joints. Adhesively-bonded joints are especially vulnerable when water is present, either in liquid or vapour form. However, it has been suggested that organosilane primers are particularly good in protecting the adhesive/adherend interface from water attack. In the current project, the organosilane primer, GPS is compared with the GBD and CAE surface treatments. Accelerated testing was carried out to compare the three surface treatments mentioned above for the aluminium alloy adherends.

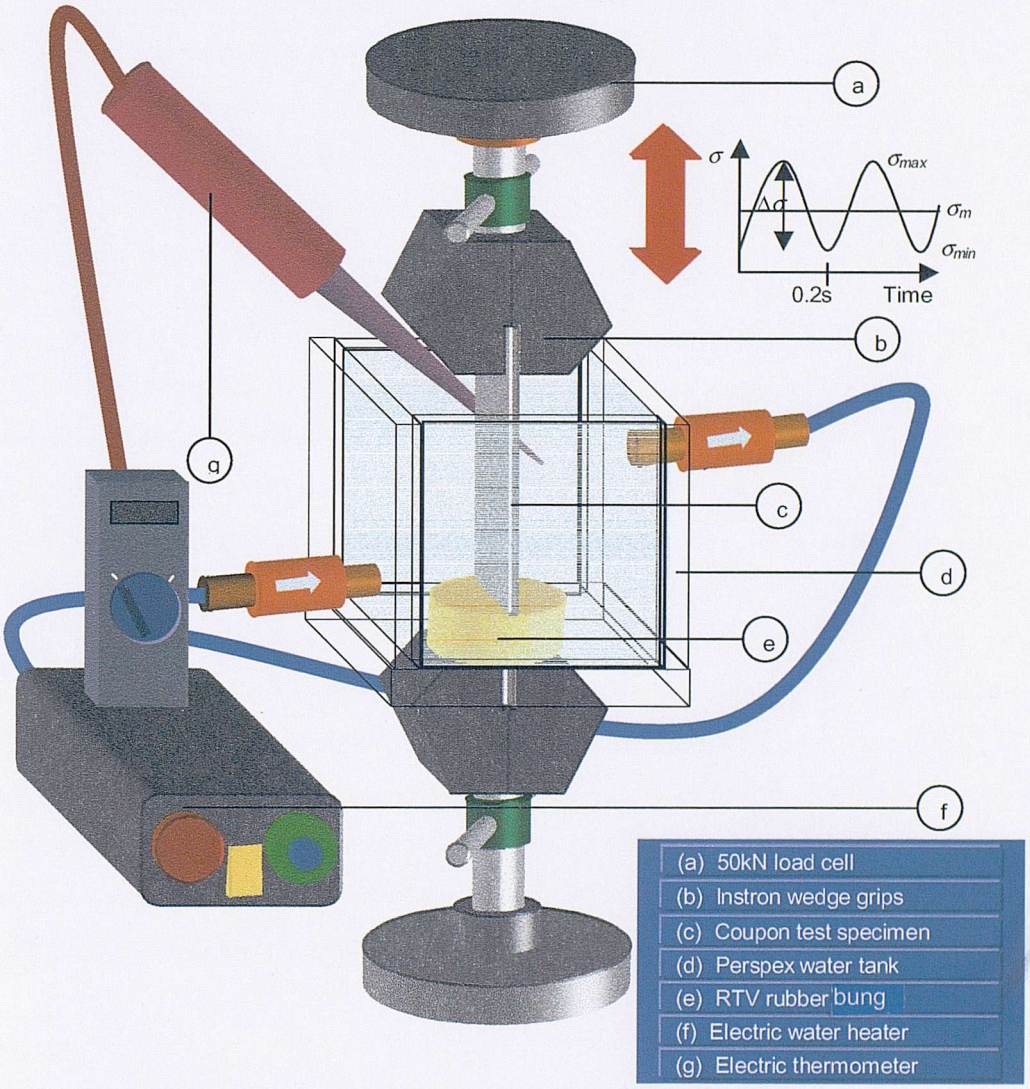


Figure 3.7: Schematic diagram showing the experimental setup of the 'hot/wet' accelerated fatigue tests

The tests were carried out by immersing the adhesively-bonded coupon test specimens in a water bath where a heater pump was used to maintain a constant water flow at a temperature of 28°C. Distilled water was used throughout the experiments. In addition, the test specimens were subjected to fatigue loads with constant load amplitudes. The tests were carried out using a sinusoidal waveform with a frequency, f of 5Hz and a stress ratio R ($\sigma_{max}/\sigma_{min}$) of 0.1. These test parameters were used in conjunction with the fracture mechanics tests of Adams [4] where the fracture mechanics data of the same adhesive systems, as used in the present project, were obtained. The experimental procedure for the accelerated tests using the coupon test joints described in section 3.3 is shown in Figure 3.7. A 'Perspex' water tank is connected up to an electrical heater pump and is used to contain water. A hole at the bottom of the tank was cut out and refilled with a RTV silicone rubber bung. A slit was then cut into the middle of the rubber bung to allow the specimen to slide through it. Once the specimen is in place, rubber sealant was then used to close the slit in the rubber bung to prevent water from leaking out of the tank.

3.5.3.3 'Back face strain gauging technique'

The back face strain gauging technique was used to evaluate the crack initiation and crack propagation periods of an adhesively-bonded joint loaded in tension-tension fatigue. A strain gauge was positioned at the opposite face to the joint end (i.e. opposite a scarf tip for the scarf joint design), see Figure 3.8a. As a crack initiates from the joint end, the stiffness at the local region of the strain gauge will reduce and this will be shown by a change in the strain gauge reading, see Figure 3.8b. This method has been used successfully by previous workers [80,81] (see section 2.7.4). However, the position of the strain gauge is crucial to the sensitivity of the strain gauge to detect the change in stiffness. Nevertheless, this has proved to be a cost effective way to assess the number of fatigue cycles occupied by the crack initiation period during the fatigue life of an adhesively-bonded overlap joint.

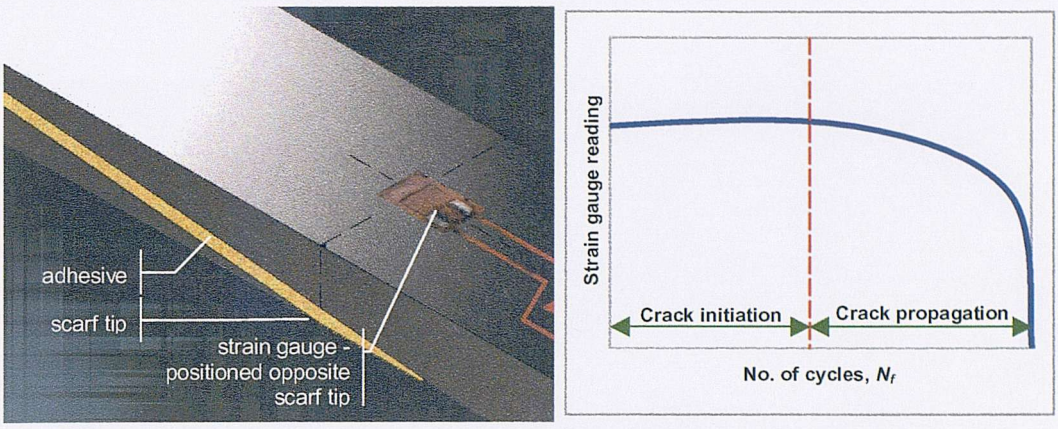


Figure 3.8: (a) diagram showing positioning of strain gauge on adhesively-bonded joint (b) typical strain gauge reading curve observed for crack initiation and crack propagation periods in tension-tension fatigue tests

3.6 Adhesively-bonded repairs

3.6.1 Introduction

In many of the repair examples given in Table 2.8, the adhesively-bonded repair of metallic structures using composite materials had been shown to be capable of restoring the strength of the damaged structures [60]. The current use of adhesively-bonded repair of aerospace structures using composite materials has been discussed in section 2.8. In the current project, adhesively-bonded repair of cracked aluminium alloy panels were carried out to investigate the effect of surface treatments on the durability of the repaired panels. The crack patch repair technique pioneered by ARL [64] is used in the current project. The following sections will discuss the manufacture of the repair panels and the experimental procedures. Experimental results, as well as the theoretical and finite element predictions of the repair efficiency, are given in Chapter Seven.

3.6.2 Repair procedure

3.6.2.1 Inserting a stress raiser for fatigue pre-cracking

The aluminium alloy, L157, is used in this investigation. The aluminium alloy panels were machined to the dimensions of 610mm x 200mm x 2mm and a hole of radius 3mm was drilled into the middle of the panels. Two notches of length 2mm each were manually inserted into the horizontal sides of the centre hole using a fine jeweller's saw. These

notches serve as stress raisers for fatigue cracks to initiate, see Figure 3.9.

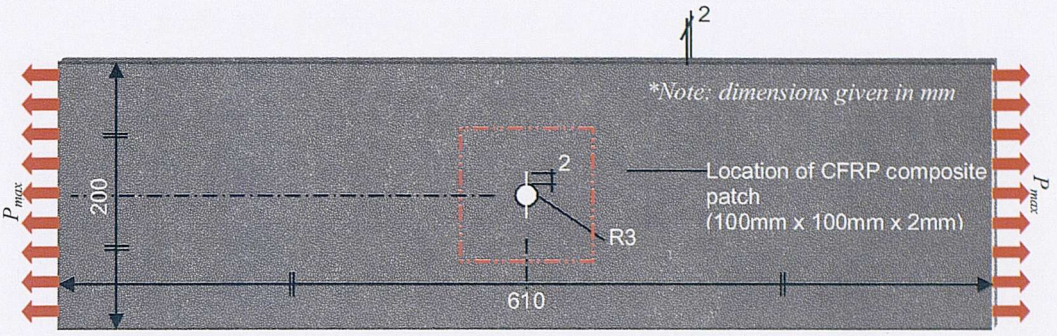


Figure 3.9: Schematic diagram showing the location of the centre hole and the two sawed notches from the horizontal sides of the centre hole in the aluminium alloy panel

The notched panels were then fatigued to initiate fatigue cracks from the two notches. This fatigue pre-cracking process is carried out at a frequency, *f*, of 3Hz using a sinusoidal waveform. The maximum applied load was 30kN with a stress ratio, *R* of 0.1. The fatigue pre-cracked panels were taken out of the Instron fatigue machine when the fatigue pre-cracks had each reached a length of 8mm. Grid lines, with a line spacing of 10mm width, were hand drawn onto the aluminium alloy panels to act as visual guides for the measurement of the length of the cracks. A commercially-available digital video camcorder was used to measure the crack length.

3.6.2.2 Repair of cracked aluminium alloy panels using composite patch

Adhesively-bonded repairs of the cracked aluminium alloy panels were carried out by using the epoxy film adhesive FM73 M. Material properties of the adhesive were given in section 3.2.1. CFRP composite patches of dimensions 100mm x 100mm x 2mm were used in this repair procedure. The CFRP composite patches were made up of 16 plies of uni-directional laminae with a stacking order of $[0,\pm45,90]_{2s}$. Material properties of this composite were given in section 3.2.3. The cracked aluminium alloy panels were repaired by adhesively bonding the composite patch to one side of the panel. The pre-cured composite patch was positioned in the middle of the panel, see Figure 3.9. As the dimensions of the aluminium alloy panels were too large to fit into the available hot press machine, the repair panels were therefore cured in an oven. The curing temperature of the adhesive was 120°C and the repaired panels were cured for one hour. A rig was constructed to hold the repair panel components (aluminium alloy panel, composite patch

and adhesive) together in the oven, Figure 3.10. Rubber spacers were used on the repair side of the panel to control the thickness of the adhesive layer. Two 10mm thick aluminium alloy panels were used on either sides of the repair panel and steel brackets were used to support the rig. A thermo couple was also used to measure the temperature at the free surface of the composite patch. A film of non-stick cloth was used to prevent the adhesive from extending out onto the supporting aluminium alloy panels.

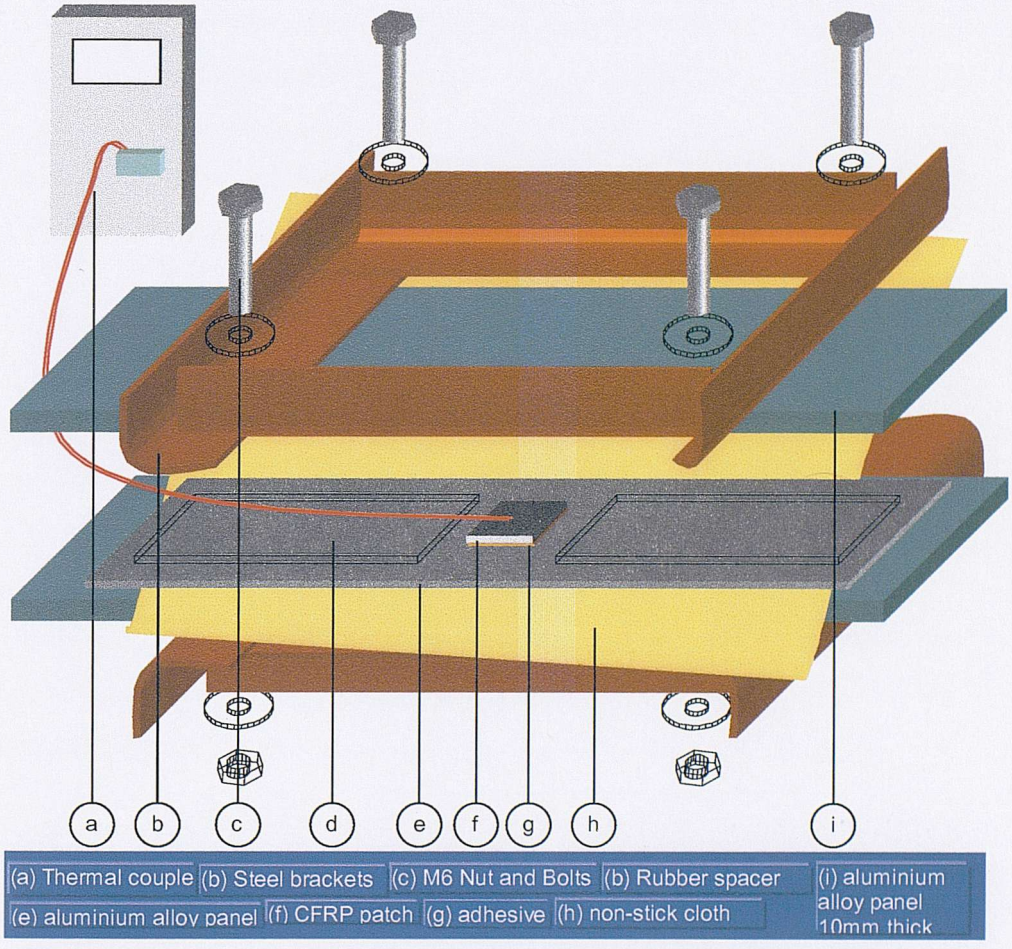


Figure 3.10: Schematic diagram showing the configuration used to produce the adhesively-bonded repair panels

3.6.3 Durability test of adhesively-bonded repair panel

Fatigue tests of the adhesively-bonded repair panels were carried out in both 'dry' and 'hot/wet' conditions. The panels were loaded to a maximum load of 30kN with a stress ratio, R, of 0.1. The panels were fatigued at 3Hz, using a sinusoidal waveform. The details of the experimental setup are shown in Figure 3.11. Two aluminium alloy plates of

dimensions 205mm x 200mm x 10mm were bolted on to each end of the repair panel, see Figure 3.11. Bell-shaped fixtures with a 40mm diameter pin-hole were used to load the repair panels. The fatigue tests were carried out using an ESH servo-hydraulic testing machine.

In order to measure the crack growth in the repair panel, a digital video camcorder was used. Ten pictures of the crack in the repair panel were taken at intervals of thirty seconds. The frame rate used was 30fps (frames per second). The camera was mounted on an adjustable platform and was connected to a computer. The camera was positioned at the unbonded face of the repair panel where grid lines of 10mm spacing were hand drawn onto the unbonded surface of the repair panel. Spotlights were used to provide sufficient lighting onto the repair panel, whenever necessary.

For the 'hot/wet' durability tests, a repair panel was inserted into a 'Perspex' water tank that has a RTV silicone rubber bung sitting at the bottom of the tank. The RTV silicone rubber bung had a slit cut into the middle of it to allow a single repair panel to slide through it. Once a specimen was secured in the rig, rubber sealant was then applied to close the slit in the rubber bung to prevent water from leaking from of the tank. A rig was constructed using steel brackets to allow the 'Perspex' tank to sit on it. 'G-grips' were used to secure the 'Perspex' tank onto the steel rig. The temperature of the water was maintained at 28°C by using an electrical heater pump. Distilled water was used throughout the experiment.

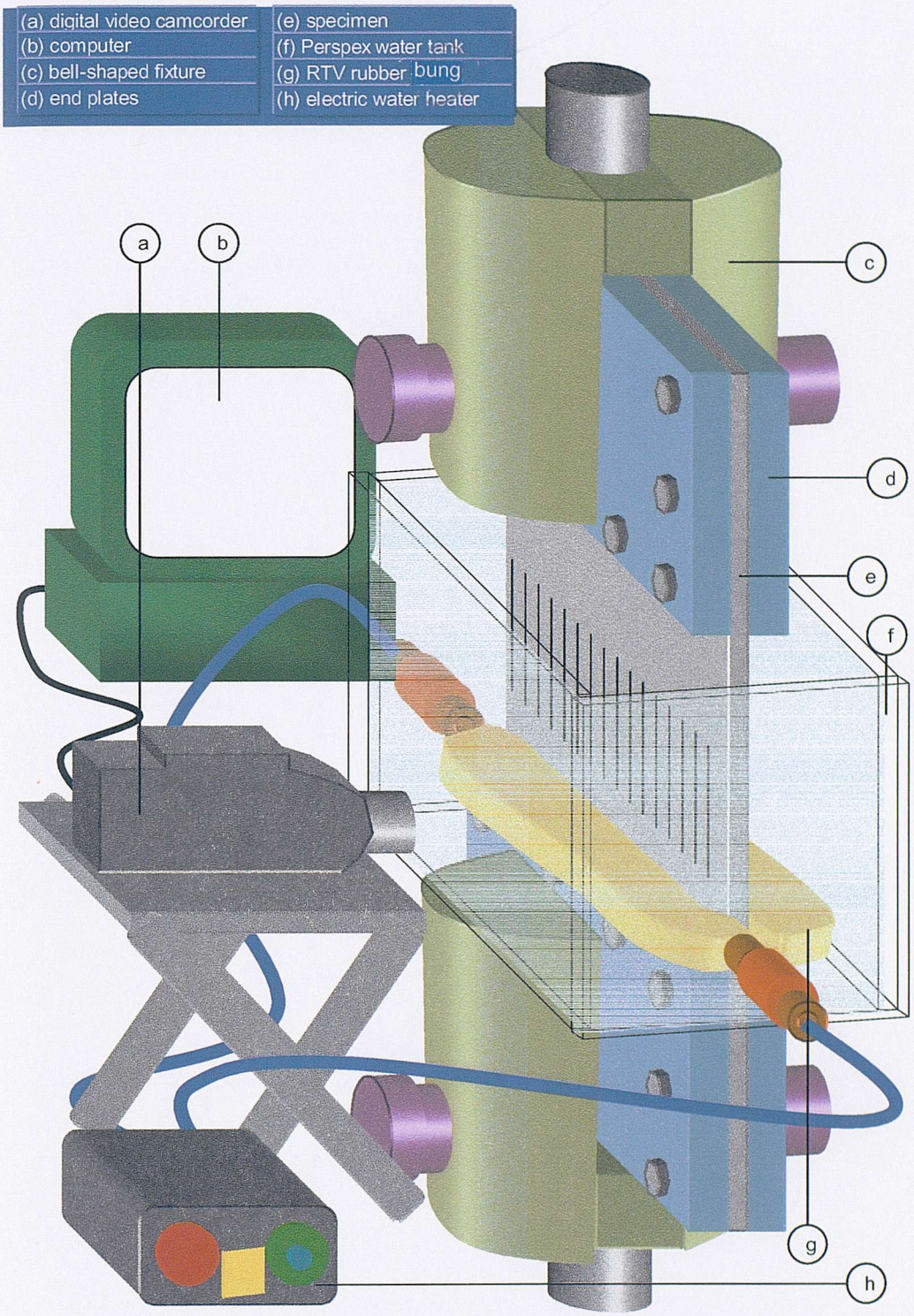


Figure 3.11: Schematic diagram of the experimental setup of the adhesively-bonded repair panel tests conducted in water

3.7 Chapter summary

The material properties of the various materials used in the construction of the experimental specimens were given in this chapter. In addition, procedures for the curing of the adhesive and composite materials were also given in detail. The manufacturing processes of the adhesively-bonded coupon joints were also given. Also detailed in this chapter are the three experimental procedures used in the present project. They are the monotonically-loaded tests and the 'dry' and 'hot/wet' fatigue tests. Lastly, description of the manufacturing and test procedure of the medium scale repair panels were presented.

CHAPTER 4

OPTIMIZATION OF THE SCARF JOINT DESIGN

4.1 Introduction

As mentioned in Chapter One, one of the main aims of the present project is to optimize the scarf joint design. This will be discussed in the present chapter. Analytical, finite element and experimental methods were used to optimize the scarf joint design. Analytical solutions of the scarf joint design have been briefly reviewed in section 2.5.4 and the analytical method used in the present project will be further discussed in section 4.2. This is followed by a discussion of the finite element method used to optimize the geometrical parameters of the scarf joint design (section 4.3). Monotonically-loaded tests are also carried out on selected scarf joint designs to compare with the theoretical results and the experimental procedures which were discussed in Chapter Three.

The scarf joint design owes its name to the orientation of the adhesive plane where it is at an angle to the direction of loading. The obvious advantages of the scarf joint design are (a) the reduced loading eccentricity and (b) the flat outer surface that will eliminate aerodynamic inefficiencies. However, as explained in section 3.4, a milled scarf angle on an adherend will inevitably leave a finite scarf tip thickness, t_{st}. Hence, if the

scarf angle is small, a significantly large gap will appear outside the overlap terminus. This region is defined as the adhesive fillet (see Figure 4.1).

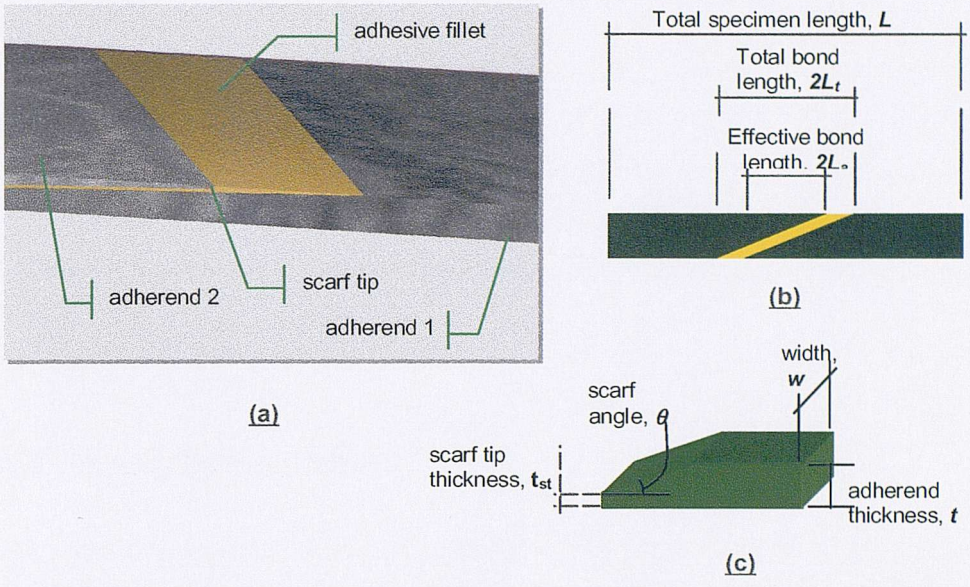


Figure 4.1: Schematic diagram of a scarf joint and definition of symbols used in subsequent sections (a) 3D image of a scarf joint showing the presence of the adhesive fillet as a result of the scarf tip thickness (b) front view of a scarf joint (c) front, detailed, view of a scarf adherend

The thickness of a scarf tip is related to the scarf angle, scarf length and the thickness of the adherend. Simple trigonometry gives:

$$\sin\theta = \frac{t - t_{st}}{L_a + L_t} \quad \text{.....(4.1)}$$

where θ is the scarf angle, t is the thickness of the adherend, t_{st} is the thickness of the scarf tip, L_a is half the effective bond length and L_t is half the total bond length (see Figure 4.1). Equation (4.1) shows that changing one of these variables will inevitably alter at least one of the other variables in the equation.

The geometrical parameters of the scarf joint design that were investigated in the present project are the scarf tip thickness, t_{st}, the scarf angle, θ and the adhesive fillet size and entry angle, θ_f. These were considered to be of importance since previous work has revealed that predictions based on ideal scarf joint models (i.e. with no scarf tip) often overestimate the strength of scarf joints [37], whilst other workers have shown that the scarf angle significantly affects the performance of a scarf joint design (see section 2.5.4).

The presence and shape of any adhesive fillet were also shown to significantly affect the performance of the overlap joint geometry (see section 2.5.3.4).

In addition, the effect of the temper grade of the aluminium alloy adherend on the static strength of geometrically similar scarf joint designs was also investigated (see section 4.8). Lastly, a comparison between the scarf joint design and the overlap joint design is discussed in section 4.9. Further details of the investigations for each of the variables considered are given in the introduction to the individual sections (see section 4.5-4.9).

4.2 Analytical analysis

The simplified analytical solution for the scarf joint design of Nguyen and Kedward [14] was used in the present project. Assuming no bending effects and elastic material properties, the shear strain distribution in the adhesive layer of a scarf joint can be solved analytically using a second order differential equation, equation (4.2), of the shear strain in the adhesive [14]. This is essentially a boundary value problem and this equation can be solved numerically using the Runge-Kutta method or the finite difference method. The second order differential equation of the shear strain in the adhesive is given in equation (4.2):

$$\frac{d^2\gamma_a}{dx^2}=\frac{\mu}{\eta}\frac{d\gamma_a}{dx}+\frac{G_a w\gamma_a\eta}{t_a}+\frac{P\cos(\theta)}{t_a A_2(x)E_2}\left[\frac{\mu}{\eta}+\frac{1}{A_2(x)}\frac{d}{dx}A_2(x)\right] \quad \text{.....(4.2)}$$

$$\eta=\left(\frac{1}{A_1(x)E_1}+\frac{1}{A_2(x)E_2}\right) \qquad \mu=\frac{d}{dx}\eta$$

The free body diagram of a scarf joint is given in Figure 4.2, where the symbols, x, t_a, P, θ in equation (4.2) are defined. G_a and E_2 are the adhesive shear modulus and the adherend elastic modulus respectively. The variable $A(x)$ is the cross section area of the adherend within the effective bond length. The subscripts 1 and 2 denote adherend 1 and adherend 2 (see Figure 4.2).

Assuming that the scarf tip thickness, t_{st}, of both the adherends are the same and that the thickness of the adherend changes linearly along the bond length, $2L_a$, the adherend thickness as a function of x is:

$$t_1(x) = \frac{1}{2L_a}(t - 2t_{st} - t_a\cos(\theta))x + \frac{1}{2}(t - t_a\cos(\theta))...(4.3a)$$

$$t_2(x) = \frac{-1}{2L_a}(t - 2t_{st} - t_a\cos(\theta))x + \frac{1}{2}(t - t_a\cos(\theta))...(4.3b)$$

The cross section area of the adherend, $A_i(x)$ in a scarf joint changes with, x and is related to the adherend thickness, $t_i(x)$ (equation (4.3)) and the width of the joint, w by:

$$A_i(x) = wt_i(x).....(4.4)$$

Substituting equations (4.3a and b) into equation (4.4) gives the change in cross section area of the adherend along the bond length of a scarf joint. Subscript i can be substituted for subscript *1* or *2* of the adherend. For equal adherends, the boundary conditions for equation (4.2) can be shown to be equal at both ends of the joint [14]. From equation 4.3, the boundary conditions, in the form of the first derivative of the shear strain in the adhesive, can be shown as:

$$\frac{d}{dx}\gamma_a(-L_a) = \frac{\cos(\theta)}{t_a}\left(\frac{P}{A_2(x)E_1}\right).....(4.5a)$$

$$\frac{d}{dx}\gamma_a(L_a) = \frac{\cos(\theta)}{t_a}\left(\frac{P}{A_1(x)E_2}\right).....(4.5b)$$

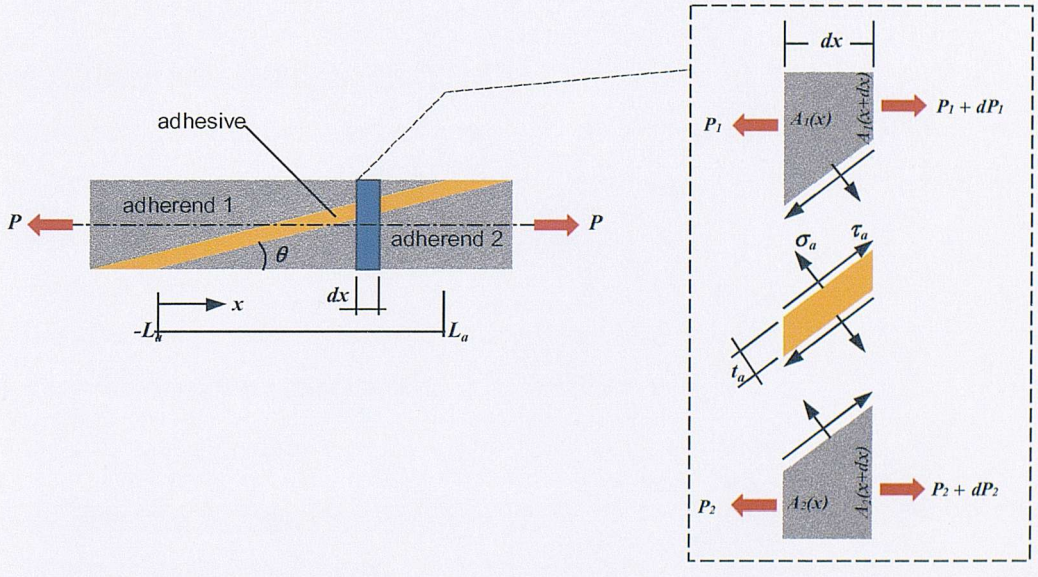


Figure 4.2: Free body diagram of scarf joint

The incremental step size, h, used to solve this second order differential equation is defined as the bond length divided by the number of increments, n. The number of increments was defined by the number of increments whereby the calculated result is within 1% of the expected value. Equation 4.2 was solved using the 'MathCAD 6' program. The shear stress distribution in the adhesive is then calculated from the shear strain distribution by multiplying by the shear modulus. In the following investigations, an applied load of 5kN was used throughout. This load will be shown later to be well within the elastic region of the various adhesively-bonded joint designs.

4.3 Finite element analyses

4.3.1 Introduction

The two main reasons for using finite element analysis to optimize the scarf joint design are: (a) the complexity of analytical solution when bending of the joint and plasticity effects are included and (b) the non-uniform geometry of the scarf joint design, especially at the overlap terminus. Two-dimensional finite element models were used throughout the following investigations. Plane strain conditions and non-linear geometrical deformation were assumed for all cases. Continuum elements were used to model the adhesive joint. Both elastic and elastic-plastic material properties were considered in separate analyses.

4.3.2 Linear-elastic finite element analyses

Linear-elastic finite element analyses were used to investigate the stress distributions in the adhesive and the adherend. A load of 5kN was applied to the models, which from experiments proved to be well within the elastic region of the joints. By comparing the maximum stresses in the joints, the effects of the geometrical parameters under investigation can be ranked. The stress distributions were normalized with respect to the critical stress components given in Table 4.1 (see section 4.4.2).

4.3.3 Elastic-plastic finite element analyses

Elastic-plastic finite element analyses were used to predict the static failure load of the joints investigated. The reason for using the elastic-plastic finite element analysis is because adhesively-bonded joints, when loaded to failure, often show evidence of having

undergone plastic deformation. Results from the elastic-plastic finite element analyses can hence be compared directly with the experimental results. A number of failure criteria were compared and the failure criterion to occur first is taken to be the most relevant failure criterion. Table 4.2, in section 4.4.3, summarises the various failure criteria used.

4.3.4 Mesh dependencies of the finite element models

One of the fundamental problems of using the finite element analysis is that errors in the analysis increase significantly at high stress concentration regions. One way of reducing the errors in the analysis is by refining the mesh at such high stress regions. Thus, a number of models with increasing numbers of element layers in the adhesive were produced to quantify the effect of mesh refinement in these high stress regions. Three models with (a) three element layers, (b) five element layers and (c) seven element layers were used for this comparison. The mesh grids are shown in Figure 4.3. All three models have the same geometrical parameters. The direct stress, σ_{xx}, peel stress, σ_{yy}, and shear stresses τ_{xy}, in the adhesive, normalised with the applied stress were evaluated, see Figure 4.4. The normalised stresses were compared between the three models (see Figure 4.4a and b).

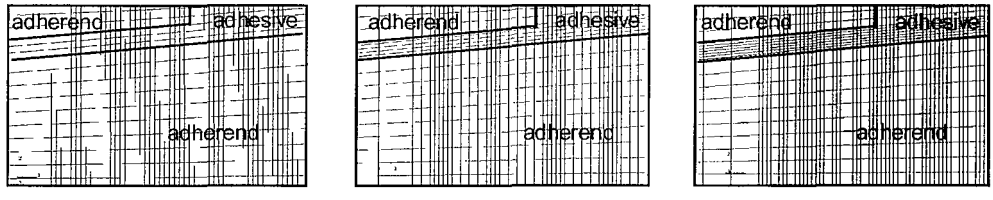


Figure 4.3: Mesh refinement of the adhesive layer

At the centre of the bond-line, the values of the normalised direct, peel and shear stresses are independent of the mesh employed, see Figure 4.4a. Near the adhesive/adherend interface, the normalised peel and shear stresses were almost independent for all three models, see Figure 4.4b. However, the normalised direct stress increases by 17% with an increase of element layers from three elements to seven elements across the adhesive thickness. However, an increase of less than 6% in the maximum direct stress at the interface of the adhesive was observed for an increase of element layers from five elements to seven elements across the adhesive thickness. This investigation suggests that, by a finite element model the five element layer, the number

of elements in the finite element analysis can be kept relatively low, but whilst the numerical errors from this analysis are minimal.

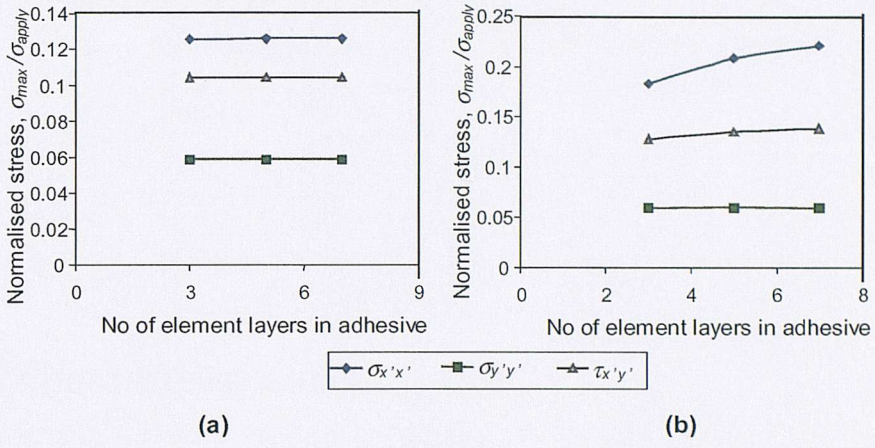


Figure 4.4: Effect of mesh density in the adhesive layer on the stress components at the (a) centre of the adhesive layer, $y' = 0$ (b) near the interface, $y' = 0.4t_a$

4.4 Definition of coordinate systems and failure criteria

4.4.1 Coordinate systems

The global coordinate system, x-y, originates from the bottom left hand end of the joint, Figure 4.5. In the adhesive, three stress components were obtained from the finite element analyses. They are the horizontal ($\sigma_{x'x'}$), vertical ($\sigma_{y'y'}$) and shear stresses ($\tau_{x'y'}$) and are oriented in the local Cartesian coordinate system x'- y' (see Figure 4.5). The origin of the local coordinate system, x'- y', is at the middle of the joint adhesive layer.

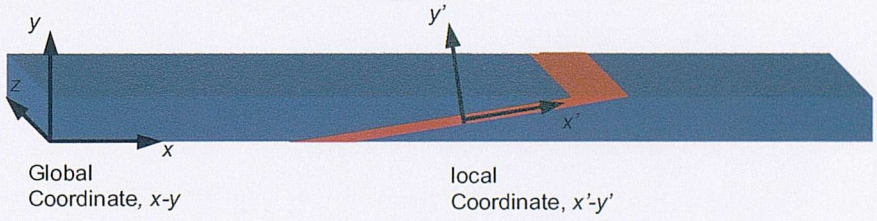


Figure 4.5: Global and local coordinate system used to define stress orientation

4.4.2 Critical stress value for linear-elastic analyses

The stress components obtained from the analytical and elastic finite element analyses that will be shown in the following sections were normalised with respect to their corresponding critical stress values. These critical stresses correspond to the yield stresses of the various materials used in the following investigations. Table 4.1 summarizes the

critical stresses of the adhesive and the adherend using the material properties of the FM73 M and 2014A 'L157' aluminium alloy respectively.

Table 4.1: Critical stress values used to normalize stress components †

Stress components	Critical stress (MPa)
Adhesive (FM73 M) Direct stress, $s_{x'x'}$	62
Peel stress, $s_{y'y'}$	62
Shear stress, $s_{x'y'}$	31
Adherend (2014A L157) Direct stress, s_{xx}	450

4.4.3 Failure criteria for elastic-plastic analyses

As mentioned in section 4.3.3, failure criteria are required in order to predict the static failure load, as well as the failure locus, of adhesively-bonded joints. Naturally, failure criteria for the adhesive as well as for the adherend are needed. Table 4.2 shows the commonly used failure criteria to determine both adhesive failure and adherend failure.

Table 4.2: Failure criteria used in elastic-plastic finite element analysis

Failure criteria	value	Failure criteria	value
Adhesive		Adherend	
Fracture shear strain, γ_f (%)	61	ultimate tensile strength, σ_{UTS} (MPa)	
Fracture shear stress, τ_f (MPa)	44	T6 'L157'	480
Fracture Mises stress, σ_f (MPa)	74	T4 'L156'	440

4.5 Effects of scarf tip thickness

4.5.1 Introduction

The first geometrical parameter investigated is the scarf tip thickness, t_{st}, see Figure 4.1c. Analytical and finite element analyses were used to investigate scarf joints with scarf tip thickness: $0 < t_{st} < 0.4$mm. The geometrical parameters of the models investigated are summarized in Table 4.3.

As explained in the previous chapter, the thickness of a scarf tip can be accurately machined by employing a vacuum-suction holding-device on the milling machine, since this can minimize the high reaction force of the milling action. It was found that this method could produce a scarf tip thickness, t_{st}, of 0.15mm. On the other hand, a scarf tip

† *Peel and direct stresses taken to be 2 x 31 = 62 MPa*

thickness, t_{st}, of 0.4mm can be produced using a mechanical screw-locking holding-device. Hence, two scarf joint models were produced with a scarf tip thickness of, 0.4mm and 0.15mm and were tested in monotonically-loaded tests. The scarf angle for both models was kept at 1.8°. Hence, the effective bond length was approximately 34 mm and 48 mm respectively, according to equation (4.1). All the other geometrical parameters were kept constant. The CAE surface treatment was used for both joint models, to try to ensure that failure did not occur at the interface.

Table 4.3: Geometrical parameters of scarf joint models, with 2mm thick adherends, used to investigate the effects of scarf tip thickness, t_{st}

Scarf tip thickness, t_{st} (mm)	Bond length, $2L_a$ (mm)	Scarf angle, θ (°)	Adherend thickness, t (mm)	Adhesive thickness, t_a (mm)
0.5*	25.5	1.8	2	0.2
0.4*^	31.8	1.8	2	0.2
0.3*	38.2	1.8	2	0.2
0.2*^	44.6	1.8	2	0.2
0.15*^	47.8	1.8	2	0.2
0.12^	49.7	1.8	2	0.2
0.1*	50.9	1.8	2	0.2
0.08^	52.2	1.8	2	0.2
0.05^	54.1	1.8	2	0.2
0^	57.3	1.8	2	0.2

* investigated using analytical solution
^ investigated using linear elastic FE

4.5.2 Analytical analysis

As mentioned in section 4.1, the bond length of a scarf joint is related to the scarf angle and the scarf tip thickness. Table 4.3 shows that a small change in the scarf tip thickness can result in a significant change in the bond length. This is of course due to the small scarf angle used. The definition of the analytical governing equation for the shear strain distribution in the adhesive layer was given in section 4.2. It was mentioned that the boundary conditions used to solve the second order differential equation (equation 4.2) are given by the first derivatives of the shear strain in the adhesive layer, (see equation 4.5). In addition, the first derivatives of the shear strain at both ends of the overlap will be equal in magnitude but are of opposite signs. This special case will only be valid for identical adherends with a constant scarf angle and scarf tip thickness. Table 4.4 shows an example of the accuracy of this iteration procedure using 50 iterations.

Table 4.4: Example of the iteration procedure used to calculate the maximum shear strain in the adhesive layer at the overlap terminus for different scarf tip thickness, t_{st}

Scarf tip thickness, t_{st} (mm)	Thickness ratio, t_{st}/t (%)	Number of iterations, n	Calculated from equation (4.5) $\gamma'_a(-L_a)$	Calculated from Runge-Kutta iterations $\gamma'_a(L_a)$	Percentage error* (%)	Calculated maximum shear strain, $\gamma_a(-L_a)$
0.5	25	50	-11.61	11.62	0.16	0.04
0.4	20	50	-10.78	10.77	0.05	0.03
0.3	15	50	-10.06	10.02	0.34	0.03
0.2	10	50	-9.43	9.46	0.34	0.02
0.15	7.5	50	-9.14	9.14	0.10	0.02
0.1	5	50	-8.88	8.91	0.36	0.02
0.05	2.5	50	-8.62	8.67	0.54	0.01

*Note: Percentage error = $[(\gamma'_a(-L_a) - \gamma'_a(L_a))/\gamma'_a(-L_a)]\%$
Values are correct to 2 decimal places.

From Table 4.4 it can be seen that the reduction of the scarf tip thickness reduces the maximum shear strain at the overlap terminus. A reduction of the scarf tip thickness from 0.5mm to 0.05mm yields a 62% reduction in the maximum shear strain at the overlap terminus. This is accompanied by an increase of approximately 112% in the overlap bond length (see Table 4.3).

However, it is unclear from Table 4.4 whether the contributing factor to the reduction of the maximum shear strain at the overlap terminus is due the reduction of the scarf tip thickness or the corresponding increase in the overlap length. Hence, the maximum shear strain in the adhesive is plotted against the thickness ratio (t_{st}/t) and this is given in Figure 4.6. Therefore, in addition, scarf joints with adherend thickness of 4mm and 6mm were also analysed using the same procedure as described in section 4.1.1. Two conclusions can be made from Figure 4.6. First, the reduction in the thickness ratio reduces the maximum shear strain in the adhesive layer at the overlap terminus. This confirms the contribution of the reduction in the scarf tip thickness to the reduction of the maximum shear strain. Secondly, the plots for the three scarf joints with different adherend thickness are different, in that the 6mm thick scarf joint shows the lowest maximum shear strain while the 2mm thick scarf joint shows the highest maximum shear strain in the adhesive at the overlap terminus, for a given t_{st}/t ratio. This is because for the thicker adherends, the overlap length will be longer for the same thickness ratio, t_{st}/t, and scarf angle, θ. These data shown in Figure 4.6 therefore suggest that the increase in

overlap length, which results due to the increase in the adherend thickness, t, makes a significant contribution to the reduction in the maximum shear strain, γ_{amax}.

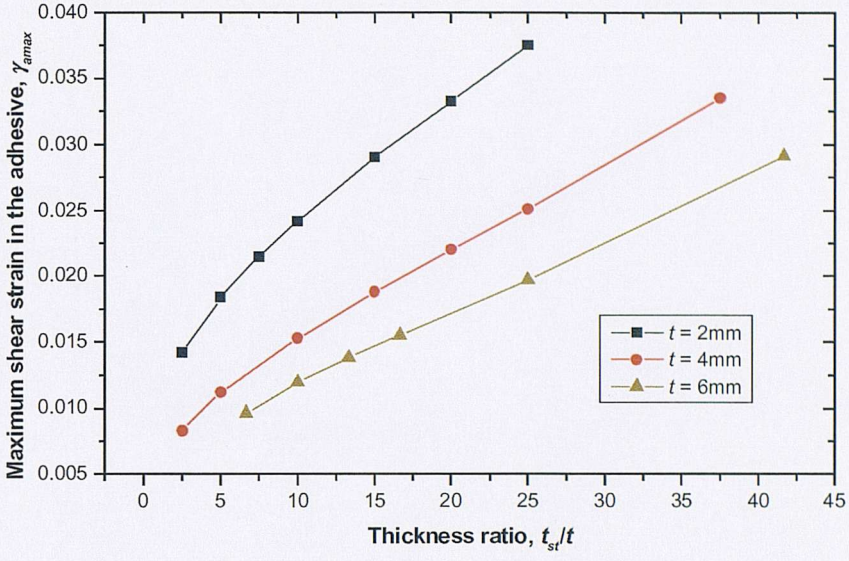


Figure 4.6: Plots of maximum shear strain in the adhesive against the thickness ratio, t_{st}/t for scarf joints with adherend thickness 2mm, 4mm and 6mm

The normalised shear stress distribution in the adhesive layer is shown in Figure 4.7, for a value of adherend thickness, t, of 2mm (as used in the experimental work described in section 4.5.5). The shear stress distribution is obtained by multiplying the shear strain distribution by the shear modulus, which is then normalised by the critical shear stress given in Table 4.1. A sudden increase of the shear stress occurs near the terminus of the overlap. In the middle of the joint, the shear stress is relatively low and is almost constant. In addition, it can be observed that as the overlap length is reduced, the length of the constant stress region in the middle of the joint reduces.

However, the above analytical analysis does not take into account adherend bending effects and the elastic-plastic nature of the adhesive and the adherends. In addition, the analytical solution assumes that there is no stress variation across the thickness of the adhesive layer. In order to investigate the stress distribution at different locations across the thickness of the adhesive, linear elastic finite element analysis will be used. This is discussed in the next section where all three stress components which act in the adhesive (i.e. direct stress, shear stress and peel stress) will be shown in detail. In

addition, the effect of scarf tip thickness on the stress concentration in the adherend will also be discussed.

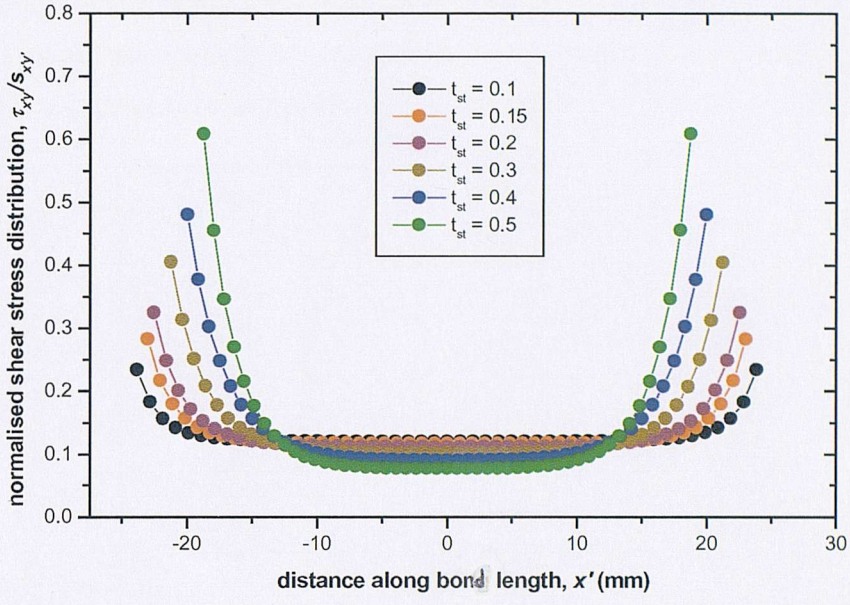


Figure 4.7: Shear stress distribution in the adhesive layer for different scarf tip thickness, t_{st} using the analytical solution

4.5.3 Elastic finite element analysis

As mentioned in the previous paragraph, linear elastic finite element analysis was used to investigate the effect of scarf tip thickness, t_{st}, on the stress distribution in the adhesive and the adherend. The finite element analysis is simpler to use compared to analytical solutions when adherend bending effects may be included into the analysis. Details of the numerical procedure were given in section 4.3. The geometrical parameters of the scarf joint models investigated using the elastic finite element analyses were given in Table 4.3.

Variations of the stress components at the middle of the adhesive ($y' = 0$) with the scarf tip thickness are given in Figures 4.8-4.10. Similarly, Figures 4.11-4.13 show the variations of the stress components near the adhesive/adherend interface ($y' = 0.4t_a$). From these figures, it may be observed that increasing the scarf tip thickness increases the maximum stress components in the adhesive. From Figures 4.8-4.10 for y' = 0, it can be seen that the relative height of the two peaks in the stress concentrations at both ends of the overlap region are the same. It is interesting to note that the peel stress, $\sigma_{y'y'}$,

distribution (see Figure 4.9) shows an abrupt increase at the joint terminus and is zero for most of the overlap length. In addition, there is a sharp change in the direction of the peel stress at the joint terminus. This is because, when the joint is loaded, the sudden change of stiffness before and after the scarf tip causes the joint to bend and hence causes the change in direction of the peel stress near the scarf tip.

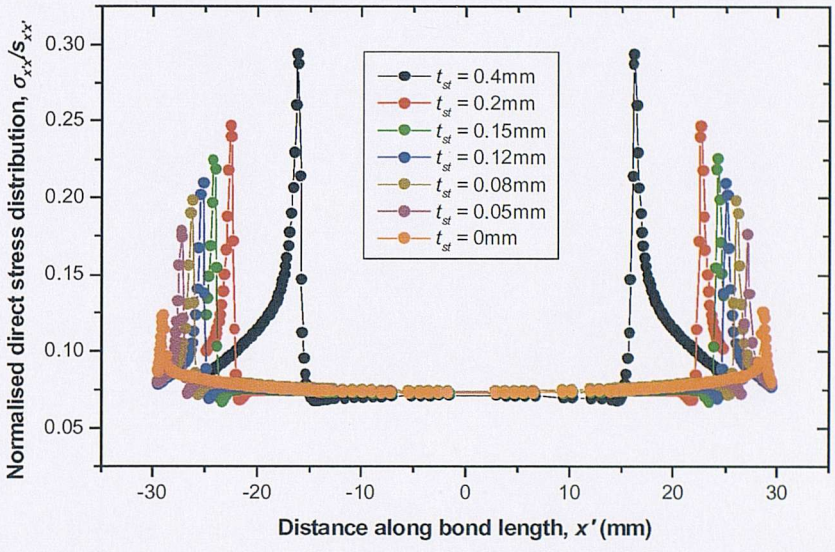


Figure 4.8: Normalised direct stress distribution at the centre of the adhesive layer (y' = 0) plotted against distance along the bond length for different scarf tip thickness, t_{st}

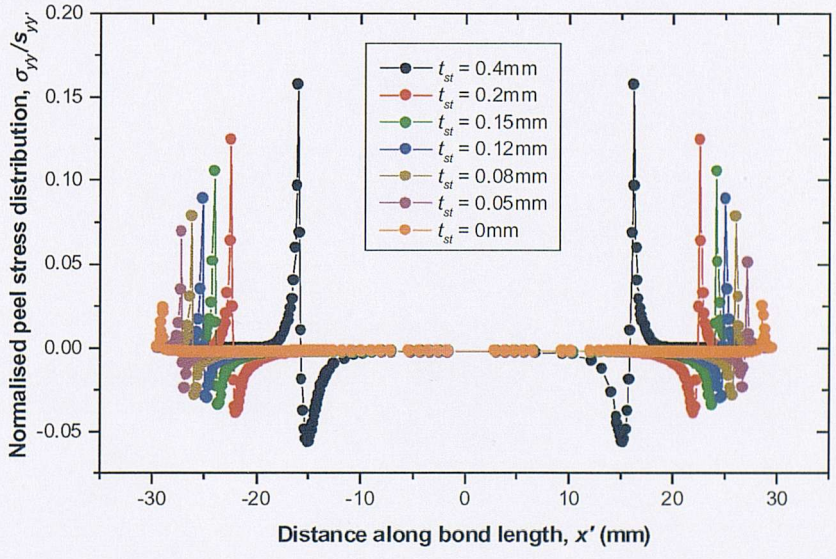


Figure 4.9: Normalised peel stress distribution at the centre of the adhesive layer (y' = 0) plotted against distance along the bond length for different scarf tip thickness, t_{st}

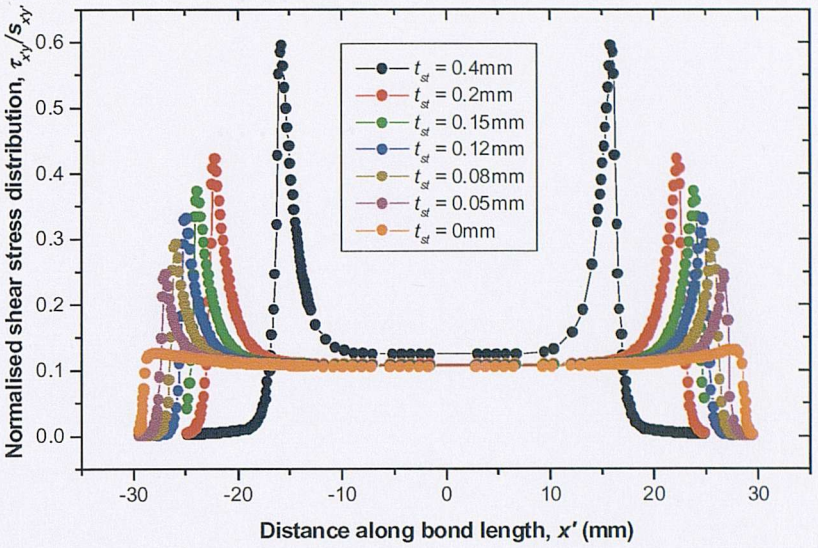


Figure 4.10: Normalised shear stress distribution at the centre of the adhesive layer (y' = 0) plotted against distance along the bond length for different scarf tip thickness, t_{st}

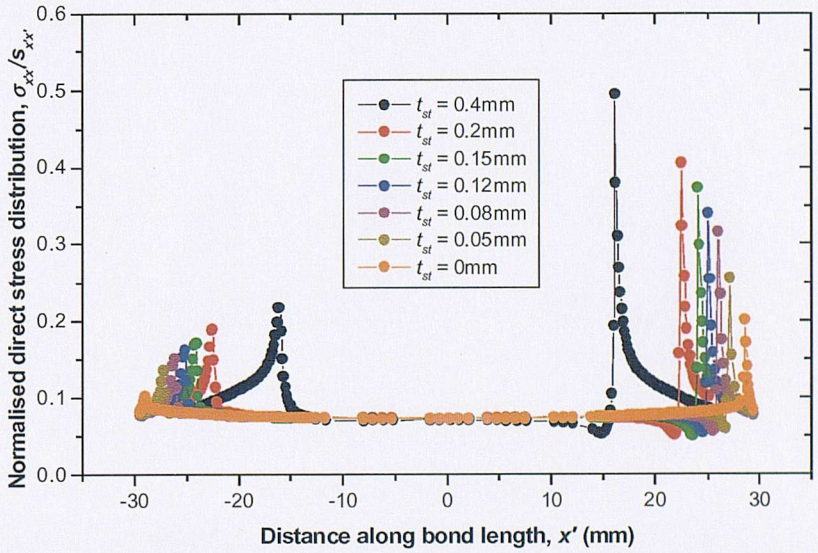


Figure 4.11: Normalised direct stress distribution near the adhesive/adherend interface ($y' = 0.4t_a$) plotted against distance along the bond length for different scarf tip thickness, t_{st}

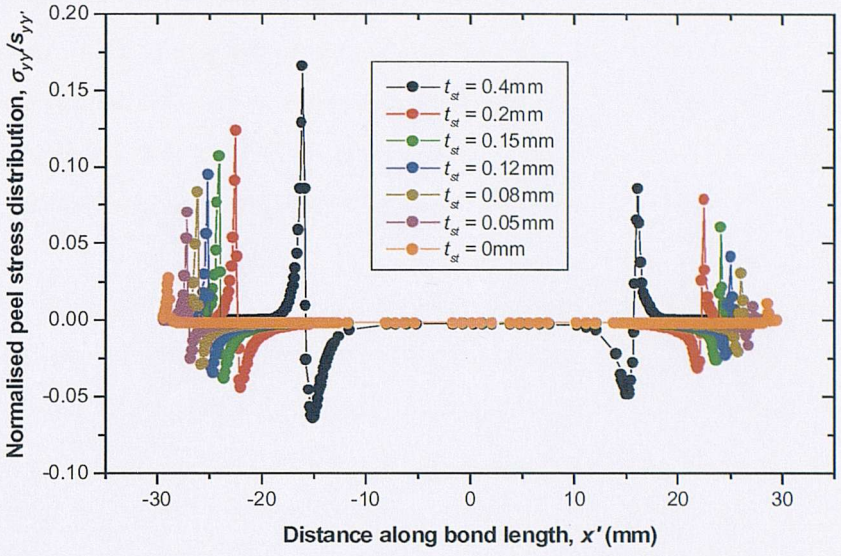


Figure 4.12: Normalised peel stress distribution near the adhesive/adherend interface ($y' = 0.4t_a$) plotted against distance along the bond length for different scarf tip thickness, t_{st}

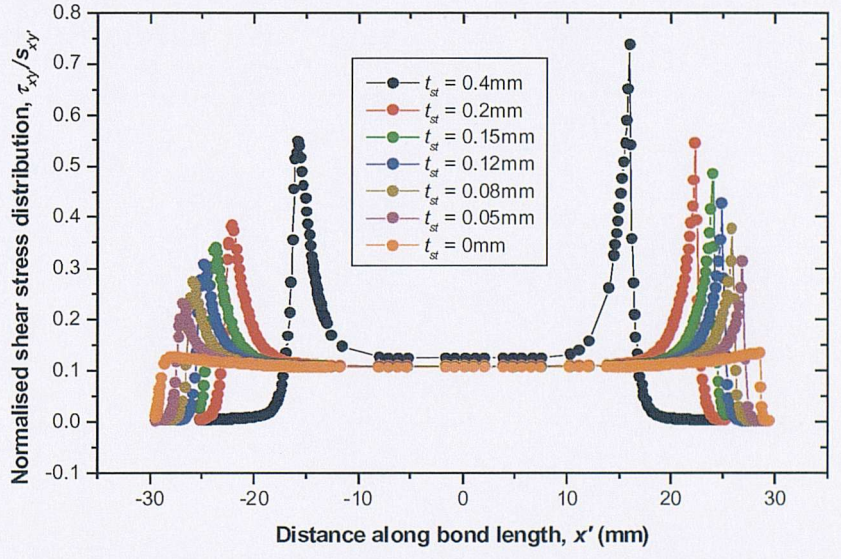


Figure 4.13: Normalised shear stress distribution near the adhesive/adherend interface ($y' = 0.4t_a$) plotted against distance along the bond length for different scarf tip thickness, t_{st}

However, the stress distributions near the adhesive/adherend interface, i.e. y' = $0.4t_a$, are not symmetrical, see Figures 4.11-4.13. From Figure 4.11 and Figure 4.13, it can be seen that the maximum direct and shear stress components occur at the interface adjacent to the scarf tip (i.e. $x' = L_a$). On the other hand, from Figure 4.12, the maximum peel stress component occurs at the interface opposite the scarf tip (i.e. $x' = -L_a$).

Nevertheless, as for the peel stress distribution at the centre of the adhesive layer, $y' = 0$ (see Figure 4.9), the peel stress distribution in the middle of the bond at the adhesive/adherend interface is also zero, see Figure 4.12. Comparing Figures 4.8-4.13, it can be concluded that the shear stress component in the adhesive is the dominant stress component that is acting and is likely to initiate failure in the joint.

It is interesting to see how the scarf tip thickness affects the stresses in the adherend. It was found that a stress concentration occurs in the adherend opposite a scarf tip. Figure 4.14 shows the effect of scarf tip thickness on the direct stress in the adherend opposite a scarf tip. The horizontal axis is the thickness of the adherend and the direct stress is normalised with the critical direct stress given in Table 4.1. It can be seen that high direct stresses are present at the adherend/adhesive interface. In addition, increasing the scarf tip thickness increases the maximum direct stress in the adherend. It is somewhat worrying that this stress concentration is rather high. This indicates that adherend failure is possible in the joint and the ultimate failure locus of the joint will be dependent on the material properties of the adherend, as well those of the adhesive used.

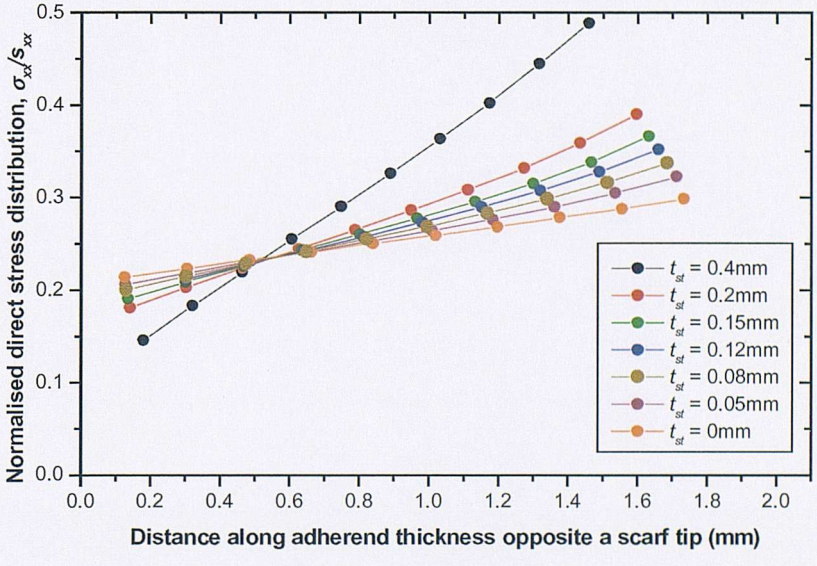


Figure 4.14: Variation of the direct stress distribution across the thickness of the adherend opposite a scarf tip with scarf tip thickness, t_{st}

The analytical and finite element analyses used to investigate the effect of scarf tip thickness on the stress concentration in the scarf joint design has been presented. It can be concluded that, by increasing the scarf tip thickness, the stress concentrations at the overlap terminus increase. However, these analyses cannot be used to predict the static

failure load and failure locus of the joints. Predictions of the static failure load and failure locus are given in the next section where results from the elastic-plastic finite element analysis are given.

4.5.4 Elastic-plastic finite element analysis

For long scarf joints such as those used in the present investigation, it is important to model the adhesive and adherend with their full material properties in order to predict the static failure load and failure locus. This section will discuss the use of an elastic-plastic finite element analysis to predict the failure loads and failure loci of scarf joints with different values of the scarf tip thickness, t_{st}. These analyses were carried out in conjunction with the experimental tests, given in section 4.5.5. Thus, scarf joints with a scarf tip thickness of 0.4mm and 0.15mm will be investigated. The elastic-plastic material properties of the adhesive and the adherend were given in Figure 3.1 and Figure 3.2b respectively.

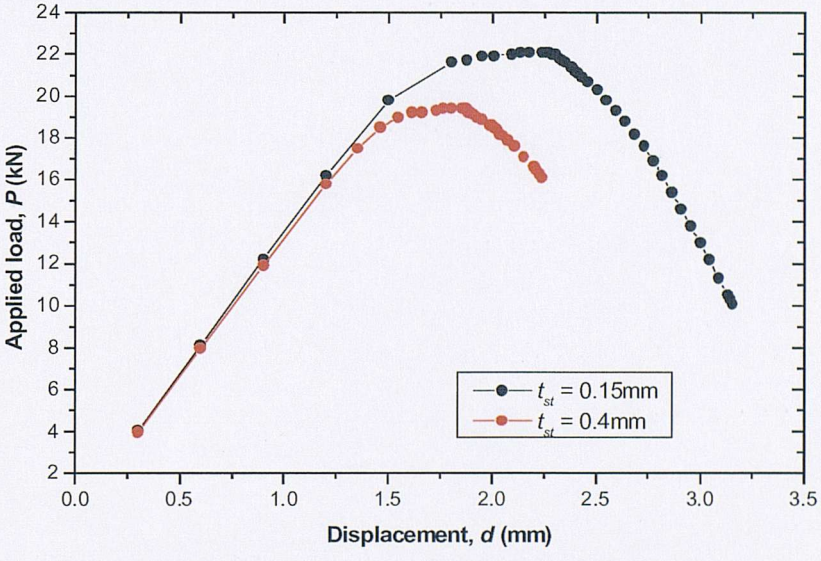


Figure 4.15: Predicted load-displacement curves of scarf joints with scarf tip thickness, t_{st} = 0.15mm and 0.4mm using elastic-plastic finite element analysis

A number of failure criteria were used to predict the static failure load and failure locus of the joints. The Mises equivalent stress was used as the criterion to predict failure in the aluminium alloy adherend. Three other criteria were used to predict failure in the adhesive. These were based upon the attainment of a critical failure value of the shear strain, shear stress and Mises equivalent stress in the adhesive. The critical values of the

failure criteria employed were given in Table 4.2. The predicted load versus displacement curves of these two scarf joint designs are shown in Figure 4.15.

From Figure 4.15, it can be seen that a reduction in scarf tip thickness increases the failure load of the joint. In addition, the scarf joint with the thinner scarf tip thickness yields at a higher load. Neither scarf joint shows however significant plastic yielding. This is because the adherend used in this analysis is the 'L157' alloy (see Table 3.2) which only has an elongation of 9%.

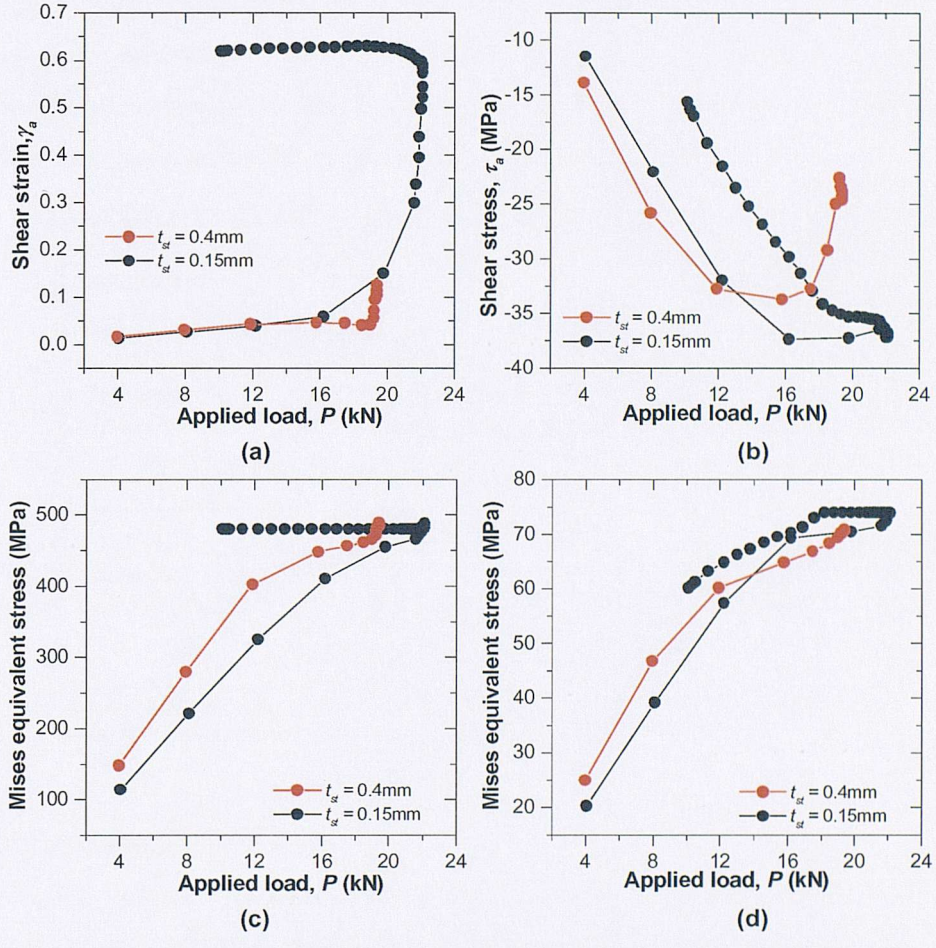


Figure 4.16: Comparison of the maximum (a) shear strain, (b) shear stress, (c) adherend Mises equivalent stress and (d) adhesive Mises equivalent stress in the adhesive layer for scarf joints with scarf tip thickness, t_{st} = 0.4mm and 0.15mm

In order to predict the failure load and the failure locus of the two scarf joint designs, the fracture criteria used in this investigation are plotted against the applied load in Figure 4.16. It can be seen that the scarf joint design with the thinner scarf tip thickness (i.e. t_{st} = 0.15mm) attains the values of the various fracture criteria at a higher applied

load when compared with the thicker scarf tip model. It appears that the Mises equivalent stress in the adherend is the dominating failure criterion for both of the joint designs. However, for the scarf joint design with t_{st} = 0.15mm, the adhesive fracture shear stress and adhesive Mises equivalent stress criteria appear to give very similar predictions of the failure load compared to the adherend Mises equivalent stress criterion. This indicates that joint failure might initiate from the adhesive. However, due to the high stress concentration in the adherend, and that the fact that the adhesive is much more ductile than the adherend, adherend failure could still be the final failure mode for this joint design. For the scarf joint design with a scarf tip thickness of t_{st} = 0.4mm, the adherend Mises equivalent stress was the first to reach its critical failure criterion, indicating that adherend failure would be the dominating failure mode. A summary of the predicted failure loads based on the four failure criteria is given in Table 4.5.

Table 4.5: Summary of the predicted failure load of scarf joints with scarf tip thickness, t_{st} = 0.4mm and 0.15mm using elastic-plastic finite element analysis

Joint design	Failure criterion	Predicted failure load, *P* (kN)
Scarf joint t_{st} = 0.15mm	Adherend ultimate tensile strength	22.13
	Adhesive fracture shear strain	21.41*
	Adhesive fracture shear stress	22.10
	Adhesive ultimate tensile strength	22.10
Scarf joint t_{st} = 0.4mm	Adherend ultimate tensile strength	19.42
	Adhesive fracture shear strain	-
	Adhesive fracture shear stress	17.62*
	Adhesive ultimate tensile strength	-

* Predicted failure load occurred at negative slope of the load-deflection curve
\- Analysis termined before failure criterion was reached

4.5.5 Experimental results

In order to verify the predictions given above, the two scarf joint designs with scarf tip thicknesses, t_{st}, of 0.4mm and 0.15mm were tested using the monotonically-loaded test procedure, see section 3.5.2. At least four specimens were tested for each joint design. Results from the experimental tests are shown in Figure 4.17. It can be seen from Figure 4.17 that the increase in scarf tip thickness has resulted in a decrease of approximately 18% in the applied load for failure.

The majority of the joints tested failed in the adherend. Although some of the specimens failed in the adhesive, the failure load for these joints was very similar to the specimens that failed in the adherend. The crack path is schematically shown in Figure 4.18. A crack initiates from the scarf tip face and propagates, through the adhesive, to the opposite interface. The crack then changes direction and continues to propagate along this opposite interface. At this point, the applied load is being sustained by adherend 2, see Figure 4.18. This results in an increase of the stress concentration on the adherend near the interface with the adhesive. With further crack propagation, the cross section area of adherend 2 effectively decreases, hence lowering the ultimate load carrying capability of the adherend. This causes another change of crack propagation direction and the crack grows across the thickness of the joint and breaks through the adherend. This typically occurs at about 2mm into the effective bond length from the scarf tip.

From this analysis, it can be concluded that the scarf tip affects the joint performance in two ways. Firstly, the thicker the scarf tip, the higher the stress concentration at the overlap terminus, resulting with a reduced load carrying capability for the joint. Secondly, as the scarf tip thickness was increased, the thickness of the adherend opposite the scarf tip reduces. Hence, the ultimate load carrying capability of the thinner adherend opposite the scarf tip results in a lower failure joint strength. Both these points explain the reduction in joint strength of the different scarf joint models investigated here.

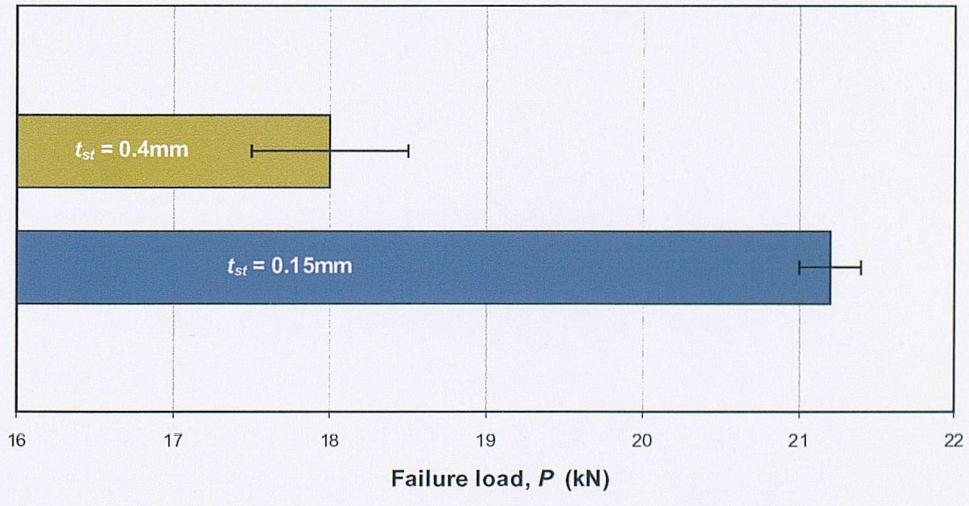


Figure 4.17: Results from the experimental monotonically-loaded tension tests of scarf joints with a scarf tip thickness of t_{st} = 0.4mm and 0.15mm

The experimental failure loads of the two scarf joint designs compared well with the predicted failure loads (see section 4.5.4). Table 4.6 summarizes the comparisons between the experimental and predicted failure loads. In addition, the failure loci of both scarf joint designs were predicted using the elastic-plastic finite element analysis. Thus, whilst the elastic finite element analysis was able to provide an indication of the relative joint strength of the scarf joints, accurate predictions of the failure load and failure locus required more accurate modelling of the material properties of the adhesive and the adherend.

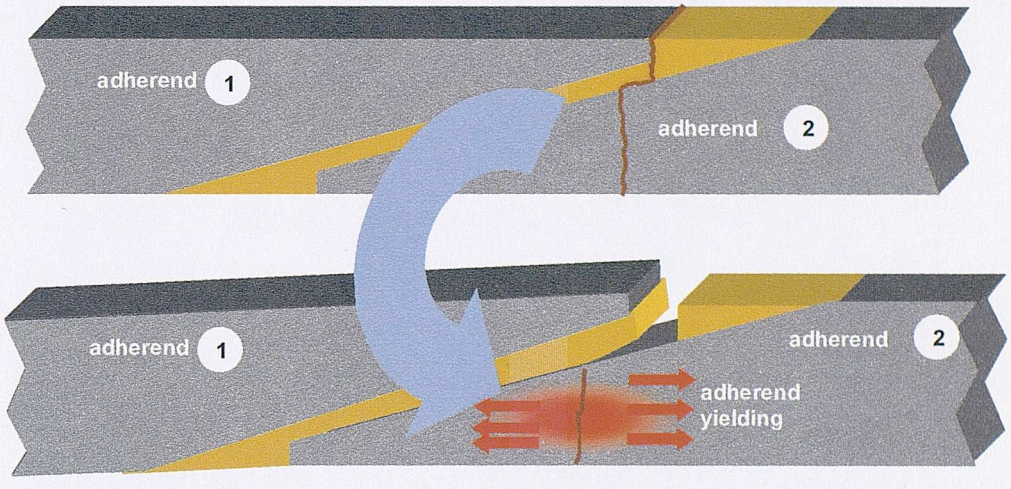


Figure 4.18: Schematic diagram showing adherend failure in scarf joint specimens. Adherend yielding was observed before final fracture of the specimens

Table 4.6: Comparison between the experimental and predicted failure load and failure locus of scarf joints with scarf tip thickness, t_{st} = 0.15mm and 0.4mm

Scarf joint design	Experimental failure locus	Predicted failure locus	Experimental failure load, P (kN)	Predicted failure load, P (kN)	Percentage error, %
t_{st} = 0.15mm	adherend	adherend	21.2 ± 0.2	22.13*	4.4
t_{st} = 0.4mm	adherend	adherend	18.0 ± 0.46	19.42*	7.9

* prediction based on adherend Mises equivalent stress criterion

This investigation has established that reducing the scarf tip thickness will result in an increase in the joint efficiency. Although the ideal scarf joint would be one that has an infinitely-small scarf tip thickness, it is however impractical to produce such a design. However, a scarf joint design with a scarf tip thickness of, t_{st} = 0.15mm can be produced using the vacuum-suction holding-device (see section 3.4).

4.6 Effects of scarf angle

4.6.1 Introduction

A number of researchers have investigated the effects of varying the scarf angle on adhesively-bonded scarf joints (see section 2.5.4). The underlying conclusion was that small scarf angles are preferred because this will allow the joint to be primarily loaded in shear. Increasing the scarf angle will shorten the bond length (see equation 4.1) and could result in higher stresses in the joint. In the present section, results from a parametric study, using analytical, finite element and experimental procedures, of the effects of varying the scarf angle on the stress distributions in the adhesive and the adherend are presented.

In order to reduce the data scale of the present study, it was decided to keep constant a number of geometrical design parameters. A scarf tip thickness of 0.15mm was used, since this gives rise to relatively low stress concentrations and can be machined in practice. The adherend thickness and adhesive thickness were also assumed to be constant, i.e. 2mm and 0.2mm respectively. For the linear elastic analyses (both analytical and finite element), scarf joints with scarf angles between $1° < \theta < 10°$ will be investigated. A summary of the geometrical parameters of these joint models is given in Table 4.7.

Three designs of scarf joint models were selected for experimental testing. The three scarf joint designs had scarf angles of 1.5°, 1.8° and 5°. Referring to equation 4.1, the scarf tip thickness was kept constant at 0.15mm and, therefore, the bond length changed directly according to the change in the scarf angle. Analytical and finite element models, using elastic material properties, will be discussed in the following two sections, with a finite element approach using elastic-plastic properties of the adhesive and adherends being employed in section 4.6.4.

Table 4.7: Geometrical parameters of scarf joint models, with 2mm thick adherends, used to investigate the effects of scarf angle, θ

Scarf angle, θ (°)	Bond length, $2L_a$ (mm)	Scarf tip thickness, t_{st} (mm)	Adherend thickness, t (mm)	Adhesive thickness, t_a (mm)
10*	8.64	0.15	2	0.2
9*	9.59	0.15	2	0.2
8*	10.9	0.15	2	0.2
7*	12.3	0.15	2	0.2
6*	14.4	0.15	2	0.2
5*^	17.2	0.15	2	0.2
4*^	21.5	0.15	2	0.2
3*^	28.7	0.15	2	0.2
1.8^	47.8	0.15	2	0.2
1.5^	57.3	0.15	2	0.2
1^	85.9	0.15	2	0.2

* investigated using analytical solution
^ investigated using linear elastic FE

4.6.2 Analytical analysis

Analytical analyses were used to investigate the effect of the scarf angle on the shear stress distribution in the adhesive layer. The governing equation for the shear strain was given in equation (4.2). The results from the iteration process used to determine the maximum shear strain at the overlap terminus is given in Table 4.8. It can be seen from Table 4.8 that the percentage error of the input and calculated γ_a' is insignificant. The results show that by increasing the scarf angle, the maximum shear strain in the adhesive layer increases.

The predicted shear stress distributions in the adhesive layer are shown in Figure 4.19. It can be seen that by increasing the scarf angle, the shear stress distribution in the adhesive layer is shifted upwards. In addition, the curves become shorter as the scarf angle is increased. This is because, by increasing the scarf angle and keeping the other geometrical parameters constant, the overlap length reduces according to equation 4.1. Another observation is that the slopes at the overlap terminus for the different scarf angles are very similar. This is confirmed in Table 4.8. The significance of this observation is that the distance by which the shear stress increases from the minimum value (the flat region in the middle of the joint) to the maximum value at the overlap terminus is

independent of the scarf angle. This is in contrast to the previously discussed investigation of the effect of scarf tip thickness, whereby the first derivatives of the shear stress reduce with reduction of the scarf tip thickness (see Figure 4.7).

Table 4.8: Results from the iteration procedure used to calculate the maximum shear strain in the adhesive layer at the overlap terminus for different scarf angles, θ

Scarf angle, θ (°)	Number of iterations, n	Calculated from equation (4.5) $\gamma'_a(-L_a)$	Calculated from Runge-Kutta iterations $\gamma'_a(L_a)$	Percentage error* (%)	Calculated maximum shear strain, $\gamma_a(-L_a)$
10	30	-8.99	8.99	0.00	0.05
9	30	-9.02	9.02	0.00	0.04
8	30	-9.05	9.05	0.00	0.04
7	30	-9.07	9.07	0.01	0.04
6	30	-9.09	9.09	0.01	0.03
5	30	-9.11	9.11	0.01	0.03
4	30	-9.12	9.12	0.02	0.03
3	30	-9.14	9.13	0.01	0.03

*Note: Percentage error = $[(\gamma'_a(-L_a) - \gamma'_a(L_a))/\gamma'_a(-L_a)]\%$
Values are correct to 2 decimal places.

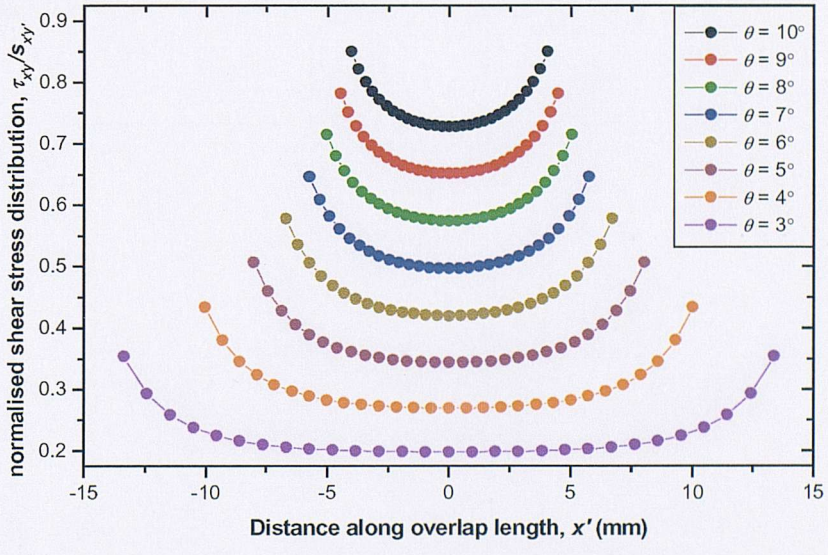


Figure 4.19: Shear stress distribution in the adhesive layer for different scarf angle, θ predicted using the analytical solution

4.6.3 Elastic finite element analysis

Elastic finite element analyses were also used to investigate the effect of the scarf angle on the stress components in the adhesive, as well as in the adherend. In addition, the effect of adherend bending was also included in the analyses. Figures 4.20-4.22 show the normalised stress components at the mid-plane of the adhesive ($y' = 0$). From these figures, it can be seen that by increasing the scarf angle the peak stresses in the adhesive increases. In addition, all three stress components (i.e. the direct, peel and shear stresses) increase with an increase in the scarf angle. As a result, the average stresses in the adhesive layer increase with an increase in the scarf angle.

Figure 4.21 shows that the peel stress distribution in the adhesive has two peaks, of opposite signs, at the overlap terminus. The opposite signs of the peak peel stresses at the overlap terminus indicate that high shear stresses will be present. It is interesting to note that for scarf angles of $\theta \geq 3°$ the minimum peel stress at the middle of the joint has a non-zero value. On the other hand, for $\theta \leq 3°$, the minimum peak stress at the middle of the joint is zero. This is in contrast to the previous investigation (see section 4.5.3) of the effects of the scarf tip thickness where, for all the scarf tip thickness investigated, the peel stress distribution in the middle of the joint is at a zero value. This can be explained by the increasingly shortened overlap length as the scarf angle, θ, is increased.

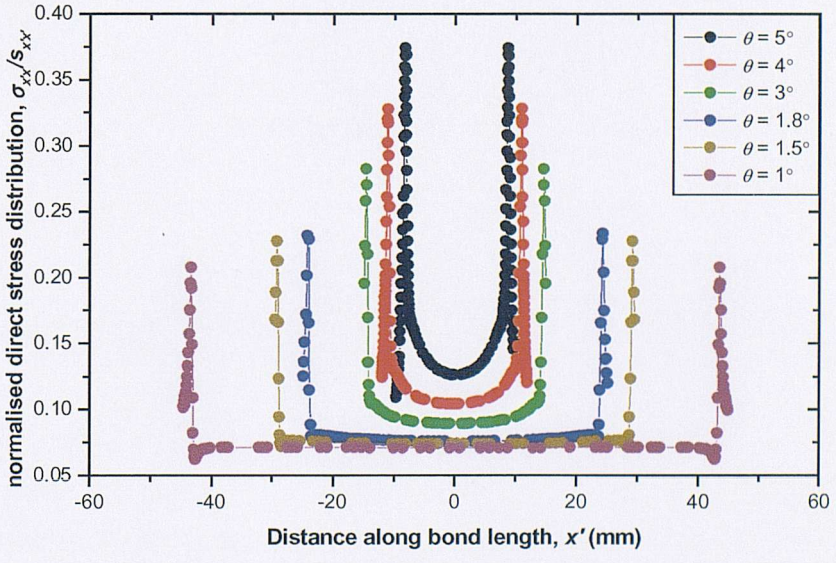


Figure 4.20: Normalised direct stress distribution in the middle of the adhesive layer ($y' = 0$) plotted against the distance along the bond length for different scarf angles, θ

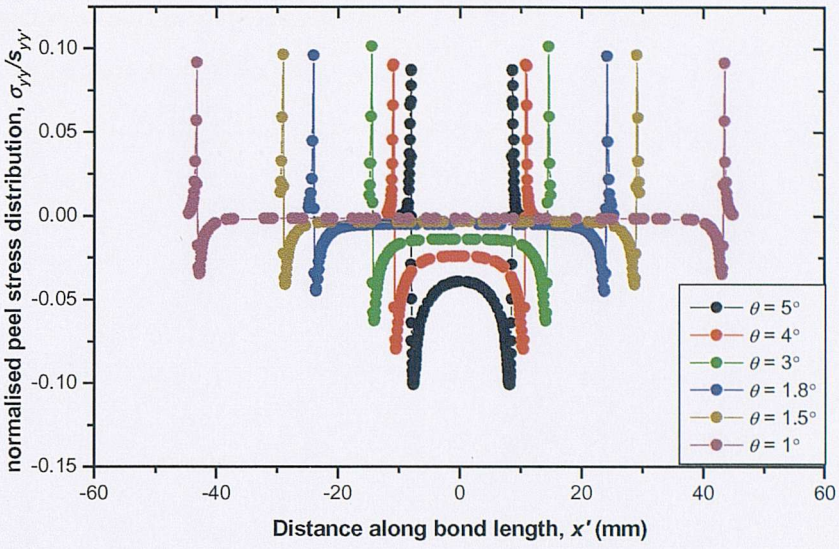


Figure 4.21: Normalised peel stress distribution in the middle of the adhesive layer (y' = 0) plotted against the distance along the bond length for different scarf angles, θ

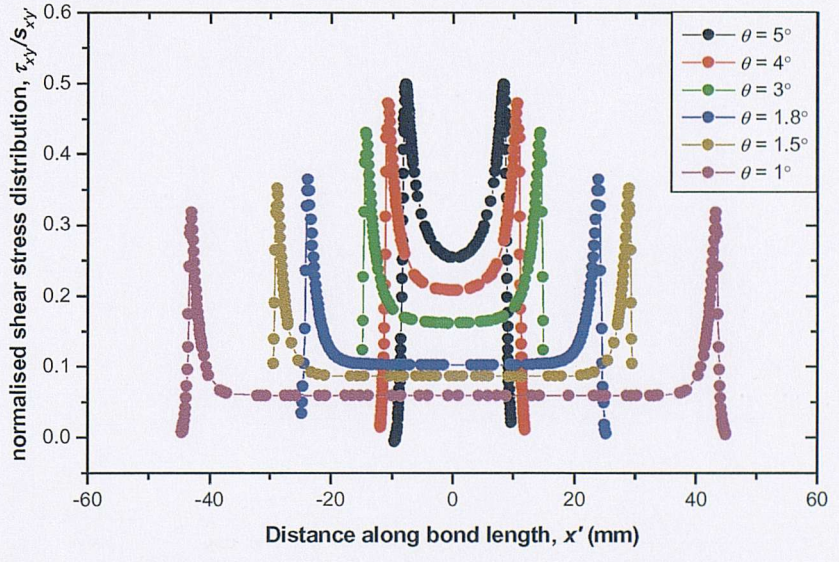


Figure 4.22: Normalised shear stress distribution in the middle of the adhesive layer ($y' = 0t_a$) plotted against the distance along the bond length for different scarf angles, θ

Figures 4.23-4.25 show the normalised stress components in the adhesive near the adhesive/adherend interface ($y' = 0.4t_a$). Similar to the observations noted above (see section 4.5.3) on the effects of the scarf tip thickness, the direct and shear stress distribution in the adhesive show a higher peak at the interface adjacent to the scarf tip (i.e. $x' = L_a$), see Figure 4.23 and 4.25. This is due to the relatively high stress

concentration at the scarf tip face. On the other hand, the highest peel stress occur at the interface opposite a scarf tip (i.e. $x' = -L_a$).

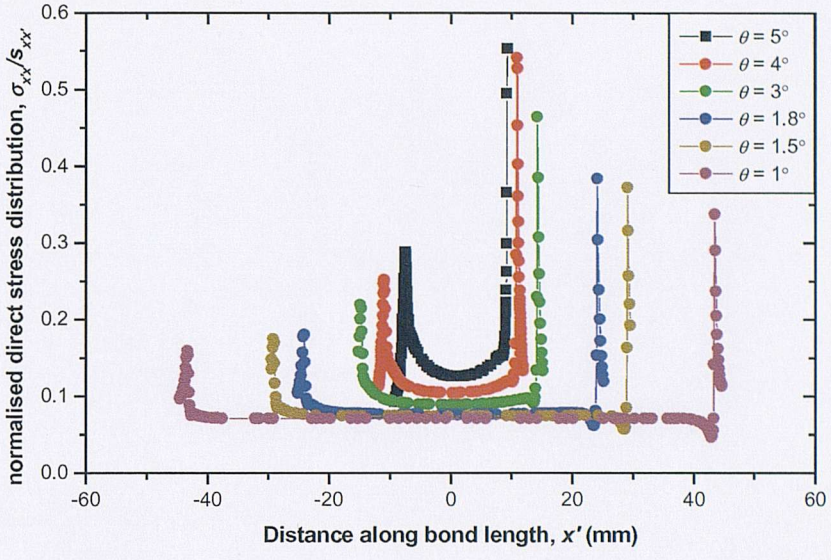


Figure 4.23: Normalised direct stress distribution near the adhesive/adherend interface ($y' = 0.4t_a$) plotted against the distance along the bond length for different scarf angles, θ

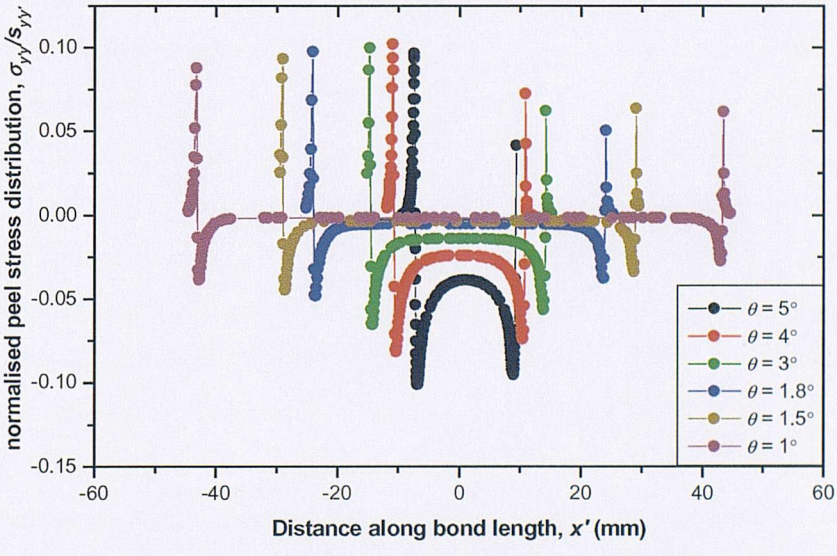


Figure 4.24: Normalised peel stress distribution near the adhesive/adherend interface ($y' = 0.4t_a$) plotted against the distance along the bond length for different scarf angles, θ

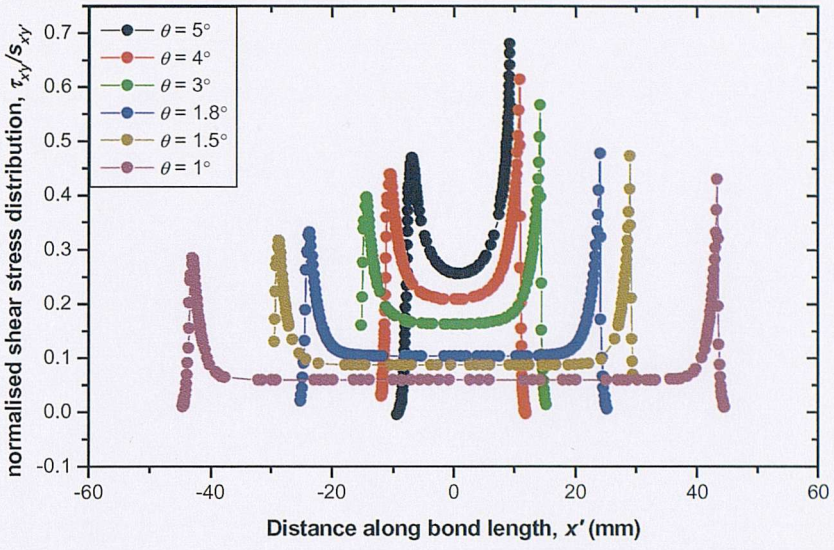


Figure 4.25: Normalised shear stress distribution near the adhesive/adherend interface ($y' = 0.4t_a$) plotted against the distance along the bond length for different scarf angles, θ

The maximum direct stress in the adherend is compared with the maximum stress components in the adhesive in Figure 4.26. It appears that increasing the scarf angle does not significantly affect the stress concentration in the adherend. For small scarf angles below 2°, the normalized stresses appear to reach a threshold value. This indicates that a further reduction of the scarf angle will not give a significant improvement in the joint efficiency. However, for scarf angles higher than 2°, it appears that the maximum shear stress in the adhesive increases more rapidly than the direct stress in the adherend. This indicates that adhesive failure will be more dominant for higher scarf angle models. It may also be noted that, based on this investigation, adhesive failure will be the predicted failure locus for all the scarf angles investigated. However, this is clearly not the case, as was shown above (see Table 4.6), where for a scarf angle of 1.8° adherend failure was observed in the experiments. Indeed, it was observed experimentally that the scarf joints with a scarf angle of 1.8° failed in the adherend, but that the crack initiated from the scarf tip face and propagated approximately 2mm along the adhesive/adherend interface before breaking through the adherend (see Figure 4.18). This observation of the failure behaviour of the scarf joint specimens with a scarf angle of 1.8° explains the higher shear stress concentration in the adhesive compared to the direct stress concentration in the adherend, as predicted in the present analysis. This observation clearly indicates the inadequacy of the stress concentration approach for predicting failure in adhesively-

bonded joints. However, undeniably this method was able to rank joint designs based on variations in the geometrical parameters. Furthermore, the ease of approach of this method allows an initial, sound design for the joint to be readily formulated.

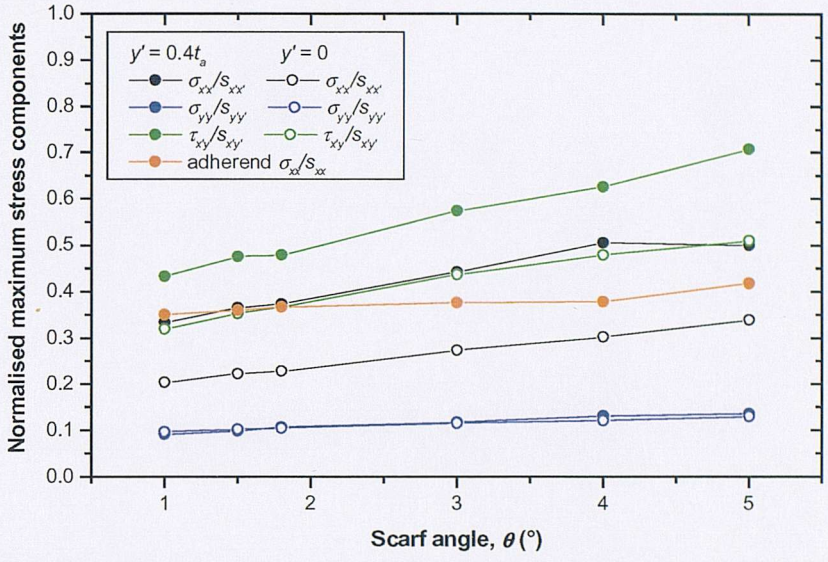


Figure 4.26: Comparison of the maximum stress components in the adhesive and the adherend for different scarf angles, θ

4.6.4 Elastic-plastic finite element analysis

Elastic-plastic analyses were carried out for scarf joints with scarf angles of 5°, 1.8° and 1.5°. These scarf joint designs were also tested using the monotonically-loaded tests of the scarf joints, see section 4.6.5.

Figure 4.27 shows the load-displacement curves of the three scarf joint designs predicted using the elastic-plastic finite element method. The figure shows that there is only a small difference between the predicted joint strengths of the scarf joint designs with scarf angles 1.5° and 1.8°. However, a significantly lower failure load was observed for the scarf joint design with a scarf angle of 5°. These results are consistent with the observations discussed in the previous section (see section 4.6.3), where the shear stress concentrations in the adhesive increase significantly when the scarf angle is higher than about 3°. As for the elastic-plastic analysis used in section 4.5.4, four failure criteria were used to predict the failure load and failure locus of these joint designs. The failure criteria were given in Table 4.2.

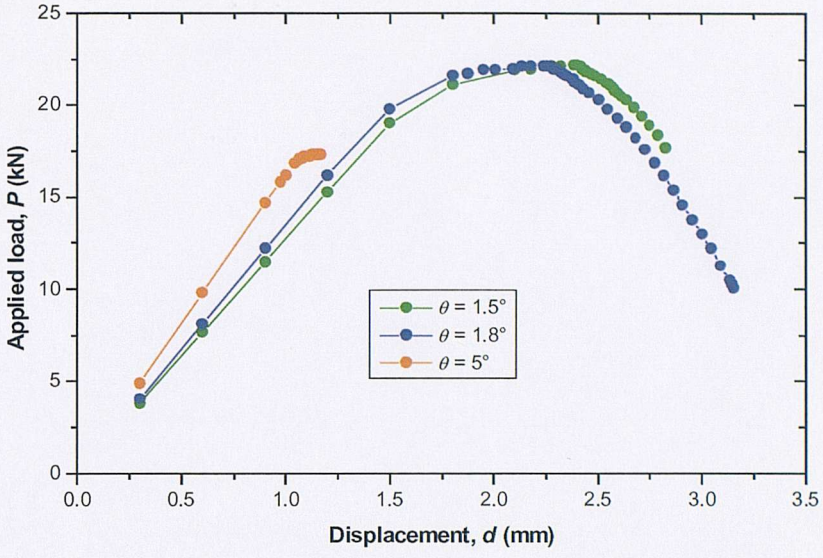


Figure 4.27: Predicted load-displacement curves of scarf joints with scarf angles, θ = 1.5°, 1.8° and 5° using elastic-plastic finite element analysis

The predicted maximum shear stress, shear strain, adhesive and adherend Mises equivalent stress are plotted in Figure 4.28 against the applied load, *P*. Comparing the three scarf joint designs, it can be seen from Figure 4.28 that the scarf joint design with a scarf angle of 1.5° would fail in the adherend since the adherend ultimate tensile strength is the first failure criterion to be reached (see also Table 4.9). On the other hand, both the shear stress and adhesive Mises stress criteria for the scarf joint design with a scarf angle of 1.8°, predicted a similar failure load to that of the adherend ultimate tensile strength criteria. However, the shear strain criterion was only reached after the joint has passed its maximum load carrying capability, see Table 4.9. This implies that the scarf joint design with a scarf angle of 1.8° would most likely fail in the adherend. It is observed that lowering the scarf angle (from 1.8° to 1.5°) reduces the stress concentrations in the joint. However, the effect is small and it can be seen that these two scarf joint designs showed similar joint strength (see Figure 4.27).

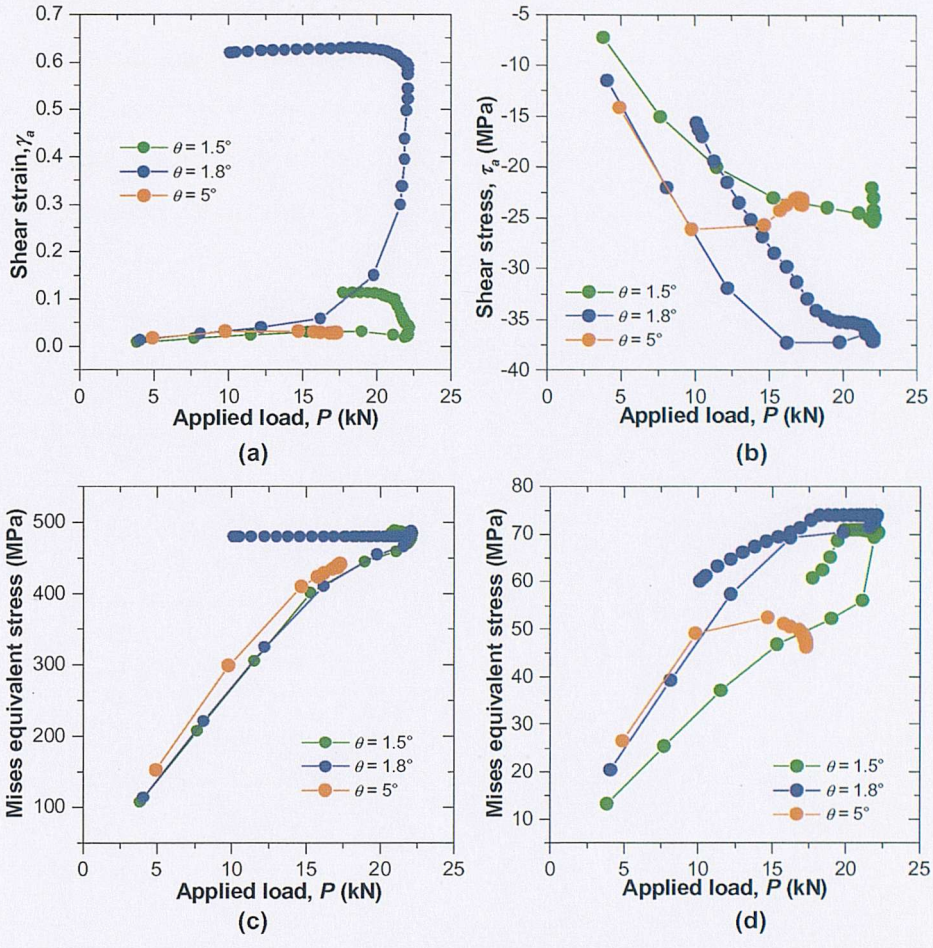


Figure 4.28: Comparison of the maximum (a) shear strain, (b) shear stress, (c) adherend Mises equivalent stress and (d) adhesive Mises equivalent stress in the adhesive layer for scarf joints with scarf angles, θ = 1.5°, 1.8° and 5°

On the other hand, failure in the adhesive appears to be likely to occur for the scarf joint model with a scarf angle of 5°. It is observed that the adhesive yielded at a much lower value than the failure criteria, Figure 4.28b. Similarly, the maximum Mises equivalent stress in the adhesive for this scarf joint model also experiences premature yielding, see Figure 4.28d. Conversely, the maximum shear strain in the adhesive remains at a relatively low value and does not show any sign of reaching its critical value, see Figure 4.28a. This suggests that the critical shear stress criteria would give a conservative prediction of the failure load for this scarf joint model. In support of this statement, it can be seen from Figure 4.27 and Figure 4.28d that the load carrying capability of this scarf joint model continues to increase after the maximum shear stress in the adhesive has begun to decrease. Hence, from Figures 4.27 and 4.28d, it can be seen that the adhesive Mises equivalent stress criterion would give a better prediction of the failure load of this

scarf joint model. Comparing the maximum stresses and strains in the adhesive with that of the adherend, see Figure 4.28, it can be clearly seen that the adherend Mises equivalent stress never reaches the ultimate tensile strength of the adherend. Table 4.9 summarises the predicted failure loads of the three scarf joint designs investigated using the elastic-plastic finite element analysis.

Table 4.9: Summary of the predicted failure load of scarf joints with scarf angles, θ = 1.5°, 1.8° and 5° using elastic-plastic finite element analysis

Joint design	Failure criterion	Predicted failure load, P (kN)
Scarf joint θ = 1.5°	Adherend ultimate tensile strength	22.18
	Adhesive fracture shear strain	17.74 *
	Adhesive fracture shear stress	17.74 *
	Adhesive ultimate tensile strength	20.28*
Scarf joint θ = 1.8°	Adherend ultimate tensile strength	22.13
	Adhesive fracture shear strain	21.41*
	Adhesive fracture shear stress	22.10
	Adhesive ultimate tensile strength	22.10
Scarf joint θ = 5°	Adherend ultimate tensile strength	-
	Adhesive fracture shear strain	-
	Adhesive fracture shear stress	9.82#
	Adhesive ultimate tensile strength	14.66

* Predicted failure load occurred at negative slope of the load-deflection curve
\- Analysis termined before failure criterion was reached
Conservative prediction – explanation given in Section 4.6.4

4.6.5 Experimental results

The three scarf joint designs investigated in the elastic-plastic finite element analysis were also tested experimentally. Results from the monotonically-loaded tests carried out on scarf joints with scarf angles 5°, 2° and 1.5° are shown in Figure 4.29. The results show that increasing the scarf angle reduces the static failure strength of the joints. In addition, failure locus of the scarf joints changes from adherend failure to adhesive failure with increase of the scarf angle. Adhesive failure was observed for the scarf joint design with a scarf angle, θ = 5°. The crack path is schematically shown in Figure 4.30. Scarf joints with scarf angles 1.5° and 2° failed in the adherend, and the crack path was shown in Figure 4.18.

Comparison between the predicted failure loads using elastic-plastic finite element analysis and the experimental results is shown in Table 4.10. The table shows that the predictions compare well with the experimental results. In addition, the failure loci of the joints are accurately predicted.

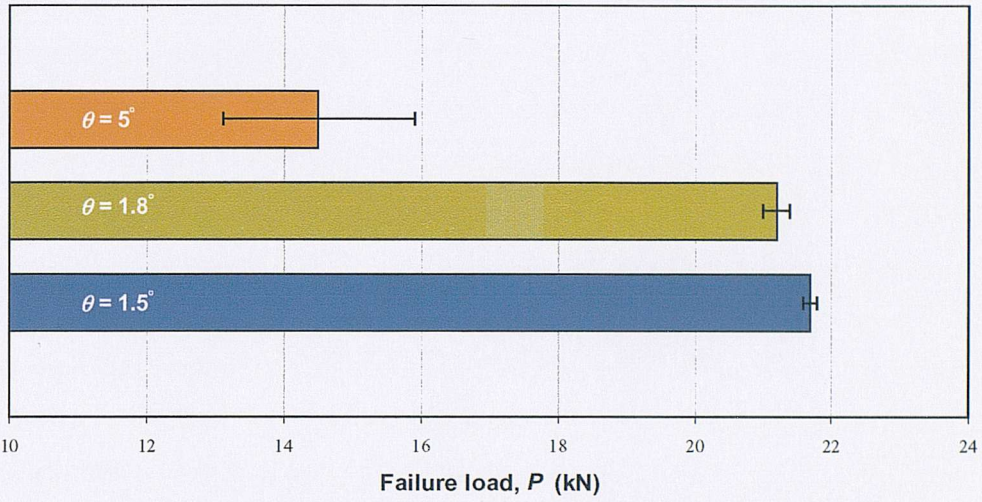


Figure 4.29: Results from the experimental monotonically-loaded tension tests of scarf joints with scarf angles, $\theta = 1.5°$, 1.8° and 5°



Figure 4.30: Schematic diagram showing adhesive failure in scarf joint specimens

Table 4.10: Comparison between the experimental and predicted failure load and failure locus of scarf joints with scarf angles, $\theta = 1.5°$, 1.8° and 5°

Scarf joint design	Experimental failure locus	Predicted failure locus	Experimental failure load, P (kN)	Predicted failure load, P (kN)	Percentage error, %
$\theta = 1.5°$	adherend	adherend	21.7 ± 0.08	22.18*	2.2
$\theta = 1.8°$	adherend	adherend	21.2 ± 0.2	22.13*	4.4
$\theta = 5°$	adhesive	adhesive	14.5 ± 1.4	14.66^	1

* prediction based on adherend Mises equivalent stress criterion
^ prediction based on adhesive Mises equivalent stress criterion

4.7 Effect of fillet size

4.7.1 Introduction

It has been shown in section 4.5 that the increase of the scarf tip thickness reduces the strength of adhesively-bonded scarf joints. The presence of a scarf tip also leaves a gap between the two adherends at the overlap terminus, see Figure 4.31. The size of this gap between the two adherends can be significant when the scarf angle is small (see equation 4.1). For a scarf angle of 1.8°, the length of the gap is approximately 11mm. Naturally, this gap is of a triangular shape and could be filled with adhesive. In this section, the effect of the fillet size and the entry angle, θ_f, on the maximum stress components in the adhesive fillet is reported. Two-dimensional finite element analysis is used in this investigation. The adhesive and the adherend were modelled using elastic material properties. The material properties of the adhesive and the adherend were given in Table 3.1 and 3.2. The scarf joint design used in this investigation has a scarf angle of 1.8°, scarf tip thickness of 0.15mm and the thickness of the adhesive and the adherend used were 0.2mm and 2mm, respectively.

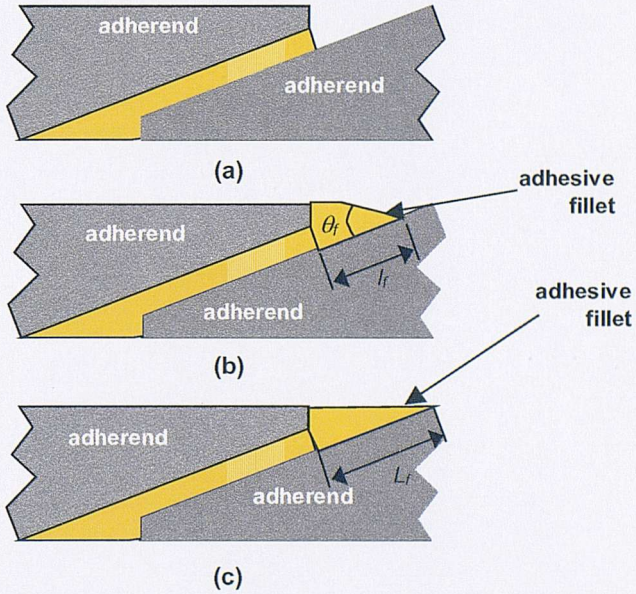


Figure 4.31: Schematic diagram showing the adhesive fillet outside the effective bond length in a scarf joint. (a) no fillet (b) fillet with entry angle, θ_f and (c) full adhesive fillet

The aim of this investigation is to compare the percentage reduction of the maximum stress components in the adhesive fillet that occur by changing the fillet size

and entry angle. The percentage reduction of the maximum stress components in the adhesive fillet was obtained using equation 4.6:

$$\%\sigma_{ij}^{r} = \frac{\sigma_{ij}^{\max} - \sigma_{ij}^{b\max}}{\sigma_{ij}^{b\max}} \quad \text{.....(4.6)}$$

where σ_{ij}^{max} is the maximum stress component and the superscript b denotes the base model (no adhesive fillet, Figure 4.31a). The subscripts i and j correspond to the x' and y' axes defined in Figure 4.5.

4.7.2 The effect of adhesive fillet size

This investigation was carried out by increasing the adhesive fillet size from the base model with no adhesive fillet up to the scarf joint model with a full adhesive fillet (see Figure 4.31). The fillet angle, θ_f was kept constant at 60°. Figure 4.32 compares the percentage reduction of the maximum stress components in the adhesive for different fillet sizes. Also included in the figure is the maximum direct stress in the adherend. The horizontal axis in Figure 4.32 shows the length of the adhesive fillet, l_f (x' direction) normalized with the maximum fillet length, L_f (i.e. the full adhesive fillet – see Figure 4.31c).

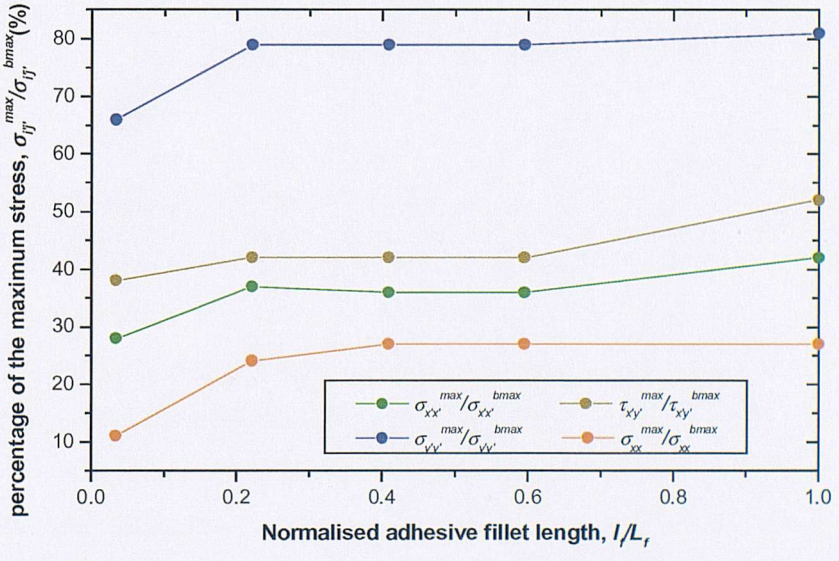


Figure 4.32: Percentage reduction of the maximum stress components in the adhesive and adherend for different fillet sizes

From Figure 4.32, it can be seen that the percentage reduction of the maximum stresses in the adhesive and the adherend increases with the increase of the fillet size. It

was also observed that the most affected stress component was the peel stress in the adhesive. This is consistent with Lang and Mallick's work [29] on the overlap joint design where they also observed that the peel stress in the adhesive fillet is most sensitive to the adhesive fillet size. From Figure 4.32, it was also observed that for a normalized fillet length, $l_f/L_f > 0.2$, no significant changes of the stress components were observed.

4.7.3 The effect of adhesive fillet entry angle, θ_f

The adhesive fillet entry angle is the angle the adhesive makes with the adherend at the free edge of the adhesive fillet (see Figure 4.31b). Fillet angles between $10° < \theta_f < 60°$ were investigated. The results were compared with the base scarf joint model where there is no adhesive fillet (see Figure 4.31a). It was found that the location of the stress concentration in the adhesive fillet changes with the adhesive fillet entry angle. Most notably is the peel stress distribution and this is shown in Figure 4.33.

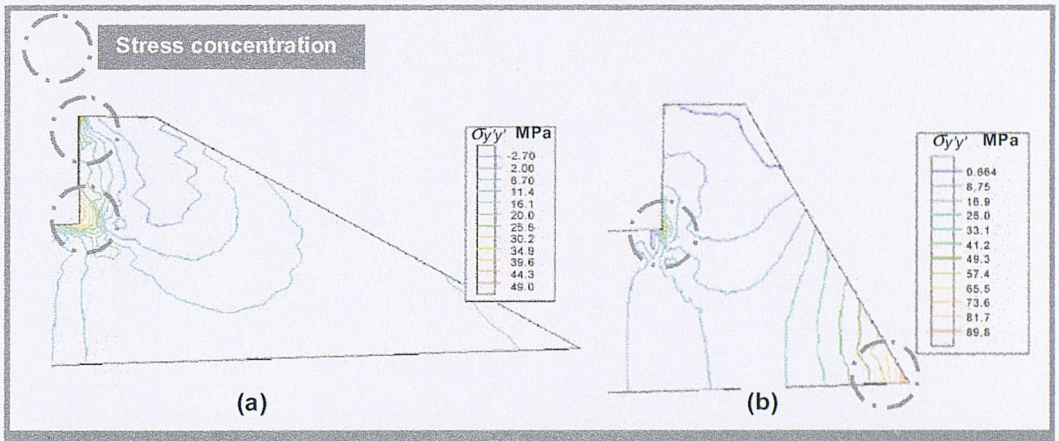


Figure 4.33: Peel stress contour plots of scarf joint designs with adhesive entry angle (a) $\theta_f = 30°$ and (b) $\theta_f = 60°$

There are three regions in the adhesive fillet where a stress concentration might occur. Figure 4.33 shows the peel stress distribution in an adhesive fillet for two scarf joint models with adhesive fillet entry angle of 60° and 30° respectively. It can be seen that for the scarf joint design with the adhesive fillet entry angle of 30°, the peel stresses in the adhesive fillet are concentrated mainly on the scarf tip face. On the other hand, for the scarf joint design with an adhesive fillet entry angle of 60°, a stress concentration is also present at the free end of the adhesive/adherend interface in addition to the stress concentrations at the scarf tip face. This additional stress concentration at the free end of the adhesive/adherend interface can be explained by the relatively larger angle the

adhesive makes with the adherend. It is noted that the peel stresses in the scarf joint model increases with the adhesive fillet entry angle.

Figure 4.34 shows the percentage reduction of the maximum stress components in the adhesive and adherend for different adhesive fillet entry angles. As was seen in Figure 4.32, the peel stress component in the adhesive fillet is the most affected by the presence of the adhesive fillet. However, for adhesive fillet entry angles, $\theta_f < 4\,5°$, no significant changes to the percentage reduction of the stress components were observed. On the other hand, for adhesive fillet entry angles, $\theta_f > 4\,5°$, a 20% drop in the percentage reduction of the peel stress component in the adhesive fillet was observed.

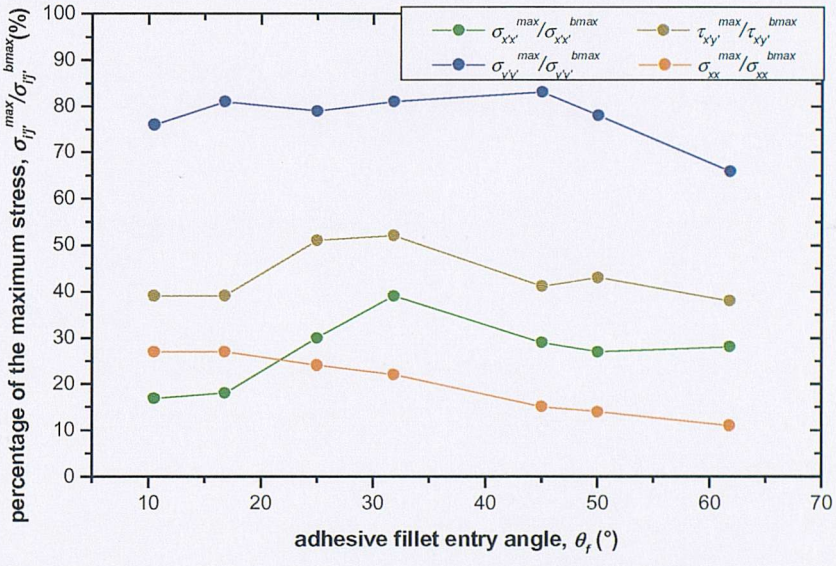


Figure 4.34: Percentage reduction of the maximum stress components in the adhesive fillet and the adherend for different adhesive fillet entry angles, θ_f

It is, however, unclear from this analysis whether the change in the percentage reduction of the stresses in the adhesive and the adherend was caused by the change of the adhesive fillet entry angle or by the corresponding change in the size of the adhesive fillet. In order to clarify this uncertainty, the adhesive fillets were modelled with different adhesive fillet entry angles but the adhesive fillet area was kept constant at 1mm^2. The percentage reduction of the maximum stress components was then plotted against the change in adhesive fillet entry angle, Figure 4.35. No variation of the stress components was observed for different adhesive fillet entry angle when the size of the adhesive fillet was kept constant. This indicates that the maximum stress components are not affected by the adhesive fillet entry angle.

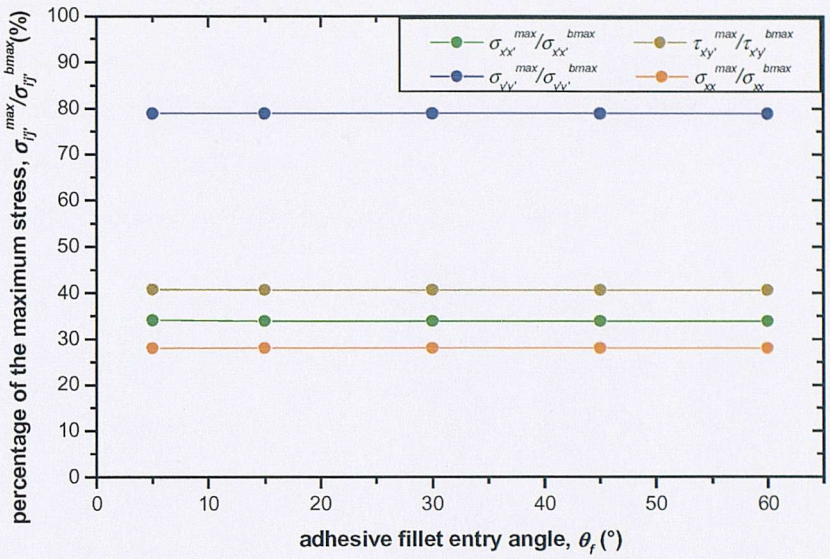


Figure 4.35: Percentage reduction of the maximum stress components in the adhesive fillet and the adherend for different adhesive fillet entry angle, θ_f and equal adhesive fillet area of 1mm^2

4.8 Effect of temper grade of the aluminium alloy adherends

4.8.1 Introduction

The previous three investigations have concentrated on the effect of geometrical parameters on the stress concentrations and static failure strength of the scarf joint design. In this section, the effects of adherend material property on the joint performance of adhesively-bonded scarf joints are discussed. Aluminium alloys are commonly produced with different temper grades. This is often carried out by heat treating the alloy to allow for variations in strength and ductility. As mentioned in Chapter Three, two variations of the aluminium alloy, 2014A were used in this project. The main difference between these two variations is the strength and ductility of the alloys, where the 'L157' alloy (T6) has a higher strength but lower ductility when compared to the 'L156' alloy (T4). The material properties of these two alloys were given in Figures 3.2a and b.

It has been discussed in section 4.5.5 that adherend failure of the scarf joint design is often accompanied by gross plastic yielding of the adherends. Finite element modelling of the scarf joint design described in the previous paragraph shows that, with substantially high loads, plastic yielding is observed at the adherends adjacent to the overlap terminus, see Figure 4.36. Hence, it can be for seen that different material responses of the adherend

could result in very different failure mechanisms. The results from this investigation are given in section 4.8.2. Monotonically-loaded tests were also carried out to investigate the effect of adherend temper grade on the joint strength of adhesively-bonded aluminium alloy scarf joints. The scarf joint models used in this investigation have a scarf angle, θ = 1.8°, scarf tip thickness, t_{st} = 0.15mm and adherend thickness, t = 2mm.

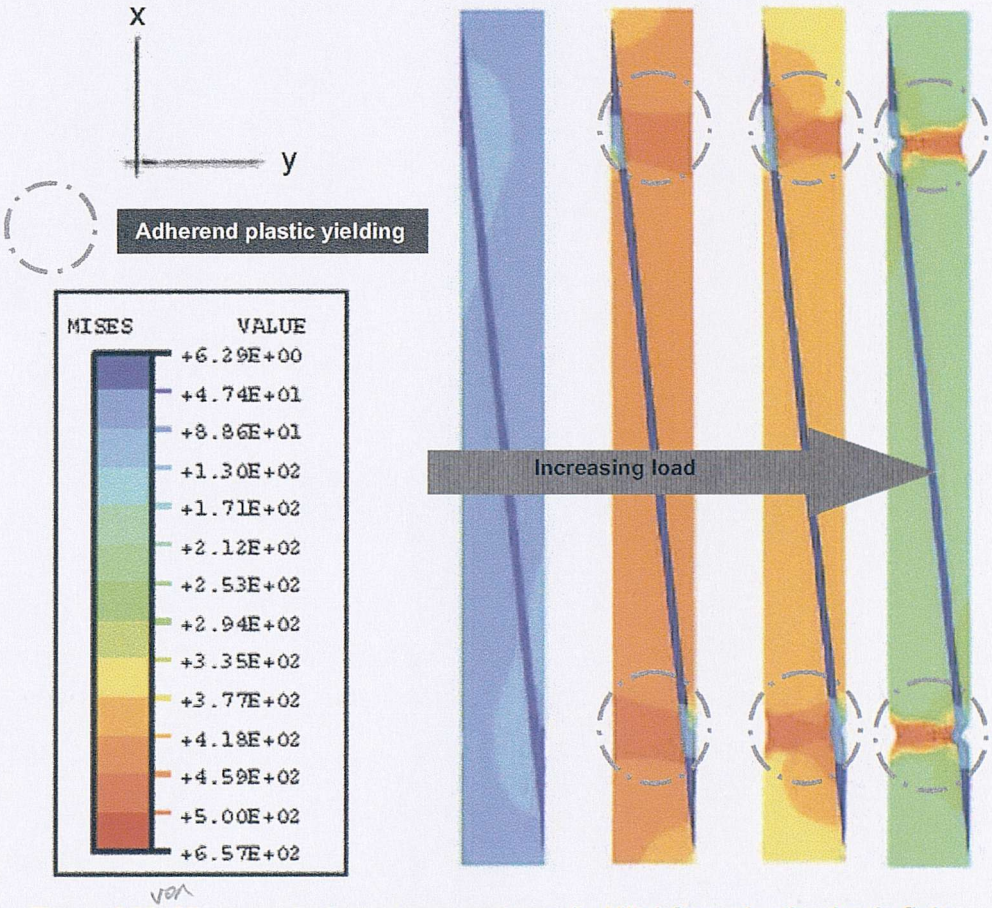


Figure 4.36: Mises equivalent stress contours (in MPa) from elastic-plastic finite element analysis showing gross adherend plastic yielding with increase of applied load

4.8.2 Elastic-plastic finite element analysis

A number of failure criteria were used to predict the failure loads and the failure loci of these two scarf joint models. These are the same failure criteria used in the investigation of the effect of scarf tip thickness (section 4.5) and scarf angle (section 4.6), and are given in Table 4.2. Figure 4.37 compares the predicted load-deflection curves of the scarf joint models with the two temper grades mentioned above. It can be seen that the 'L156' (T4) scarf joint model yields at a much lower load compared to the 'L157' (T6) scarf joint model. In addition, the 'L156' (T4) scarf joint model has a longer elongation compared to

the 'L157' (T6) scarf joint model. This difference in the load-displacement behaviour of the two types of adherend indicates that the failure mode of these two joints could be different.

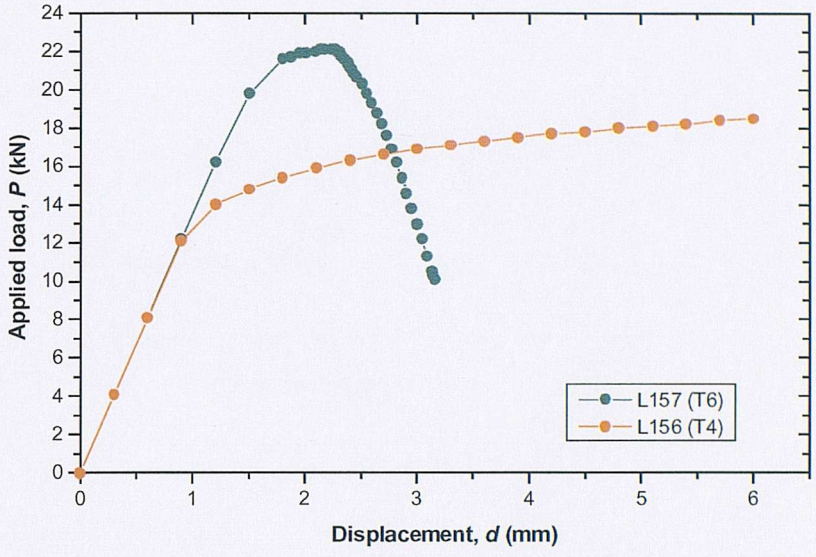


Figure 4.37: Predicted load-displacement curves of scarf joints with L157 (T6) and L156 (T4) aluminium alloy adherends using elastic-plastic finite element analysis

Figures 4.38 compares the critical shear stress, shear strain and Mises equivalent stress in the adhesive as well as the adherend Mises equivalent stress for scarf joints using 'L157' (T6) or 'L156' (T4) aluminium alloy adherends. It can be seen that the scarf joint model with the 'L156' (T4) aluminium alloy adherends yields at a lower load compared to the scarf joint model with the 'L157' (T6) aluminium alloy adherends. Although the critical shear stress and Mises equivalent stress in the adhesive and the adherend for the scarf joint model with the 'L156' (T4) aluminium alloy adherends had reached their respective failure criteria, there is no indication that the model is suffering from material softening. The same observation can be made in Figure 4.37 where the scarf joint model with the 'L156' (T4) aluminium alloy adherends had been extended by 6mm with no indication of material softening. However, judging from the high shear strain values in the adhesive, the joint had reached its ultimate tensile load.

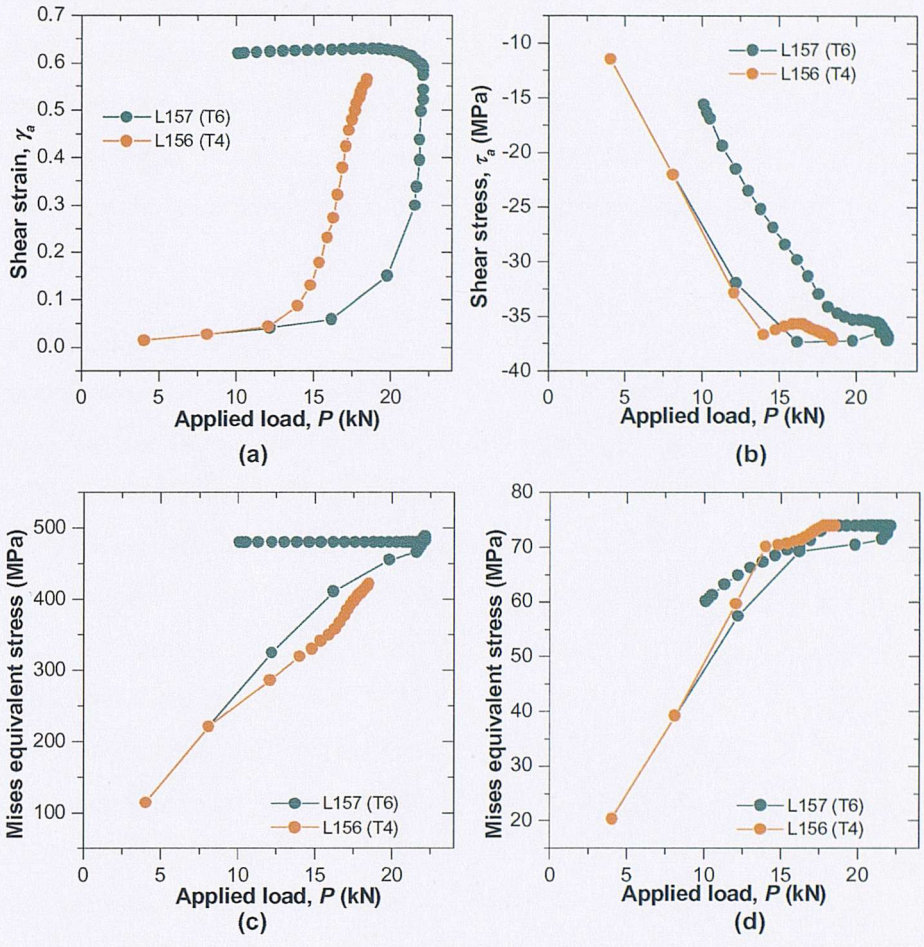


Figure 4.38: Comparison of the maximum (a) shear strain, (b) shear stress, (c) adherend Mises equivalent stress and (d) adhesive Mises equivalent stress in the adhesive layer for scarf joints with 'L157' (T6) and 'L156' (T4) aluminium alloy adherends

Table 4.11: Summary of the predicted failure load of scarf joints with 'L157' (T6) and 'L156' (T4) aluminium alloy adherends using elastic-plastic finite element analysis

Joint design	Failure criterion	Predicted failure load, P (kN)
Scarf joint 'L157' (T6)	Adherend ultimate tensile strength	22.13
	Adhesive fracture shear strain	21.41*
	Adhesive fracture shear stress	22.10
	Adhesive ultimate tensile strength	22.10
Scarf joint 'L156' (T4)	Adherend ultimate tensile strength	18.91
	Adhesive fracture shear strain	18.74
	Adhesive fracture shear stress	18.90
	Adhesive ultimate tensile strength	17.81

* Predicted failure load occurred at negative slope of the load-deflection curve

On the other hand, the scarf joint model with the 'L157' (T6) aluminium alloy adherends yielded at a much higher load but suffered from a lack of adherend ductility. It is clear from this investigation that by tempering the aluminium alloy to give relatively low yield strength, the adhesive was able to reach its full potential. A summary of the predicted failure loads using the various failure criteria are given in Table 4.11.

4.8.3 Experimental results

Monotonically-loaded tests on the effect of adherend temper grade were also carried out. At least four specimens were tested for each model. The results are given in Figure 4.39. It can be seen that the scarf joint design with the 'L156' (T4) aluminium alloy adherends failed at a lower load compared to the scarf joint model with the 'L157' (T6) aluminium alloy adherends. The difference between these two adherend temper grades causes an increase of approximately 17% in the joint strength when the 'L157' (T6) aluminium alloy adherends are employed. In addition, it was observed that the scarf joint design with the 'L156' (T4) aluminium alloy adherends failed in the adhesive (see Figure 4.30). On the other hand, the scarf joint with the 'L157' (T6) aluminium alloy adherends failed in the adherend (see Figure 4.18). The experimental results compare well with the elastic-plastic finite element predictions given in the previous section, see Table 4.12.

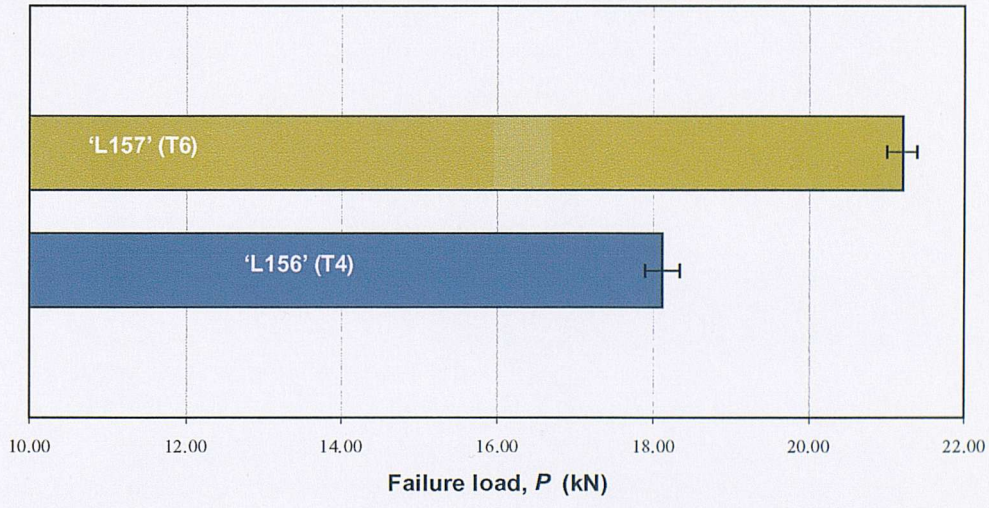


Figure 4.39: Results from the experimental monotonically-loaded tension tests of scarf joints with 'L157' (T6) and 'L156' (T4) aluminium alloy adherends

Table 4.12: Comparison between the experimental and predicted failure load and failure locus of scarf joints with 'L157' (T6) and 'L156' (T4) aluminium alloy adherends

Scarf joint design	Experimental failure locus	Predicted failure locus	Experimental failure load, *P* (kN)	Predicted failure load, *P* (kN)	Percentage error, %
'L157' (T6)	adherend	adherend	21.2 ± 0.2	22.13*	4.4
'L156' (T4)	adhesive	adhesive	18.1 ± 0.22	18.74*	3.6

* prediction based on adherend Mises equivalent stress criterion
^ prediction based on adhesive shear strain criterion

4.9 Comparison between the scarf joint and overlap joint designs

4.9.1 Introduction

The previous five sections have focussed on the optimization of the scarf joint design. Now, it is interesting to compare the scarf joint design with the overlap joint design. The overlap joint design has received much more attention from other researchers because it is easier to produce compared to the scarf joint design. The main difference between the two joint designs is the orientation of the adhesive plane with respect to the loading plane. In the overlap joint design, the adhesive plane is parallel to the loading plane, see Figure 4.40. On the other hand, the adhesive plane in a scarf joint design is dependent on the scarf angle, see Figure 4.5. However, when a load is applied, the overlap joint design is expected to experience more bending compared to the scarf joint design, Figure 4.41. This is due to the higher loading eccentricity in the overlap joint design.

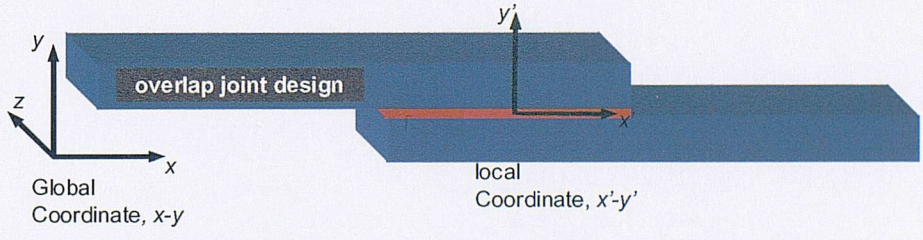


Figure 4.40: Schematic diagram of the global and local coordinate systems used for the overlap joint design

In order to compare the joint efficiency of these two joint designs, the overlap length and the adherend thickness were kept constant at 34mm and 2mm respectively. This overlap length corresponds to the previously investigated scarf joint design with a

scarf tip thickness, t_{st} = 0.4mm and scarf angle θ = 1.8°. The 'L157' (T6) aluminium alloy was used as the adherends for both joint designs and the adhesive used was the FM73 M film adhesive. The material properties of the adhesive and the adherend were given in Figure 3.1 and Figure 3.2 respectively.

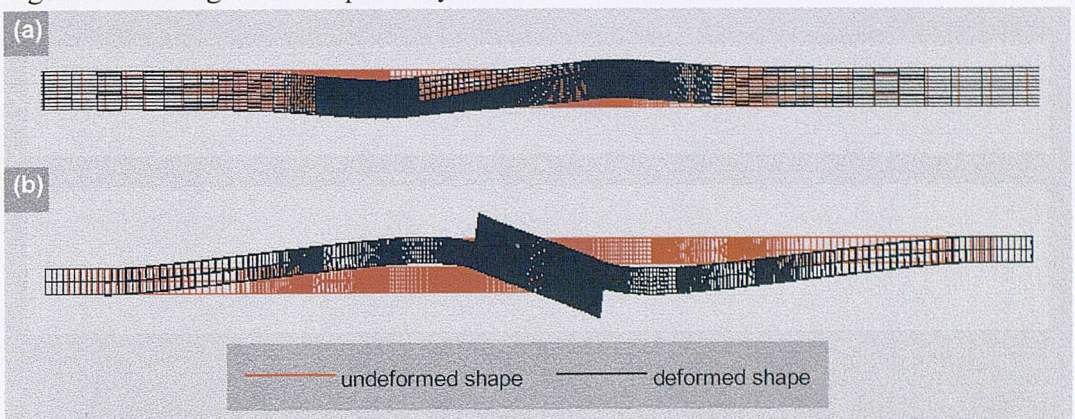


Figure 4.41: Joint bending observed in adhesively-bonded (a) scarf joint and (b) overlap joint with an applied load, *P* of 5kN

Linear elastic finite element analyses were used to investigate the stress concentration in the adhesive of both joint designs. In addition, elastic-plastic finite element analyses were used to investigate the post-yield behaviour of these two joint designs. Details of the finite element methods used in this investigation were given in sections 4.3.2 and 4.3.3. The elastic-plastic finite element predictions are then compared with the monotonically-loaded test results.

4.9.2 Elastic finite element analysis

Figures 4.42-4.44 show the comparison of the normalised stress components in the mid-plane of the adhesive between the scarf joint and overlap joint design. Figure 4.42 shows that the minimum direct stress in the adhesive of a scarf joint is relatively high compared to the overlap joint design. This can be explained by the orientation of the adhesive plane where the adhesive plane in the scarf joint is orientated at an angle to the loading plane. As a result, the adhesive in the scarf joint design will be subjected to higher direct stresses. Interestingly, the maximum direct stress in the overlap joint design is higher than that in the scarf joint design.

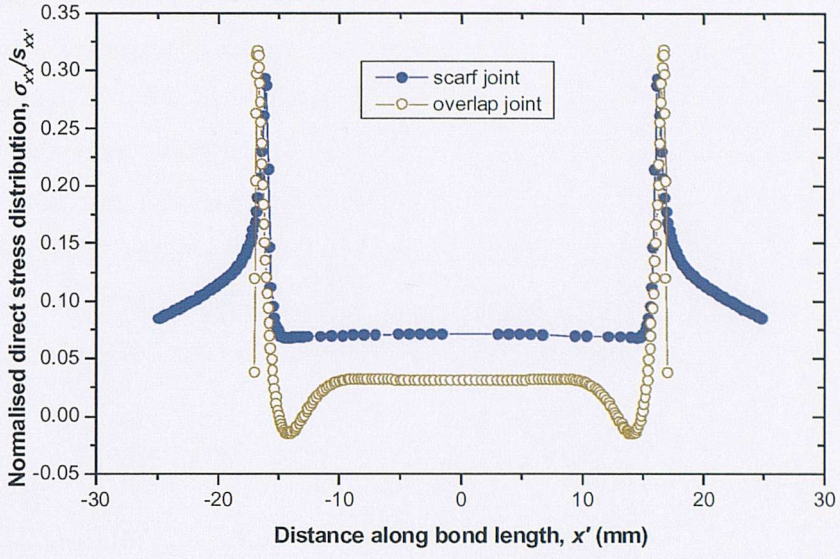


Figure 4.42: Normalized direct stress distribution at the centre of the adhesive layer (y' = 0) plotted against distance along the bond length for the scarf joint and overlap joint design

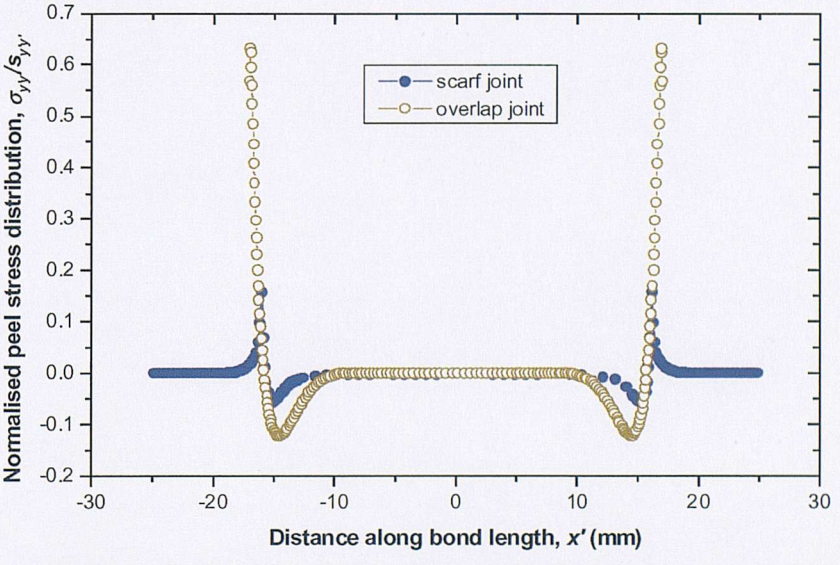


Figure 4.43: Normalized peel stress distribution at the centre of the adhesive layer (y' = 0) plotted against distance along the bond length for the scarf joint and overlap joint design

From Figures 4.43 and 4.44, it can be seen that the maximum peel and shear stresses in the overlap joint design are much higher than those in the scarf joint design. From Figure 4.43, the maximum peel stress in the overlap joint design is almost four times that of the scarf joint design. The shear stress distribution shown in Figure 4.44 indicates that the maximum shear stress in the overlap joint design has reached the yield

stress of the adhesive (see Table 4.1) for an applied load of 5kN. In contrast, the maximum shear stress in the scarf joint design is only at 60% of the adhesive yield stress. It is believed that the higher loading eccentricity in the overlap joint design results in these significantly higher stresses at the overlap joint terminus. Nevertheless, the current investigation does not take into account adhesive and adherend plasticity. Hence, the results presented here would not represent an accurate prediction of the static strength of these two joint designs. Results from the elastic-plastic finite element analysis of these two joint designs will be presented in the next section.

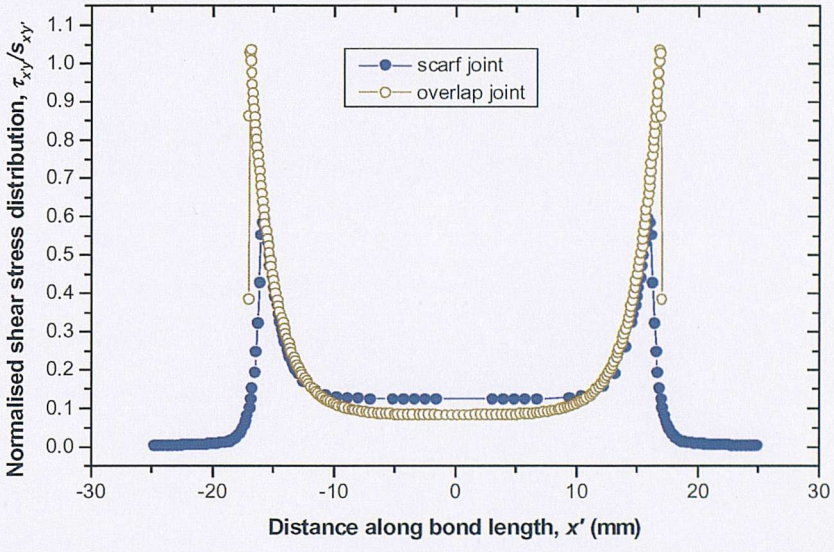


Figure 4.44: Normalized shear stress distribution at the centre of the adhesive layer (y' = 0) plotted against distance along the bond length for the scarf joint and overlap joint design

4.9.3 Elastic-plastic finite element analysis

Figure 4.45 compares the predicted load-displacement curves of the overlap joint and the scarf joint design. The figure shows that the overlap joint design is predicted to fail at a higher load compared with the scarf joint model. In addition, it can be seen that the overlap joint design is more ductile than the scarf joint model. It is noted that the same material properties were used for the adhesive and adherend for these two joint designs. The results here clearly contradict the elastic finite element prediction presented in the previous section. Hence, it is clear that material plasticity plays an important role to the prediction of the static strength of the adhesively-bonded joints. This is especially true when relatively ductile adhesives are used.

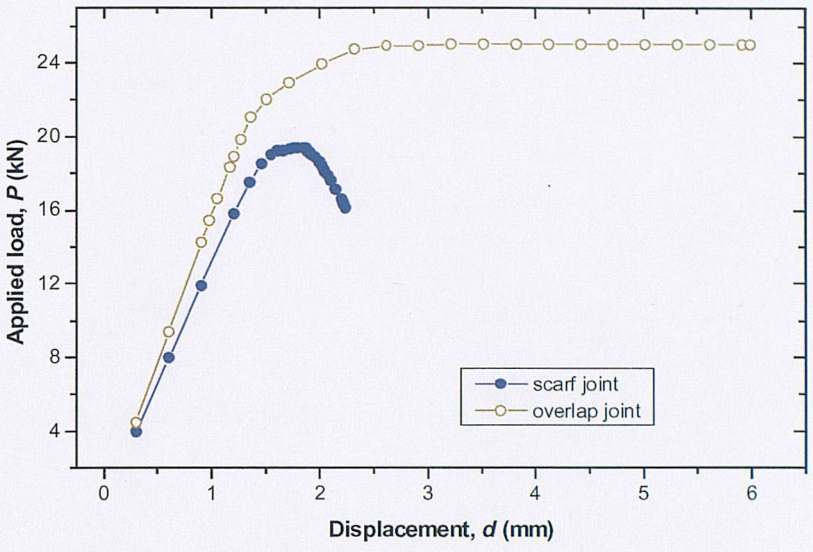


Figure 4.45: Predicted load-displacement curves of the scarf joints and overlap joint design using elastic-plastic finite element analysis

Figure 4.46 compares the critical stresses and strains in the adhesive and in the adherend between the two joint models. It is observed that the stresses in the adhesive for the overlap joint design reach their respective critical values at a higher applied load compared to that of the scarf joint design (see Figure 4.46b and d). In addition, it can be seen that the maximum Mises equivalent stress in the adherend for the overlap joint design did not reach its failure criterion, Figure 4.46c. This indicates that the overlap joint design will fail in the adhesive. On the other hand, the maximum direct stress in the adherend of the scarf joint design is the first to reach its failure criterion. This indicates that the scarf joint design will fail in the adherend. Table 4.13 summarizes the predicted failure loads using the elastic-plastic finite element analysis.

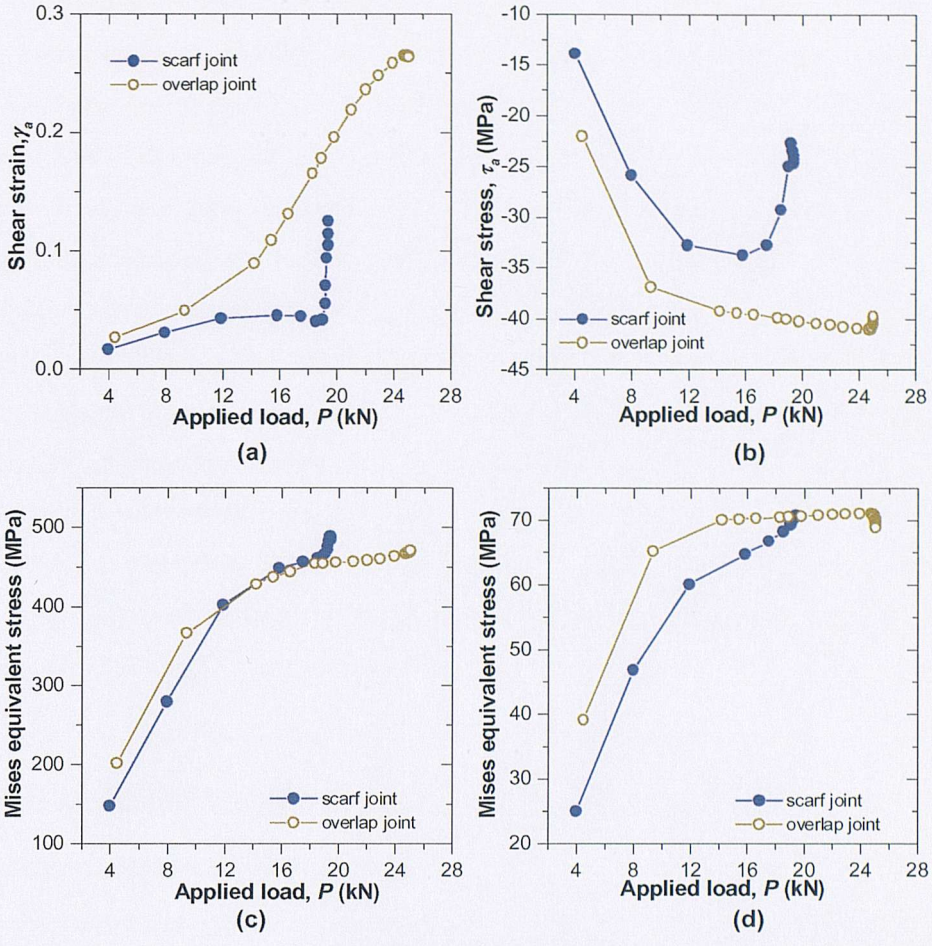


Figure 4.46: Comparison of the maximum (a) shear strain, (b) shear stress, (c) adherend Mises equivalent stress and (d) adhesive Mises equivalent stress in the adhesive layer for the scarf joint and overlap joint design

Table 4.13: Summary of the predicted failure load of the scarf and the overlap joint designs using elastic-plastic finite element analysis

Joint design	Failure criterion	Predicted failure load, P (kN)
Scarf joint	Adherend ultimate tensile strength	19.42
	Adhesive fracture shear strain	-
	Adhesive fracture shear stress	17.62*
	Adhesive ultimate tensile strength	-
Overlap joint	Adherend ultimate tensile strength	-
	Adhesive fracture shear strain	-
	Adhesive fracture shear stress	22.01
	Adhesive ultimate tensile strength	22.01

* Predicted failure load occurred at negative slope of the load-deflection curve
\- Analysis termined before failure criterion was reached

Comparison between the elastic and elastic-plastic finite element analysis shows two contradicting conclusions. From the elastic finite element analysis, it was found that the scarf joint design would be the better joint design when compared to the overlap joint design. This is because the stress concentrations in the scarf joint design are much lower than those in the overlap joint design. On the other hand, the elastic-plastic finite element analysis indicates that the overlap joint design will attain a higher joint strength compared to the scarf joint design. Since this analysis indicates that when the applied stress is lower than the yield stress of the adhesive and the adherend (i.e. such as may be seen in fatigue and creep tests), the scarf joint will be the better joint design. Similarly, for applied stress levels higher than the yield stress (i.e. such as when using monotonic loading to failure), the overlap joint design will be the better joint design. In order to confirm these observations, experimental testing of these two joint designs was performed using monotonically-loaded tests and fatigue tests. Details of the testing procedures were given in section 3.5.2 and 3.5.3 respectively.

4.9.4 Experimental results

4.9.4.1 Monotonically-loaded tests

Coupon specimens of the overlap joint and scarf joint design were tested using the monotonically-loaded testing procedure given in section 3.5.2. Results from the tests are shown in Figure 4.47. The results show that the overlap joint design failed at a higher load compared to the scarf joint design. In addition, the overlap joints failed at the adhesive. On the other hand, the scarf joints failed in the adherend (see Figure 4.18). This compares well with the predictions from the elastic-plastic finite element analysis shown in the previous section. A summary of the comparisons between the experimental test results and the predicted results are given in Table 4.14.

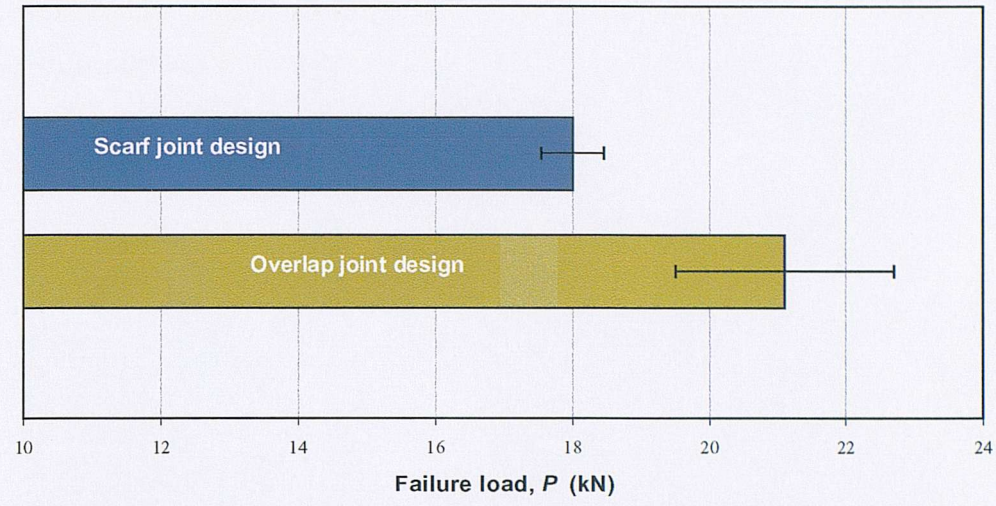


Figure 4.47: Results from the experimental monotonically-loaded tension tests of the scarf joints and overlap joint design

Table 4.14: Comparison between the experimental and predicted failure load and failure locus of the scarf joint and overlap joint design

Joint design	Experimental failure locus	Predicted failure locus	Experimental failure load, *P* (kN)	Predicted failure load, *P* (kN)	Percentage error, %
Scarf joint	adherend	adherend	18.0 ± 0.46	19.42*	7.9
Overlap joint	adhesive	adhesive	21.1 ± 1.62	22.01^	4.3

* prediction based on adherend Mises equivalent stress criterion
^ prediction based on adhesive shear stress criterion

4.9.4.2 Fatigue tests

Fatigue tests were carried out to compare the joint efficiency of the scarf joint and overlap joint designs. The fatigue tests were carried out in 'hot/wet' conditions as part of the investigation of the effect of surface treatments on the durability of adhesively-bonded joints (see Chapter Five). Details of the experimental procedure were given in section 3.5.2. In this section, the durability of the scarf joint and overlap joint will be discussed. As shown in the finite element predictions given above, the contradiction between the elastic and elastic-plastic finite element analysis indicates that the overlap joint design is inferior compared to the scarf joint design only when the applied stress is below the yield stress of the adhesive and the adherend.

Figure 4.48 compares the fatigue life of the scarf joint and overlap joint designs using (a) the GBD surface treatment and (b) the GPS surface treatment. It can be seen that

the overlap joints are less durable compared to the scarf joints. This confirms the finite element predictions which indicated that, when the applied stress is lower than the yield stress of the adhesive and the adherend, the scarf joint design is the better joint design compared to the overlap joint design.

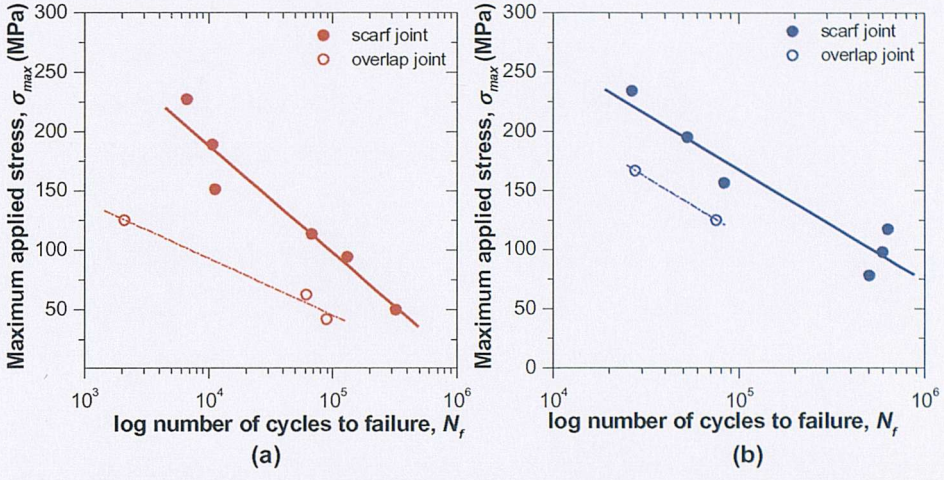


Figure 4.48: Comparison of the durability of adhesively-bonded scarf joints and overlap joints surface treated with (a) the GBD surface treatment and (b) the GPS surface treatment

4.10 Chapter summary

The following conclusions are drawn from this chapter

1. The effect of the scarf tip thickness was investigated using an analytical analysis, a finite element analysis and experimental testing. It was found that an increase in the scarf tip thickness increases the stress concentrations at the overlap termini. In addition, increasing the scarf tip thickness also increases the stress concentration in the adherend opposite the scarf tip. It was also found that the scarf tip thickness should not be neglected from any analytical or finite element analyses as the presence of the scarf tip thickness significantly affects the length of the overlap region. This is especially true when the scarf angle is small.

2. It was found that for scarf joints with an adherend thickness of, t = 2mm, a scarf angle, θ = 1.8° and a scarf tip thickness of t_{st} = 0.4mm or 0.15mm,

failure occurred in the adherend opposite the scarf tip. This was as predicted using the elastic-plastic finite element analysis.

3. The effect of scarf angle was also investigated using an analytical analysis, a finite element analysis and experimental testing. It was found that an increase in the scarf angle increases the stress concentrations in the adhesive and the adherend. However, the effect of the scarf angle on the stress concentration in the adherend is small compared to that in the adhesive.

4. It was also found from the elastic finite element analysis that for a scarf angle of $\theta > 2°$, the increase in the shear stress component in the adhesive is significantly higher compared to scarf joints with scarf angles of $\theta < 2°$. This indicates that failure in the adhesive will be more likely for scarf joints with scarf angles of $\theta > 2°$. Elastic-plastic finite element analysis and experimental testing of scarf joint specimens with scarf angles, $\theta = 1.5°$, $1.8°$ and $5°$ show that for scarf joints with scarf angles, $\theta = 1.5°$, $1.8°$, failure in the adherend was observed. On the other hand, for scarf joint specimens with the scarf angle of $5°$, failure was observed to occur in the adhesive. This change in failure locus was also accompanied by a predicted decrease in joint strength. The experimental results compared very well with the elastic-plastic finite element predictions.

5. The effect of the adhesive fillet size and adhesive fillet entry angle for the scarf joint design was also investigated using elastic finite element analyses. It was found that the peel stress component in the adhesive fillet was the most affected by changes in the adhesive fillet size. However, the percentage reduction of the maximum peel stress in the adhesive fillet did not vary significantly for the normalised fillet length, $l_f/L_f > 0.2$. It was also found that the maximum stress components at the overlap terminus were not affected by the change in adhesive fillet entry angle.

6. The studies on the geometrical optimization of the scarf joint design indicates that the optimized scarf joint design, for 2mm thick aluminium alloy

adherends and rubber-toughened epoxy adhesives, have a scarf tip thickness of t_{st} = 0.15mm and a scarf angle of θ = 1.8°. The results from this chapter indicate that this scarf joint design is capable of yielding in excess of 90% of the ultimate tensile strength of the adherends.

7. The effect of the temper grade of the aluminium alloy adherends was also investigated using an elastic-plastic finite element analysis and experimental testing. It was found that for scarf joints made using the L156 (T4) aluminium alloy adherends a significant increase in the plastic yielding which occurred in the adherends was observed. However, the joints yielded at a lower load compared to the scarf joints made using the L157 (T6) aluminium alloy adherends. These observations are similar to those recorded for the comparison between the stress-strain relationships of these two alloys. It was also found that the scarf joints with the L156 (T4) aluminium alloy adherends failed in the adhesive, while the scarf joints with the L157 (T6) aluminium alloy adherends failed in the adherend. The experimental results again compared very well with the predictions from the elastic-plastic finite element analysis.

8. A comparison between the scarf joint design and the overlap joint design was carried out using elastic finite element analysis, elastic-plastic finite element analysis and experimental testing. Interestingly, it was found that from the elastic finite element analysis, the overlap joint was found to be inferior compared to the scarf joint design. On the other hand, the elastic-plastic finite element analysis predicts that the overlap joint design is much stronger than the scarf joint design. This was also observed from the monotonically-loaded tests carried out on the scarf joint and overlap joint designs. The scarf joint and overlap joints were also tested in fatigue conditions. It was found from the fatigue tests that the fatigue strength of the scarf joint design is higher than the overlap joint design. Hence, it can be concluded that due to the reduced loading eccentricity in the scarf joint design, the scarf joint design will be better than the overlap joint design if the yield stress of the adhesive and the adherend is not exceeded (i.e. fatigue or creep tests). On the other hand,

because of the reduced cross section area of the adherends in the scarf joint, the static tensile strength of the scarf joint design will be lower compared to the overlap joint design.

CHAPTER 5

EFFECT OF SURFACE TREATMENTS – COUPON TEST RESULTS

5.1 Introduction

The importance of the choice of the surface treatment on the performance of adhesively-bonded joints has been reviewed in section 2.4. Surface treatments play an important role in determining the durability of adhesively-bonded joints, particularly for aluminium alloy adherends. This is because aluminium alloys have a high surface energy. Hence, they are highly susceptible to atmospheric contamination, as well as moisture attack upon the bonded joint. As mentioned in Chapter One, one of the main aims of the present project is to investigate the performance of a silane (i.e. γ-glycidoxypropyltrimethoxysilane (GPS)) surface treatment. This has been carried out by comparing the static and fatigue performance of GPS surface treated adhesively-bonded joints with similar joints but surface treated using the grit-blast and degrease (i.e. GBD) and chromic acid etching (i.e. CAE) treatments. The application procedures for these surface treatments were given in section 3.3. In the present chapter, results from static and fatigue tests of adhesively-bonded joints using the above mentioned three surface treatments are given.

5.2 Monotonically-loaded tests

5.2.1 Introduction

Before undertaking the cyclic fatigue tests, it was necessary to measure the strength of the scarf and overlap joints under simple monotonic loading conditions. The experimental test procedures for the monotonically-loaded tests were given in section 3.5.2. These tests were carried out at a constant displacement rate of 1mm/min. Six different joint designs were used in this investigation. The geometrical design parameters of these test geometries are given in Table 5.1. For all the joints tested in this investigation, the adhesive and adherend thickness were 0.2mm and 2mm respectively. A scarf angle of 1.8° was used for all the scarf joint designs. It should be noted that the scarf joint design with a scarf tip thickness of t_{st} = 0.15 was found to be the optimum design for the scarf joint, as discussed in Chapter Four.

The aluminium alloy/CFRP hybrid joints were tested to investigate (a) the effect of residual thermal stresses from the curing of the adhesive and (b) the strength of the aluminium alloy/adhesive interface compared to the CFRP/adhesive interface.

Table 5.1: Geometrical parameters of the various joint designs used in the investigation of the effects of surface treatments using the monotonically-loaded test method

Joint design	Scarf tip thickness, t_{st} (mm)	Adherends	Bond length, L_a (mm)	Aluminium alloy temper grade
Single scarf joint	0.4	Al-alloy/Al-alloy	34	L157 (T6)
Single scarf joint	0.15	Al-alloy/Al-alloy	48	L157 (T6)
Single scarf joint	0.15	Al-alloy/Al-alloy	48	L156 (T4)
Overlap joint	-	Al-alloy/Al-alloy	34	L157 (T6)
Single hybrid scarf joint	0.15	Al-alloy/CFRP	48	L156 (T4)
Double hybrid scarf*	0.15	Al-alloy/CFRP	48	L157 (T6)

Note:
1. * made by adhesively bonding two single hybrid scarf joints, back-to-back
2. Scarf angle was 1.8°

5.2.2 Scarf joint (t_{st} = 0.4mm; 'L157' T6) [Al-alloy/Al-alloy]

Before concentrating on the use of the optimized scarf joint design, a few tests were undertaken using a scarf tip thickness of t_{st} = 0.4mm (it will be recalled that for the optimized design, t_{st} = 0.15mm). Figure 5.1 compares the static failure load of aluminium

alloy scarf joints with a scarf tip thickness of t_{st} = 0.4mm for the three surface treatments. It can be seen that there is no significant difference in the failure loads for the different surface treatments. For all three surface treatments, the failure load is approximately 18kN and the average joint efficiency is approximately 79%, i.e. when normalized relative to the ultimate tensile strength of the aluminium alloy adherend, see Table 5.2. However, it was found that the GBD surface treated joints failed in the adhesive. On the other hand, the majority of the GPS and CAE surface treated joints failed in the aluminium alloy adherend. (A schematic diagram of the adherend failure mode was given in Figure 4.18). However, it should be noted that the occurrence of these different failure loci did not cause a significant change in the ultimate strength of the joints. The results are summarised in Table 5.2.

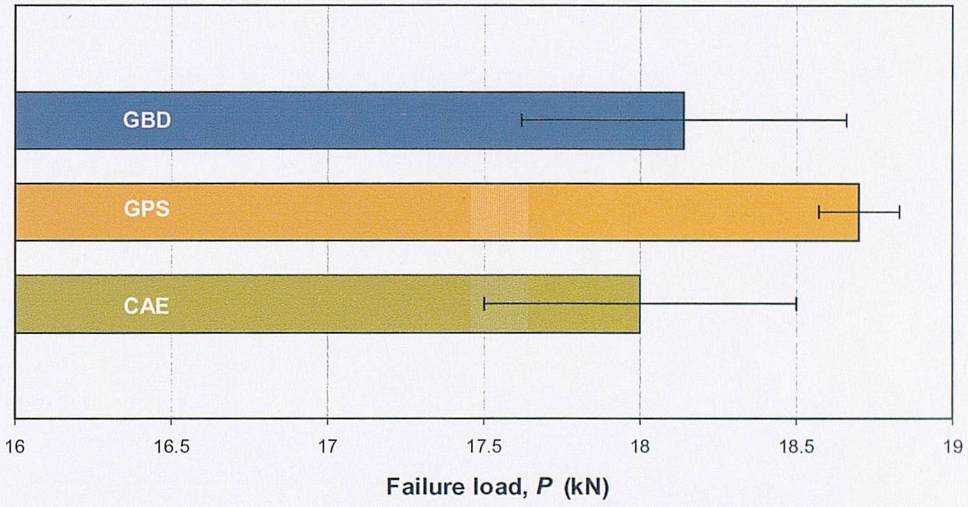


Figure 5.1: Comparison of the static failure loads of aluminium alloy scarf joints with a scarf tip thickness of t_{st} = 0.4mm and 'L157' (T6) for different surface treatments

Table 5.2: Summary of the comparison of the failure loads and failure loci of aluminium alloy scarf joints with a scarf tip thickness of t_{st} = 0.4mm and 'L157' (T6) for different surface treatments

Surface treatments	Average failure load, P(kN)	Failure locus	Joint efficiency σ_{max}/$UTS_{Al\text{-}alloy}$ (%)
GBD	18.15 ± 0.57	adhesive	78.78 ± 0.02
GPS	18.30 ± 0.10	adherend	79.43 ± 0.00
CAE	18.00 ± 0.46	adherend	78.13± 0.02

σ_{max} = P/cross section area of adherend
$UTS_{Al\text{-}alloy}$ = ultimate tensile strength of aluminium alloy adherend
Al-alloy = 'L157' (T6)

5.2.3 Scarf joint (t_{st} = 0.15mm; 'L157' T6) [Al-alloy/Al-alloy]

Considering the optimized scarf joint design, Figure 5.2 compares the static failure loads of aluminium alloy scarf joints with a scarf tip thickness of t_{st} = 0.15mm for the three different surface treatments. No significant differences in the failure loads were observed for the different surface treatments. However, it should be noted that the joints surface treated using the GBD surface treatment failed at the adhesive/adherend interface. On the other hand, the GPS and CAE surface treated joints failed in the adherend, as shown in Figure 4.18. Figure 5.2 shows that this change in the failure locus (i.e. from adherend to the adhesive/adherend interface) resulted in a decrease in the joint efficiency of approximately 5%, as may be seen by comparing the results shown in Tables 5.3 and 5.2. It may be observed from Table 5.3 that the average joint efficiency of the GPS and CAE surface treated joints is approximately 93%, when compared to the ultimate tensile strength of the aluminium alloy adherend. As discussed in section 4.5, this increase in the joint strength of this optimized joint design, compared to the scarf joint design with a scarf tip thickness of t_{st} = 0.4mm, is due to the reduced scarf tip thickness and increased bond length. Thus, the work reported in Chapter Four on optimizing the design of the scarf joint is clearly of direct relevance and benefit to the present durability studies.

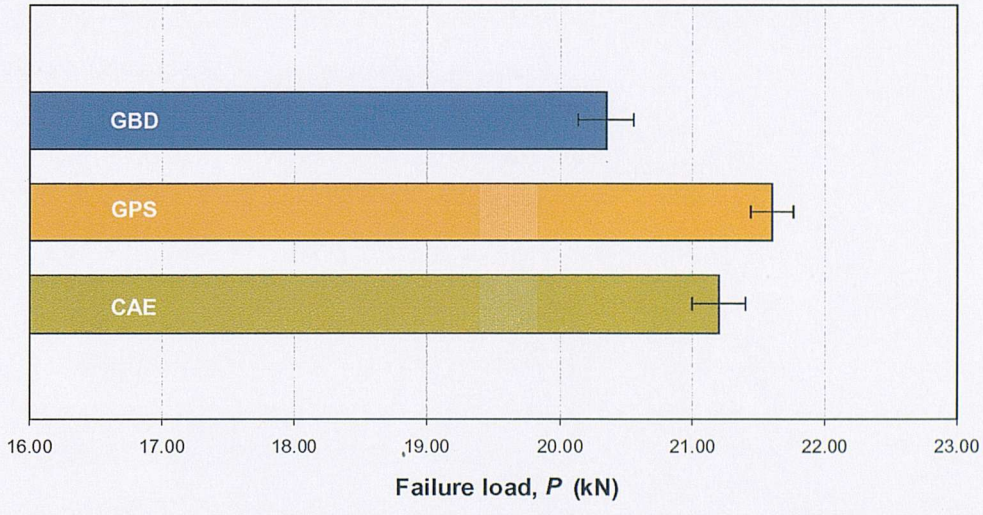


Figure 5.2: Comparison of the static failure loads of aluminium alloy scarf joints with a scarf tip thickness of t_{st} = 0.15mm and 'L157' (T6) for different surface treatments

Table 5.3: Summary of the comparison of the failure loads and failure loci of aluminium alloy scarf joints with a scarf tip thickness of t_{st} = 0.15mm and 'L157' (T6) for different surface treatments

Surface treatments	Average failure load, P(kN)	Failure locus	Joint efficiency $\sigma_{max}/UTS_{Al\text{-}alloy}$ (%)
GBD	20.35 ± 0.21	interface	88.32 ± 0.01
GPS	21.60 ± 0.16	adherend	93.75 ± 0.01
CAE	21.20 ± 0.2	adherend	92.01 ± 0.01

σ_{max} = P/cross section area of adherend
$UTS_{Al\text{-}alloy}$ = ultimate tensile strength of aluminium alloy adherend
Al-alloy = 'L157' (T6)

5.2.4 Scarf joint (t_{st} = 0.15mm; 'L156' T4) [Al-alloy/Al-alloy]

The effect of the temper grade of the aluminium alloy adherend was discussed in section 4.8. It was shown that by using the 'L156' (T4) aluminium alloy adherends, the scarf joints used in the present project invariably failed in the adhesive. This is due to the relatively high ductility of this alloy compared to the 'L157' (T6) aluminium alloy adherend used to attain the results reported in sections 5.2.2 and 5.2.3. Figure 5.3 compares the effects of the surface treatments on the joint efficiency of the 'L156' (T4) aluminium alloy scarf joint design. It was observed that all the GPS and CAE surface treated joints failed in the adhesive (i.e. cohesive failure). On the other hand, the GBD surface treated joints failed at the adhesive/adherend interface.

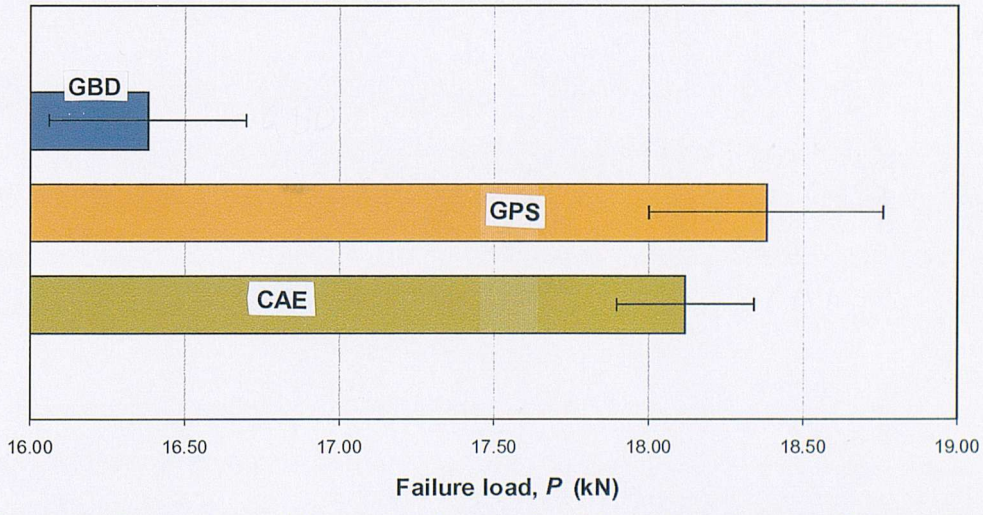


Figure 5.3: Comparison of the static failure loads of aluminium alloy scarf joints with a scarf tip thickness of t_{st} = 0.15mm and 'L156' (T4) aluminium alloy adherends for different surface treatments

Overall, the joint efficiency of the GPS and CAE surface treated joints is approximately 87%, when normalized to the ultimate tensile strength of the aluminium alloy adherend. However, comparing these results with those from the previous investigation of the 'L157' (T6) aluminium alloy adherend, see section 5.2.3, the scarf joint with the higher temper grade, 'L157' (T6) alloy, attained a higher joint efficiency compared to the scarf joint with the 'L156' (T4) alloy, see Tables 5.3 and 5.4. The GBD surface treated joints typically failed at a lower load compared to the GPS and CAE surface treated joints. However, the decrease in joint efficiency is small for the GBD treated scarf joints; i.e. by approximately 10% of the joint efficiency of the GPS and CAE surface treated joints. The reason for this is suggested to arise from the inferior interfacial strength of the GBD surface treated joints, compared to the GPS and CAE surface treated joints where failure occurred in the adhesive.

Table 5.4: Summary of the comparison of the failure loads and failure loci of aluminium alloy scarf joints with a scarf tip thickness of t_{st} = 0.15mm and 'L156' (T4) aluminium alloy adherends for different surface treatments

Surface treatments	Average failure load, P(kN)	Failure locus	Joint efficiency $\sigma_{max}/UTS_{Al\text{-}alloy}$ (%)
GBD	16.38 ± 0.32	interface	77.56 ± 0.01
GPS	18.38 ± 0.38	adhesive	87.03 ± 0.01
CAE	18.12 ± 0.22	adhesive	85.80 ± 0.01

σ_{max} = P/cross section area of adherend
$UTS_{Al\text{-}alloy}$ = ultimate tensile strength of aluminium alloy adherend
Al-alloy = 'L156' (T4)

5.2.5 Overlap joint ('L157' T6) [Al-alloy/Al-alloy]

The overlap joint geometry was also studied in the comparison between the overlap and scarf joint geometry, as discussed in section 4.9. It was shown that the overlap joint design, see Table 5.1, has a higher static joint strength compared to the scarf joint design with the same overlap length (i.e. L_a = 34mm).

Figure 5.4 compares the effects of the three surface treatments on the joint strength of this overlap joint design. It can be seen that the failure loads are relatively high compared to the scarf joint models used in the previous investigations. Interestingly however, the GBD surface treated joints failed via a mixture of adhesive (i.e. cohesive) and adhesive/adherend interfacial failure. On the other hand, the GPS and CAE surface treated joints failed in the adhesive. However, the difference in failure locus did not

significantly affect the joint strength. In fact, no significant difference was found between the joint strengths of the overlap joints using the three different surface treatments. Joint efficiency is high, with an average across the three surface treatments in the region of 95% of the ultimate tensile strength of the aluminium alloy adherend. Table 5.5 summarises the failure loads and failure loci of this joint design.

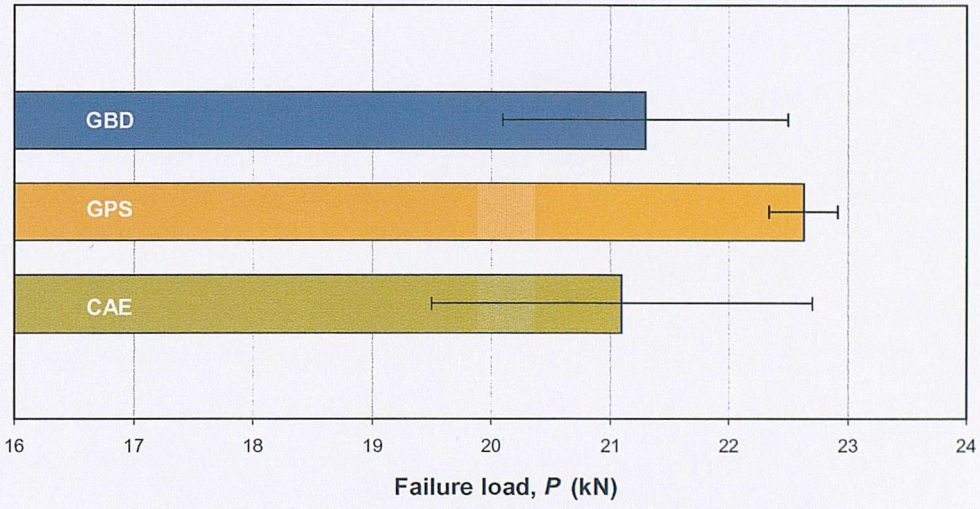


Figure 5.4: Comparison of the static failure loads of 'L157' (T6) aluminium alloy overlap joints for different surface treatments

Table 5.5: Summary of the comparison of the failure loads and failure loci of 'L157' (T6) aluminium alloy overlap joints for different surface treatments

Surface treatments	Average failure load, P(kN)	Failure locus	Joint efficiency $\sigma_{max}/UTS_{Al\text{-}alloy}$ (%)
GBD	21.30 ± 1.20	Interface/adhesive	92.45 ± 0.05
GPS	22.63 ± 0.29	adhesive	98.22 ± 0.01
CAE	21.10 ± 1.60	adhesive	91.58 ± 0.07

σ_{max} = P/cross section area of adherend
$UTS_{Al\text{-}alloy}$ = ultimate tensile strength of aluminium alloy adherend
Al-alloy = 'L157' (T6)

5.2.6 Single hybrid scarf joint (t_{st} = 0.15mm, 'L156' T4) [Al-alloy/CFRP]

Aluminium alloy/CFRP hybrid scarf joints were produced in a similar manner as the scarf aluminium alloy joints, see Figure 3.6. The manufacturing procedure for the CFRP composite and the bonding procedures were given in sections 3.2.3 and 3.4, respectively. Since the GPS and CAE surface treated aluminium alloy joints discussed above did not

show any significant differences in the failure loads or failure loci of the joints, the use of the CAE surface treatment was excluded from these studies.

The difference in the thermal expansion coefficient of the aluminium alloy and the CFRP composite resulted in a 'bowed' joint after the curing of the adhesive (at 120°C), see Figure 5.5. Figure 5.6 compares the failure load of the hybrid joints using the GBD and GPS surface treatments. As found in the above studies, the failure load of the GPS treated joints is relatively high compared to the GBD treated joints. It can be seen that, by comparing Figures 5.3 and 5.6, the failure loads of the single hybrid joints are relatively low compared to the aluminium alloy joints (see section 5.2.4). Both the GBD and GPS surface treated hybrid joints failed at the adhesive/aluminium alloy adherend interface with a small amount of tearing in the composite. Table 5.6 summarises the failure loads and failure loci of this joint design. It was observed that crack initiation occurs at the CFRP scarf tip face and propagates towards the aluminium alloy scarf tip. This is due to the relatively high stress concentration in the adhesive, at the CFRP scarf tip, compared to the stress concentration in the adhesive at the Al-alloy scarf tip, see Figure 5.5.

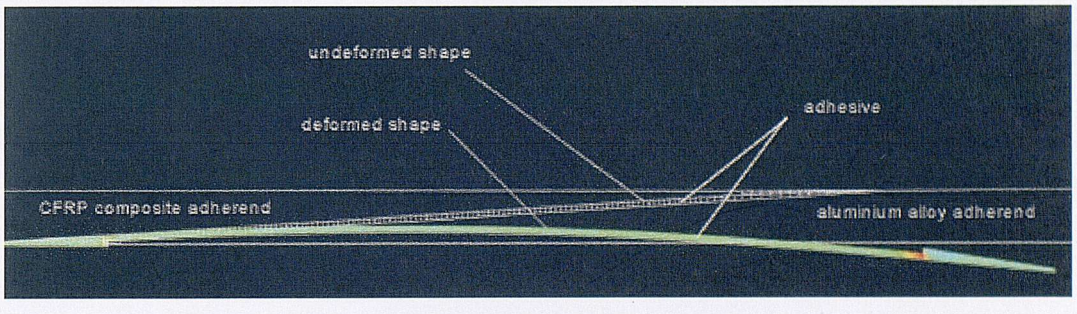


Figure 5.5: Finite element analysis of the aluminium alloy/CFRP hybrid scarf joint. The outline diagram is the undeformed shape while the deformed shape is represented by the adhesive (in colour)

**Note: Stress concentration regions are indicated by the colours red (highest stress concentration) and orange/yellow*

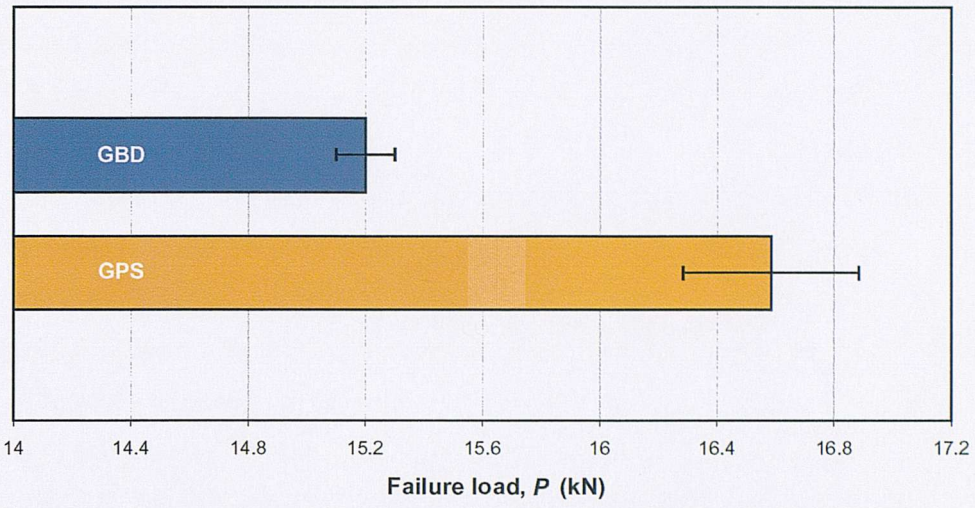


Figure 5.6: Comparison of the static strength of GBD and GPS surface treated CFRP/'L156' (T4) aluminium alloy hybrid scarf joints

Table 5.6: Summary of the comparison of the failure loads and failure loci of single hybrid CFRP/'L156' (T4) aluminium alloy scarf joints for different surface treatments

Surface treatments	Average failure load, P(kN)	Failure locus	Joint efficiency $\sigma_{max}/UTS_{Al\text{-}alloy}$ (%)
GBD	15.20 ± 0.10	Interface	71.97± 0.01
GPS	16.60 ± 0.30	Interface	78.60± 0.01

σ_{max} = P/cross section area of adherend
$UTS_{Al\text{-}alloy}$ = ultimate tensile strength of aluminium alloy adherend
Al-alloy = 'L156' (T4)

5.2.7 Double hybrid scarf joint (t_{st} = 0.15mm, 'L157' T6) [Al-alloy/CFRP]

It has been shown in the previous section that the single hybrid scarf joints were bowed after curing of the adhesive. This is due to the different thermal expansion coefficient of the aluminium alloy adherend and the CFRP composite adherend. A way of rectifying this is to use a symmetrical joint design (see section 2.8.2.2). Hence, the double hybrid scarf joint was produced. This joint was produced by adhesively bonding two single hybrid scarf joints back-to-back, with the CFRP composite adherend positioned at the outer surface of the joint, see Figure 3.5d and 5.8b.

Figure 5.7 compares the failure loads of the double hybrid scarf joints using the three surface treatments (i.e. the GBD, GPS and CAE treatments). It can be seen from the data that no significant differences in the failure loads were recorded and all the joints failed with a mixture of adhesive and composite failure. However, the failure loads are

extremely high. The average failure load for this joint design is approximately 44kN. Clearly, this is more than twice the failure load of the single hybrid scarf joint model, see section 5.2.6.

The reason for this is suggested to arise from the high rigidity and fracture stress of the composite adherend. In order to explain this observation, double hybrid scarf joints with the aluminium alloy adherend positioned at the outer surface of the joint were produced, see Figure 5.8a. Considering the double hybrid scarf joint with the aluminium alloy adherend positioned at the outer surface of the bond, a crack initiates at the aluminium alloy scarf tip face and grows into the effective bond length (i.e. in the adhesive). The 'released' adherend will bow out in an attempt to open up the crack. This allows the crack to propagate the length of the effective bond if the CFRP composite adherend is able to sustain the applied load, see Figure 5.8c. On the other hand, if the 'released' adherend is made of CFRP composite, see Figure 5.8b, it will not open up as much as the aluminium alloy adherend because of the higher rigidity of the CFRP composite, see Figure 5.8d. This forces high direct stresses into the CFRP adherend. As a result, CFRP composite failure will accompany adhesive failure, see Figure 5.8d. The high fracture stress of the CFRP composite allows the failure load to increase above the expected failure load (i.e. double of the single hybrid scarf joint). A summary of the failure loads and failure loci of the double hybrid scarf joints using the three different surface treatments are given in Table 5.7.

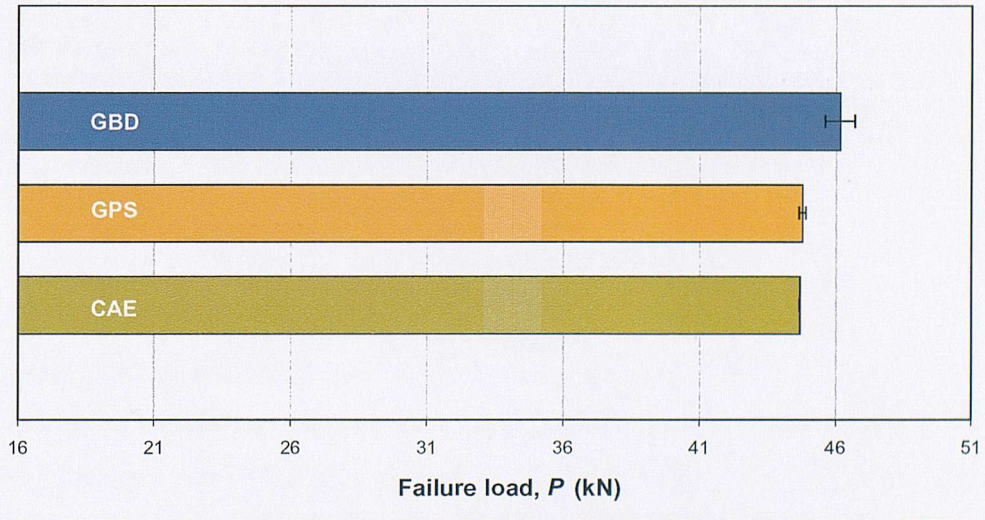


Figure 5.7: Comparison of the static failure loads of 'L157' (T6) aluminium alloy/CFRP double scarf joints for different surface treatments

Table 5.7: Summary of the comparison of the failure loads and failure loci of 'L157' (T6) aluminium alloy/CFRP double hybrid scarf joints for different surface treatments

Surface treatments	Average failure load, P(kN)	Failure locus	Joint efficiency $\sigma_{max}/UTS_{Al\text{-}alloy}$ (%)
GBD	44.18 ± 0.54	adhesive/CFRP	100.00 ± 0.01
GPS	44.78 ± 0.14	adhesive/CFRP	97.18± 0.00
CAE	44.69 ± 0.01	adhesive/CFRP	96.98± 0.00

? $_{max}$ = P/cross section area of adherend
$UTS_{Al\text{-}alloy}$ = ultimate tensile strength of aluminium alloy adherend
Al-alloy = 'L157' (T6)

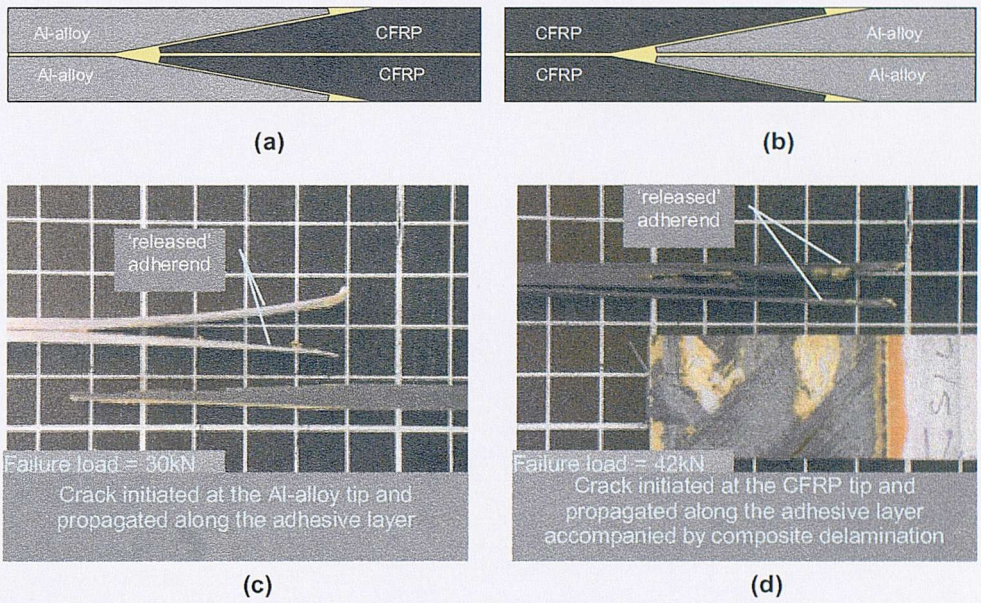


Figure 5.8: Pictures showing the (a) double hybrid scarf joint with the aluminium alloy adherends positioned at the outer surface of the joint, (b) double hybrid scarf joint design with the CFRP adherends positioned at the outer surface of the joint, (c) bending of the 'released' adherend (aluminium alloy) and crack propagation in the adhesive layer and (d) non-bending of the 'released' adherend (CFRP composite) and failure in adhesive and composite

5.2.8 Comparison of Joint Designs

Monotonically-loaded tests of the effect of surface treatments on various joint designs have been presented in the previous six sections. Table 5.8 summarises the failure loads, failure loci and joint efficiencies of the various joint designs and different surface treatments. It can be seen from Table 5.8, that the effect of surface treatment on the monotonically-loaded strength of adhesive joints affects the failure loci of the joints.

It can be seen that a difference in the monotonically-loaded strength of adhesive joints is only present when there is a distinct difference in the failure locus of the different surface treated joints (i.e. the scarf joint designs with a scarf tip thickness of t_{st} = 0.15mm and 'L156' (T4) and 'L157' (T6) aluminium alloy adherends, see Table 5.8).

Table 5.8: Summary of the failure loads, failure loci and joint efficiencies of the various joint designs employed in the present project tested under monotonically-loaded test conditions for different surface treatments

Joint Designs	GBD			GPS			CAE		
	P (kN)	Failure locus	ζ (%)	P (kN)	Failure locus	ζ (%)	P (kN)	Failure locus	ζ (%)
Scarf joint, t_{st} = 0.4mm 'L157' (T6) [Al-alloy/Al-alloy]	18.15 ± 0.57	Ad	78.78 ± 0.02	18.70 ± 0.10	A	81.16 ± 0.00	18.00 ± 0.46	A	78.13 ± 0.02
Scarf joint, t_{st} = 0.15mm 'L157' (T6) [Al-alloy/Al-alloy]	20.35 ± 0.21	I	88.32 ± 0.01	21.60 ± 0.16	A	93.75 ± 0.01	21.20 ± 0.20	A	92.01 ± 0.01
Scarf joint, t_{st} = 0.15mm 'L156' (T4) [Al-alloy/Al-alloy]	16.38 ± 0.32	I	77.56 ± 0.01	18.38 ± 0.38	Ad	87.03 ± 0.01	18.12 ± 0.22	Ad	85.80 ± 0.01
Overlap joint, 'L157' (T6) [Al-alloy/Al-alloy]	21.30 ± 1.20	I/Ad	92.45 ± 0.05	22.63 ± 0.29	Ad	98.22 ± 0.01	21.10 ± 1.60	Ad	91.58 ± 0.07
Single hybrid scarf joint, t_{st} = 0.15mm 'L156' (T4) [CFRP/ Al-alloy]	15.20 ± 0.10	I	71.97 ± 0.01	16.60 ± 0.30	I	78.60 ± 0.01	-	-	-
Double hybrid scarf joint*, t_{st} = 0.15mm 'L157' (T6) [CFRP /Al-alloy]	46.18 ± 0.54	Ad/ CFRP	100.00 ± 0.01	44.78 ± 0.14	Ad/ CFRP	97.18 ± 0.00	44.69 ± 0.01	Ad/ CFRP	96.98 ± 0.00

σ_{max} = P/cross section area of adherend
$UTS_{Al\text{-}alloy}$ = ultimate tensile strength of aluminium alloy adherend
$\zeta = \sigma_{max} / UTS_{Al\text{-}alloy}$ = joint efficiency
P = Average failure load
I = Interface failure
Ad = adhesive failure (i.e. cohesive failure)
A = adherend failure
I/Ad = interface/adhesive failure
Ad/CFRP = adhesive/CFRP failure
* Double hybrid scarf joint design with CFRP composite adherend positioned at the outer surface of the joint, see Figure 5.8b.

5.3 Constant amplitude 'dry' fatigue tests

5.3.1 Introduction

Results from the 'dry' fatigue coupon tests will be presented in the present section. The experimental procedure for this test was given in section 3.5.3.1. Two joint designs were used in this investigation, (a) aluminium alloy scarf joints with a scarf tip thickness of t_{st}

= 0.4mm and (b) aluminium alloy scarf joints with a scarf tip thickness of t_{st} = 0.15mm. The reason that only these two joint designs were tested in 'dry' fatigue will become apparent in the following sections, see section 5.3.2 and 5.3.3, where the majority of the joints from both types of joint designs were found to fail in the adherend.

5.3.2 Scarf joint (t_{st} = 0.4mm) [Al-alloy/Al-alloy]

Before concentrating on the optimized scarf joint design, as shown in Chapter Four, a few tests were carried out using the scarf joint design with a scarf tip thickness of t_{st} = 0.4mm. This scarf joint model has been used previously in this project to investigate the effect of the scarf tip thickness (see section 4.5) and the effect of surface treatment on the static joint strength (see section 5.2.2). In this section, results from 'dry' fatigue tests using this joint design will be presented. Figure 5.9 compares the fatigue performance of this joint design for different surface treatments. The fatigue threshold stress is approximately 90.6 ± 16.3MPa, and this represents 21% of the average static strength of this joint design.

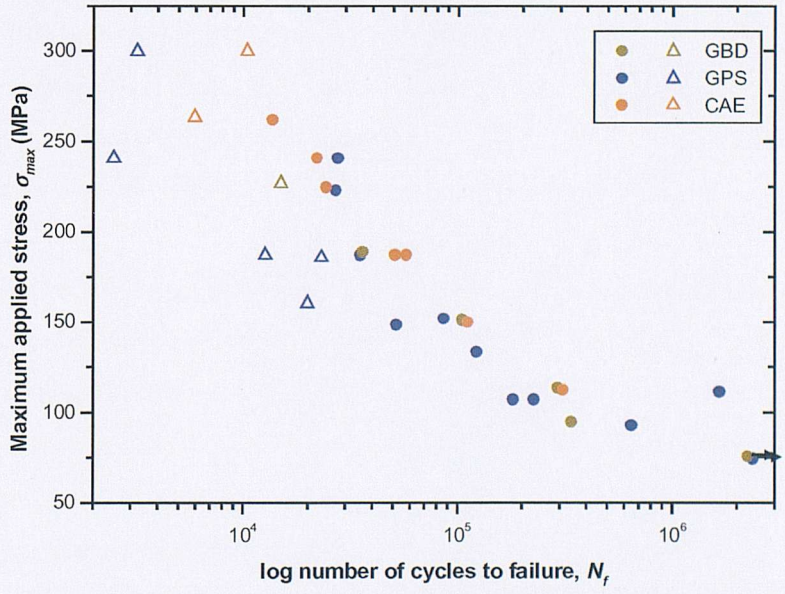


Figure 5.9: Comparison of the fatigue performance of aluminium alloy scarf joints with a scarf tip thickness of t_{st} = 0.4mm for different surface treatments

Note: 1. Arrow denotes specimens that did not fail
2. All open triangles denote adhesive failure
3. All filled circles denote adherend failure

Most of the joints failed in the adherend and failure occurred just outside the effective bond length, see Figure 5.10. However, at higher applied loads, it was found that

some of the joints failed in the adhesive, see Figure 5.9. From the relatively high standard deviation in the static test results of this batch of tests, it can be concluded that the surface treatment on some of the joints was improperly undertaken. Nevertheless, no significant difference in the fatigue threshold was observed for the different surface treatments.

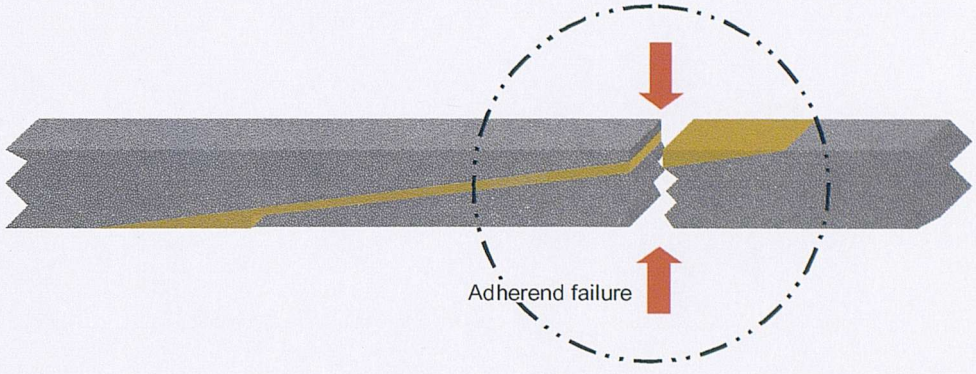


Figure 5.10: Schematic diagram of the adherend failure locus observed in fatigue tests

5.3.3 Scarf joint (t_{st} = 0.15mm) [Al-alloy/Al-alloy]

This joint design represents the optimized joint design as discussed in Chapter Four. Both 'L156' (T4) and 'L157' (T6) aluminium alloy adherends were used in this design. However, the different temper grades of the aluminium alloy adherends do not significantly affect the fatigue performance of the joints as different temper grades only affect the post-yield behaviour of the aluminium alloy, see section 4.8.

Figure 5.11 compares the fatigue performance of this joint design for the three different surface treatments. It can be seen that there is no significant difference in the fatigue performance of these joints. This is because all the joints failed in the adherend and the failure locus of these joints was similar to that shown in Figure 5.10. It can be seen from Figure 5.11 that the fatigue threshold for this joint design is 103.5 ± 17.2MPa. Comparing the data shown in Figure 5.9 with Figure 5.11, it can be seen that the reduction of the scarf tip thickness from t_{st} = 0.4mm to t_{st} = 0.15mm increased the fatigue threshold by approximately 14%. Interestingly, the increase in the static joint strength of these two joint designs was observed to be 18% (see section 4.5.5).

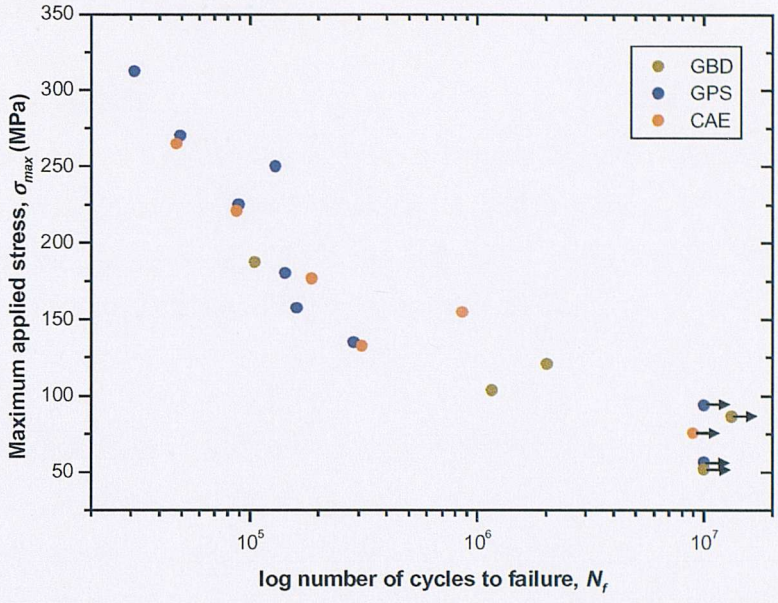


Figure 5.11: Comparison of the fatigue performance of aluminium alloy scarf joints with a scarf tip thickness of t_{st} = 0.15mm for different surface treatments

Note: 1. Arrow denotes specimens that did not fail
2. All filled circles denote adherend failure

5.3.4 Comparison of joint designs

Aluminium alloy scarf joints with a scarf tip thickness of t_{st} = 0.4mm and 0.15mm were tested under 'dry' fatigue test conditions. Table 5.9 compares the fatigue threshold values and failure locus of these joints.

Table 5.9: Summary of the fatigue thresholds and failure loci of the scarf joint designs with a scarf tip thickness of t_{st} = 0.4mm and 0.15mm tested in 'dry' fatigue conditions for different surface treatments

Joint Designs	GBD		GPS		CAE	
	σ_{thres} (MPa)	Threshold failure locus	σ_{thres} (MPa)	Threshold failure locus	σ_{thres} (MPa)	Threshold failure locus
Scarf joint, t_{st} = 0.4mm [Al-alloy/Al-alloy]	90.6 ± 16.3	A	90.6 ± 16.3	A	90.6 ± 16.3	A
Scarf joint, t_{st} = 0.15mm [Al-alloy/Al-alloy]	103.5 ± 17.2	A	103.5 ± 17.2	A	103.5 ± 17.2	A

σ_{thres} = Fatigue threshold (MPa)
A = adherend failure

**Note: σ_{th} was calculated by taking the average of the lowest data point for the 'failed' specimens and the highest data point for the specimens that did not fail*

5.4 Constant amplitude 'hot/wet' durability tests

5.4.1 Introduction

As mentioned in Chapter One, a main aim of the current project is to compare the durability of GPS surface treated aluminium alloy joints with GBD surface treated aluminium alloy joints. In this section, results from the cyclic fatigue 'hot/wet' tests will be presented. The experimental procedures for these tests were given in section 3.5.3.2.

5.4.2 Scarf joint (t_{st} = 0.4mm) [Al-alloy/Al-alloy]

As for the monotonically-loaded tests (see section 5.2) and the 'dry' fatigue tests (see section 5.3), a few 'hot/wet' fatigue tests were carried out using scarf joints with a scarf tip thickness of t_{st} = 0.4mm, before concentrating on the optimized scarf joint design (i.e. a scarf joint with a scarf tip thickness of t_{st} = 0.15mm).

Figure 5.12 compares the durability of this scarf joint design using the GBD and GPS surface treatments. It can be seen that the fatigue threshold of the GBD surface treated joints is relatively low when compared to the GPS treated joints. The estimated fatigue threshold of the GBD surface treated joints is approximately 37.5 ± 12.5MPa. This corresponds to 10% of the average static strength of this joint design. The GPS surface treated joints failed in the adherend, similar to the failure locus shown in Figure 5.10, and the fatigue threshold was 90.6 ± 16.3MPa, which corresponds to 24% of the average static strength for this joint design. The poorer performance of the former joint design was due to the GBD treated joints failing at the adhesive/adherend interface. It was observed that a crack grew from one end of the joint and propagated the entire length of the bond, towards the other end of the joint subsequently causing final fracture of the joint.

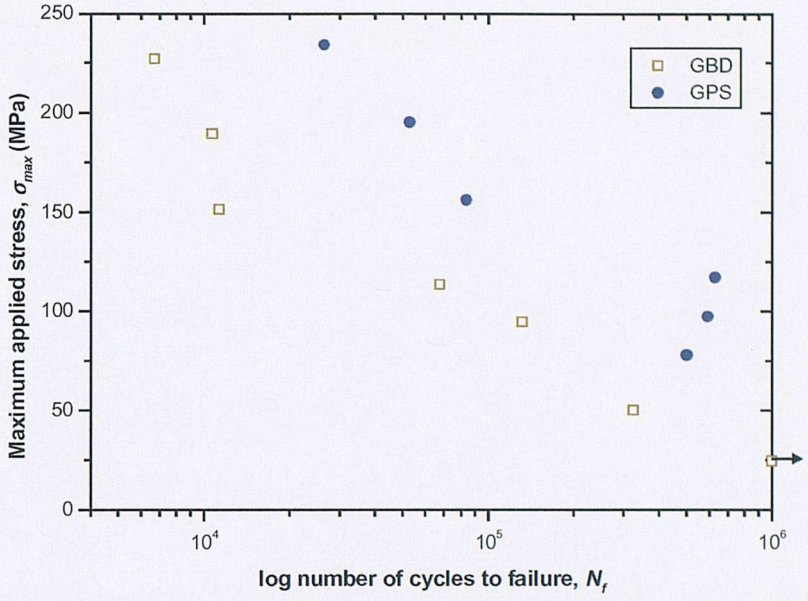


Figure 5.12: Comparison of the 'hot/wet' durability performance of aluminium alloy scarf joints with a scarf tip thickness of t_{st} = 0.4mm for GBD and GPS surface treatments

Note: 1. Arrow denotes specimens that did not fail
2. All open squares denote interfacial failure
3. All filled circles denote adherend failure

In order to observe the effect of water on the fatigue performance of these joints, the durability test results were compared with the 'dry' fatigue test results, see Figure 5.13. It can be observed from this figure that the GPS surface treated joints were not significantly affected by the presence of water. In fact, all the GPS surface treated joints (in 'dry' and 'hot/wet' conditions) failed in the adherend. However, it was observed that, in the presence of water, the GBD treated joints failed in the adhesive/adherend interface. On the other hand, in 'dry' fatigue conditions, the GBD surface treated joints failed in the adherend. The estimated reduction in the fatigue threshold for the GBD surface treated joints tested in the 'hot/wet' condition is about 40% of the fatigue threshold in the 'dry' test condition. The results clearly show, that in the presence of water, the GBD surface treated joints experience a reduction in performance. This is caused by the instability of the adhesive/adherend interface in the presence of water, see Table 2.5.

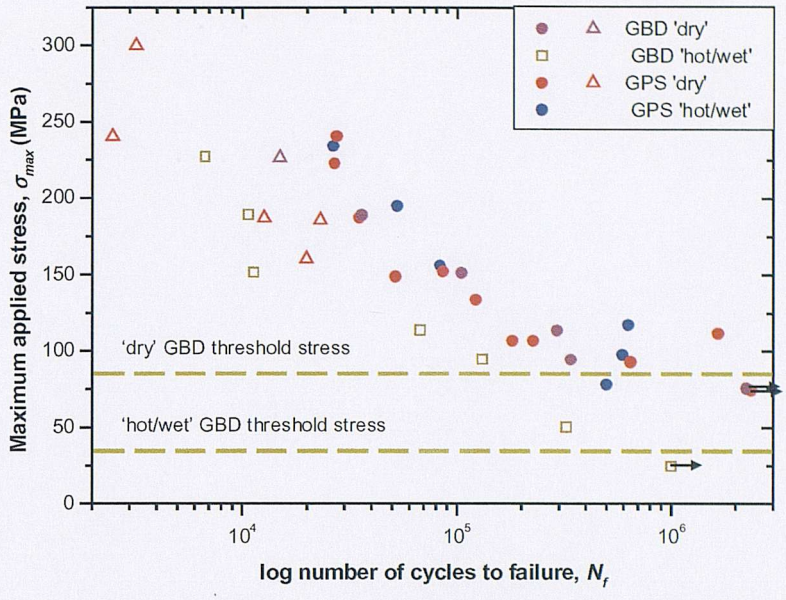


Figure 5.13: Comparison of the 'dry' and 'hot/wet' fatigue performance of aluminium alloy scarf joints with a scarf tip thickness of t_{st} = 0.4mm for the GBD and GPS surface treatments

Note: 1. Arrow denotes specimens that did not fail
2. All open triangles denote adhesive failure
3. All filled circles denote adherend failure
4. All open squares denote interfacial failure

5.4.3 Scarf joint (t_{st} = 0.15mm) [Al-alloy/Al-alloy]

Figure 5.14 compares the durability performance of aluminium alloy scarf joints with a scarf tip thickness of t_{st} = 0.15mm. It can be seen that the fatigue performance of the GBD surface treated joints is significantly inferior when compared to the GPS treated joints. Furthermore, the GBD surface treated joints all failed at the adhesive/adherend interface, see Figure 5.15. On the other hand, the GPS surface treated joints failed in the adherend, similar to the failure locus shown in Figure 5.10, and has similar fatigue strength as those tested in the 'dry' test condition. This observation is similar to that found in the previous investigation of the aluminium alloy scarf joints but with a scarf tip thickness of t_{st} = 0.4mm. The estimated fatigue threshold of the GBD surface treated joints is 42.5 ± 8.8MPa. This is a 12% increase in the fatigue threshold compared to the GBD treated aluminium alloy scarf joints with a scarf tip thickness of t_{st} = 0.4mm. Again, this increase in fatigue strength of the scarf joints with a scarf tip thickness of t_{st} = 0.15mm is similar to that observed in the 'dry' tests, see section 5.3.3.

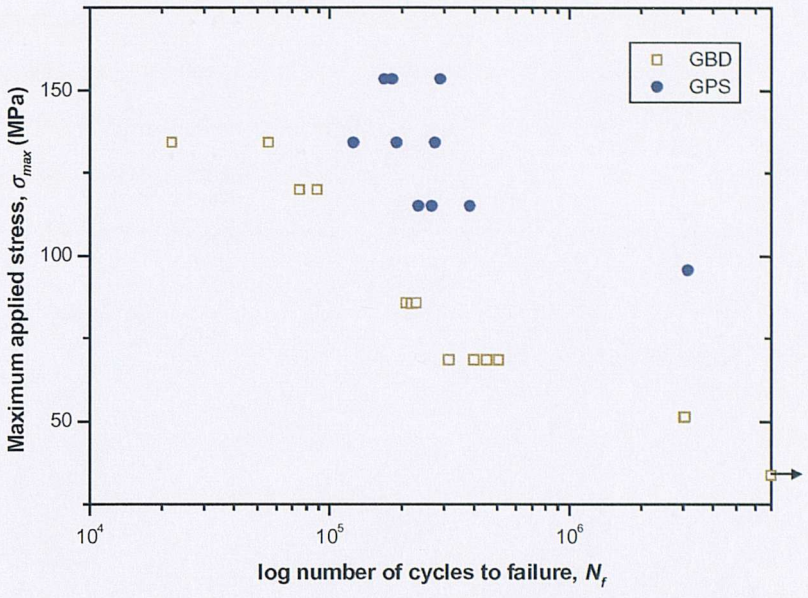


Figure 5.14: Comparison of the 'hot/wet' durability performance of aluminium alloy scarf joints with a scarf tip thickness of t_{st} = 0.15mm for GBD and GPS surface treatments

Note: 1. Arrow denotes specimens that did not fail
2. All open squares denote interfacial failure
3. All filled circles denote adherend failure



Figure 5.15: Typical fracture surface of GBD surface treated aluminium alloy scarf joints tested in 'hot/wet' fatigue conditions

The 'hot/wet' test results were compared with the 'dry' fatigue test results to quantify the effect of moisture on the fatigue performance of this scarf joint design, see Figure 5.16. It can be seen from this figure that the GBD surface treated joints tested in 'hot/wet' test conditions have a lower fatigue threshold compared to the tests carried out in the 'dry' test condition. This reduction in fatigue threshold is estimated to be about 40% of the fatigue threshold in the 'dry' test condition. Again, this is similar to the decrease in the fatigue threshold observed for the aluminium alloy scarf joints but with a

scarf tip thickness of t_{st} = 0.4mm. However, for the GPS treated joints, no significant reduction in the fatigue strength of these joints were observed for the 'dry' and 'hot/wet' test conditions. In fact, all the GPS treated joints tested in both the 'dry' and 'hot/wet' test conditions failed in the aluminium alloy adherend.

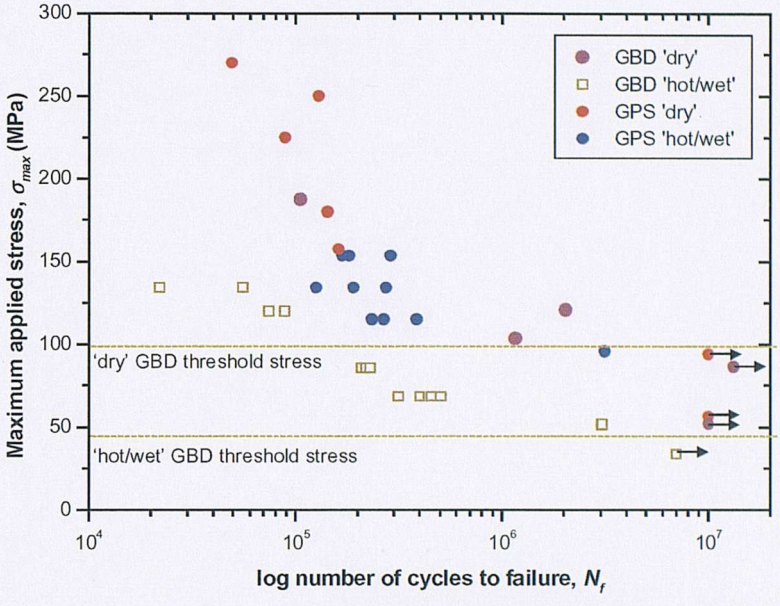


Figure 5.16: Comparison of the 'dry' and 'hot/wet' fatigue performance of aluminium alloy scarf joints with a scarf tip thickness of t_{st} = 0.15mm for the GBD and GPS surface treatments

Note: 1. Arrow denotes specimens that did not fail
2. All open squares denote interfacial failure
3. All filled circles denote adherend failure

5.4.4 Overlap joint [Al-alloy/Al-alloy]

This joint design was initially used to compare with the scarf joint design (see section 4.6). A few tests were also carried out to investigate the effect of surface treatment on the durability of this joint design. Figure 5.17 compares the durability of the aluminium alloy overlap joints for the GBD and GPS surface treatments. The figure also shows results from 'dry' fatigue tests. It can be seen that the GBD surface treated joints are inferior compared to the GPS surface treated joints. The GBD surface treated joints all failed at the adhesive/adherend interface, see Figure 5.18a. On the other hand, the GPS surface treated joints failed with a mixture of adhesive and interfacial failure, see Figure 5.18b. Interestingly, cracks initiated from both ends of the overlap region. This observation was also reported by Little [56]. At the same time as this project was being undertaken,

Underhill [82] produced experimental results that compared the durability of GBD and GPS surface treated overlap joints. He also showed that the GBD surface treated joints were inferior compared to the GPS surface treated joints. However, due to time restrictions, no further experiments were carried out using this joint design.

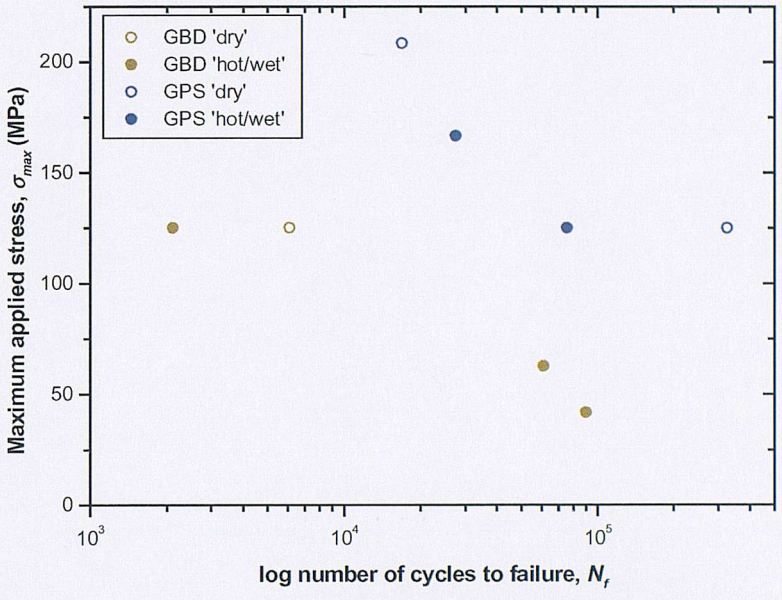


Figure 5.17: Comparison of the fatigue strength of GBD and GPS surface treated aluminium alloy overlap joints

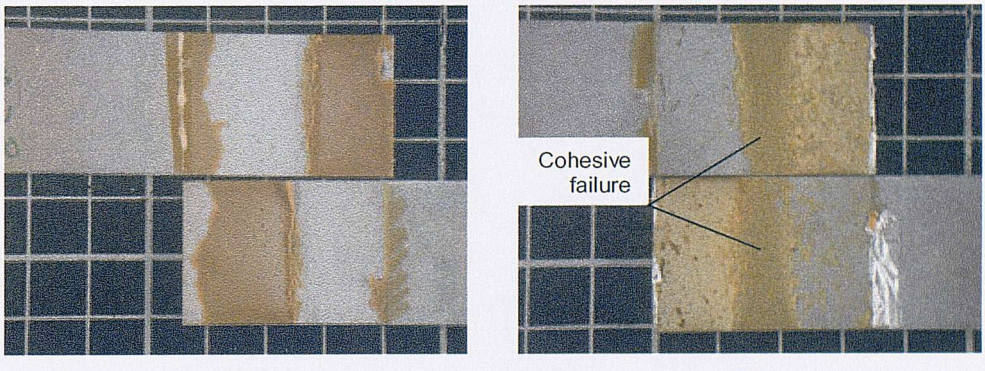


Figure 5.18: Typical fracture surface of (a) GBD surface treated aluminium alloy overlap joints and (b) GPS surface treated aluminium alloy overlap joints tested in 'hot/wet' fatigue conditions

5.4.5 Single hybrid scarf joint (t_{st} = 0.15mm) [Al-alloy/CFRP]

The aluminium alloy/CFRP hybrid scarf joints were produced to investigate the effectiveness of bonding CFRP composite to aluminium alloy. Results from the

monotonically tests were given in section 5.2.6. It was observed that the coupon specimens were bowed after the curing of the adhesive. This is due to the difference in thermal expansion coefficients of the composite and the aluminium alloy adherends. Nevertheless, the joints were tested in 'hot/wet' fatigue conditions and the results are presented in Figure 5.19.

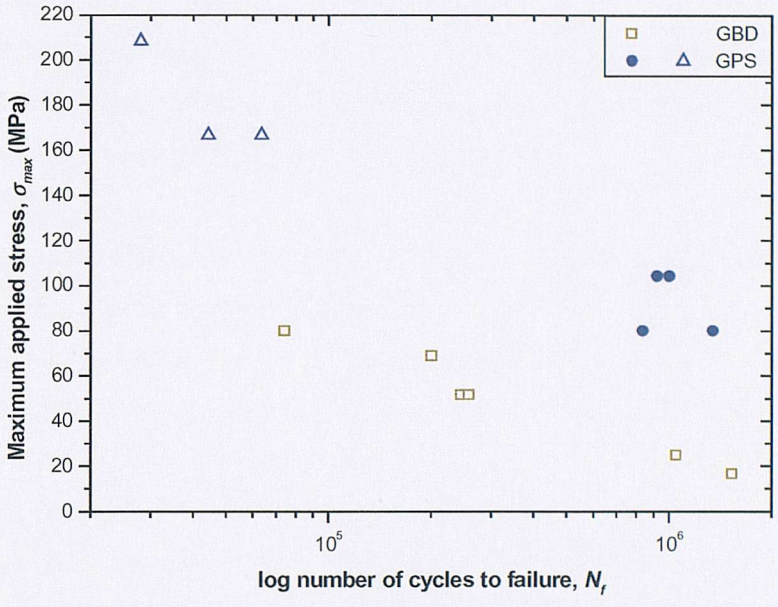


Figure 5.19: Comparison of the 'hot/wet' fatigue performance of aluminium alloy/CFRP hybrid scarf joints with a scarf tip thickness of t_{st} = 0.15mm for the GBD and GPS surface treatments

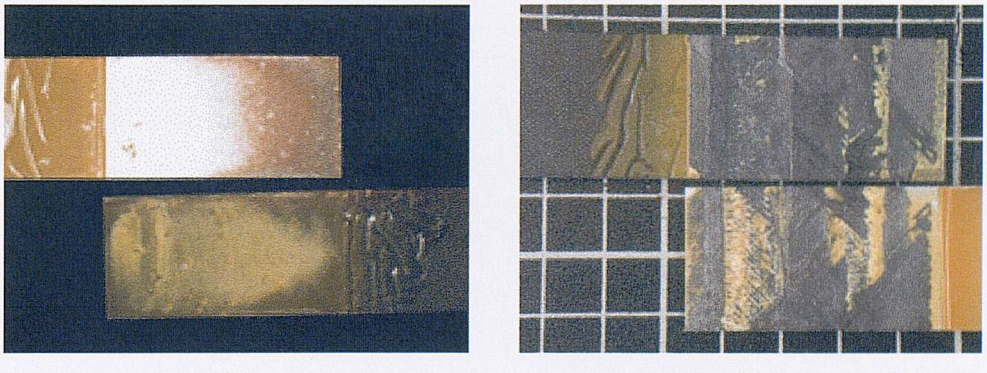
Note: 1. All open squares denote interfacial failure
2. All open triangles denote adhesive failure
3. All filled circles denote adherend failure

Figure 5.19 compares the durability of the GBD and GPS surface treated hybrid scarf joints. It should be noted that throughout this investigation, the composite adherends were surface treated using the GBD surface treatment. From Figure 5.19, it may be observed that the durability of the GBD surface treated joints is inferior compared to the GPS surface treated joints. In fact, the longest test carried out on a GBD surface treated joint was for 1.5 million cycles at a maximum applied stress of 16.7MPa. This applied stress is less than 50% of the estimated fatigue threshold for the aluminium alloy scarf joint model with a scarf tip thickness of t_{st} = 0.15mm, see section 5.4.3. Thus, this clearly shows the effect of the thermal residual stress, arise from the curing of the adhesive at elevated temperatures, on the fatigue strength of the single hybrid joints and that this pre-

stress in the joint may become significant at low applied loads (i.e. near the fatigue threshold).

As observed in the above studies using aluminium alloy adherends, the GBD surface treated joints failed at the adhesive/aluminium alloy adherend interface, see Figure 5.20a. On the other hand, at low fatigue cycles, the GPS surface treated joints failed in the adhesive layer accompanied by some degree of composite failure, see Figure 5.20b. At high fatigue cycles, it was observed that the GPS surface treated joints failed in the aluminium alloy adherend, as shown in Figure 5.10.

It is interesting to note that the crack in the GBD surface treated joints initiated from the aluminium alloy scarf tip. This observation is in contrast to that observed from the monotonically-loaded tests where the crack in the joint was observed to initiate from the CFRP scarf tip end of the joint. The reason for this difference can be explained by the influence of moisture on the adhesive/aluminium alloy interface. In the monotonically-loaded tests, the joints were not subjected to significant moisture attack. Hence, failure in the joint initiated from the CFRP scarf tip where it was shown that the adhesive in this region is subjected to relatively high stress, see Figure 5.5. On the other hand, in the 'hot/wet' fatigue tests, the integrity of the GBD surface treated adhesive/aluminium alloy adherend interface was clearly adversely affected by the presence of water. This caused the crack to initiate from the aluminium alloy scarf tip.



(a) (b)

Figure 5.20: Fracture surface of (a) GBD and (b) GPS surface treated aluminium alloy/CFRP hybrid scarf joints tested in 'hot/wet' fatigue conditions

Figure 5.21 compares the durability performance of the aluminium alloy scarf joints with the aluminium alloy/CFRP hybrid scarf joints (i.e. both joint designs with a scarf tip thickness of t_{st} = 0.15mm). It can be seen that the fatigue performance of the GBD surface treated aluminium alloy/CFRP hybrid scarf joints is inferior compared to that of the GBD surface treated aluminium alloy scarf joints. On the other hand, the fatigue performance of the GPS surface treated joints appears to be unchanged. The reduction of the durability performance observed for the GBD surface treated hybrid joints can be attributed to the effect of residual thermal stresses in the joints. This will be discussed further in the next chapter where the effect of the residual thermal stresses in the hybrid joints is discussed.

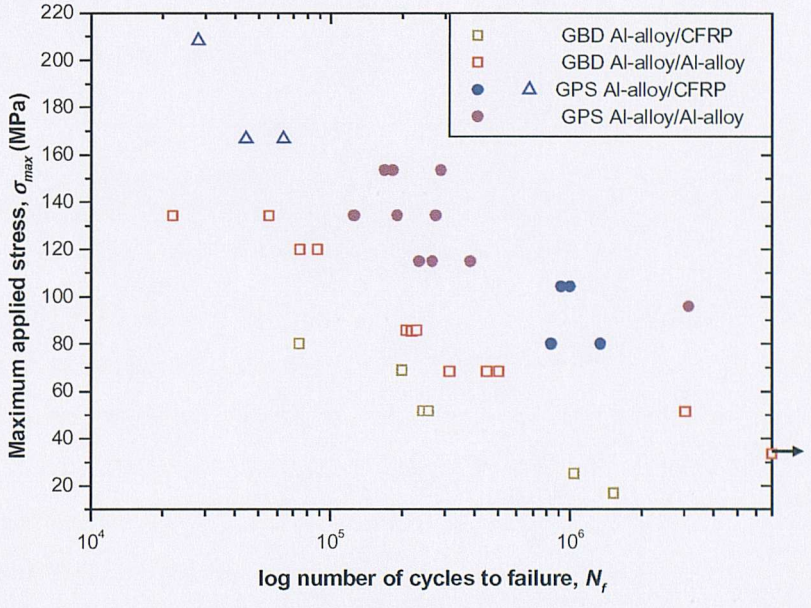


Figure 5.21: Comparison of the 'hot/wet' fatigue performance of aluminium alloy scarf joints and aluminium alloy/CFRP scarf joints with a scarf tip thickness of t_{st} = 0.15mm for GBD and GPS surface treatments

Note: 1. Arrow denotes specimens that did not fail
2. All open triangles denote adhesive failure
3. All filled circles denote adherend failure
4. All open squares denote interfacial failure

5.4.6 Double hybrid scarf joint (t_{st} = 0.15mm) [Al-alloy/CFRP]

Double hybrid scarf joints were used in this project to bond aluminium alloy adherends to CFRP composite adherends. The use of this symmetrical joint design eliminates the problem of bowed joints as seen from the single aluminium alloy/CFRP hybrid joints. It

was shown in section 5.2.7 that this joint design failed in the adhesive accompanied by composite failure when tested in monotonically-loaded tests.

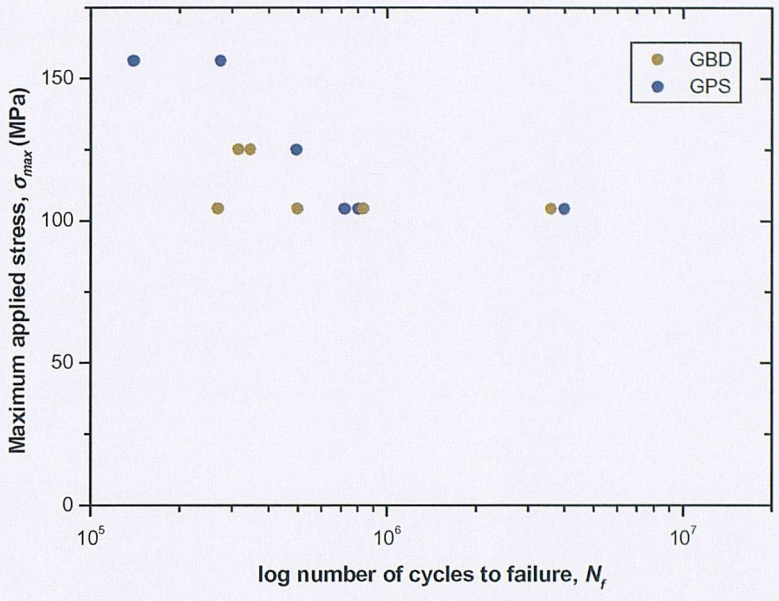


Figure 5.22: Durability performance of GBD and GPS surface treated double aluminium alloy/CFRP hybrid scarf joints with a scarf tip thickness of t_{st} = 0.15mm

Note: All filled circles denote adherend failure

Figure 5.22 shows the durability performance of this joint design tested in 'hot/wet' fatigue test conditions. It was observed that all the joints tested failed in the aluminium alloy adherend, outside the bonded region. This indicates that even in the presence of water, the effect of surface treatment is rendered insignificant by the presence of very high stress concentrations in the aluminium alloy adherend. The high stress concentrations at the terminus of the bonded region, similar to those seen in the single scarf joint designs in Chapter Four, is especially high in this double hybrid scarf joint design where the CFRP composite adherends were positioned at the outer surface of the bond. As mentioned in section 5.2.7, when loaded monotonically to failure, this arrangement caused the joints to fail in the adhesive accompanied by CFRP composite failure. In cycle fatigue test conditions, these stress concentrations apparently caused the aluminium alloy adherend to fail instead. The reason for this observation could be explained by the relatively low applied loads which thus do not allow the aluminium alloy adherend to yield and transfer much of the stresses into the bonded region and the CFRP composite adherends. It is noted that this observation is in contrast to all the results presented in the previous sections using unsymmetrical joint designs (see sections 5.4.2-

5.4.5). Finite element analysis of the fatigue strength and failure loci of this joint design will be further discussed in section 6.4.2.3.

5.4.7 Comparison of joint designs

Fatigue tests in 'hot/wet' conditions were performed on a number of joint designs, see section 5.4.2 – 5.4.6). Generally, it was observed that adhesive joints surface treated with the GBD surface treatment show a lower fatigue threshold compared to adhesive joints surface treated with the GPS surface treatment. This trend was observed for five out of the six joint designs employed in the present study, where only the double hybrid scarf joints did not appear to be affected by the different surface treatments of the joints. Table 5.10 summarises the fatigue threshold stress and failure locus of the various joint designs.

Table 5.10: Summary of the fatigue thresholds and failure loci of the joint designs tested in 'hot/wet' fatigue conditions for different surface treatments (taken at a number of fatigue cycles, N_f = 1 million cycles)

Joint Designs	GBD		GPS	
	σ_{thres} (MPa)	Threshold failure locus	σ_{thres} (MPa)	Threshold failure locus
Scarf joint, t_{st} = 0.4mm [Al-alloy/Al-alloy]	37.5 ± 12.5	I	90.6 ± 16.3	A
Scarf joint, t_{st} = 0.15mm[Al-alloy/Al-alloy]	42.5 ± 8.8	I	103.5 ± 17.2	A
Single hybrid scarf joint, t_{st} = 0.15mm [CFRP/Al-alloy]	25*	I	80*	A
Double hybrid scarf joint, t_{st} = 0.15mm [CFRP/Al-alloy]	108*	A	108*	A

σ_{thres} = Fatigue threshold (MPa)
A = Adherend failure
I = Interfacial failure
* Values without standard deviation because of a lack of experimental data

5.4.8 'Back face' strain gauging results

The fatigue results shown in the previous sections only considered the total life of the various adhesively-bonded joint designs. In this section, results of the 'back face' strain gauging technique are discussed. The 'back face' strain gauging technique has been discussed in section 3.5.3.3. This investigation was only carried out at the later stages of this project. Hence, the results presented here are incomplete. Nevertheless, the results indicate that the crack initiation period in the optimized scarf joint design is significant, especially in the low fatigue cycles region.

Figure 5.23 shows the typical strain gauge readings from a fatigue test carried out in 'hot/wet' fatigue test conditions where the GBD surface treated joints were found to fail at the adhesive/adherend interface. Due to time constraints, only the aluminium alloy scarf joint design with a scarf tip thickness of t_{st} = 0.15mm was used in this investigation. From Figure 5.23, it can be seen that before a crack is initiated, the strain gauge reading is constant. As a crack initiates and grows in the joint, the strain reading deviates from the essentially constant value and increases until total failure of the joint.

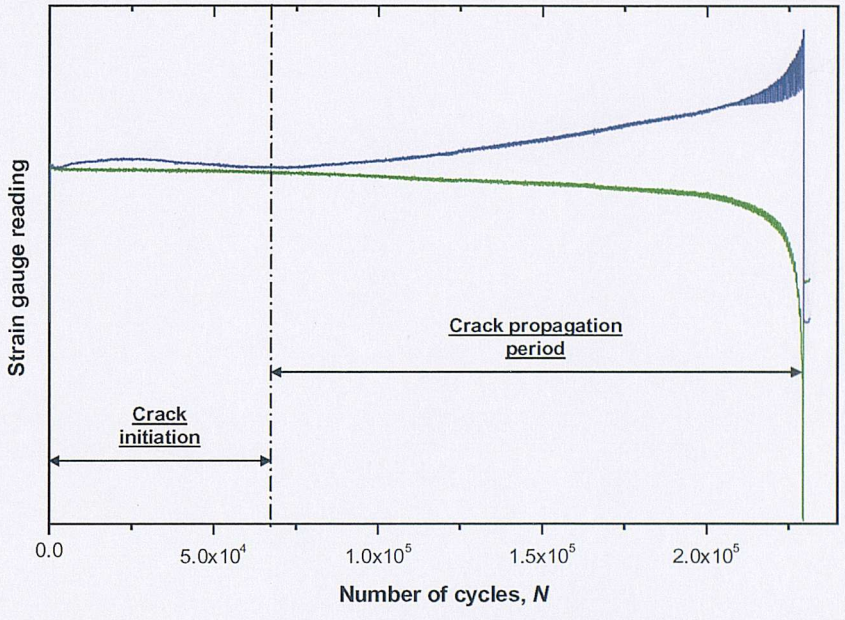


Figure 5.23: Typical strain gauge reading plot for an aluminium alloy scarf joint model with a scarf tip thickness, t_{st} = 0.15mm tested in 'hot/wet' fatigue conditions where failure was observed to be at the adhesive/adherend interface

Figure 5.24 compares the crack initiation period with the total fatigue life for aluminium alloy scarf joints with a scarf tip thickness of t_{st} = 0.15mm. It can be seen that as the applied load is increased, the percentage of the crack initiation period over the total fatigue life of the joints increases. This is expected as, higher the applied load, the lower is the resistance of the joint to crack propagation. It is interesting to note that the percentage of the crack initiation period is significant when compared to the crack propagation period. The results here show that the percentage of the crack initiation period for joints that have a fatigue life of 7 – 50 thousand cycles is approximately 35 ± 5%. This indicates that the prediction of the fatigue life-time using the modified Paris law

equation as discussed in section 2.7.3 would be conservative, as this method only predicts the crack propagation period of the joints. The prediction of the fatigue life-times of the scarf joint designs will be discussed in the next chapter.

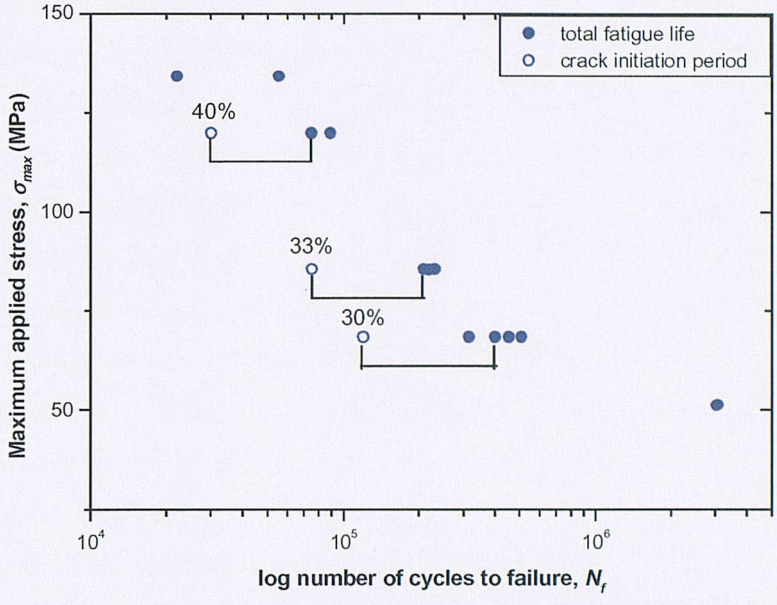


Figure 5.24: Comparison of the crack initiation period with the total fatigue life of GBD surface treated aluminium alloy scarf joints with a scarf tip thickness of t_{st} = 0.15mm tested in 'hot/wet' fatigue conditions

Note: The percentage is given for the crack initiation period and the brackets relates the data for the crack initiation period with the corresponding total fatigue life data

5.5 Chapter summary

1. The effect of surface treatments on the static and fatigue strength of adhesively-bonded joints was investigated. Aluminium alloy scarf joints and overlap joints, as well as CFRP/aluminium alloy hybrid single and double scarf joints, have been employed.

2. From the monotonically-loaded tests, it was found that the failure locus and failure loads of the joints depend not only on the surface treatment employed but also on the joint design and the material behaviour of the adherends. For all the joint designs investigated, it was found that the static failure loads and failure loci of the joints using GPS and CAE surface treatments are essentially the same. The GPS and CAE surface treated joints failed either in the adhesive or in the

aluminium alloy adherend. In addition, it was found that failure in the aluminium alloy adherend and in the adhesive both yielded approximately the same failure loads.

3. In the monotonically-loaded tests, the GBD surface treatment on aluminium alloy adherends can sometimes cause interfacial failure in the joint that results in a decrease in the joint strength (approximately 10% compared to the GPS and CAE surface treated joints). This was observed for three of the joint designs tested. They are (a) the aluminium alloy scarf joints with a scarf tip thickness of t_{st} = 0.15mm with aluminium alloy adherends 2014A 'L157' (T6) and (b) 'L156' (T4) and (c) the single CFRP/aluminium alloy hybrid scarf joints. On the other hand, the GBD surface treatment did not cause a significant difference to the joint strength or a change in the failure locus of (a) the aluminium alloy scarf joints with a scarf tip thickness of t_{st} = 0.4mm, (b) the aluminium alloy overlap joints and (c) the double CFRP/aluminium alloy hybrid scarf joints. From these results, it can be concluded that the GBD surface treatment causes a weak adhesive/adherend interface but this will only be apparent if the joint design and the adherend materials allow the interface to be subjected to relatively high stresses.

4. The static failure loads of the various joints tested in this investigation are relatively high when compared to the ultimate tensile strength of the aluminium alloy adherends. The highest joint efficiency recorded was in the region of 93%. This was observed for three joint designs: (a) the scarf joint design with a scarf tip thickness of t_{st} = 0.15mm and 'L157' (T6) aluminium alloy adherends, (b) the aluminium alloy overlap joint design and (c) the double CFRP/aluminium alloy hybrid scarf joint design.

5. The single CFRP/aluminium alloy hybrid joints were found to be 'bowed' after curing of the adhesive. This is caused by the different thermal expansion coefficients of the CFRP and aluminium alloy adherends. The failure loads of these hybrid joints were found to be lower, by approximately 3kN, compared to the aluminium alloy joints with the same geometrical design parameters.

6. Fatigue tests carried out in 'dry' test conditions were only undertaken for the aluminium alloy scarf joints with a scarf tip thickness of t_{st} = 0.4mm and t_{st} = 0.15mm. It was found that the joints mainly failed in the adherend, just outside the effective bond length. This indicates that the different surface treatments do not play a dominant part in determining the fatigue strength of these joints when tested in the 'dry' environment. It was found that the fatigue threshold of these joints is approximately 21% of the static strength of the joints.

7. Fatigue tests in 'hot/wet' test conditions were performed using all the different joint designs. For these tests, only the GBD and GPS surface treatments were used. It was found that the GBD treated joints often show a decrease in fatigue strength compared to the GPS treated joints. It was observed for four of the five joint designs tested that the GBD surface treatment caused the joints to fail at the adhesive/aluminium alloy adherend interface. Only for the double CFRP/aluminium alloy hybrid scarf joints did the different surface treatments show no effect on the durability of the joints. On the other hand, the GPS joints failed in the aluminium alloy adherend for all the various types of joint design.

8. Interfacial failure was observed for the GBD surface treated joints tested in the 'hot/wet' test conditions and this led to a significant reduction in the fatigue strength of these joints. It was found that the decrease in the fatigue threshold of the GBD treated joints tested in the 'hot/wet' test conditions was approximately 40% compared to the fatigue threshold of the 'dry' fatigue tests.

9. Residual thermal stress in the GBD treated single CFRP/aluminium alloy hybrid joints was clearly seen to affect the fatigue strength of the joints. However, this was not shown to significantly affect the fatigue strength of the GPS surface treated single hybrid joints. This is because the GPS surface treated joints failed in the aluminium alloy adherend. On the other hand, the GBD surface treated single hybrid joints failed at the adhesive/aluminium alloy interface. The longest test carried out on the GBD surface treated single hybrid joints lasted for 1.5 million cycles at a maximum applied stress of 16.5MPa. This is less than 50% of the observed fatigue threshold of the aluminium alloy scarf joints with the same geometrical parameters as the single hybrid joints. However, due to time

restrictions, no further tests were carried out to determine the fatigue threshold of this joint design.

10. The double CFRP/aluminium alloy hybrid scarf joints were also tested in 'hot/wet' fatigue conditions. However, it was found that, regardless of the surface treatment used for the aluminium alloy adherends, the joints failed at the aluminium alloy adherend. This is believed to be caused by the rigid CFRP composite adherend being positioned at the outer surface of the bond. This prevents crack initiation in the adhesive or at the adhesive/adherend interface. In addition, the alignment of the joint components of the double hybrid scarf joints proved to be difficult and any misalignment of the joint components could have caused the joints to be loaded in an unsymmetrical manner and hence caused the development of stress concentrations in the aluminium alloy adherend.

11. Results from the 'back-face' strain gauging technique used for the aluminium alloy scarf joints with a scarf tip thickness of t_{st} = 0.15mm indicated that the significance of the crack initiation period increases as the applied load is increased. It was also observed that for joints which failed between 7-50 thousand cycles, the percentage of the crack initiation period is about 35% of the total fatigue life of the joints.

CHAPTER 6

PREDICTION OF THE FATIGUE LIFE-TIME OF ADHESIVELY-BONDED JOINTS

6.1 Introduction

Adhesively-bonded joints in aerospace applications are often subjected to fatigue stresses. In the previous chapter, experimental results concerning the effects of surface treatments and joint design on the fatigue performance of adhesively-bonded joints have been presented. It was shown that different surface treatments and joint designs have a significant effect on the fatigue strength of the joints. Hence, it is important for design engineers to be able to predict the fatigue performance of various joint designs and adhesive systems. In the present chapter, predictions of the fatigue life-time of adhesively-bonded joints are discussed. It was shown in the previous chapter that adhesively-bonded joints could fail in the adhesive, at the adhesive/adherend interface or in the adherend. Hence, the prediction of the fatigue life-time of adhesively-bonded joints has to be able to consider these three different loci of failure, in order to predict accurately the behaviour of adhesively-bonded joints when subjected to fatigue conditions. The next two sections will discuss the methods used to predict these three failure loci. This is followed by the results from the predictions of the fatigue life-times of the adhesively-bonded joints.

The first joint design to be included in this investigation is the aluminium alloy scarf joint with a scarf tip thickness of t_{st} = 0.4mm. This joint design was also used in the geometrical optimization process of the scarf joint design as discussed in Chapter Four, see Table 4.3. This is followed by the results for the optimized aluminium alloy scarf joint design (i.e. with a scarf tip thickness of t_{st} = 0.15mm, see Table 4.3). The final two joint designs used in this investigation are the single and double CFRP/aluminium alloy hybrid scarf joints. Both of these joint designs use the geometrical properties of the optimized aluminium alloy scarf joint design, see sections 5.2.6 and 5.2.7. The production of the CFRP adherend and the CFRP/aluminium alloy hybrid joints were described in Chapter Three, see Figure 3.6. Below is a summary of the four joint designs used in the present investigation:

- Aluminium alloy single scarf joint with a scarf tip thickness of t_{st} = 0.4mm (see Table 4.3)
- Aluminium alloy single scarf joint with a scarf tip thickness of t_{st} = 0.15mm (i.e. optimized scarf joint design, see Table 4.3)
- CFRP/aluminium alloy single hybrid scarf joint design with a scarf tip thickness of t_{st} = 0.15mm (see section 5.2.6)
- CFRP/aluminium alloy double hybrid scarf joint design with a scarf tip thickness of t_{st} = 0.15mm (see section 5.2.7)

6.2 Prediction of adherend failure

It was observed in the previous chapter that most of the GPS treated joints failed in the adherend. This failure locus is shown in Figure 5.10. The same failure locus was also observed for GBD surface treated joints tested in 'dry' conditions. The reason for this mode of failure is clearly due to a stress concentration occurring in the adherend at the overlap terminus. This stress concentration is caused by the presence of the scarf tip and the associated change in stiffness of the joint before and after the scarf tip. Finite element results showed that this stress concentration in the adherend is sufficiently high to cause adherend failure in the static tests, see section 4.5.5 and Figure 4.18.

This stress concentration will also, of course, reduce the fatigue life-time of the aluminium alloy adherends. The stress concentration in the aluminium alloy adherend can

be calculated using finite element analysis, and the results for the four joint designs are given in Table 6.1. The fatigue strength, σ_{Sc}, of the aluminium alloy adherends may then be calculated by dividing the maximum applied stress, $\sigma_{Sc=1}$, from plain specimens, e.g. round bar specimens, where the stress concentration, S_c, is equal to unity, as obtained from the literature [83], by the predicted stress concentration of the joint designs used in the present project, see equation 6.1.

$$\sigma_{S_c} = \frac{\sigma_{S_c=1}}{S_c} \quad \text{.....(6.1)}$$

The effect of this stress concentration on the fatigue strength of the aluminium alloy adherend is shown in Figure 6.1. This method of predicting the fatigue strength of the aluminium alloy adherends is based on the assumption that the fatigue strength of aluminium alloy varies linearly with the stress concentration factor. In addition, it is assumed that the surface finish of the coupon joint specimens is of relatively good quality and that the deleterious effect of the surface flaws from machining the joints on the fatigue strength is negligible. Furthermore, it was found that there was a significantly large scatter (e.g. a range of number of cycles to failure, N_f, of 6 x 10^5 to 1000 x 10^5 for an applied stress of approximately 200MPa) in the fatigue strength of plain (i.e. round bar specimens) aluminium alloy specimens (S_c = 1) [83]. All these observations suggest that the current method of predicting the fatigue strength of the aluminium alloy adherends would only serve as a first approximation to the true fatigue strength of the aluminium alloy adherends.

The predicted stress concentration factor for the various joint designs used in the present investigation may also be used to indicate the fatigue performance of these joint designs. It can be seen from Table 6.1 that the aluminium alloy scarf joint with a scarf tip thickness of t_{st} = 0.4mm has a relatively high stress concentration factor compared to the other three joint designs. Consequently, this joint design would have a lower fatigue strength and fatigue threshold when compared to the other three joint designs, see Figure 6.1. Conversely, the predicted stress concentration in the single hybrid scarf joint is relatively low compared to the other three joint designs. Hence, it can be seen from Figure 6.1, that this joint design would have the highest fatigue strength and fatigue

threshold among the four joint designs investigated here. However, these statements will only be true if the following two assumptions hold true:

- All joints will invariably fail in the adherend.
- The integrity of the adhesive and the bond interface does not play a role in the fatigue strength of the joints.

Table 6.1: Predicted stress concentration in the aluminium alloy adherend for the various joint designs used in this project

Joint designs	Stress concentration S_c
Al-alloy scarf joints, t_{st} = 0.4mm	2.1
Al-alloy scarf joints, t_{st} = 0.15mm	1.7
CFRP/Al-alloy single scarf joints t_{st} = 0.15mm	1.4
CFRP/Al-alloy double scarf joints t_{st} = 0.15mm	1.63

Note: see section 6.1 for details

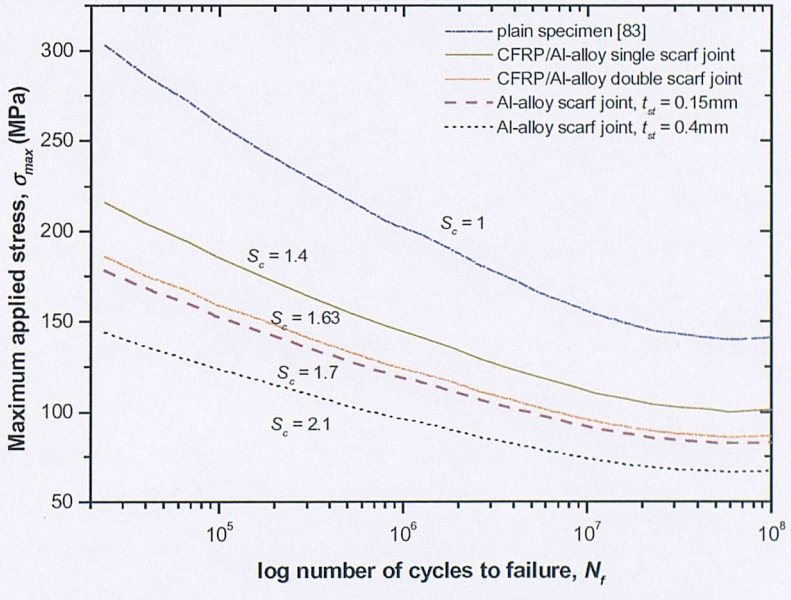


Figure 6.1: Predicted fatigue strength of the aluminium alloy adherend for the various joint designs

6.3 Prediction of adhesive and interfacial failure

6.3.1 Introduction

It had been shown by previous researchers [54,56,63] that, by using fracture mechanics data obtained from fracture mechanics tests such as the tapered double cantilever beam (TDCB), the fatigue life-time of adhesively-bonded overlap joints using the same adhesive system can be predicted, see section 2.7.3. This method involves the use of the energy balance approach where the maximum strain energy release rate is related to the crack length and the applied load.

6.3.2 Fracture mechanics approach to fatigue failure predictions

As discussed in section 2.7.1, mode I fracture mechanics data of adhesively-bonded joints can be easily obtained using the tapered double cantilever beam (TDCB) joint geometry, Figure 6.2. The results are usually plotted in the form of a logarithmic graph of da/dN against the maximum strain energy release rate, G_{max}. It is interesting to note that the fracture mechanics data is of a sigmoidal form where the plot diverges at the lower and upper limit (see Figure 2.17). The upper limit is termed the fracture toughness, G_c. The fracture toughness, G_c, is the critical strain energy release rate of an adhesive system under essentially static loading conditions. At the lower limit of the graph, the curve attains a value called the threshold strain energy release rate, G_{th}. The significance of this material parameter is that the propagation of fatigue cracks is not possible when the strain energy release rate of the system is below this value. Hence, the value of G_{th} is a valuable parameter when designing aerospace structures against fatigue crack growth.

The sigmoidal shape of the fracture mechanics data can be fitted using the modified Paris law, see equation 2.28. In order to predict the fatigue life-time of adhesively-bonded joints using fracture mechanics data, the term G_{max} in the modified Paris law equation has to be related to the crack length, a and the maximum applied load per unit width, T_{max} of the joint geometry that is to be predicted.

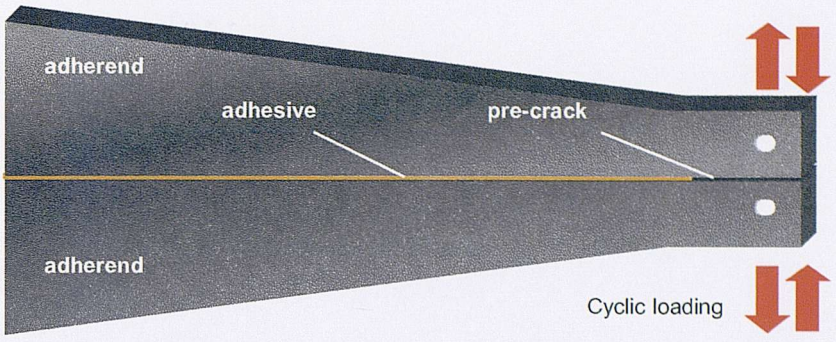


Figure 6.2: The tapered double cantilever beam (TDCB) joint geometry used to obtain fracture mechanics data of an adhesive system

As noted above, the relationship between G_{max}, a and T_{max} has to be calculated for the joint geometry whose fatigue performance is to be predicted. This can be formulated using closed-form analytical solutions or the finite element approach (see section 2.7.3). In the present work, the finite element approach will be used to predict the relationship between the maximum strain energy release rate, G_{max}, the crack length, a, and the applied load per unit width, T_{max}, for the four joint designs used, see section 6.1. This is carried out by calculating the J-integral for different crack lengths and applied loads. The fact that fatigue is a phenomenon that often appears when the joint is subjected to pre-yield loads greatly simplifies this calculation, as linear elastic fracture mechanics theory (LEFM) can be used in the analysis. LEFM theory assumes that the J-integral is equal to the strain energy release rate, G. Hence, the relationship between G_{max}, a and T_{max} can be obtained directly from finite element analysis. Obviously, finite element modelling of the required joint geometry has to be carried out and a crack is grown (quasi-statically) into the adhesive layer to simulate crack growth. Once, a set of the data of the crack length, a with the corresponding G_{max} and T_{max} is obtained, this relationship is then substituted into the modified Paris law equation and integrated with respect to a to obtain the number of cycles to failure, N_f. Thus, we have equation 6.2:

$$N_f = \int_{a_0}^{a_f} \frac{1}{C_T G_{\max}^n} \frac{1-\left(\frac{G_{\max}}{G_c}\right)^{n_2}}{1-\left(\frac{G_{th}}{G_{\max}}\right)^{n_1}} da \qquad (6.2)$$

The integration limits, a_0 and a_f are the initial flaw size and the final crack length before the occurrence of unstable crack growth. Curley *et. al* [63] showed that the initial

flaw size, a_0 can be deduced by modifying the Griffith equation for a through-thickness crack in an infinitely-wide plate with a constant, χ, such that:

$$a_0 = \frac{E_a G_c}{\chi \pi \sigma_a^2} \quad \text{.....(6.3)}$$

where σ_a is the adhesive fracture stress, E_a is the adhesive modulus and G_c is the fracture toughness. However, Curley *et. al* [63] also showed that the exact value of the initial flaw size does not significantly affect the predicted fatigue lifetimes. This is because the relationship between G_{max}, T_{max} and a is often expressed by a third order polynomial form, where the coefficient of a reduces as the order of a increases. Furthermore, a_0 is invariably small compared to the independent constant in the polynomial equation. For example, equation 6.4 shows the relationship between G_{max}, T_{max} and a for the aluminium alloy scarf joint design with a scarf tip thickness of t_{st} = 0.4mm. (The derivation of this equation is discussed in detail later in section 6.3.5.) It can be seen that for any small values of a_0, the ratio of G_{max}/T_{max}^2 would be approximately equal to $2 \cdot 10^{-9}$.

$$\frac{G_{\max}}{T_{\max}^2} = 3.7 \cdot 10^{-3} \cdot a^3 - 7.2 \cdot 10^{-5} a^2 + 8.6 \cdot 10^{-7} \cdot a + 2.4 \cdot 10^{-9} \quad \text{.....(6.4)}$$

Fracture mechanics data of the adhesive systems used in the current project are shown in Figures 6.3 and 6.4. These data were obtained from Adams [4]. Clearly, it can be seen that the fracture mechanics data follows a sigmoidal form as mentioned above. In addition, it can be observed from Figure 6.3 that there is no significant difference between the GPS and CAE surface treatments. More significantly, Adams reported that the value of the threshold strain energy release rate, G_{th}, for both of these treatments is the same [4]. On the other hand, it can be observed by comparing Figures 6.3 and 6.4 that the value of G_{th} for the GBD treated joints tested in 'hot/wet' conditions is significantly lower than for the GPS and CAE treated joints. Further, the value of G_{th} for the GBD treated joints tested in the 'hot/wet' condition is significantly lower than the value of G_{th} observed from the 'dry' test conditions. Table 6.2 summarizes the value of the threshold strain energy release rates, G_{th}, and the fracture toughness, G_c, of the various adhesive systems.

Table 6.2: The fracture toughness and threshold strain energy release rates of the various adhesive systems [4]

	GBD 'dry'	GBD 'hot/wet'	GPS 'dry'	GPS 'hot/wet'
G_c (J/m^2)	680	680	1465	1465
G_{th} (J/m^2)	85	13	250	100

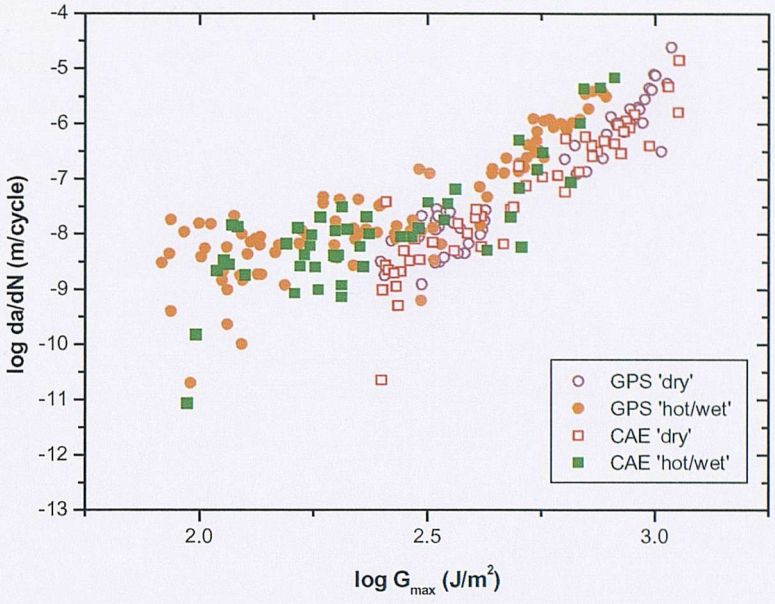


Figure 6.3: Comparison of the fatigue data of GPS and CAE surface treated TDCB joints tested in 'dry' and 'hot/wet' conditions [4]

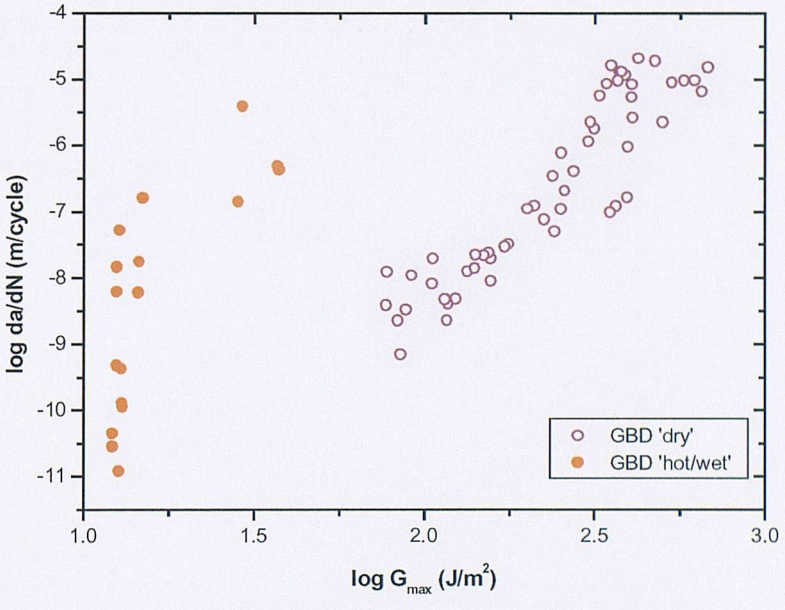


Figure 6.4: Comparison of the fatigue data of GBD surface treated TDCB joints tested in 'dry' and 'hot/wet' conditions [4]

6.3.3 Curve fitting the fracture mechanics data

6.3.3.1 Curve fitting method

A linear regression method was used to obtain two of the four curve fitting parameters of the modified Paris law. These are the y-axis intercept, C_T, and the slope, n, of region 2 of

the fracture mechanics data, see Figure 2.17. The values of the other two curve fitting parameters, n_1 and n_2, were obtained by visual inspection of the fit of the predicted curve onto the available experimental data. The relevance of the fitting parameters will be discussed in more detail in section 6.3.4. The upper and lower limits of the prediction curve were determined by the values of the fracture toughness, G_c, and fatigue threshold, G_{th}, as given in Table 6.2.

6.3.3.2 GBD surface treatment

Fracture mechanics data for the GBD treated TDCB joints is shown in Figure 6.4. Curve fitting of this data using the modified Paris law (equation 2.28) was carried out to determine the various fitting parameters for this adhesive system. Figures 6.5a and b show the curve fitting of the GBD system in 'dry' and 'hot/wet' conditions respectively. It can be seen that the experimental data of the 'dry' system follows the sigmoidal form. However, a lack of experimental data in the 'hot/wet' system makes the fitting of the data difficult. Nevertheless, the threshold strain energy release rate is clearly indicated in the plot. The values of the curve fitting parameters are summarized in Table 6.3.

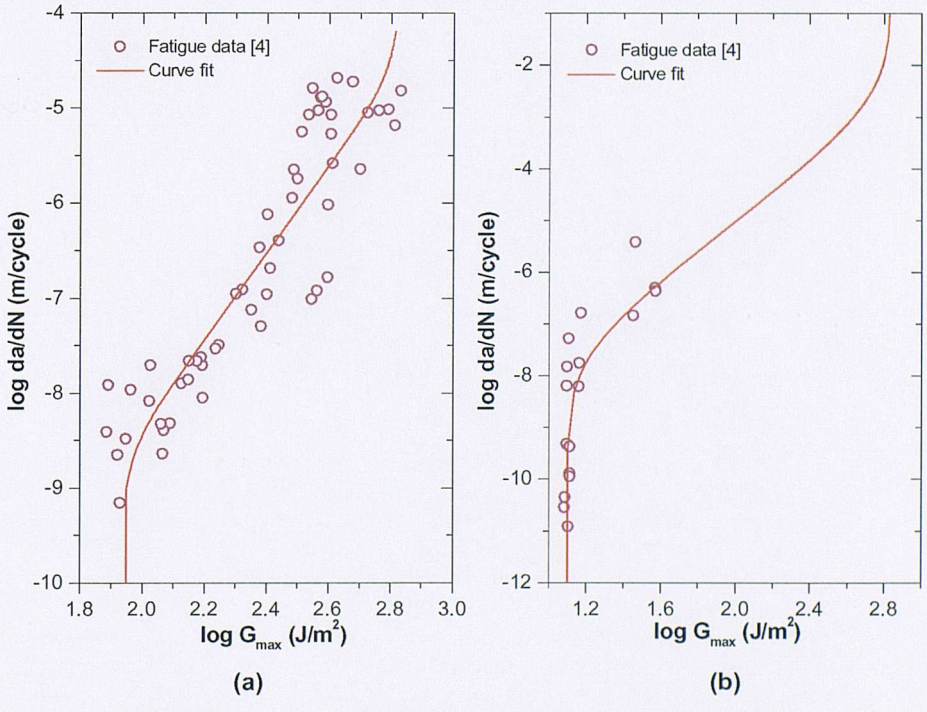


Figure 6.5: Curve fitting of the TDCB fatigue data obtained from [4] using equation 2.3 for the (a) GBD 'dry' tests and (b) GBD 'hot/wet' tests

Table 6.3: Curve fitting data used to curve fit the experimental fracture mechanics data of the GBD system obtained from [4]

Fitting parameters	GBD 'dry'	GBD 'hot/wet'
C_T (m^2/N cycle)	3.13×10^{-19}	7.36×10^{-11}
n	4.58	2.55
n_1	10	1
n_2	10	1
G_{th} (J/m^2)	85	13
G_c (J/m^2)	680	680

6.3.3.3 GPS surface treatment

Fracture mechanics data for the GPS treated TDCB joints is given in Figure 6.3. It was observed that the values of the threshold strain energy release rate in 'dry' and 'hot/wet' conditions are $100J/m^2$ and $250J/m^2$, respectively. Figure 6.6 shows the linear regression curve fit of this data using the modified Paris law (equation 2.28). It can be seen that both sets of data follow the sigmoidal form of the modified Paris law. Table 6.4 summarizes the values of the curve fitting parameters.

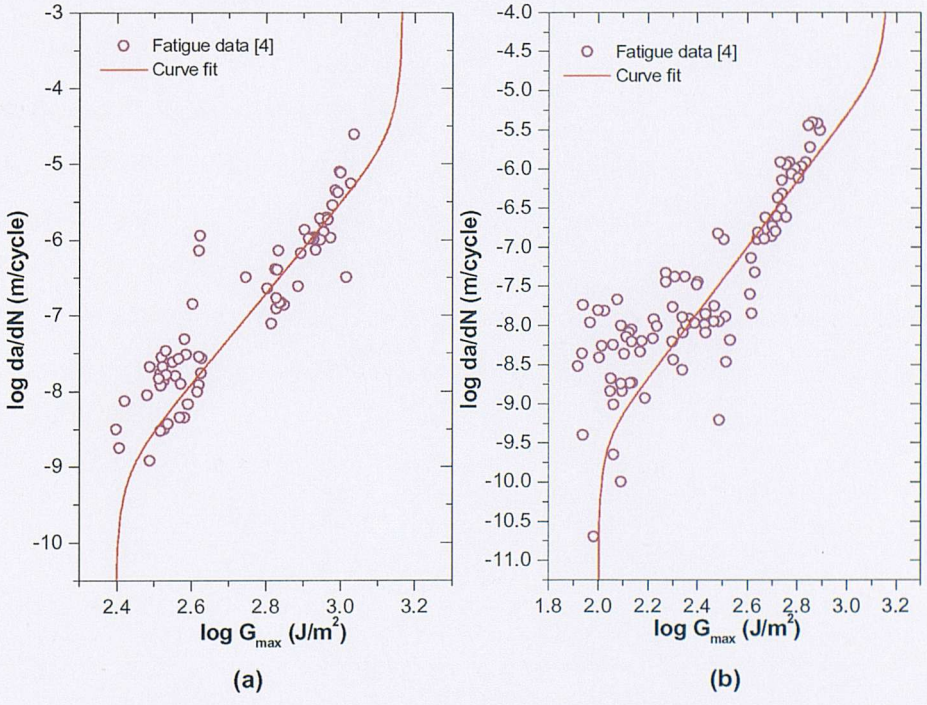


Figure 6.6: Curve fitting of the TDCB fatigue data obtained from [4] using equation 2.3 for the (a) GPS 'dry' tests and (b) GPS 'hot/wet' tests

Table 6.4: Curve fitting data used to curve fit the experimental fracture mechanics data of the GPS system obtained from [4]

Fitting parameters	GPS 'dry'	GPS 'hot/wet'
C_T (m²/N cycle)	4.34×10^{-24}	1.30×10^{-18}
n	5.95	4.19
n_1	10	10
n_2	10	10
G_{th} (J/m²)	250	100
G_c (J/m²)	1465	1465

6.3.4 Relevance of the curve fitting parameters

It can be seen that there is considerable scatter in the fracture mechanics data (see Figures 6.3 and 6.4). This is especially true for the 'hot/wet' systems, where the influence of moisture on the fatigue crack propagation decreases as the crack growth rate increases. Hence, curve fitting of these sets of data will invariably be difficult. In the present section, the importance of the exact values of the curve fitting parameters to the predicted shape of the σ_{max}-N_f curve will be discussed.

There are four fitting parameters, i.e. C_T, n, n_1 and n_2, in equation 2.28. It is clear from equation 2.30 that the parameters C_T and n are the axis intercept and slope for region 2 of the fracture mechanics data according to the classical Paris law for crack propagation, see equation 2.29. In order to examine the relevance of these curve fitting parameters on the predicted shape of the σ_{max}-N_f curve, we may assume for convenience that G_{max} is related to T_{max} and a according to equation 6.4. Further, the curve fitting parameters given for the GBD treated joints tested in the 'hot/wet' environment will be used, see Table 6.3.

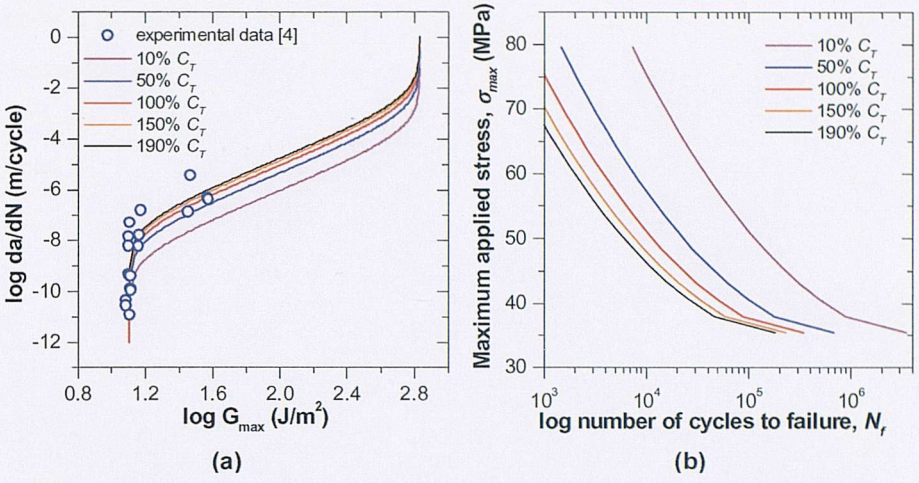


Figure 6.7: Effect of the C_T fitting parameter of the modified Paris law on (a) the curve fitting of the fracture mechanics data and (b) the predicted shape of the σ_{max}-N_f curve

Figures 6.7a and b show the effect of the value of the C_T parameter on the curve fitting of the fracture mechanics data and the predicted σ_{max}-N_f curve respectively. From Figure 6.7a, it can be observed that by reducing the value of C_T, the predicted sigmoidal curve translates downwards. Consequently, from Figure 6.7b, reducing the C_T value translates the predicted σ_{max}-N_f curve to the right. Conversely, increasing the C_T value translates the predicted σ_{max}-N_f curve to the left. However, it can be seen that the effect of increasing C_T from the best fit value (i.e. 100% C_T), using the linear regression method, on the predicted σ_{max}-N_f curve is relatively small compared to the effect of decreasing the value of C_T from the best fit value. It may also be observed that changing the C_T parameter does not rotate the curve. This is as expected, as the C_T parameter is the intercept of the log da/dN axis and hence changing it leads to a horizontal translation of the predicted σ_{max}-N_f curve.

The effect of the n fitting parameter is shown in Figure 6.8. It can be seen that changing the value of the n fitting parameter from 10% to 190% of the best fit value (i.e. that obtained using the linear regression method) significantly changes the shape of the curve fitting of the fracture mechanics data and also of the predicted σ_{max}-N_f curve, see Figures 6.8a and b. The n fitting parameter is the slope of region 2 of the fracture mechanics data. Hence, changing the n value changes the slope of the curve fitting plot of

the fracture mechanics data. This has the effect of rotating the predicted σ_{max}-N_f, curve, as well as translating it horizontally.

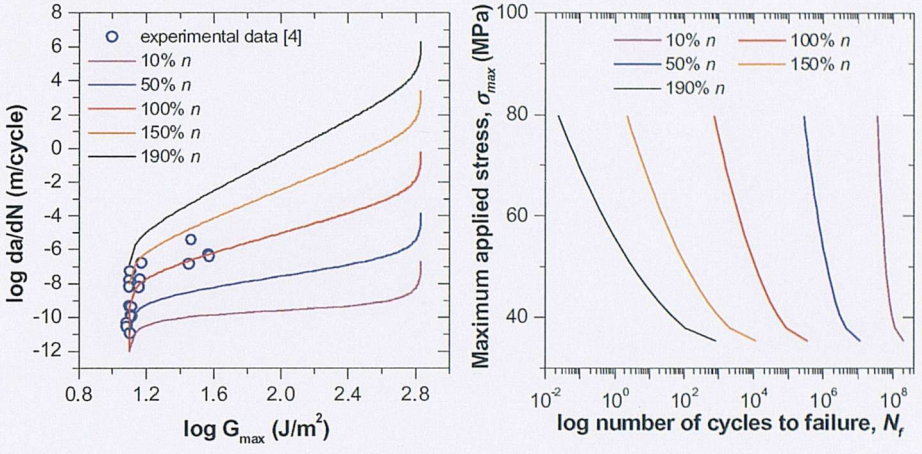


Figure 6.8: Effect of the *n* fitting parameter of the modified Paris law on (a) the curve fitting of the fracture mechanics data and (b) the predicted shape of the σ_{max}-N_f curve

The effect of the n_1 and n_2 fitting parameters on the predicted σ_{max}-N_f curve are shown in Figures 6.9 and 6.10, respectively. It can be seen that changes to these two parameters leads to a horizontal translation, as well as a rotation, of the predicted σ_{max}-N_f curve. However, these effects are less significant compared to the effects from varying the C_T and n fitting parameters. This is to be expected as the n_1 and n_2 parameters are essentially the fitting parameters of the fracture mechanics data that determine the position where region 2 of the fracture mechanics data changes to region 1 and region 3 respectively, see Figure 2.17. It can be observed that, if both n_1 and n_2 parameters were to be changed by the same amount, the curve fit on the fracture mechanics data would only translate vertically. This will cause a horizontal translation of the predicted σ_{max}-N_f curve as observed from changing the C_T fitting parameter. Hence, in order to reduce the number of variables in the modified Paris law equation, the n_1 and n_2 fitting parameters are usually set to be equal in value.

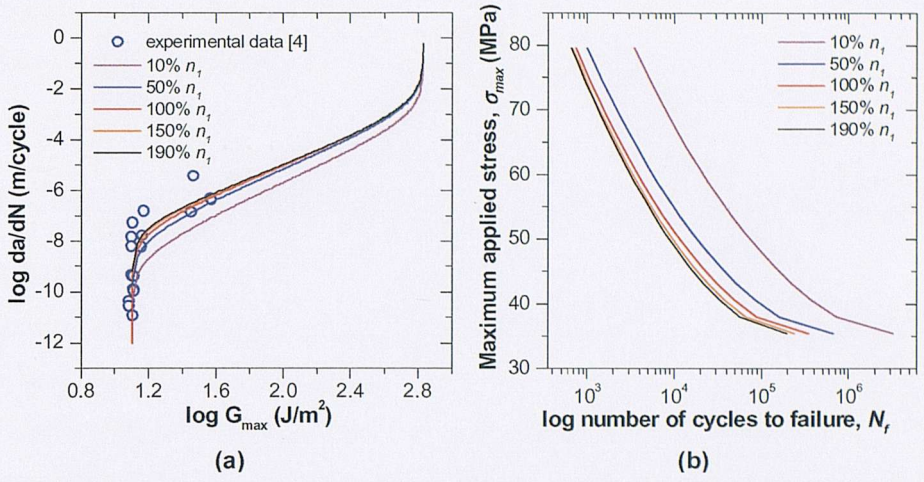


Figure 6.9: Effect of the n_1 fitting parameter of the modified Paris law on (a) the curve fitting of the fracture mechanics data and (b) the predicted shape of the σ_{max}-N_f curve

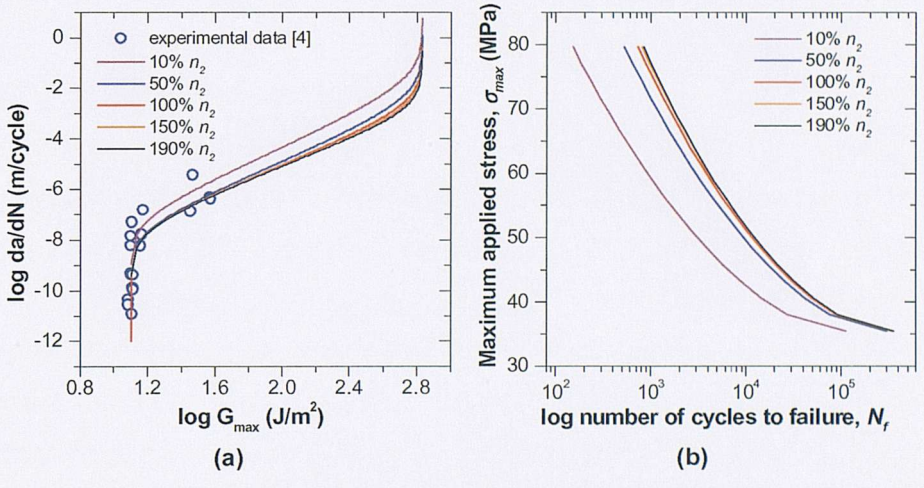


Figure 6.10: Effect of the n_2 fitting parameter of the modified Paris law on (a) the curve fitting of the fracture mechanics data and (b) the predicted shape of the σ_{max}-N_f curve

From the above analyses, it can be concluded that the slope of region 2 of the fracture mechanics data, n, is the fitting parameter that most significantly affects the shape of the predicted σ_{max}-N_f curve. It may also be noted that changing the curve fitting parameters does not affect the predicted fatigue threshold. It only affects the horizontal position and slope of the predicted σ_{max}-N_f curve. In other words, this method of predicting the fatigue life-time of adhesively-bonded joints can actually be used to predict relatively accurately the fatigue threshold stress. This is of considerable importance, since

the fatigue threshold stress is especially relevant to design engineers as real-life structures may be designed to be always loaded below this stress level.

6.3.5 Relationship between G_{max}, a and T_{max} for different joint designs

6.3.5.1 Introduction

As commented earlier, the fatigue life associated with adhesive and adhesive/adherend interfacial failure for adhesively-bonded coupon specimens can be predicted by obtaining the relationship between G_{max}, T_{max} and a. This relationship may then be substituted into the modified Paris law (equation 6.2) and integrated to obtain the number of cycles to failure, N_f. In this section, results from the finite element modelling of the various scarf joint designs are given.

6.3.5.2 Finite element models to calculate G_{max}

The finite element models are based upon 2-dimensional models and assume plane strain characteristics. The adhesive and adherends were modelled using linear elastic material properties. The material properties of the adhesive and the adherends are given in Tables 3.1 and 3.2 respectively. In the modelling procedure, a crack is grown quasi-statically into the joint according to the expected failure locus of a particular adhesive system. For example, the GBD adhesive system in 'hot/wet' conditions will require the crack to be grown along the adhesive/adherend interface. The J-integral (equivalent to G_{max}, according to LEFM assumptions) is calculated implicitly using the finite element package, ABAQUS. This is then related to the applied load per unit width, T_{max}, and the crack length, a.

6.3.5.2 Al-alloy/Al-alloy single scarf joint designs

Figure 6.11 shows the graph of G_{max} plotted against T_{max}^2 for different crack lengths. It can be seen that for any crack length, a, G_{max} varies linearly with T_{max}^2. This would be expected for a linear elastic system, see equations 6.5-6.9. It may also be observed that by increasing the crack length, a, the ratio of G_{max}/T_{max}^2 increases.

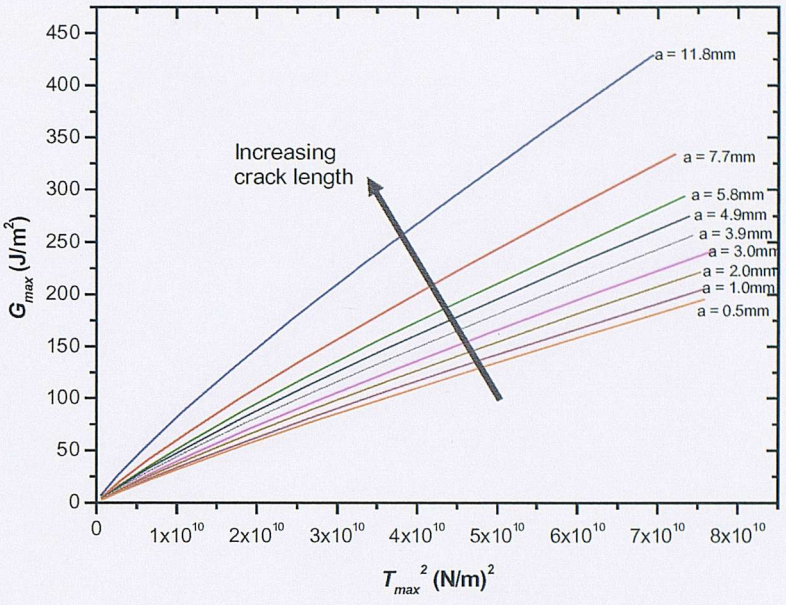


Figure 6.11: Typical relationship between G_{max}, T_{max} and a for an adhesive system assuming linear elastic material properties

From Figure 6.11 it can be seen that by plotting the ratio of G_{max}/T_{max}^2 for a set of crack lengths, a single relationship for these three parameters can be obtained. This is shown in Figure 6.12 for the scarf joint design with a scarf tip thickness of t_{st} = 0.4mm. It can be seen that the data can be readily fitted using a third order polynomial regression method. The relationships between G_{max}/T_{max}^2 and a for interfacial and adhesive (cohesive) crack growth in the scarf joint design with a scarf tip thickness of t_{st} = 0.4mm are given in equations 6.5a and b respectively. As mentioned in section 6.3.2, the y-axis intercept of the curves is significant to the determination of the fatigue threshold.

$$\frac{G_{\max}}{T_{\max}^2} = 3.7 \cdot 10^{-3} \cdot a^3 - 7.2 \cdot 10^{-5} a^2 + 8.6 \cdot 10^{-7} \cdot a + 2.4 \cdot 10^{-9} \quad \text{.....(6.5a)}$$

$$\frac{G_{\max}}{T_{\max}^2} = 8.9 \cdot 10^{-4} \cdot a^3 + 7.8 \cdot 10^{-6} a^2 + 4.9 \cdot 10^{-7} \cdot a + 3.7 \cdot 10^{-9} \quad \text{.....(6.5b)}$$

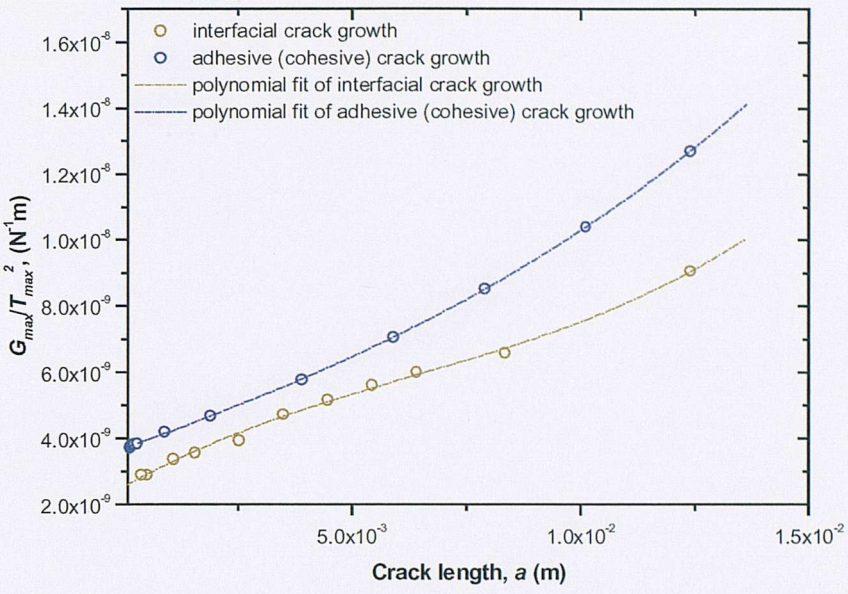


Figure 6.12: The predicted relationship between G_{max}, T_{max} and a for interfacial and adhesive (cohesive) crack growth in the scarf joint design with a scarf tip thickness of t_{st} = 0.4mm

Similarly, the relationship between G_{max}, T_{max} and a was obtained for the scarf joint design with a scarf tip thickness of t_{st} = 0.15mm, see Figure 6.13. Again, this relationship can be easily fitted using a third order polynomial regression method. By comparing Figures 6.12 and 6.13, it can be observed that the y-axis intercept for the scarf joint design with a scarf tip thickness of t_{st} = 0.15mm is relatively low when compared to that of the scarf joint design with a scarf tip thickness of t_{st} = 0.4mm. This indicates that the scarf joint design with a scarf tip thickness of t_{st} = 0.15mm would have the higher fatigue threshold. The relationships between G_{max}/T_{max}^2 and a for interfacial and adhesive (cohesive) crack growth in the scarf joint design with a scarf tip thickness of t_{st} = 0.15mm are given in equations 6.6a and b, respectively.

$$\frac{G_{\max}}{T_{\max}^2} = 2.2 \cdot 10^{-4} \cdot a^3 + 7.1 \cdot 10^{-6} a^2 + 2.0 \cdot 10^{-7} \cdot a + 1.0 \cdot 10^{-9} \quad \text{.....(6.6}a\text{)}$$

$$\frac{G_{\max}}{T_{\max}^2} = 6.7 \cdot 10^{-4} \cdot a^3 + 3.3 \cdot 10^{-6} a^2 + 2.4 \cdot 10^{-7} \cdot a + 1.0 \cdot 10^{-9} \quad \text{.....(6.6}b\text{)}$$

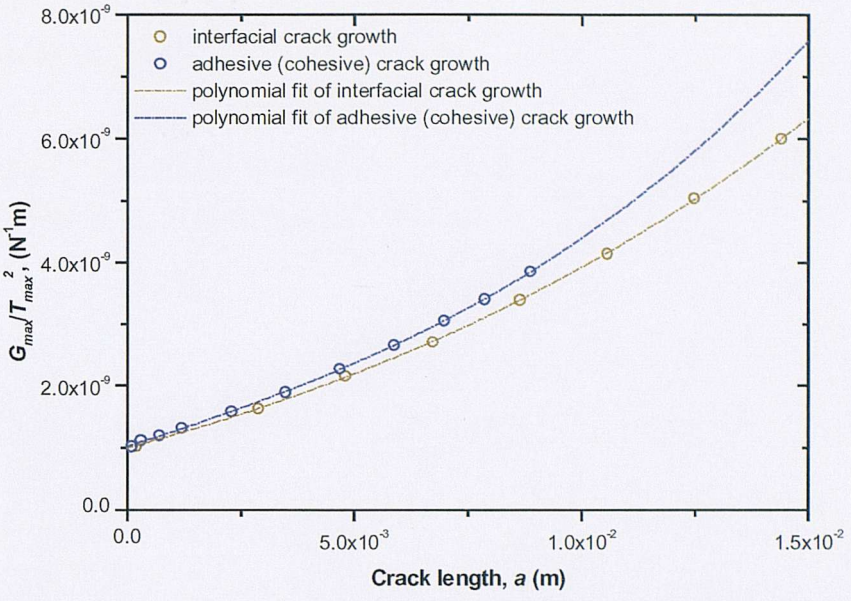


Figure 6.13: The predicted relationship between G_{max}, T_{max} and a for interfacial and adhesive (cohesive) crack growth in the scarf joint design with a scarf tip thickness of t_{st} = 0.15mm

6.3.5.3 Single CFRP/Al-alloy hybrid scarf joint design

As discussed in section 5.4.5, aluminium alloy/CFRP hybrid scarf joints were tested to investigate the viability of repairing aluminium alloy structures with CFRP composite materials. It was found that, for unsymmetrical joint designs, the joint came out bowed after the curing of the adhesive. This is due to the different thermal expansion coefficients of the aluminium alloy and the CFRP composite, see section 5.2.6. It was also found that by testing these hybrid joints in 'hot/wet' fatigue conditions, the fatigue threshold of the GBD surface treated joints was lower than that of the GBD surface treated aluminium alloy joints, see section 5.4.5. In order to predict the fatigue life-time of these joints, the effect of residual thermal stresses on the fatigue performance of these joints has to be taken into account. This can be carried out by predicting the residual thermal stresses in the adhesive.

A heat transfer finite element analysis was carried out to predict the stress state induced in the adhesive from curing of the adhesive at an elevated temperature. A temperature drop of 100°C was used to simulate the change in temperature of the curing of the adhesive (i.e. 120° to 20°). The highest stresses in the adhesive at the two overlap termini were found to be 30MPa and 22MPa respectively, where the higher stress was

found to be at the CFRP scarf tip end of the joint. These stresses act as pre-stresses in the joints and the total stress in the joint can be calculated as:

$$\sigma_{total} = \sigma_{applied} + \sigma_{thermal} \quad \text{.....(6.7)}$$

where $\sigma_{applied}$ is the applied stress from the fatigue test and $\sigma_{thermal}$ is the residual thermal stress which arises from the curing of the adhesive.

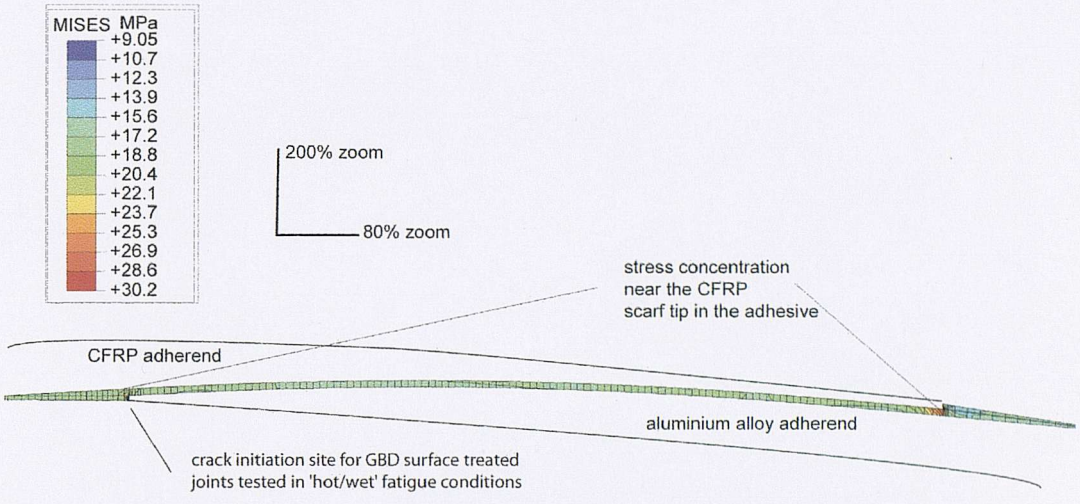


Figure 6.14: Stress contour plot in the adhesive subjected to a temperature drop of ΔT=100°C.

As mentioned in section 5.4.5, the GBD treated joints failed at the adhesive/aluminium alloy interface, with the crack initiating from the aluminium alloy scarf tip. On the other hand, the GPS treated joints failed in the adhesive layer accompanied by composite failure, with the crack initiating from the CFRP scarf tip, see Figure 5.20. Hence, two separate analyses had to be carried out to model these two failure loci. Figure 6.15 shows the predicted relationship between G_{max}, T_{max} and a for these two failure loci. It can be seen that the y-axis intercept for the adhesive failure loci is relatively low compared to that for the interfacial failure. This is in contrast to the previous analysis of the aluminium alloy scarf joints. The reason for this is because the adhesive at the CFRP scarf tip end of the joint is at a higher stress state compared to that at the aluminium alloy scarf tip end (see Figure 6.14). The relationships between G_{max}, T_{max} and a for these hybrid joints are also different compared to the aluminium alloy joints. This is because, the different adherends in the hybrid joints react differently when a crack is present in the adhesive (or at the adhesive/adherend interface). The CFRP

adherend is incapable of plastic deformation, and hence will not peel open as much as an aluminium alloy adherend. As a result, the calculated *J*-integral will be higher, as the energy required to propagate the crack would be higher. Again, the relationship between G_{max}, T_{max} and a can be fitted using a third order polynomial regression method. The relationships between G_{max}/T_{max}^2 and a for interfacial and adhesive (cohesive) crack growth in the hybrid scarf joints are given in equations 6.8a and b, respectively.

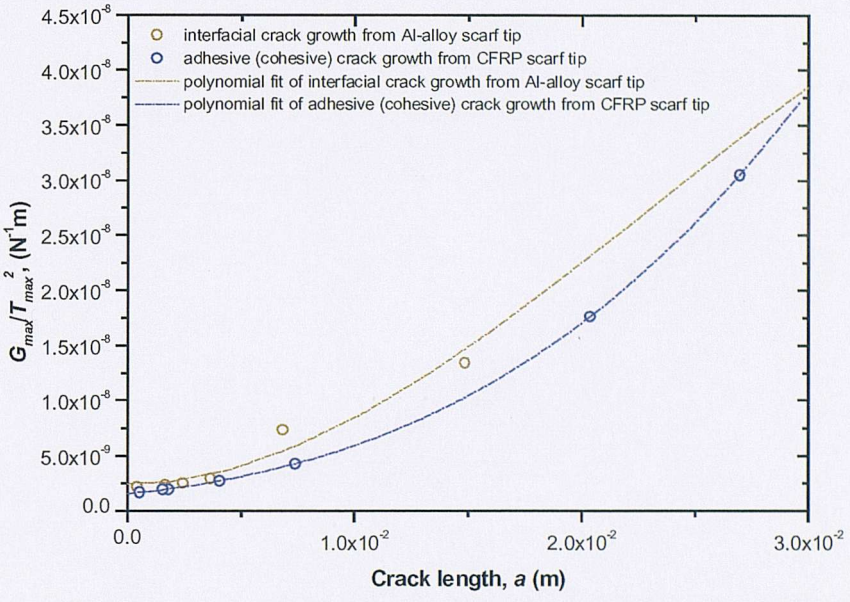


Figure 6.15: The predicted relationship between G_{max}, T_{max} and *a* for interfacial and adhesive (cohesive) crack growth in the single CFRP/Al-alloy hybrid scarf joint design with a scarf tip thickness of t_{st} = 0.15mm

$$\frac{G_{\max}}{T_{\max}^2} = -5.83 \cdot 10^{-4} \cdot a^3 + 5.75 \cdot 10^{-5} a^2 - 2.86 \cdot 10^{-7} \cdot a + 3.36 \cdot 10^{-9} \quad \text{.....(6.8}a\text{)}$$

$$\frac{G_{\max}}{T_{\max}^2} = 5.42 \cdot 10^{-4} \cdot a^3 + 1.68 \cdot 10^{-5} a^2 + 2.3 \cdot 10^{-7} \cdot a + 1.49 \cdot 10^{-9} \quad \text{.....(6.8}b\text{)}$$

6.3.5.4 Double CFRP/Al-alloy hybrid scarf joint design

Double CFRP/aluminium alloy hybrid scarf joints were also tested in 'hot/wet' fatigue conditions. The experimental results were given in section 5.4.6. The relationship between G_{max}, T_{max} and a for this joint design was obtained to predict interfacial and

adhesive (cohesive) failure. Although these joints were observed to fail in the aluminium alloy adherend, it is interesting to see whether the predicted fatigue loads for adhesive and interfacial failure would be higher than that for failure in the aluminium alloy adherend. The same procedure, as detailed above, was used to obtain the relationship between G_{max}, T_{max} and a for the double hybrid scarf joint design. The results are shown in Figure 6.16. The relationships between G_{max}/T_{max}^2 and a for interfacial and adhesive (cohesive) crack growth in the double hybrid scarf joints are given in equations 6.9a and b, respectively.

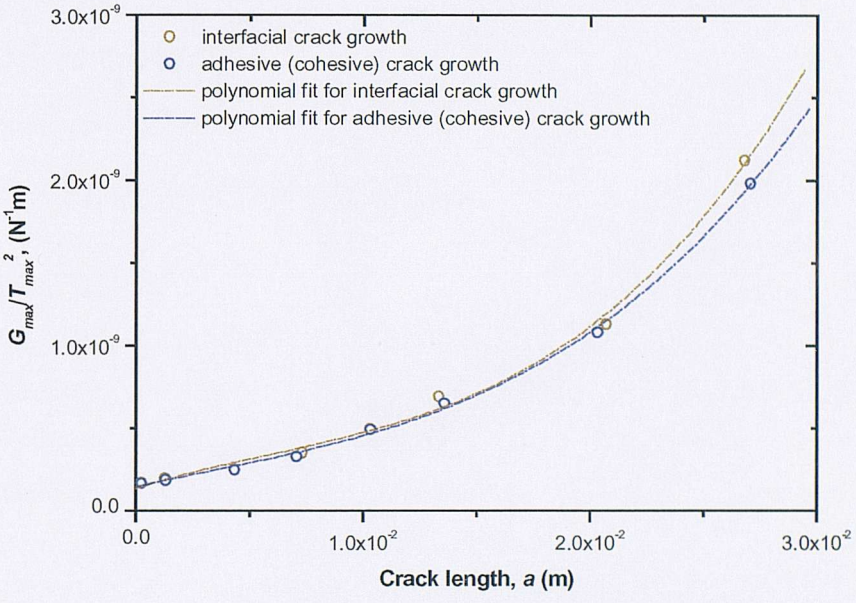


Figure 6.16: The predicted relationship between G_{max}, T_{max} and a for interfacial and adhesive (cohesive) crack growth in the double CFRP/Al-alloy hybrid scarf joint design with a scarf tip thickness of t_{st} = 0.15mm

$$\frac{G_{\max}}{T_{\max}^2} = 1.23 \cdot 10^{-4} \cdot a^3 - 2.17 \cdot 10^{-6} \cdot a^2 + 4.28 \cdot 10^{-8} \cdot a + 1.35 \cdot 10^{-10} \quad \text{.....(6.9}a\text{)}$$

$$\frac{G_{\max}}{T_{\max}^2} = 7.92 \cdot 10^{-5} \cdot a^3 - 7.82 \cdot 10^{-7} \cdot a^2 + 3.08 \cdot 10^{-8} \cdot a + 1.45 \cdot 10^{-10} \quad \text{.....(6.9}b\text{)}$$

6.3.5.5 Summary

The relationships between G_{max}/T_{max}^2 and a for interfacial and adhesive (cohesive) failure of the four joint designs have been discussed above. It can be seen that these relationships may be readily fitted using a third order polynomial regression method. For the two

aluminium alloy joint designs (section 6.3.5.2), the y-axis intercept of the predicted relationship between G_{max}/T_{max}^2 and a for adhesive (cohesive) failure is relatively high compared to that for interfacial failure. This implies a relatively higher fatigue threshold for joints that failed along the adhesive when compared to joints that failed in the interface. The reverse is true for the single hybrid scarf joint design where the y-axis intercept of the predicted relationship between G_{max}/T_{max}^2 and a for adhesive (cohesive) failure is relatively low compared to that for interfacial failure. The predicted relationships between G_{max}/T_{max}^2 and a for adhesive (cohesive) failure and interfacial failure of the double hybrid scarf joint design are very close to each other, implying a similar fatigue performance for the two failure loci.

6.4 Fatigue life-time prediction

6.4.1 Introduction

The fatigue life-time predictions for the various joint designs and adhesive systems will be discussed in this section. The prediction methods, for adherend, adhesive and interfacial failure loci, have been discussed in sections 6.2 and 6.3. Discussion of the fatigue life-time predictions will be given in section 6.4.3, after the presentation of the results.

In the previous section, the strain energy release rate, G_{max}, was related to the maximum applied load per unit width, T_{max}. However, in the following subsections, the fatigue life-time predictions will be presented with the maximum applied stress, σ_{max}, instead of T_{max}. The maximum applied stress, σ_{max}, is obtained by dividing the maximum applied load per unit width, T_{max}, by the width of the specimen. There are two reasons for doing this. Firstly, the maximum applied stress, σ_{max}, can be readily compared with the predictions for adherend failure. Secondly, the use of the maximum applied stress to indicate the fatigue strength of the joints can be readily compared with the static strength of the joints, as presented in Chapter Five.

6.4.2 Fatigue life-time predictions

6.4.2.1 Al-alloy scarf joints [t_{st} = 0.4mm]

The fatigue life-time predictions of the aluminium alloy scarf joint design with a scarf tip thickness of t_{st} = 0.4mm, tested in 'dry' fatigue conditions are shown in Figure 6.17. As may be seen, the joints would be predicted to tend to fracture via failure in the adherend, or possibly in the case of the GBD pretreated joints, via failure along the interface. From the experimental studies, it was observed that failure mainly occurred in the adherend. However, the predicted values of σ_{max} were only in good agreement with the experimental measured values at relatively high N_f values, i.e. around the threshold region.

Figure 6.18 shows the predicted fatigue strength of the aluminium alloy scarf joints with a scarf tip thickness of t_{st} = 0.4mm tested in 'hot/wet' fatigue conditions. The GPS treated joints were predicted to fail in the aluminium alloy adherend. On the other hand, the GBD treated joints were predicted to fail at the adhesive/adherend interface. It can be seen that the prediction of the failure loci of the joints are again accurate.

As noted above, it can be seen from both Figures 6.17 and 6.18 that the fatigue life-time predictions for relatively low numbers of fatigue cycles to failure are not very accurate. There are several possible explanations. Firstly, the fatigue life-time predictions do not take into account any crack initiation period. It was shown in section 5.4.8 that the time spent on crack initiation increases as the applied load increases. The reverse is true for the crack propagation period. Secondly, it was shown in section 6.3.4 that the values selected for the curve fitting parameters, C_T, n, n_1 and n_2, significantly affects the shape of the predicted σ_{max}-N_f curve. Furthermore, there is considerable scatter, especially in region 2, in the fracture mechanics data, see Figures 6.5 and 6.6. This is particularly true for the prediction of interfacial failure for the GBD treated joints tested in 'hot/wet' conditions, where the lack of experimental data for this adhesive system for region 2 of the fracture mechanics curve (see Figure 6.5b) makes it difficult to determine accurately the curve fitting parameters. Nevertheless, from Figures 6.17 and 6.18, the prediction for the fatigue threshold appears to accurately predict the experimental fatigue threshold.

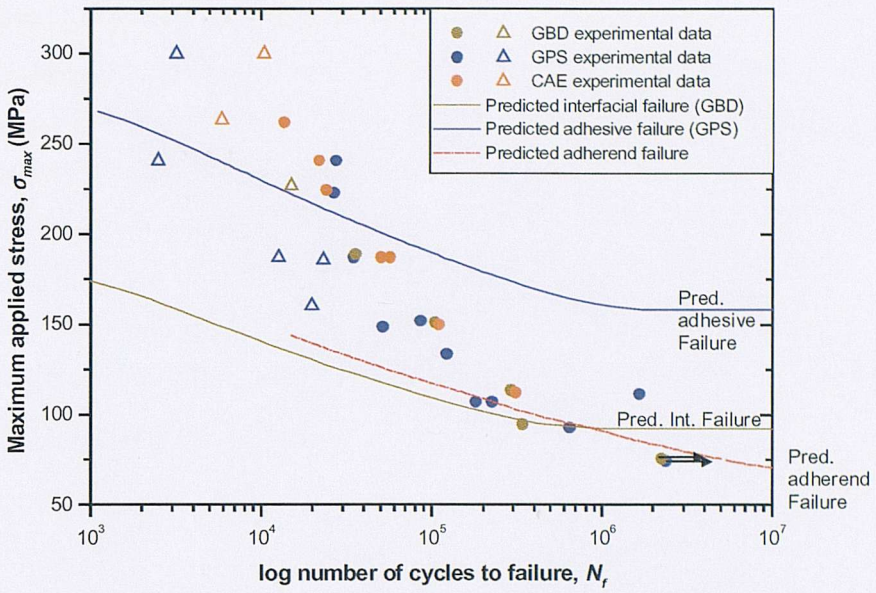


Figure 6.17: Prediction of the fatigue strength of aluminium alloy scarf joints with a scarf tip thickness of t_{st} = 0.4mm in 'dry' fatigue conditions

Note: 1. Arrow denotes specimens that did not fail
2. All open triangles denote adhesive failure
3. All filled circles denote adherend failure

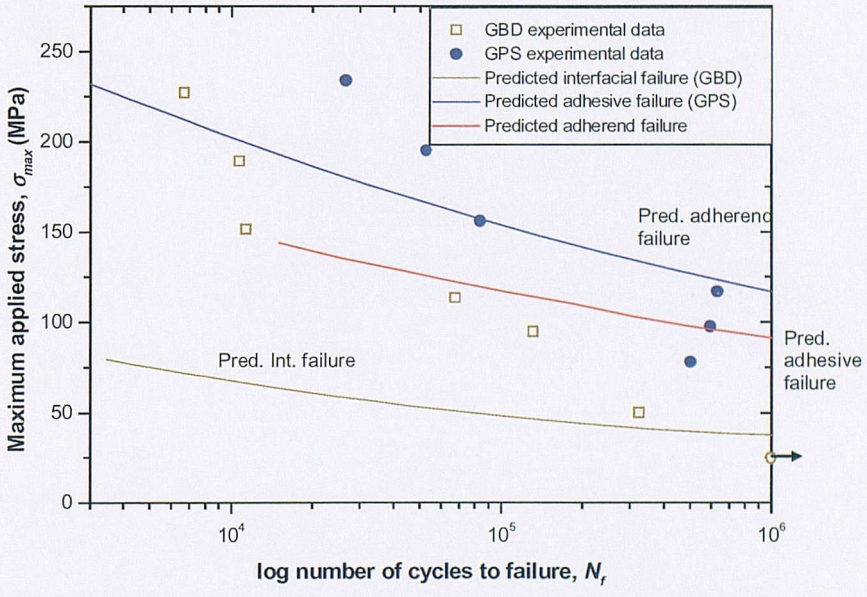


Figure 6.18: Prediction of the fatigue life-time of aluminium alloy scarf joints with a scarf tip thickness of t_{st} = 0.4mm in 'hot/wet' fatigue conditions

Note: 1. Arrow denotes specimens that did not fail
2. All filled circles denote adherend failure
3. All open squares denote interfacial failure

6.4.2.2 Al-alloy scarf joints [t_{st} = 0.15mm]

Figure 6.19 shows the prediction of the fatigue strength of the aluminium alloy scarf joints with a scarf tip thickness of t_{st} = 0.15mm tested in 'dry' fatigue conditions. Based on these predictions, both the GBD and GPS treated joints will always tend to fail in the aluminium alloy adherend. (Although, as noted above, the predicted fatigue threshold for interfacial failure in the GBD surface treated joints is very close to the prediction for adherend failure.) Indeed, these joints when tested in the 'dry' environment did always fracture via failure of the adherend and the threshold values of σ_{max} are predicted reasonably accurately.

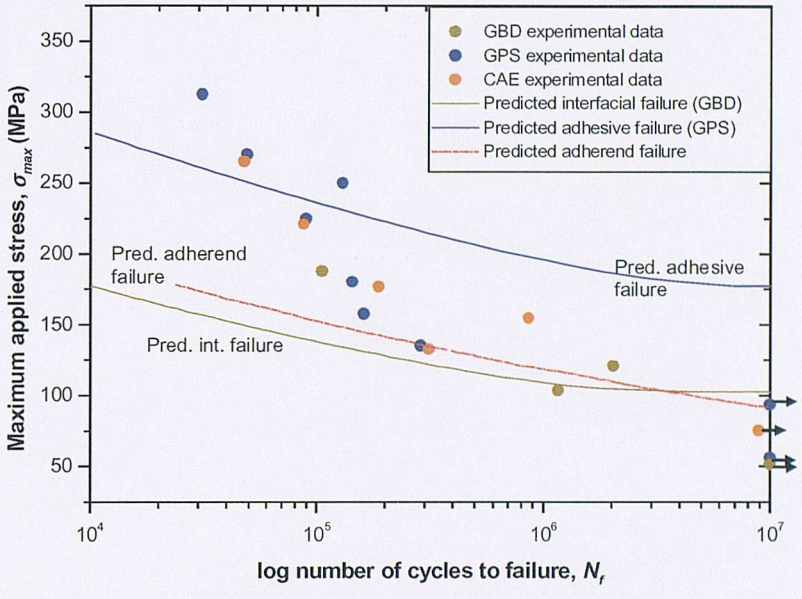


Figure 6.19: Prediction of the fatigue performance of aluminium alloy scarf joints with a scarf tip thickness of t_{st} = 0.15mm tested in 'dry' fatigue conditions for different surface treatments

Note: 1. Arrow denotes specimens that did not fail
2. All filled circles denote adherend failure

Figure 6.20 shows the prediction for the aluminium alloy scarf joints with a scarf tip thickness of t_{st} = 0.15mm tested in 'hot/wet' fatigue conditions. The figure shows that the GPS treated joints are predicted to fail in the aluminium alloy adherend. On the other hand, the GBD treated joints are predicted to fail at the adhesive/adherend interface. It should also be noted that the predicted fatigue threshold for the GBD treated joints compares well with the experimental results. However, the predicted fatigue strength of the GBD treated joints for low number of fatigue cycles appears to be relatively low

compared to the experimental results. This was also observed in the fatigue prediction of the aluminium alloy scarf joints with a scarf tip thickness of t_{st} = 0.4mm tested in 'hot/wet' fatigue conditions (see Figure 6.18). This observation will be further discussed in section 6.4.3 where possible reasons to explain this observation are discussed.

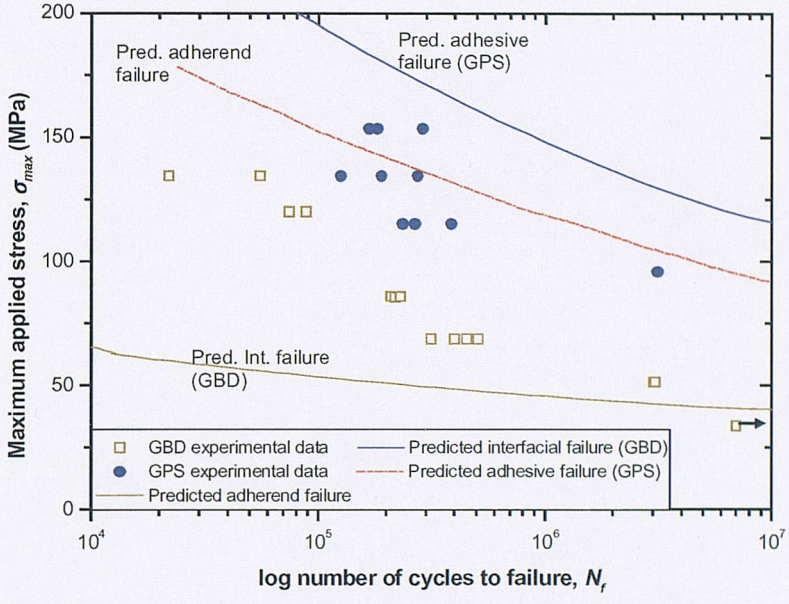


Figure 6.20: Prediction of the 'hot/wet' durability of aluminium alloy scarf joints with a scarf tip thickness of t_{st} = 0.15mm for GBD and GPS surface treatments

Note: 1. Arrow denotes specimens that did not fail
2. All open squares denote interfacial failure
3. All filled circles denote adherend failure

6.4.2.3 CFRP/Al-alloy single hybrid scarf joints [t_{st} = 0.15mm]

The predictions of the fatigue strength and failure locus of the CFRP/aluminium alloy single hybrid scarf joints are given in Figure 6.21. The effect of the residual thermal stress was also included in this analysis (see section 6.3.5.3). It can be seen that the predictions again indicate that the GPS surface treated joints will fail in the aluminium alloy adherend. On the other hand, the GBD surface treated joints will fail at the adhesive/adherend interface. As for the previous investigations, the predicted fatigue strength of the GBD surface treated joints for low number of fatigue cycles appears to be relatively low compared to the experimental results. Further discussions on the possible reasons for this observation are given in section 6.4.3.

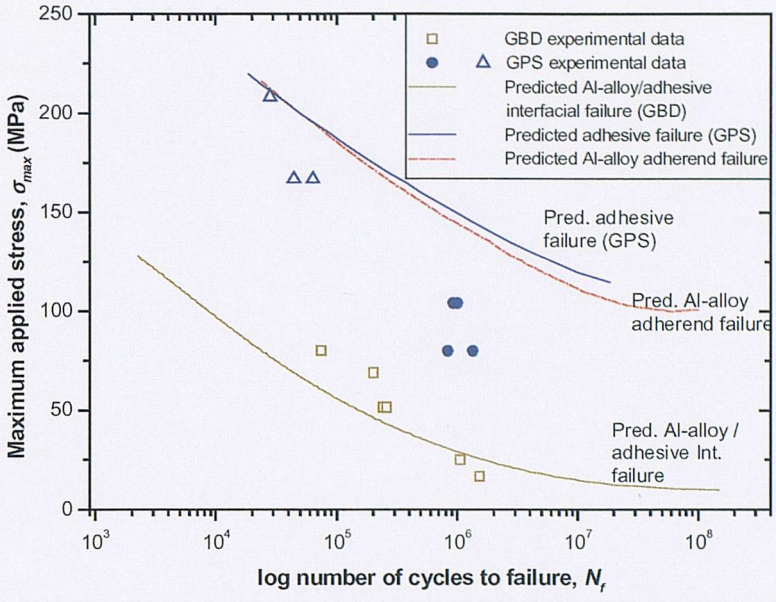


Figure 6.21: Prediction of the 'hot/wet' durability performance of CFRP/aluminium alloy single scarf joints with GBD and GPS surface treated aluminium alloy adherends

Note: 1. All open squares denote aluminium alloy/adhesive interfacial failure
2. All filled circles denote aluminium alloy adherend failure
3. All open triangles denote adhesive failure

6.4.2.3 CFRP/Al-alloy double hybrid scarf joints [t_{st} = 0.15mm]

Figure 6.22 shows the prediction of the fatigue strength for the CFRP/aluminium alloy double scarf joint design. The predictions indicate that the joints would always tend to fail in the aluminium alloy adherend. This compares well with the experimental results where all the joints were found to fail in the aluminium alloy adherend. The reason for this failure locus has been discussed in section 5.4.6.

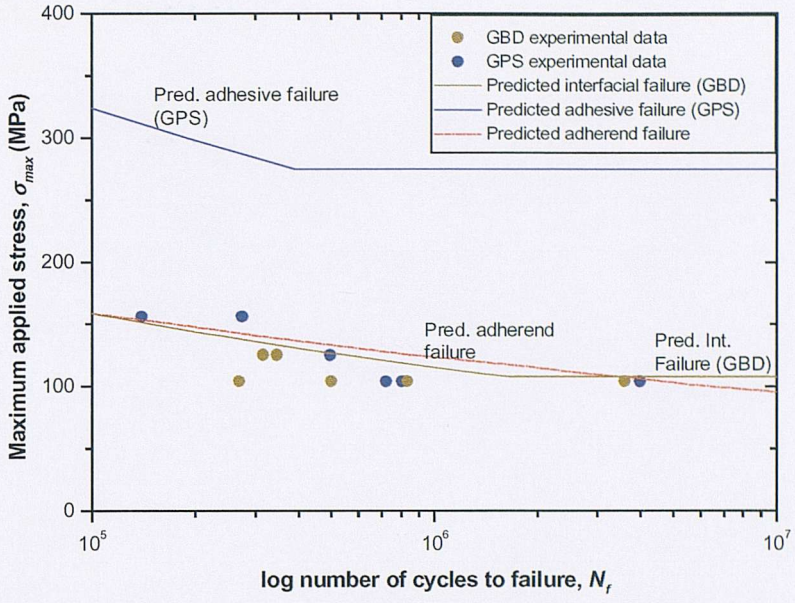


Figure 6.22: Prediction of the 'hot/wet' durability of CFRP/aluminium alloy double scarf joints with GBD and GPS surface treated aluminium alloy adherends

Note: All filled circles denote adherend failure

6.4.3 Discussion

The fatigue life-time of aluminium alloy single scarf joint designs, CFRP/aluminium alloy single and double hybrid scarf joint designs were predicted for three kinds of failure loci. Namely, aluminium alloy/adhesive interfacial failure, adhesive (cohesive) failure and aluminium alloy adherend failure. It was found that the prediction methods were capable of predicting the failure locus of the joints. In addition, the fatigue threshold of the four joint designs was also predicted. Table 6.5 summarizes the failure loci and fatigue threshold of the four joint designs.

Table 6.5: Comparison of the predicted fatigue threshold and failure locus with the experimental results

Joint designs	Surface treatment	Test condition	Experimental failure locus at 10^6 cycles	Predicted failure locus at 10^6 cycles	Experimental fatigue threshold at 10^6 cycles (MPa)	Predicted fatigue threshold at 10^6 cycles (MPa)
Al-alloy / Al-alloy scarf joint, t_{st} = 0.4mm	GBD	dry	Al-alloy adherend	Al-alloy adherend	90.6 ± 16.3	90
	GPS	dry	Al-alloy adherend	Al-alloy adherend	90.6 ± 16.3	90
	GBD	'hot/wet'	interfacial	interfacial	37.5 ± 12.5	37
	GPS	'hot/wet'	Al-alloy adherend	Al-alloy adherend	90.6 ± 16.3	90
Al-alloy / Al-alloy scarf joint, t_{st} = 0.15mm	GBD	dry	Al-alloy adherend	Al-alloy adherend	103.5 ± 17.5	118
	GPS	dry	Al-alloy adherend	Al-alloy adherend	103.5 ± 17.5	118
	GBD	'hot/wet'	interfacial	interfacial	42.5 ± 8.8	46
	GPS	'hot/wet'	Al-alloy adherend	Al-alloy adherend	103.5 ± 17.5	118
CFRP / Al-alloy single hybrid scarf joint, t_{st} = 0.15mm	GBD	'hot/wet'	Al-alloy interface	Al-alloy interface	25*	29
	GPS	'hot/wet'	Al-alloy adherend	Al-alloy adherend	80*	145
CFRP / Al-alloy double hybrid scarf joint, t_{st} = 0.15mm	GBD	'hot/wet'	Al-alloy adherend	Al-alloy adherend	108*	124
	GPS	'hot/wet'	Al-alloy adherend	Al-alloy adherend	108*	124

Note: * Values given without a standard deviation because of lack of experimental data

One of the main problems observed from the predictions of the fatigue life-time of adhesively-bonded joints is the prediction of the fatigue strength at relatively low number of fatigue cycles, N_f, i.e. at relatively high values of the maximum applied stress, σ_{max}, in the fatigue tests. In particular, the predictions for interfacial failure of the GBD treated joints appeared to be poor at low values of N_f. This observation was recorded for all the joint designs tested in the current project. Considering Figure 6.5b, there is a lack of the experimental fracture mechanics data for the GBD treated TDCB joints tested in 'hot/wet' conditions. It has been discussed in section 6.2 that the curve fitting parameters, C_T and n for region 2 of the fracture mechanics data significantly affect the shape and horizontal location of the predicted σ_{max}-N_f curve. Nevertheless, the predictions shown in section

6.4.2 indicate that the predicted fatigue threshold invariably compares well with the experimental results. This is because the predicted fatigue threshold is independent of the curve fitting parameters, C_T, n, n_1 and n_2. In fact, the predicted fatigue threshold is only related to the threshold strain energy release rate, G_{th} and the initial flaw size, a_0, via the relationship between G_{max}, a and T_{max}. However, it has been shown in section 6.1 that a_0 is invariably small and that the relationship between G_{max}, a and T_{max} indicates that the influence of a_0 on the fatigue threshold would be small. Hence, assuming that $a_0 \rightarrow 0$, the fatigue threshold will solely depend on the threshold strain energy release rate. The fatigue threshold of a particular adhesive system and joint design can hence be carried out without using the modified Paris law. Thus, we now have:

$$\sigma_{th} = \frac{1}{w}\sqrt{\frac{G_{th}}{\Theta}} \qquad \text{.....(6.10)}$$

where σ_{th} is the fatigue threshold value of σ_{max}, w is the specimen width, G_{th} is the threshold strain energy release rate and Θ is the constant of the G_{max}, T_{max} and a relationship when $a = 0$. Table 6.6 shows the predictions of the fatigue thresholds of the two adhesive systems and joint designs based on equation 6.10 where poor predictions of interfacial failure was observed in the above investigations, see sections 6.4.2.1 and 6.4.2.2.

Table 6.6: Predictions of the 'hot/wet' fatigue thresholds of the GBD surface treated aluminium alloy scarf joints using equation 6.10

Joint design	Environmental condition/ failure locus	Surface treatment	Predicted fatigue threshold based on equation 6.10 (MPa)	Experimental fatigue threshold (MPa)
Al-alloy scarf joint with scarf tip thickness, t_{st} = 0.4mm	'hot/wet'/ interface	GBD	36	37.5 ± 12.5
Al-alloy scarf joint with scarf tip thickness, t_{st} = 0.15mm	'hot/wet'/ interface	GBD	56	42.5 ± 8.8

Finally, the discrepancy of the predicted fatigue strength at low fatigue cycles may possibly be explained by the increasing significance of the crack initiation period to the total fatigue life of the joints as the fatigue load is increased. The prediction method used to predict adhesive or interfacial failure only considers the crack propagation period.

However, it was shown in section 5.4.7 that the significance of the crack initiation period increases as the applied fatigue load is increased. In addition, it was found that for the aluminium alloy scarf joints, with a scarf tip thickness of t_{st} = 0.15mm, the percentage of the crack initiation period of the total fatigue life of the joints in the regime of 7-50 thousand fatigue life cycles is in the region of 35%. Nevertheless, although this will move the predicted curve towards the right of the graph, it can be surmised that the predictions will still be relatively conservative compared to the experimental results.

6.5 Chapter summary

1. Methods for predicting of the cyclic fatigue strength of the scarf joint designs used in the present project have been given. It was found that the predicted failure loci of the various joint designs tested in the 'dry' and 'hot/wet' environment were in good agreement with the experimental observations.

2. The predictions for interfacial failure using the modified Paris law equation for the GBD surface treated joints tested in 'hot/wet' fatigue conditions were in relatively poor agreement with the experimental results at low numbers of fatigue cycles to failure, N_f. However, the predicted fatigue threshold values of the maximum applied fatigue stress, σ_{th}, were in good agreement with the experimental results.

3. The fatigue strength predictions were also able to show that the GPS surface treated joints will never fail cohesively in the adhesive even in the presence of water. In addition, from experimental observations, the GPS surface treated joints never fail at the adherend/adhesive interface even in the presence of water. This is in good agreement from previous work by Adams where fatigue tests of GPS surface treated TDCB joints also showed no signs of interfacial failure [4].

4. The effect of residual thermal stresses on the fatigue performance of the hybrid joints was predicted and it was demonstrated that they reduced the fatigue strength of the GBD treated single hybrid joints. However, this effect did not significantly affect the fatigue performance of the GPS surface treated joints. This is due to the

relatively high fatigue strength of these joints compared to the values of the residual thermal stresses.

5. It was also shown that the predictions of the fatigue threshold stresses, σ_{th}, could be undertaken without using the modified Paris law. This is noteworthy, since it is suggested from the present results that predicting the fatigue threshold, σ_{th}, would be the preferable route for design engineers to follow.

CHAPTER 7

REPAIRED ALUMINIUM ALLOY PANELS

7.1 Introduction

The previous three chapters have discussed the effects of joint design and surface treatment on the static and fatigue performance of coupon joint specimens. In this chapter the effects of surface treatments on the crack growth rate in panels of cracked aluminium alloy repaired with an adhesively-bonded patch of CFRP is considered. Such repaired panels were tested in both 'dry' and 'hot/wet' fatigue conditions. The aim of this investigation is to compare the fatigue performance of the grit blast and degrease (i.e. GBD) and the silane (i.e. GPS) surface treated aluminium alloy panels. The repair of the crack panels were carried out by adhesively bonding a CFRP composite patch onto a centrally-cracked aluminium alloy panel to give a single-sided repair, see Figure 3.9. Details of the experimental procedure and the materials used have been described in section 3.6.

This crack patched-repair technique has been successfully used in previous work, most notably by Baker [60]. Some of his work was discussed in section 2.8 and in the present research, the same philosophy of a single sided repair of a cracked aluminium alloy panel is used. Clearly, the repair patch serves as an alternative route for an applied load to be transferred from one side of the crack to the other. Thus, the increase in the cross sectional area at the crack will reduce the stress intensity factor, K, at

the crack tip. Apart from the experimental studies, finite element analysis of the crack patched panels was also carried out to predict the reduction of the stress intensity factor of the repaired aluminium alloy panel. A brief discussion of the theoretical analysis of the crack patched-repair technique has been given in section 2.8.2. Further details of the analytical analysis, as well as the finite element analysis, will be discussed in the following sections. Since the aim of this investigation is to investigate the effect of the aluminium alloy surface treatments, the design of the repair patch was not optimized to give optimum repair efficiency. The CFRP composite patches consisted of 16 plies of IM7/8552 CFRP laminae. The stacking order of these composite patches is $[0, \pm 45, 90]_{2s}$; similar to that used in the hybrid scarf joints, see section 5.2.6.

7.2 Experimental results

7.2.1 introduction

The crack-patched repair design is essentially a lap joint configuration. Figure 3.9 shows the geometrical parameters of the repair panel specimens whilst the bonding procedure and experimental details were given in Figures 3.10 and 3.11 respectively. Both the parent and repair components were of the same thickness of 2 mm. The parent component had an overall length of 610 mm and a width of 200 mm. Two 10 mm end plates were mechanically fastened on either ends of the specimen and were then connected to the fatigue machine via a 40 mm diameter pin. The gauge area was 200 x 200 mm. The repair patch covered an area of 100 x 100 mm in the centre of the panel. A hole, 3 mm in diameter, was drilled through the centre of the panel and two notches of length 2 mm were sawed, using a wire saw, through both sides of the hole in the x-direction, see Figure 3.9. The notched panels were then fatigued in tension to initiate two fatigue cracks from both sides of the centre hole. The cracks were fatigued to a length of 8 mm before the panels were repaired with the CFRP composite patch.

Five panels were tested, where one panel was unrepaired and four panels were repaired, all with the same geometrical parameters, see Table 7.1. The un-repaired specimen was used as a control specimen to assess the performance of the repaired panels. The four repair panels were surface treated using either the GBD or the GPS surface treatment. Two specimens were tested in the 'hot/wet' condition, while the other

two specimens were tested in the 'dry' test condition (Descriptions of the GBD and the GPS surface treatments were given in section 3.3).

Fatigue tests were carried out using constant load amplitude control. The maximum applied load, P_{max} was 30 kN and a stress ratio, R of 0.1 was used. A constant fatigue frequency of 3 Hz was employed. Grid lines of 5 mm spacing were drawn on to the un-repaired surface of the panels. A video camera linked to a computer was used to record the crack growth history. In the 'hot/wet' tests, a transparent 'Perspex' water tank was constructed in which the panel was tested with a temperature-controlled water flow at 28°C. Distilled water was used for the 'hot/wet' tests.

Table 7.1: Surface treatment and testing environment of the crack patched repair panels used in this investigation

Panel	Aluminium alloy panel surface treatment	Testing environemt
Unrepaired (1)	-	'dry'
repaired (2)	GBD	'dry'
repaired (3)	GBD	'hot/wet'
repaired (4)	GPS	'dry'
repaired (5)	GPS	'hot/wet'

7.2.2 Fatigue test results

Figure 7.1 shows the crack growth data of the five panels tested. Two cracks originate from the centre hole of each panel and the crack growth of both these cracks is shown in Figure 7.1. The unrepaired cracked aluminium alloy panel gave a fatigue life-time of approximately 30 thousand cycles. On the other hand, the adhesively repaired panels show a significant increase in the fatigue life-time of the panels compared to the unrepaired panel.

The GBD treated panel tested in the 'hot/wet' condition was the first repaired panel to fail, where the fatigue life-time is approximately 200 thousand cycles. This is an increase of approximately 600% compared to the unrepaired panel. It was observed that interfacial failure had occurred at the adhesive/aluminium alloy adherend interface.

Further discussion of the failure locus will be given in the next section. The GBD treated panel tested in 'dry' condition, however, showed a fatigue life-time of approximately 300 thousand cycles. Interfacial failure at the adhesive/aluminium alloy adherend interface was observed to occur over about half of the fracture surface, while CFRP delamination was observed over the other half, see Figure 7.3. This will be further discussed in the next section. Comparing both of the GBD treated repair panels, a reduction of approximately 30% of the fatigue life-time of the panels was observed for the GBD treated panel tested in the 'hot/wet' condition when compared to the GBD treated panel tested in the 'dry' condition.

The GPS treated panel tested in the 'hot/wet' condition gave a fatigue life-time of approximately 290 thousand cycles. This is comparable to the GBD treated panel tested in the 'dry' condition. However, the longest serving repair panel was the GPS treated panel tested in the 'dry' condition. This panel was able to sustain approximately 340 thousand cycles before catastrophic failure at the fastener holes in the bottom loading plates. This is an increase of approximately 1100% of the fatigue life-time compared to the unrepaired panel. The reason for the catastrophic failure at the fastener holes is further discussed in the next section. Nevertheless, the left hand crack in the panel was able to propagate to the left hand free surface of the panel before the occurrence of the catastrophic failure at the fastener holes.

For the five panels tested, the two cracks propagating from the centre hole appeared to propagate in a symmetrical fashion, although not necessarily at the same propagation rate. Generally the cracks propagated in the plane of the x-axis. The growth rate of the two cracks showed a larger discrepancy when the crack length exceeded the length of the bonded region, see Figure 7.1. This is probably due to the misalignment of the bonded patch at the centre of the panel.

An approximation of the crack growth rate of the experimental tests described previously could be carried out by taking the slope of the curves shown in Figure 7.1. The crack growth rate data can then be plotted against crack length to investigate the changes in crack growth rate as the crack length increases, see Figure 7.2.

According to the Paris Law, the log of the crack growth rate, *da/dN* is proportional to the log of the stress intensity factor, *K*. Similarly, this can be rewritten, for a given maximum stress level, by relating the crack growth rate, *da/dN* to the crack length, *a*: since *K* is directly proportional to the square root of the crack length, *a*. For the unrepaired panel, a straight line of log *da/dN* as a function of log *a* could be used to approximate the data, see Figure 7.2. On the other hand, the data for the repaired panels were fitted by taking the average of the data points. This curve fitting method, although crude, is sufficient to show the general trend of the crack growth rate of the repaired panels. As can be seen from Figure 7.2, there is considerable scatter in the graph for the repaired panels. Nevertheless, it may be seen that the curves for the repaired panels all exhibit a low crack growth rate before approaching the edge of the repair patch, i.e. $a <$ 50mm, when compared to the unrepaired panel. However, as the cracks propagated pass the repair patch, i.e. $a >$ 50mm, the crack growth rate appears to increase significantly, and catastrophic failure rapidly follows.

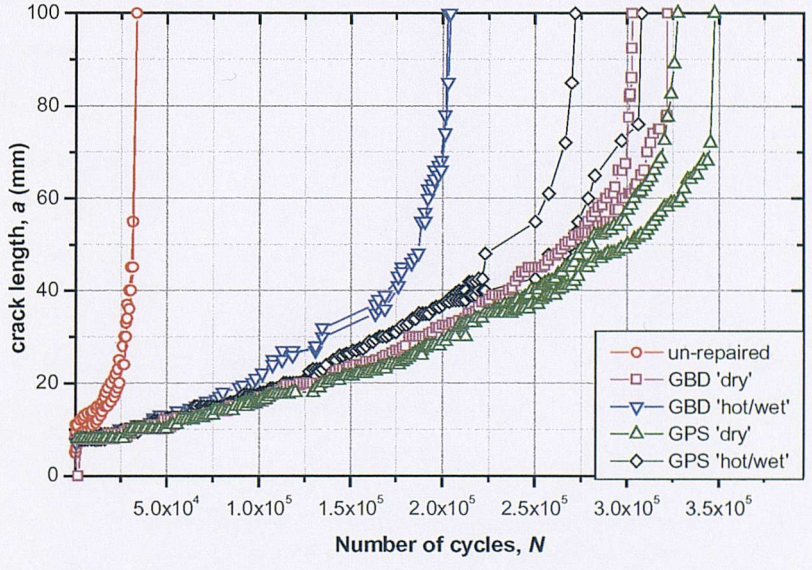


Figure 7.1: Comparison of fatigue the crack growth of un-repaired and repaired panels for the GBD and GPS surface treatments

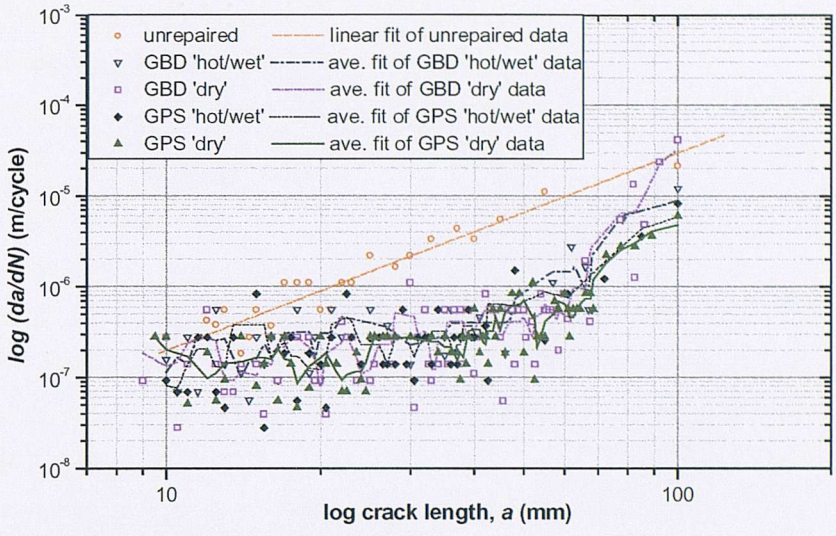


Figure 7.2: Comparison of the fatigue crack growth rate between the repaired and un-repaired crack patched panels

Note: ave.fit denotes where the average of three adjacent data points were taken to calculate the average fit of the data points

7.2.3 Failure loci of crack patched repair panels

It was observed that final fracture, via rapid crack growth, of the repair panels occurred after the fatigue cracks have propagated approximately 80% of the width of the panel. Figure 7.3 shows the fracture surface of the GBD treated panel tested in 'dry' condition. It can be observed that the fracture surface can be approximately divided in half, where one part shows CFRP delamination whilst the other shows a mixture of cohesive and adhesive/aluminium alloy failure. The cohesive failure mechanism can be observed to mainly occur at the centre of the fracture surface, i.e. away from the boundaries of the fracture surface. On the other hand, the adhesive/aluminium alloy interfacial failure was observed to be mainly located near the boundaries of the fracture surface. Cohesive failure, as well as CFRP delamination, is most probably caused by the sudden tearing of the joint as final fracture occurs. On the hand, the interfacial failure around the boundaries of the repair patch can be attributed to the effects of fatigue loading.

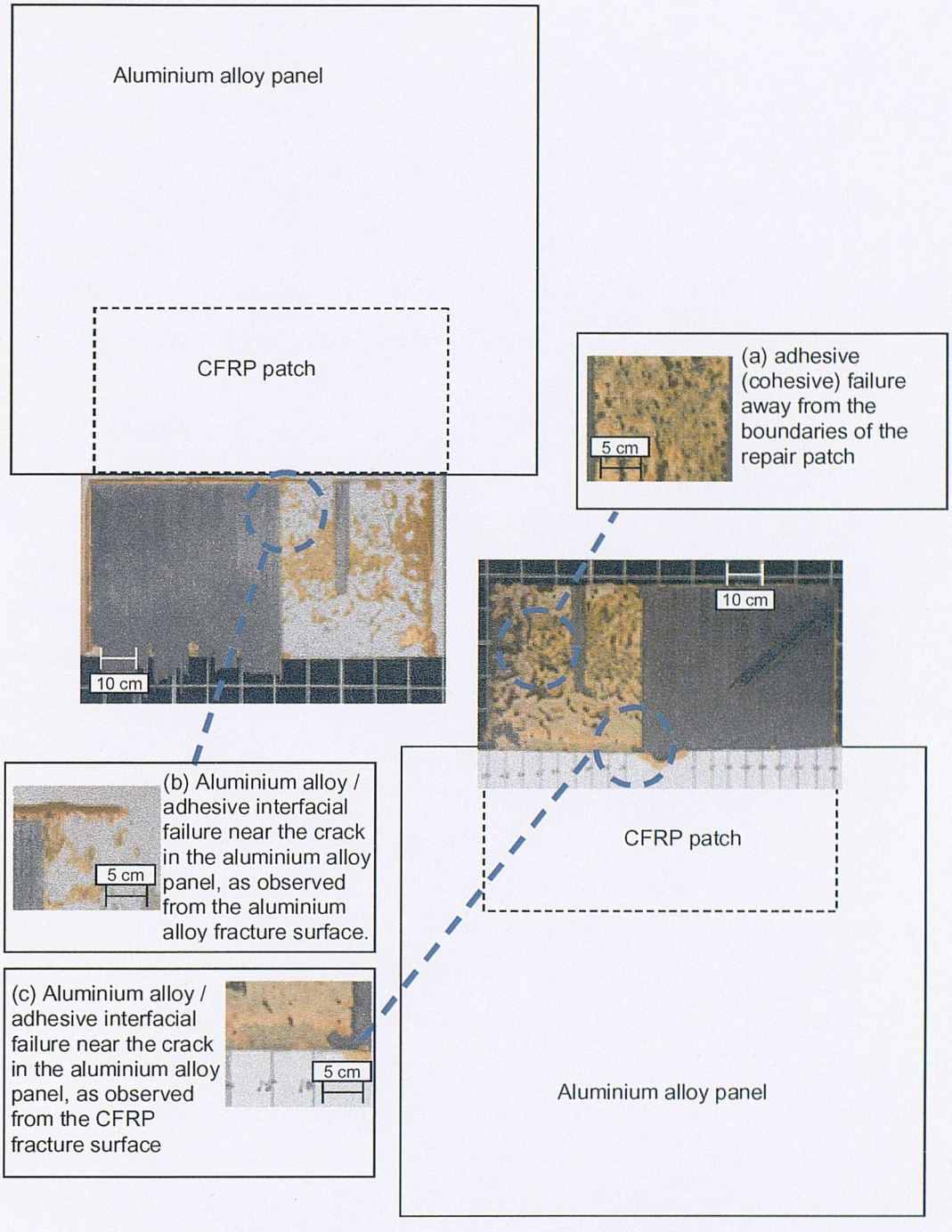


Figure 7.3: Fracture surface of the GBD 'dry' specimen (a) adhesive failure (b) adhesive/aluminium alloy adherend interfacial failure viewed from the aluminium alloy fracture surface(c) adhesive/aluminium alloy adherend interfacial failure viewed from the CFRP composite fracture surface

In the case of the GBD treated panel tested in the 'hot/wet' condition, the fracture surface of the bonded region shows that water had attacked the integrity of the adhesive bond around the boundaries of the patch, since interfacial failure can be clearly seen in Figure 7.4. Comparing Figures 7.3 and 7.4, it can be clearly seen that the presence of

water had adversely affected the integrity of the adhesive bond to the aluminium alloy adherend. Evidence of final fracture was observed at the middle of the patch where adhesive tearing was observed. However, unlike the GBD treated panel tested in the 'dry' condition, significant CFRP delamination was not observed. In contrast to the GBD treated panel tested in 'dry' condition, the lack of CFRP delamination, as well as the widespread interfacial failure at the adhesive/aluminium alloy interface, suggested that the GBD treated panel tested in the 'hot/wet' condition has lost considerable strength during the cycle fatigue loading before the occurrence of final fracture.

The GPS 'dry' specimen failed catastrophically at the fastening bolts in the lower end plates. Residual thermal stresses in the panel caused by the high temperature curing of the adhesive resulted in a slightly distorted specimen. Hence, when fatigued it was observed that significant bending in the specimen was present. However, final fracture of the panel occurred after the left hand crack had reached the free surface of the panel and the right hand crack had reached a length of 80 mm. Hence, it is believed that the crack growth data is not significantly compromised by the presence of the residual stresses.

The GPS 'hot/wet' specimen shows no clear sign of moisture ingress into, and attack upon, the adhesive bond. In fact fibre failure in the composite appears to be the main failure mechanism, see Figure 7.5. Interfacial failure was observed at the right hand side edge of the repair patch. However, the separation appears not to be confined to a single interface, but to occur randomly from both interfaces. Some form of crack propagation during the fatigue life of the panel could have occurred here. However, the relatively low percentage of interfacial failure throughout the adhesive bond suggests that, even if the integrity of the adhesive bond has been compromised during the fatigue history of the panel, the ultimate failure mechanism of the repair patch is due to fibre breaking at the centre of the patch. This illustrates the considerable durability advantage offered by the GPS surface treatment compared to the GBD surface treatment. In fact, the GPS surface treatment shows little reduction in fatigue performance when fatigued in the 'hot/wet' condition, see Figure 7.5, compared to that seen in the 'dry' condition.

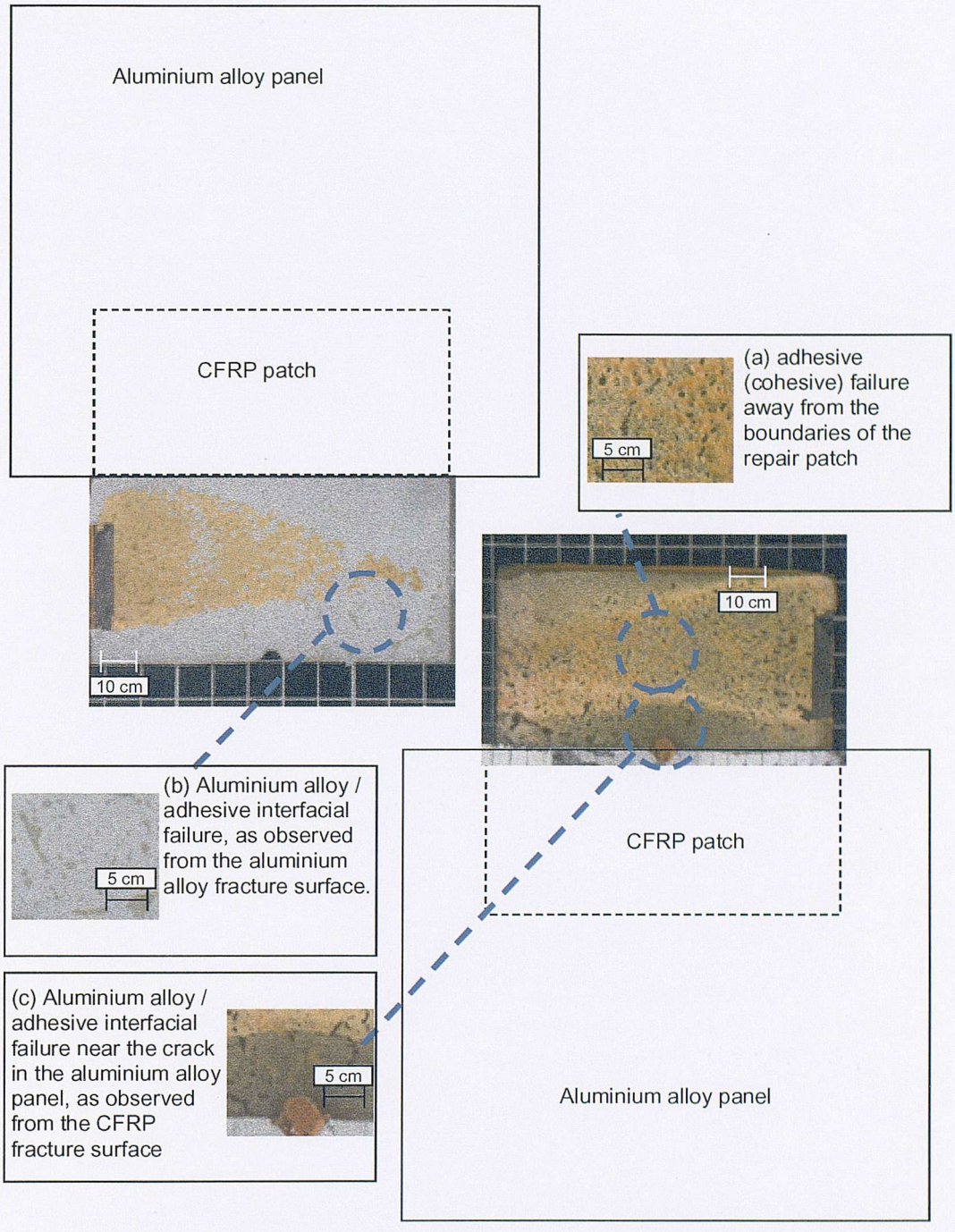


Figure 7.4: Fracture surface of the GBD 'hot/wet' specimen (a) adhesive failure (b) adhesive/aluminium alloy adherend interfacial failure viewed from the aluminium alloy fracture surface (c) adhesive/aluminium alloy adherend interfacial failure viewed from the CFRP composite fracture surface

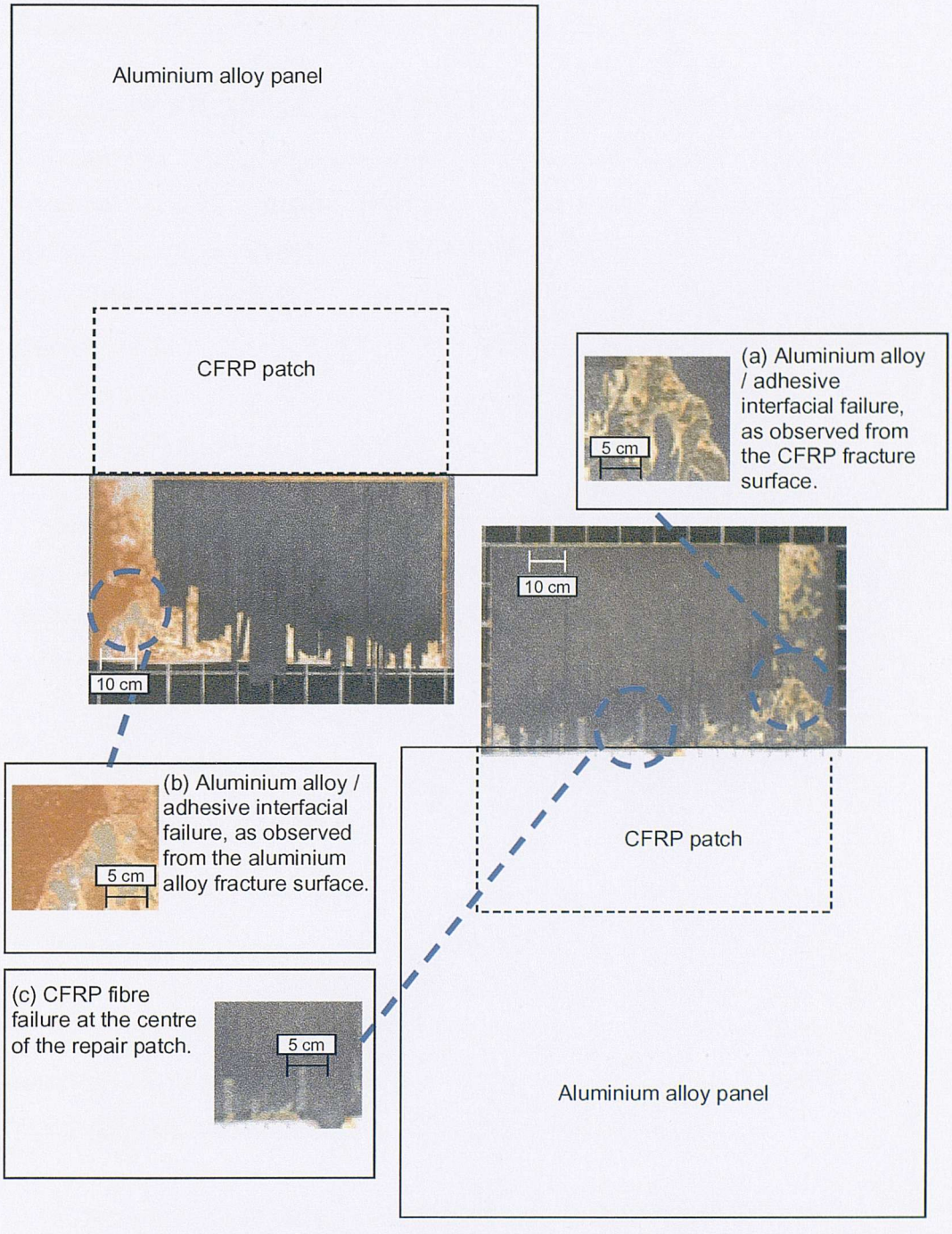


Figure 7.5: Fracture surface of the GPS 'hot/wet' specimen (a) adhesive/aluminium alloy adherend interfacial failure viewed from the CFRP composite fracture surface (b) adhesive/aluminium alloy adherend interfacial failure viewed from the aluminium alloy fracture surface (c) CFRP fibre failure at the centre of the repair patch

7.3 Analytical and Numerical analysis of crack patching

7.3.1 Analytical calculation of stress intensity factors, K_u and K_r

Description of the two-stage analytical solution of a single-sided crack patch analysis developed by Rose [76] was reviewed in section 2.8.2. It was noted that the stress intensity factor of a repaired panel, K_r can be extrapolated from two bounds; namely the stress intensity factor for an unrepaired panel, K_0, and the stress intensity factor for a semi-infinite crack in a single-sided crack patch repair, K_∞, see equations 2.35 - 2.40.

In order to calculate the stress intensity factor of the un-patched panel, the constants C_T and n were obtained from Figure 7.2 by curve fitting the log da/dN vs. log a curve for the un-patched panel, see equation 7.1. The stress intensity factor for an un-patched panel, K_u, can be expressed by equation 7.2:

$$\frac{da}{dN} = C_T K^n \quad \text{.....(7.1)}$$

$$K_u = Q\sigma^\infty \sqrt{\pi a} \quad \text{.....(7.2)}$$

where σ^∞ is the applied stress, Q is the geometry factor and a is the crack length. In order to simplify the equations, the geometry factor, Q, is assumed to be unity. (This is, however, not strictly true, since when the crack length, a, is comparable with the width of the specimen, the geometry factor becomes somewhat larger than unity [85]. Thus, the following analysis could be improved by incorporating a function for the geometry factor, Q, depending on the ratio of crack length versus specimen width.)

Now, for a crack patched panel, the stress intensity factor, K_r, will also depend on the stiffness ratio of the parent material, as well as the patch material, and also the elastic strain constant, β, see equations 2.35-2.39. The stress intensity factor for a crack patched panel was given in equation 2.40 as:

$$K_r = \sigma_0 \sqrt{\frac{\pi a \mathrm{A}}{a + \mathrm{A}}} \quad \text{.....(2.40)}$$

where σ_0 is the near field equivalent stress, a is the crack length and A is a characteristic length that is related to the material and geometrical properties of the repair design, see equation 2.37.

Rose [76] has shown that in order to solve the stress intensity factor of a crack patched panel, the equivalent crack opening stress, σ_0, has to be derived from the far field applied stress, σ^{∞}. However, here we use the far field applied stress, σ^{∞}, instead of the near field equivalent stress, σ_0, in the calculation of the stress intensity factor for the crack repaired panels. There are two reasons for doing this. The first is because it is somewhat complex to derive, analytically, the equation for the equivalent crack opening stress, σ_0, because it depends on the shape of the repair patch. (Rose had shown that by using an elliptical shaped repair patch, the stress is uniform within the repair patch region and hence the relationship between σ_0 and σ^{∞} can be analytically derived.) Secondly, Rose has also shown that for values of the ratio between the crack length and the characteristic length of a repair panel, a/A, larger than one, the reduction of stress from the far field applied stress, σ^{∞}, to the equivalent crack opening stress, σ_0, becomes less significant when compared to the characteristic length, A. For the experiments carried out here, A = 0.005 and $0.008 < a < 0.05$. Hence, the ratio, a/A is significantly greater than one.

7.3.2 Effect of bending on single sided repairs

The effect of bending in the panel, caused by the eccentricity of loading in a single sided repair panel can be quantified by a second characteristic length, $A1$, as described by Rose [76] and see equation 7.3.

$$A1 = A(1+\Omega) \quad \text{.....(7.3}a\text{)}$$

$$\Omega = \frac{1}{2}\left\{S\left(\frac{E_p}{\sigma^{\infty}}\right)(\Delta t)^2 \beta\chi_r\right\} g\{\chi_r H;\kappa_r\} \quad \text{.....(7.3}b\text{)}$$

$$\chi_r = \left\{(1+S)\sigma^{\infty} t_p/(EI)_r\right\}^{1/2} \quad \text{.....(7.3}c\text{)}$$

$$g(x;\kappa) = \left(x + \sinh x \cosh x + k \sinh^2 x\right)/(\cosh x + k \sinh x)^2 \quad \text{.....(7.3}d\text{)}$$

$$\kappa_r = \left\{(EI)_{rp}/(EI)_r\right\}^{1/2} \quad \text{.....(7.3}e\text{)}$$

where E is the Young's modulus, t is the thickness, EI is the bending stiffness and S is the stiffness ratio (see equation 2.38). The subscripts r and p denote the repair adherend and the parent adherend respectively.

Substituting $A1$ into A in equation 2.40 gives the stress intensity factor of the repair panel including bending effects. Figure 7.6 compares the predicted stress intensity factor of the crack patch panels, K_r, with and without including the effect of bending. It can be seen from Figure 7.6 that the stress intensity factor of the unrepaired panel increases with an increase in the crack length. On the other hand, the predicted stress intensity factor for the repaired panels indicates a plateau region as the crack length increases (i.e. $a/A > 1$). In addition, by including the effect of bending into the analytical analysis, via equations 7.3, the predicted stress intensity factor for the crack patch panels is reduced by approximately 60%.

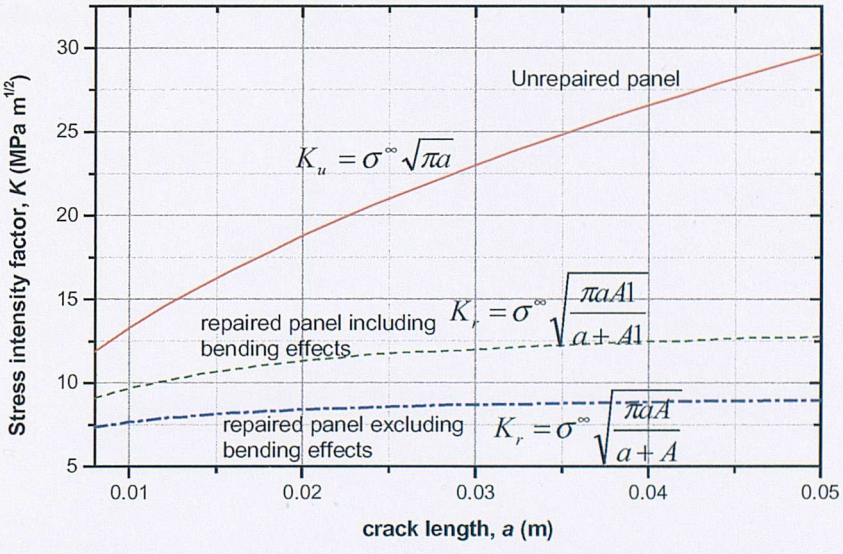


Figure 7.6: Comparison between the stress intensity factor for the unrepaired panel, K_u and the repaired panels, K_r with and without bending effects

7.3.3 Finite element calculation of $K_I(a)$

The repair panels were modelled using eight-noded brick elements in a 3-dimensional FE analysis. As the panels are symmetrical about the y- and x-axis planes, a quarter of the panels was modelled, see Figure 7.7. The aluminium alloy panels were modelled with five layers of elements across the thickness of the panel. The adhesive was modelled with one layer of elements and the carbon fibre composite was modelled with 16 layers of elements with orthotropic material properties. All three materials were modelled as elastic materials. Nonlinear geometrical deformations were allowed in the model. A crack was inserted into the model at the x-axis plane, initiating from the origin of the x-y plane, see Figure 7.7. Crack lengths, a of 10 mm, 25 mm, 50 mm and 60 mm were modelled.

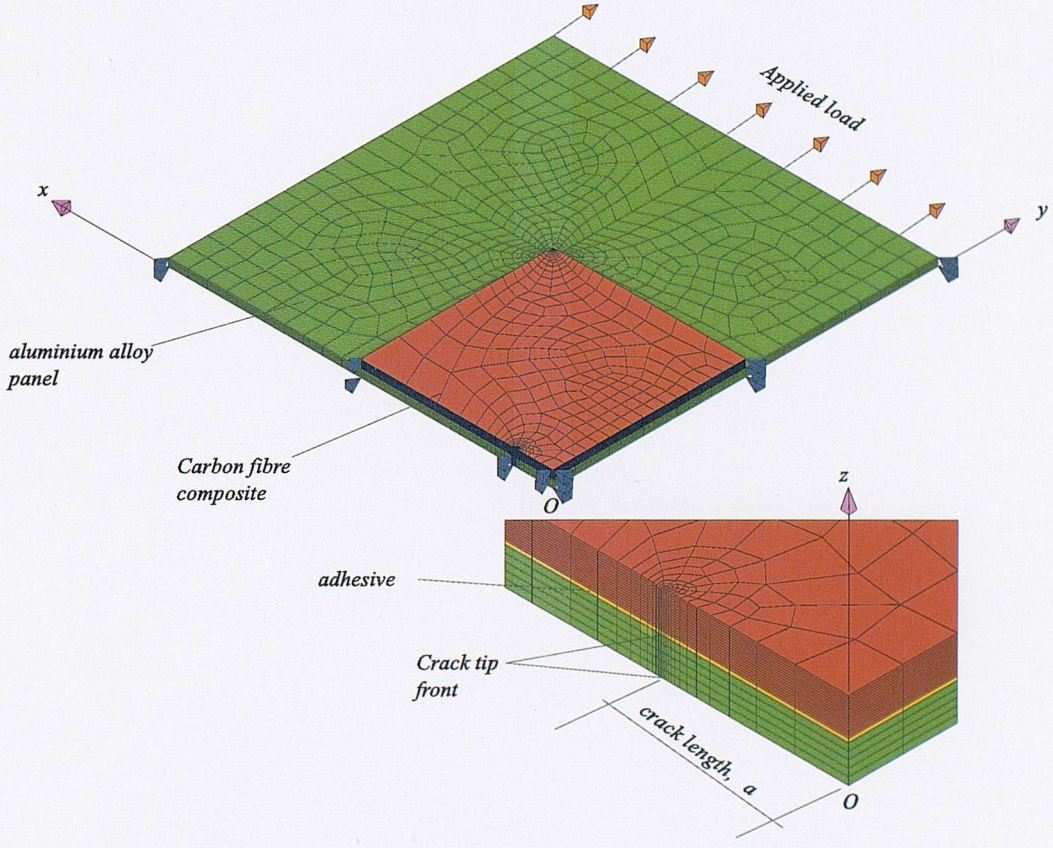


Figure 7.7: Quarter FE model of a repair panel and insert showing a blow-up view of the crack tip

Figure 7.8 shows a close-up view of the Mises equivalent stress distribution around the crack tip. The figure clearly shows a non-uniform stress field across the thickness of the aluminium alloy panel as a result of the non-symmetrical nature of the repair panel along the z-plane. At the free end of the aluminium alloy panel, the stress distribution shows a typical mode I stress contour around the crack tip. This indicates that mode I failure is dominant at the free surface and hence, the use of the *J*-integral to predict G and K_r will be valid near the free surface of the aluminium alloy panel.

The strain energy release rate, G was calculated for these crack lengths using the *J*-integral method. The definition of the *J*-integral was given in section 2.6.5.2. Using linear elastic fracture mechanics assumptions, J is equal to G and is related to the stress intensity factor according to equation 2.35. The *J*-integral was calculated from six positions across the thickness of the aluminium alloy panel. The slope of the *J*-integral against the applied load per unit width, T_{max}^2 for each crack length was obtained. Figure 7.9 shows the variation of G/T_{max}^2 against crack length for the six positions across the thickness of the panel. It can be seen from Figure 7.9 that the strain energy release rate decreases as it approaches the patched side of the panel. This is consistent with the Mises stress distribution shown in Figure 7.8. The relationship between G/T_{max}^2 and a can be fitted using a hyperbolic function. Substituting T_{max}^2 with $\sigma^{\infty} t_p$, where t_p is the thickness of the aluminium alloy panel and using equation 2.40, a relationship for K_r as a function of the crack length, a, may be obtained at the free surface of the aluminium alloy panel, i.e. $z = 0$mm, see equation 7.4.

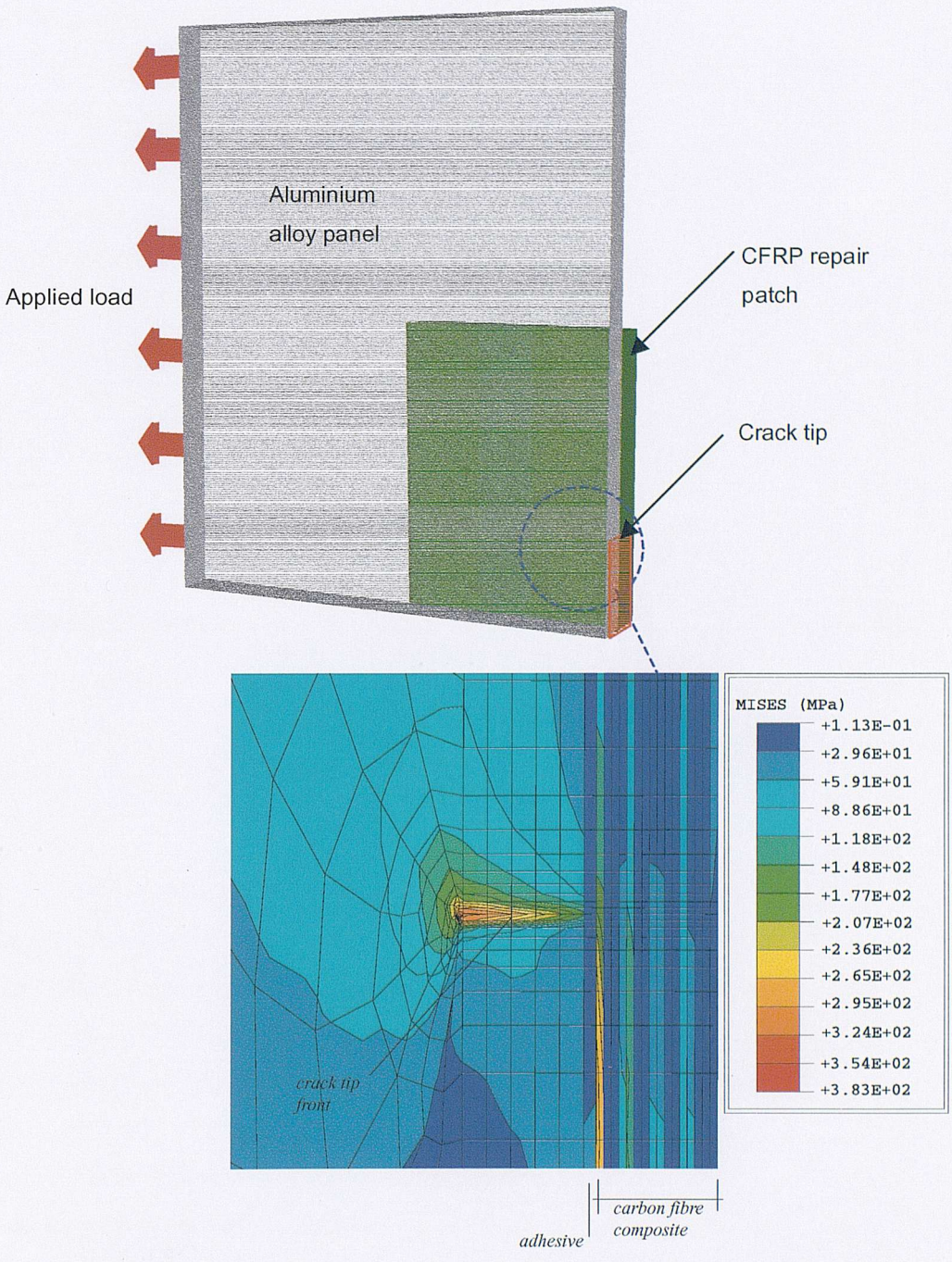


Figure 7.8: Mises stress distribution at the crack tip for with an applied stress of 75MPa

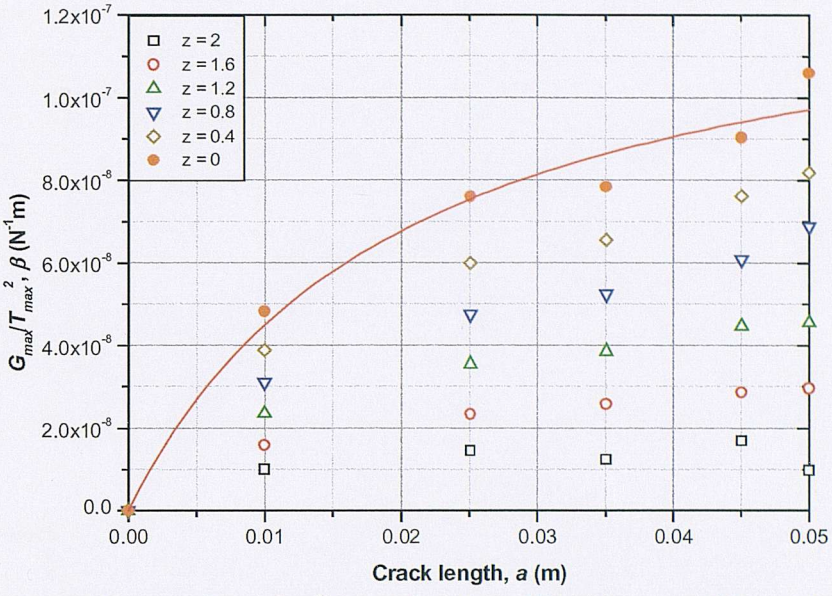


Figure 7.9: Variation of G_{max}/T_{max}^2 for different crack lengths, *a*, at different locations across the thickness of the aluminium alloy panel

$$K_r = \sigma^{\infty} t_p \left\{ E\left(\frac{1.37 * 10^{-7} a}{0.0204 + a} \right) \right\}^{\frac{1}{2}} \quad \text{.....(7.4)}$$

Using equation 7.4 and plotting for 8mm < a < 50 mm (i.e. within the repair patch length), the FE predicted stress intensity factor for the crack patch panels, K_r, compares well with the above analytical analysis, see Figure 7.10. It is interesting to note that the two methods of obtaining the stress intensity factor for the repair panels gave the same hyperbolical form for K_r as a function of crack length, a.

The predicted stress intensity factor as a function of crack length could now be used to predict the fatigue life-time of the repair panels by relating the stress intensity factor with the crack growth rate, as in a typical Paris crack growth equation, see equation 7.1. However, this requires significantly more experimental and theoretical work to be undertaken and hence due to time constraints this was not pursued in the present project.

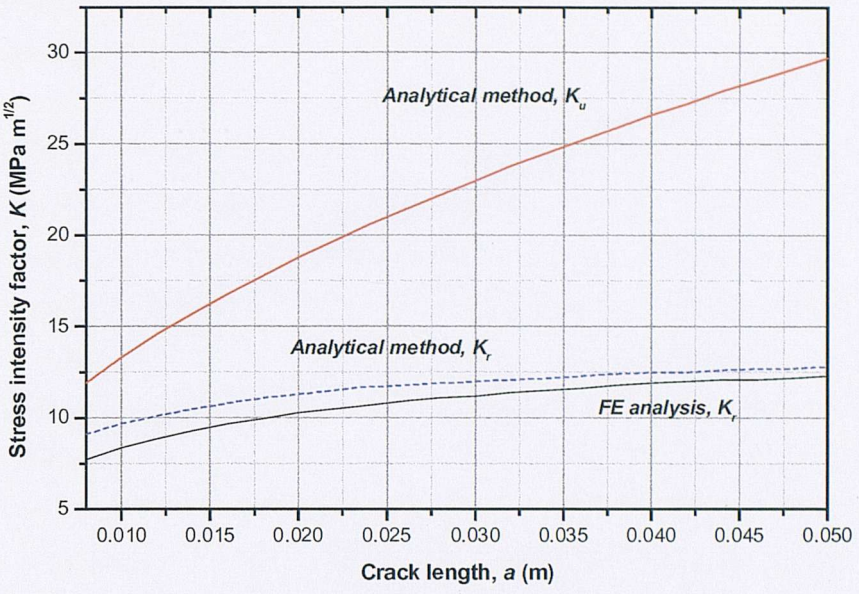


Figure 7.10: Comparison between finite element and analytical predictions of the repair stress intensity factor, K_r. (K_u is for the unrepaired panel)

7.4 Further Considerations

The use of small scale repair panels to investigate the viability of adhesively-bonded repairs further justified the use of such techniques for aerospace structures. The method illustrated here could however be improved by incorporating more factors into the prediction of the life-time of the repair panels. Due to time constraints, these factors were not incorporated into the present analysis.

The suggested factors that could more accurately predict the life-time of adhesively-bonded repair panels are listed below.

1. The incorporation of a thermal-mechanical analysis where the contribution of residual thermal stresses in the adhesive as well as the bonded repair panel is included into the analysis. It was found from the experiments carried out in the present project that the repair panels were distorted due to the relatively high temperature curing adhesive. In addition, the adhesive and adherends exhibited different coefficients of thermal expansion. This induced distortion of the repair

panel will change the stress distribution in the panel when it is loaded in the fatigue tests.

2. The present analysis assumes that the geometrical factor, Q, is unity for all crack lengths. This is not strictly true, as when the crack length increases and becomes comparable with the specimen width, the geometrical factor, Q, increases. This will in turn increase the values of the predicted stress intensity factors.

3. A more accurate method to record crack growth rates in the repair panel as well as at the bonded (i.e. repaired) region is required. This is particularly important as the crack growth rate in the aluminium panel is predicted to grow at different rates across the cross sectional area of the panel. Furthermore, the current method of recording crack growth does not provide information about the integrity of the adhesive bond.

7.5 Chapter Summary

1. Fatigue testing in 'dry' and 'hot/wet' conditions using crack aluminium alloy panels which were repaired using an adhesively-bonded CFRP repair patch were performed to investigate the effect of surface treatment of the aluminium alloy on the fatigue strength of the repair panels. Four repair panels were used, where two were treated using the GBD surface treatment, whereas the other two panels were treated using the GPS surface treatment. Fatigue tests were carried out in both 'dry' and 'hot/wet' test conditions.

3. Crack growth in the GBD repair panel tested in the 'hot/wet' fatigue conditions experienced a relatively high growth rate compared to the other three repair panels. The fatigue life of the GBD repair panel tested in the 'hot/wet' fatigue conditions was approximately 200 thousand cycles. On the other hand, the other repair panels were able to sustain a life of approximately 300 thousand cycles.

4. It was found that, using a 'hot/wet' test condition, the silane surface treated repair panels did not show any significant increase in the crack growth rate compared to test carried out in the 'dry' test condition. Thus, the GPS treatment is very effective at preventing loss of integrity of the bonded repair under 'hot/wet' test conditions.

5. Significant interfacial debonding was observed at the adhesive/aluminium alloy interface for the GBD surface treated crack patch panel tested in 'hot/wet' conditions, whilst, the other three repair panels mainly failed in the CFRP composite.

6. The predicted stress intensity factor, as a function of crack length, for the repair panels using FE analysis were in good agreement with the results obtained using the analytical approach proposed by Rose [76]. It was found that for a crack tip at the edge of the repair patch (i.e. $a = 50$mm), the repair stress intensity factor, K_r, is approximately 12.5MPam$^{0.5}$. This is significantly lower in value than that for the unrepaired panel (i.e. $K_u = 30$MPam$^{0.5}$).

CHAPTER 8

CONCLUSIONS AND RECOMMENDATIONS FOR FUTURE WORK

8.1 Introduction

A main aim of the present project was to investigate durability in an aqueous environment, under cyclic fatigue loading, of adhesively-bonded aluminium alloy and carbon fibre reinforced plastic (CFRP) joints which are typical of those used for repairing cracked aerospace structures. A second aim was to study the effect of pretreating the aluminium alloy by using a γ-glycidoxypropyltrimethoxysilane (GPS) organosilane surface treatment. The present project can be divided into four sections. The first is the optimization of the scarf joint design, which was selected as the main joint design in the present project, for optimum joint strength. Secondly, this was then followed by static and fatigue testing of these joints, and fatigue tests were also carried out in both 'dry' and 'hot/wet' test conditions. Thirdly, analytical, as well as finite element, approaches were developed to predict the failure locus and failure strength of the joints under monotonically-loaded testing conditions. In addition, the fatigue life-times of the adhesively-bonded joints were also predicted. Finally, small scale repair panels were tested in both 'dry' and 'hot/wet' fatigue conditions.

8.2 Conclusions

The following points summarise the main findings and conclusions of the project. The conclusions will be divided into four sections, in line with the four chapters given from Chapter Four to Seven.

8.2.1 Optimization of the scarf joint design

Three geometrical design parameters of the scarf joint design were optimized. These were the scarf tip thickness, scarf angle and the adhesive fillet size. In addition, the effect of the temper grade of the aluminium alloy adherend was also investigated. Lastly, the strength of the scarf joint design was compared with the overlap joint design. The following points highlight the main conclusions from this investigation.

1. It was found that an increase of the scarf tip thickness increased the stress concentrations at the overlap terminus. In addition, increasing the scarf tip thickness also increased the stress concentration in the adherend opposite the scarf tip. The experimental results showed that for scarf joints, with an adherend thickness of t = 2mm, a scarf angle, θ = 1.8° and a scarf tip thickness of t_{st} = 0.4mm and 0.15mm, loaded monotonically, failure occurred in the adherend opposite the scarf tip. This was indeed as predicted using the elastic-plastic finite element analysis.

2. Increasing the scarf angle increased the stress concentrations in the adhesive and the adherend. However, the effect of the scarf angle on the stress concentration in the adherend was relatively small compared to that in the adhesive. It was also found, from the elastic finite element analysis, that for a scarf angle, $\theta > 2°$, the increase in the shear stress component in the adhesive was significantly high when compared to scarf joints with scarf angles, $\theta < 2°$. This indicated that failure in the adhesive would be more likely for scarf joints with scarf angle, $\theta > 2°$. Elastic-

plastic finite element analysis and experimental testing of scarf joint specimens with scarf angles, θ = 1.5°, 1.8° and 5° showed that for scarf joints with scarf angles, θ = 1.5°, 1.8°, failure in the adherend was observed. On the other hand, for scarf joint specimens with a scarf angle of 5°, failure was observed to occur in the adhesive. This change in failure locus was also accompanied by a decrease in joint strength. The experimental results were in very good agreement with the predictions from the elastic-plastic finite element studies.

3. The effects of the adhesive fillet size and adhesive fillet entry angle for the scarf joint design were investigated using elastic finite element analyses. It was found that the peel stress component in the adhesive fillet was the most affected by changes in the adhesive fillet size. However, the percentage reduction of the maximum peel stress in the adhesive fillet did not vary significantly for the normalized fillet length, $l_f/L_f > 0.2$. It was also found that the maximum stress components at the overlap terminus were not affected by the change in adhesive fillet entry angle.

4. The effect of the temper grade of the aluminium alloy adherends was investigated using elastic-plastic finite element analysis and experimental testing. It was found that for scarf joints employing the L156 (T4) aluminium alloy adherends that a significant improvement in the joint ductility was observed. However, the joints yielded at a lower load compared to the scarf joints manufactured using the L157 (T6) aluminium alloy adherends. These observations were similar to the comparison between the stress-strain relationships of these two alloys, where it was observed that the L157 (T6) aluminium alloy has relatively high yield strength but low ductility when compared to the L156 (T4) aluminium alloy. It was also found that the scarf joints using the L156 (T4) aluminium alloy adherends failed in the adhesive, while the scarf joints with the L157 (T6) aluminium alloy adherends failed in the adherend. The experimental results were in good agreement with the predictions from the elastic-plastic finite element analyses.

5. A comparison between the scarf joint design and the overlap joint design was undertaken using elastic finite element analysis, elastic-plastic finite element analysis and experimental testing. Interestingly, it was found that from the elastic finite element analysis the overlap joint was predicted to possess a lower tensile strength when compared to the scarf joint design. On the other hand, the elastic-plastic finite element analysis predicted that the overlap joint design was significantly stronger than the scarf joint design. This latter prediction was in agreement with the monotonically-loaded tests carried out on the scarf joint and overlap joint designs.

6. The scarf joint and overlap joints were also tested under fatigue loading. It was found from the fatigue tests that the fatigue strength of the scarf joint design was higher than the overlap joint design. Hence, was concluded from both the experimental and analytical results that, due to the reduced loading eccentricity in the scarf joint design, the scarf joint design will exhibit better fatigue behaviour than the overlap joint design; providing the yield stress of the adhesive and the adherend are not exceeded. On the other hand, because of the reduced cross section area of the adherends in the scarf joint, the static tensile strength of the scarf joint design will be lower than that of the overlap joint design.

8.2.2 Effects of surface treatments – coupon test results

The effects of changing the surface treatment were investigated by performing tests under monotonically-loaded and fatigue loading. The fatigue testing was carried out in both 'dry' and 'hot/wet' conditions. The following points highlight the main conclusions from these investigations:

1. From the monotonically-loaded tests, it was found that the failure locus and failure loads of the joints depended not only on the surface treatment employed but also on the joint design and the material behaviour of the adherends. For all the joint designs investigated (i.e. aluminium alloy scarf joints and overlap joints, CFRP/aluminium alloy hybrid single and double scarf joints, see Figure 3.5), it was found that the static failure loads and failure loci of the joints using a silane (i.e. γ- glycidoxypropyltrimethoxysilane (GPS)) and chromic acid etching (i.e.

CAE) surface treatments were essentially the same. The GPS and CAE surface treated joints failed either in the adhesive, or in the aluminium alloy adherend. In addition, it was found that, whether failure occurred in the aluminium alloy adherend or in the adhesive, both treatments yielded approximately the same failure loads.

2. In the monotonically-loaded tests, the GBD surface treatment for the aluminium alloy adherends sometimes led to interfacial failure in the joints. This resulted in a decrease in the joint strength of approximately 10% compared to that measured for the GPS and CAE surface treated joints. This was observed for three of the joint designs tested: namely (a) the aluminium alloy scarf joints with a scarf tip thickness of t_{st} = 0.15mm with aluminium alloy adherends 2014A 'L157' (T6), (b) 'L156' (T4), and (c) the single CFRP/aluminium alloy hybrid scarf joints. On the other hand, the grit-blast and degrease (GBD) surface treatment did not cause a significant difference to the joint strength or a change in the failure locus of (a) the aluminium alloy scarf joints with a scarf tip thickness of t_{st} = 0.4mm, (b) the aluminium alloy overlap joints and (c) the double CFRP/aluminium alloy hybrid scarf joints. These results could be explained by the fact that the GBD surface treatment might indeed cause a relatively weak adhesive/adherend interface, but this will only be apparent if the joint design and the choice of adherend materials allow the interface to be subjected to relatively high stresses.

3. The static failure loads of the various joints tested in this investigation were relatively high when compared to the ultimate tensile strength of the aluminium alloy adherends. The highest joint efficiency recorded was in the region of 93%. This was observed for three joint designs: (a) the scarf joint design with a scarf tip thickness of t_{st} = 0.15mm and 'L157' (T6) aluminium alloy adherends, (b) the aluminium alloy overlap joint design, and (c) the double CFRP/aluminium alloy hybrid scarf joint design.

4. The single CFRP/aluminium alloy hybrid joints were found to be 'bowed' after curing of the adhesive. This was caused by the different thermal expansion coefficients of the CFRP and aluminium alloy adherends. The failure loads of these hybrid joints were found to be lower, by approximately 3kN, when

compared to the aluminium alloy joints employing exactly the same design parameters.

5. Fatigue tests carried out in 'dry' test conditions were only undertaken for the aluminium alloy scarf joints with a scarf tip thickness of t_{st} = 0.4mm and t_{st} = 0.15mm. It was found that the joints mainly failed in the adherend, just outside the effective bond length, independent of the surface pretreatment (i.e. GBD, GPS or CAE). This indicates that the different surface treatments do not play a dominant part in determining the fatigue strength of these joints when tested in the 'dry' environment. It was found that the fatigue threshold of these joints was approximately 20% of the static strength of the joints.

6. Fatigue tests in 'hot/wet' test conditions were performed using all the different joint designs. For these tests, only the GBD and GPS surface treatments were used. It was found that the GBD treated joints often showed a decrease in fatigue strength compared to the GPS treated joints. Indeed it was observed that the GBD surface treatment mainly caused the joints to fail at the adhesive/aluminium alloy adherend interface and that for these joints the decrease in the fatigue threshold of the GBD treated joints tested in the 'hot/wet' test conditions was approximately 40% of the fatigue threshold measured for the 'dry' fatigue tests. However, the GPS treated joints all failed in the aluminium alloy adherend and gave for better durability when fatigue tested in the 'hot/wet' environment. Since the GPS treated joints all failed in the aluminium alloy adherend, the fatigue threshold was hence essentially the same as that found in the 'dry' fatigue tests.

7. Residual thermal stress in the GBD treated single CFRP/aluminium alloy hybrid joints was clearly seen to affect the fatigue strength of the joints. However, this was not shown to significantly affect the fatigue strength of the GPS surface treated single hybrid joints. This was due to the GPS surface treated joints failing in the aluminium alloy adherend. On the other hand, the GBD surface treated single hybrid joints failed at the adhesive/aluminium alloy interface. The longest test carried out on the GBD surface treated single hybrid joints lasted for 1.5 million cycles at a maximum applied stress of 16.5MPa. This is less than 50% of

the observed fatigue threshold of the aluminium alloy scarf joints with the same geometrical parameters as the single hybrid joints.

8.2.3 Prediction of the fatigue life-time of adhesively-bonded joints

Prediction of the fatigue life-time of adhesively-bonded scarf joints was studied using the *J*-integral method.

1. Using the modified Paris law equation for the GBD surface treated joints tested in 'hot/wet' fatigue conditions, gave a poor agreement with the experimental results at low number of fatigue cycles. However, the predicted fatigue threshold was in good agreement with the experimental results. It was also found that the predicted failure locus was as observed from the experimental results.

3. The theoretical work modelling also confirmed the experimental observations by predicting that the GPS surface treated joints would never fail in the adhesive, even in the presence of water.

4. The effects of the residual thermal stresses on the hybrid joints were predicted and revealed that they would decrease the fatigue strength of the GBD surface treated single hybrid joints. However, such residual stresses did not significantly affect the fatigue performance of the GPS surface treated joints. This was due to the relatively high fatigue strength of these joints compared to the level of the residual thermal stresses.

5. It was also shown that the prediction of the fatigue threshold could be undertaken using a relatively simple model, without needing to use the modified Paris law.

8.2.4 Repaired aluminium alloy panels

Aluminium alloy panels containing a centre crack were repaired by adhesively bonding a CFRP patch over the crack. Fatigue tests in 'dry' and 'hot/wet' test conditions were carried out on the panels. The aluminium alloy panels were surface treated with either the GBD or the GPS surface treatments. Analytical and finite element modelling were

undertaken to determine the reduction of the stress intensity factor of the repaired panels, compared to an unrepaired panel. The following points highlight the main conclusions from this investigation:

1. Crack growth in the GBD repair panel tested in the 'hot/wet' fatigue conditions experienced a relatively high growth rate compared to the GBD tests undertaken in the 'dry' environment and to all the GPS treated repairs. For example, the fatigue life of the GBD repair panel tested in the 'hot/wet' fatigue conditions was approximately 200 thousand cycles. On the other hand, the other tests were able to sustain a life of approximately 300 thousand cycles. This is significantly very high when compared to the unrepaired panel, where the fatigue life was approximately 30 thousand cycles. Thus, again the use of the GPS surface treatment on aluminium alloy adherends greatly increases the durability of adhesively-bonded joints.

4. Indeed it was found that, when using the 'hot/wet' test condition, the silane (i.e. GPS) surface treated repair panels did not show any significant increase in the crack growth rate compared to tests carried out in the 'dry' test condition.

5. Significant interfacial debonding was observed at the adhesive/aluminium alloy interface for the GBD surface treated crack patch panel tested in the 'hot/wet' conditions; whilst the other three repair panels mainly failed in the CFRP composite.

6. The predicted stress intensity factors for the repair panels from using finite element analysis were in very good agreement with the values calculated from an the analytical method. For example, it was found that for a crack tip at the edge of the repair patch (i.e. crack length, a = 50mm), the repair stress intensity factor, K_r, is approximately 12.5MPam$^{0.5}$. This was significantly lower in value than for the unrepaired panel (i.e. K_u = 30MPam$^{0.5}$). This was the underlying reason for the far lower crack growth rates seen in the repaired panels compared to the unrepaired panels.

8.3 Recommendations for future work

From the present project, it may be concluded that the durability of adhesively-bonded joints, for aerospace structures, using the GPS surface treatment is far superior compared to the GBD surface treatment. The experiments used in the present project were able to clearly distinguish the higher fatigue strength of the GPS treated joints compared to the GBD treated joints. In addition, it was found that the GPS treated joints never failed at the adhesive/aluminium alloy adherend interface. However, due to time constraints, there are some aspects that were not fully explored. These are included in this section where suggestions for future work are presented. The suggestions are:

1. The use of the threshold strain energy release rate, G_{th}, as a material property to determine the fatigue threshold of adhesively-bonded joints appears to be valid for different joint designs. However, prediction of the fatigue life-time of adhesive joints using fracture mechanics (i.e. the plot of the rate of crack growth per cycle, *da/dN* versus the maximum strain energy release rate, G_{max}) does not always provide accurate predictions, especially at low numbers of fatigue cycles. The problem appears to be the inherent scatter observed in the fracture mechanics data, and also the sensitivity of the modified Paris law to these variations. Furthermore, low cycle fatigue may be influenced by micro-level variations at the bonding surfaces and defects in the bulk adhesive and the adherends. Hence, in order to predict accurately the complete fatigue life-time of adhesive joints, it is proposed that a combination of micromechanics and macro-mechanics be investigated.

2. The use of a cohesive zone model (CZM) could be used to predict post crack-initiation behaviour of adhesive joints. Furthermore, adhesive joints may exhibit a change in crack growth direction. This cannot be easily predicted using the present modified Paris law approach, but could be readily predicted using a CZM approach coupled with a finite element analysis model.

3. The data collection method for the crack patch repair panel experiments, where crack growth at the bonding surface or the adhesive/CFRP can be determined, needs to be improved. Due to time constraints, a video camera was used in the present project to record crack growth in the aluminium alloy panel. However,

with more accurate information on the crack growth at the bonding surface, or in the adhesive/CFRP patch, predictions of the reduction of the stress intensity factor in the repair panels would be more accurate. The values of the stress intensity factor could then be used to predict the fatigue crack growth behaviour of the panels.

4. A more detailed thermal-mechanical analysis to investigate the effect of residual thermal stresses in CFRP/aluminium alloy repair panels could be undertaken. It was observed from the experiments that the panels were distorted in a manner where the panel was bowed towards the aluminium alloy surface. On a one sided repair, this appears to reduce the crack opening displacement at the unrepaired side of the panel. Hence, the effect of residual thermal stresses may actually reduce the fatigue crack growth rate in the aluminium alloy panel.

REFERENCES

1. Young, T., (1805) Trans. Roy. Soc. **95**, 65.

2. Kootsier, J., (1975) *Metal-to-metal adhesive bonded aircraft structures*, National SAMPE. Tech. Conf., **7**, Albuquerque, p. 126-140.

3. Allen, K.W., Chan, S.Y.T. and Armstrong, K.B. (1981) *Cold-setting adhesives for repair purposes using various surface preparation methods*, Int. J. Adhesion Adhesives **2**(4), p. 239-247

4. Adams, A.N.N., (2001) *The durability of organosilane pretreated adhesive joints,* Mechanical engineering, Imperial College: London (PhD Thesis)

5. Wake, W.C. (1982) *Adhesion and the formulation of adhesives*, Applied Science Pub. London, p.54.

6. Volkersen, O. (1938) *Die nietkraftverteilung in zungbeanspruchten nietverbindunger mit konstanten laschenquerschnitten*, Luftfahrtforsch **15**, p. 4-47.

7. Goland, M., Buffolo, N.Y. and Reissner, E. (1944), *The stresses in cemented joints*, J. Appl. Mech. **11**, A17-A27.

8. Adams, R.D. and Peppiatt, N.A. (1974*) Stress analysis of adhesive-bonded lap joint*, J.Strain Anal. **9**, p. 185-196.

9. Kinloch, A.J., (1990) *Adhesion and adhesives: science and technology*, Chapman and Hall, London.

10. Woo, H., Reucroft, P.J., Jacob, R.J.J., (1993) *Electrodeposition of organofunctional silanes and its influence on structural adhesive bonding.* J. Adhesion, **7**(7), p. 681-697.

11. Ishida, H., (1983) in *Adhesion aspects of polymeric coatings*, K.L. Mittal, Editor., Plenum Press, NewYork. p. 45.

12. Adams, R.D., Atkins, R.W., Harris, J.A. and Kinloch, A.J., (1986) *Stress analysis of failure properties of carbon-fibre-reinforced-plastic/steel double lap joints*, J. Adhesion, **20**, p. 29-53

13. Hart-Smith, L.J., (1973) *Adhesive-bonded scarf and stepped lap joints*, NASA contractor **Report CR 112237**.

14. Nguyen, V. and Kedward, K.T., (2001) *Non-linear modeling of tubular adhesive scarf joints loaded in tension, J. Adhesion*, **76**, p. 265-292

15. Hart-Smith, L.J., (1970) *The strength of adhesive-bonded single-lap joints*, Douglas Aircraft Company IRAD **Report No. MDC-J0742.**

16. Hart Smith, L.J., (1987) *Design of adhesively bonded joints*, Joining Fibre-Reinforced Plastics, Matthews, F.L., Ed. Elsevier Applied Science, p. 271-311.

17. Hart Smith, L.J., (1981) *Stress analysis: A continuum mechanics approach*, Developments in adhesive – 2, Kinloch, A.J., Ed. Applied Science Pub.: London, p. 1-44.

18. Abel, M-L., Digby, R.P., Fletcher, I.W., Watts, J.F., (2000) *Evidence of specific interaction between gamma-glycidoxypropyltrimethoxysilane and oxidised aluminium using high mass resolution ToF-SIMS.* Surf. Inter. Anal., **29**(2), p. 115-125.

19. Anand, J.N., (1970) *Interfacial contact and bonding in autohesion – 5*, J. Adhesion, **2**, p. 23-28.

20. Gettings, M. and Kinloch, A.J., (1977) *Surface analysis of polysiloxane/metal oxide interfaces*, J.Mater. Sci. **12**, p. 2511-2518.

21. Voyutskii, S.S., (1962) *Adhesion and autohesion of polymers*, Adhesive Age **5**(4), p. 30-36.

22. van Ooij, W.J., Child, T.F., (1997) *Silane coupling agents treatments of metals for corrosion protection*, Fourth international forum and business development conference on surface modification, couplants and adhesion promotion, Boston, Massuchusetts.

23. Abel, M-L., Rattana, A., Watts, J.F., (2000 *The interaction between gamma-glycidoxypropyltrimethoxysilane with oxidised aluminium substrates: The effect of drying temperature*, J. Adhesion, **73**, p. 313-340.

24. Sennett, M.S., Wentworth, S.E., Kinloch, A.J., (1995) *Investigation of the interaction of silane-based adhesive primers with metal oxide surfaces using molecular dynamics simulations.*, J. Adhesion, **54**, p. 23-31.

25. Sung, N.H., Kaul, A., Chin, I., Sung, C.S.P., (1982) *Mechanistic studies of adhesion promotion by gamma-aminopropyltrethoxysilane in alpha-alumina/polyethylene joint*, Polym. Eng. Sci., **22**, p. 637-644.

26. Mazza, J.J., (1996) *Grit blast/silane surface treatments for structural bonding of aluminium*, Proceedings of the 9th annual meeting of the Adhesion Society, Myrtle Beach, South California.

27. Irwin, G.R., (1973) *Structural aspects of brittle fracture*, Appl. Mater. Res., **3**(2), p. 65-81.

28. Abdel Wahab, M.M., (2000) *On the use of fracture mechanics in designing a single lap adhesive joint*, J. Adhesion, **14**, p. 851-865.

29. Lang, T.P. and Mallick, P.K., (1998) *Effect of spew geometry on stresses in single lap adhesive joints,* Int. J. Adhesion and Adhesive, **18**, p. 167-177.

30. Hildebrand, M. (1994) *Non-linear analysis and optimization of adhesively bonded single lap joints between fibre-reinforced plastics and metals,* Int. J. Adhesion and Adhesives, **14**, p. 261-267.

31. Rispler, A.R., Tong, L.Y., Steven, G.P., Wisnom, M.R., (2000) *Shape optimisation of adhesive fillets*, Int. J. Adhesion and Adhesives, **20**, p. 221-231.

32. Hart Smith, L.J., (1985) *Designing to minimize peel stresses in adhesive-bonded joints*, Delamination and Debonding of Materials – **ASTM STP. 876-**, Johnson, W.S., Ed., ASTM, p. 238-266.

33. Tsai, M.Y., Oplinger, D.W. and Morton, J., (1998) *Improved theoretical solutions for adhesive lap joints*, Int. J. Solids Structures, **35**, p. 1163-1185.

34. Webber, J.P.H., (1981) *Scarf repair joints in carbon fibre reinforced plastic strips*, J. Adhesion, **12**, p. 257-281.

35. Lubkin, J.L., (1957) *Theory of adhesive scarf joints,* J. Appl. Mech., p. 255-.

36. Hart-Smith, L.J., (1981) *Further developments in the design and analysis of adhesively-bonded structural joints*, Joining of Composite Materials, **ASTM STP 749** (3).

37. Gleich, D.M., Van Tooren, M.J.L. and DeHaan, P.A.J., (2000) *Shear and peel stress analysis of an adhesively bonded scarf joint*, J. Adhesion Sci. Technol., **14**, p. 879-893.

38. Soutis, C. and Hu, F.Z., (1997) *Repair design of composites and efficiency of scarf patch repairs*, 11th Int. Conf. Composite Materials, Gold Coast, Aust., **6**(6), p. 395-404.

39. Qian, Z.Q. and Akisanya, A.R., (1999) *An investigation of the stress singularity near the free edge of scarf joints*, Eur. J. Mech. A/Solids, **18**, p. 443-463.

40. Akisanya, A.R. and Fleck, N.A., (1997) *Interfacial cracking from the free-edge of a long bi-material strip*, Int. J. Solids Struct., **34**, p. 1645-1665.

41. Groth, H.L., (1988) *Stress singularities and fracture at interface corners in bonded joints*, Int. J. Adhesion Adhesives, **8**, p. 107-113.

42. Wang, C.H. and Rose, L.R.F (2000) *Compact solutions for the corner singularity in bonded lap joints*, Int. J. Adhesion Adhesives, **20**, p. 145-154.

43. Dundurs, J., (1969) *Mathematical theory of dislocations*, American Society of Mechanical Engineers: New York.

44. Griffith, A.A., (1920) Phil. Trans. Roy. Soc., **A221**, p. 163-.

45. Orowan, E., (1948) Rept. Prog. Phys. **12**, p. 185-.

46. Rybicki, E.F. and Kanninen, M.F., (1977) *A finite element calculation of stress intensity factors by a modified crack closure integral*, Eng. Fract. Mech., **9**, p. 931-938.

47. Raju, I.S., (1986) Simple formulas for strain energy release rates with higher order and singular finite elements, NASA **CR 178186**.

48. Rice, J.R., (1968) *A path-independent integral and the approximate analysis of strain concentration by notches and cracks*, J. Appl. Mech., **35**, p. 379-386.

49. Hadavinia, H., Kinloch, A.J., Williams, J.G. and Taylor, A.C., *Mode mixity at an interface crack – single lap joint*, private communication.

50. Irwin, G.R., (1958) Fracture, Handbuch der Physik, **6**, p. 551.

51. Comyn, J., (1983) *Kinetics and mechanism of environmental attack*, Durability of Structural adhesives, ed. Kinloch, A.J., Applied Science Pub.: London and New York.

52. Althof, W., (1979) *The diffusion of water vapour in humid air into the bondlines of adhesive bonded metal joints*, 11th Nat. SAMPE Tech. Conf., **13-15**, p. 309-332.

53. Paris, P. and Erdogan, F., (1963) *A critical analysis of crack propagation laws*, J. Basic Eng., **85**, p. 528-534.

54. Kinloch, A.J. and Osiyemi, S.O., (1993) *Predicting the fatigue life of adhesively-bonded joints*, J. Adhesion, **43**, p. 79-90.

55. Kanninen, M.F. and Popelar, C.H., (1985) *Oxford Engineering Science Series: 15 Advanced fracture mechanics*, Oxford University Press: New York.

56. Little, M.S.G., (1999) *The durability of structural adhesive joints*, Mechanical engineering, Imperial College: London

57. Cotter, J.L., (1977) Developments in Adhesives-1, ed. Wake, W.C., Applied Science Pub: London.

58. Martin, R.H. and Murri, G.B., (1990), *Characterization of mode I and mode II delamination growth and thresholds in AS4/PEEK composites*, ASTEM STP **1057**, p. 251-270.

59. Mostovoy, S. and Ripling, E.J., (1975) Adhesion Science and Technology 9B, ed. Lee, L.H., Plenum Press: New York.

60. Baker, A.A., (1984) *Repair of cracked or defective metallic aircraft components with advance fibre composites – an overview of australian work*, Comp. Struct., **2**, p. 153-181.

61. Crank, J.A.P., G.S., (1968) Diffusion in Polymers, Academic Press.

62. Jones, R.M., (1998) Mechanics of composite materials, Taylor & Francis: Philadelphia.

63. Curley, A.J., Hadavinia, H., Kinloch, A.J. and Taylor, A.C., (2000) *Predicting the service-life of adhesively-bonded joints*, Int. J. Fract., **103**, p. 41-60.

64. Baker, A.A., (1993) *Repair efficiency in fatigue-cracked aluminium components reinforced with boron/epoxy patches*, Fat Fract Eng. Mat. Struct., **16**(7), p. 753-765.

65. Chang, T., Sproat, E.A., Lai, Y-H., Shephard, N.E., Dillard, D.A., (1997) *A test method for accelerated humidity conditioning and estimation of adhesive bond durability*, J. Adhesion, **60**, p. 153-162.

66. Baker, A.A. (1987) in Bonded Repair of Aircraft Structures, ed. Baker, A.A. and Jones, R., Martinus Njhoff Pub.:Dordrecht, p. 107-162.

67. Pirondi, A. and Nicoletto, G., (2002) *Mixed mode I/II fracture toughness of bonded joints*, Int. J. Adhesion & Adhesives, **22**, p. 109-117.

68. Molent, L., Callinan, R.J. and Jones, R., (1989) *Design of an all boron/epoxy doubler reinforcement for the F-111C wing pivot fitting: Structural aspects*, Comp. Struct., **11**, p. 57-83.

69. Rose, L.R.F., (1987) in Bonded Repair of Aircraft Structures, ed. Baker, A.A. and Jones, R., Martinus Njhoff Pub.:Dordrecht, p. 77-105.

70. Kelly, L.J., (1987) in Bonded Repair of Aircraft Structures, ed. Baker, A.A. and Jones, R., Martinus Njhoff Pub.:Dordrecht, p. 3-17.

71. Chalkley, P.D. and Baker, A.A., (1999) *Development of a generic repair joint for certification of bonded composite repairs*, Int. J Adhesion & Adhesives, **19**, p. 121-132.

72. Higgin, A., (2000) *Adhesive bonding of aircraft structures*, Int. J. Adhesion & Adhesives, **20**, p. 367-376.

73. Davis, M. and Bond, D. (1999) *Principles and practices of adhesive bonded structural joints and repairs*, Int. J Adhesion & Adhesives, **19**, p. 91-105.

74. Myhre, S.H. and Beck, C.E. (1979) *Repair concepts for advanced composite structures*, J Aircraft, **16**(10), p. 720-728.

75. Myhre, S.H. and Labor, J.D., (1981) *Repair of advanced composite structures,* J. Aircraft, **18**(7), p. 546-552.

76. Rose, L.R.F., (1981) *An application of the inclusion analogy for bonded reinforcements*, J. solids Struct., **17**, p. 827-838.

77. Rose, L.R.F., (1982) *A cracked plate repaired by bonded reinforcements*, Int. J. Fract., **18**(2), p. 135-144.

78. Digby, R.P., Shaw, S.J., (1998) *The international collaborative programme on organosilane coupling agents: an introduction*, Int. J. Adhesion & Adhesives, **18**, p. 261-264.

79. Chiu, W.K., Chalkley, P.D. and Jones, R., (1993) *Characterisation of FM73 film adhesive*, National conference publication – Inst. Eng. Australia NCP, **6**(2), p. 409-413.

80. Taylor, A.C., (1997) The impact and durability performance of adhesively-bonded metal joints, Mechanical engineering, Imperial College: London. (PhD Thesis)

81. Krenk, S., Jonsson, J. and Hansen, L.Pl, (1996) *Fatigue analysis and testing of adhesive joints*, Eng. Fract. Mech., **53** (6), p. 859-872.

82. Underhill, P.R. and DuQuesnay, D.L.,(2001) *The Dependence of the Fatigue Life Of Adhesive Joints on Surface Preparation*, private communication.

83. Ross, R.B., (1992) Metallic materials specification handbook, Chapman & Hall: London, 4th ed.

84. Adams, R.D. and Wake, W.C., (1984) Structural adhesive joints in engineering, Elsevier Applied Science: London.

85. Boresi, A.P., Schmidt, R.J., Sidebottom, O.M., (1993) Advanced Mechanics of Materials, John Wiley & Sons, p. 615-616.

86. Harris, C.E. and Shuart, M.J., (2001) *An assessment of the state-of-the-art in the design and manufacturing of large composite structures for aerospace vehicles,* 22nd SAMPE Europe International Conference, Paris, France (also available at http://techreports.larc.nasa.gov/ltrs/PDF/2001/mtg/NASA-2001-22sampe-ceh.pdf).